Dissertation zur Erlangung des Doktorgrades

der Fakultät für Chemie und Pharmazie

der Ludwig-Maximilians-Universität München

Analytical Imaging in the Pharmaceutical Industry and Beyond:

Intelligent Combinations – Unique Insights

Hannes Desmond Frederic Dettlaff

aus

Pinneberg, Deutschland

2021

Erklärung

Diese Dissertation wurde im Sinne von § 7 der Promotionsordnung vom 28. November 2011 von Herrn Prof. Dr. Konstantin Karaghiosoff betreut.

Eidesstattliche Versicherung

Diese Dissertation wurde eigenständig und ohne unerlaubte Hilfe erarbeitet.

München, 09.02.2021

Hannes Dettlaff

Dissertation eingereicht am: 09.02.2021

1.Gutachterin / 1. Gutachter: Prof. Dr. Konstantin Karaghiosoff

2.Gutachterin / 2. Gutachter: Prof. Dr. Thomas M. Klapötke

Mündliche Prüfung am: 20.04.2021

Die vorliegende Arbeit wurde vom Januar 2018 bis Dezember 2020 bei der Hexal AG am Standort Holzkirchen in der Abteilung „Analytical Development“ unter Aufsicht des Abteilungsleiters Dr. Hans-Christian Müller und unter Betreuung von Prof. Dr. Konstantin Karaghiosoff des Department Chemie der Ludwig-Maximillians Universität München angefertigt.

Contents

Abbreviations

°C	Degree Celsius
API	Active pharmaceutical ingredient
Avg.	Average
CAN	Ceric ammonium nitrate
CQA	Critical quality attribute
D(0.X)	The portion of particles with diameters smaller than this value is X%
DCLS	Direct classical least squares
DTA	Differential thermal analysis
EDX	Energy-dispersive X-ray spectroscopy
ESD	Electrostatic discharge
ESDv	Equivalent sphere diameter, determined via the volume
FDA	Food and Drug Administration
FDF	Full dosage form
FS	Friction sensitivity
GMP/GLP	Good Manufacturing Practice / Good Laboratory Practice
HPLC	High-performance liquid chromatography
IS	Impact sensitivity
MCR-ALS	Multivariate curve resolution – Alternating least squares
Micro-CT	Micro-computed tomography
QbD	Quality by design
SA	Stearic acid
SD	Standard deviation
SEM	Scanning electron microscope
TDD	Transdermal drug delivery
TGA	Thermogravimetric analysis

TTS	Transdermal therapeutic system
UV	Ultraviolet
WHO	World Health Organization
wt%	Percentage by weight
XRPD	X-ray powder diffraction

1 Introduction

Worldwide, there is high demand for over the counter as well as prescription drugs. According to a study of the National Center for Health Statistics (NCHS), in the United States alone, in the time between 2015 and 2016, almost half of the population, nearly 150 million people of all sexes, races and ages, used one or more prescription drugs in the past 30 days.[1]

Due to their vital importance, pharmaceutical products are subject to strict regulations to ensure safe and efficacious drugs as well as accurate and appropriate information available to the public.

Government organizations such as the Bundesinstitut für Arzneimittel und Medizinprodukte (BfArM), the European Medicine Agency (EMA) and the Food and Drug Administration (FDA) as well as the International Council for Harmonization of Technical Requirements for Pharmaceuticals for Human Use (ICH) publish and / or enforce guidelines and rules to ensure the maximum quality and safety of pharmaceutical products.[2-5]

Beginning at the start of the 20th century with the creation of the first government regulatory agencies and the passing of laws making it illegal to sell contaminated drugs, a gradual improvement process, for patient safety began. With the 1938 Federal Food, Drug and Cosmetic (FD&C) Act manufacturers had to prove the safety of their products. With changes after the 1960s Thalidomide scandal, companies were required to show efficacy of their products, regulation of clinical trials was tightened and mandatory tests on animals before testing on humans was implemented.[6]

At the end of the 1960s, the World Health Organization (WHO) published its first universal guideline on the matter of manufacturing of safe pharmaceuticals.[7] A decade later, the first Good Manufacturing Practice (GMP) for drugs and medical devices and Good Laboratory Practice (GLP) regulation were passed, leading to the rules in place today.[6]

Since this work was developed in the context of a pharmaceutical generics company, a short explanation of the pharmaceutical industry is provided.

Pharmaceutical companies can broadly be divided into two categories, innovators (also called originators) and generics. Innovators develop new drug products, starting with the search for new drug molecules to the formulation of the final dosage form. It is estimated

that this process from start to finish, including failed projects, costs about $2.6 billion dollars, showing an upward trend over the last decade.[8]

Generic medicine, as defined by the World Health Organization (WHO), are pharmaceutical products, which are interchangeable with the innovator product, are manufactured without a license from the innovator manufacturer and are marketed after the expiry of the basis patent (molecule patent) and exclusivity grant.[9]The approval route for generic drugs is significantly shortened and therefor considerable less cost intensive. Compared to new products, it has to be shown that the generic product performs bioequivalent to the originator product in a clinical study, but no further animal or bioavailability studies have to be conducted.[10] According to Chapter 21 CFR (Codes of *Federal Regulations*) Part 320.1, bioequivalence is defined as "*[...] the absence of a significant difference in the rate and extent to which the active ingredient or active moiety in pharmaceutical equivalents or pharmaceutical alternatives becomes available at the site of drug action when administered at the same molar dose under similar conditions in an appropriately designed study.*".[11]

Consequently, generics companies play a central role in creating competition on the drug market and driving down prices for consumers.

There have been two major statements in this century, leading the pharmaceutical industry as a whole, as well as the generic sector specifically towards new measurement techniques. Firstly, the FDA published its report on "Pharmaceutical cGMP for the 21st Century" with the aim to foster the modernization of pharmaceutical development processes and further improving product quality. The underlying core objective was to "*Encourage the early adoption of new technological advances by the pharmaceutical industry*".[12]

Secondly, the ICH Q8 guideline on pharmaceutical development was issued, where the core paradigm is quality by design (QbD). A philosophy, which underlines that quality cannot be tested into products but has to be designed into the product via the development and manufacturing processes. The guideline advises pharmaceutical companies to systematically evaluate, understand and refine the formulation and manufacturing process and overall encourage concepts that are more scientific. The identification of critical quality attributes (CQAs) plays a central role. It is advised that their effects on the final product and the functional relationships between characteristics of the materials and the process parameters are thoroughly investigated. The aim is to incentivize manufactures to develop greater understanding of their product and manufacturing processes to in return, permit more flexible regulatory approaches.[13]

1.1 References

[1] https://www.cdc.gov/nchs/data/databriefs/db334-h.pdf, (accessed 04.11.2020).

[2] https://www.bfarm.de/DE/Home/home_node.html, (accessed 04.11.2020).

[3] https://www.ema.europa.eu/en, (accessed 04.11.2020).

[4] https://www.fda.gov/home, (accessed 04.11.2020).

[5] https://www.ich.org/, (accessed 04.11.2020).

[6] B. K. Immel, *BioPharm.*, **2000**, 26-36.

[7] K.T. Patel, N.P. Chotai, *Pharmazie*, **2008**, 251-255.

[8] J.A. DiMasi, H.G. Grabowski, R.W. Hansen, *J. Health Econ.*, **2016**, 20-33.

[9] https://www.who.int/medicines/areas/access/NPrices_Glossary.pdf?ua=1, (accessed 04.11.2020).

[10] S. Dunne, B. Shannon, C. Dunne, W. Cullen, *BMC Pharmacol. Toxicol.*, **2013**, 14:1.

[11] U.S. Department of Health and Human Services Food and Drug Administration, *Code of Federal Regulations Title 21, Part 320*, **2019**.

[12] https://www.fda.gov/about-fda/center-drug-evaluation-and-research-cder/pharmaceutical-quality-21st-century-risk-based-approach-progress-report, (accessed 04.11.2020).

[13] https://www.ema.europa.eu/en/ich-q8-r2-pharmaceutical-development, (accessed 04.11.2020).

2 Aim of this work

Development of a generic drug product goes through several stages, starting with so-called deformulation. Here the innovator product is thoroughly investigated to get information about the physical and chemical properties of the full dosage form (FDF) as well as indicators concerning the manufacturing process. Especially for the chemical composition standard measurement techniques such as high-performance liquid chromatography, mass spectrometry and X-ray powder diffraction (XRPD) deliver reliable information. Dissolution testing is employed to get information about the release rate of the active pharmaceutical ingredient (API) and disintegration time of the product. Data about the particle size distribution of components can only be gathered on powders or suspensions using laser diffraction. A common characteristic of all these methods and a major drawback is that samples are destroyed before or during analysis. Either this is necessary to prepare the sample for analysis or the analysis step itself leads to the destruction of the specimen. This removes the possibility for multiple measurements on the same sample, with the aim of excluding statistical scattering, using different analytical tools. Another disadvantage is that the localization of the individual components is either hindered or impossible.

Based on a successful deformulation stage, starting points for the development of the manufacturing process are gained. Additionally, measurement and analysis parameters for the starting materials and the final product are established, which can be used throughout the development as reference points.

An area that is severely lacking in the pharmaceutical industry, are analytical imaging techniques that allow for the localization of individual components or chemical and physical parameters. They can be used for the detection and explanation of errors, can help to understand dissolution behavior and give insights into the employed manufacturing processes. The most prevalent methods are light microscopy and scanning electron microscopy (SEM), which allow for the collection of information primarily about the morphology, but lack the ability for chemical investigations. The combination of SEM with energy-dispersive X-ray spectroscopy (EDX) makes identification and localization of most atomic species possible, but fails when components do not have unique atoms (e.g. samples comprised of only organic substances). The localization of chemical components on 2D surfaces can be accomplished using Raman microscopy, which is compared to the previous methods an advanced analysis technique that is not regarded as a standard tool. With Raman microscopy, a multitude of individual Raman spectra is collected over a surface

area and analyzed using computer algorithms. The main problem of this method is that information for opaque samples is only obtainable in 2D. Resulting from this, if data from the interior of a sample is needed, the sample has to be cut or otherwise physically opened, destroying the sample. Another imaging technique that emerged especially over the last decade is micro computed tomography (micro-CT). A method used for a long time in the medical sector that is thanks to advances in processing power and device specific improvements now able to record at resolutions that allow for the implementation in a variety of different scientific fields. Analogous to the medical application, data is collected using the attenuation of x-ray beams traversing a sample. The main advantages of micro-CT are that it does not require any invasive sample preparation and that the measurement yields detailed information of the entire sample in 3D. The drawback of this method is that the gathered 3D information usually does not allow precise conclusions about the chemical composition of the specimen.

The focus point of this work will be the combination of different analytical imaging techniques to overcome the drawbacks of the individual methods and to give completely new insights into pharmaceutical products (see Figure 1).

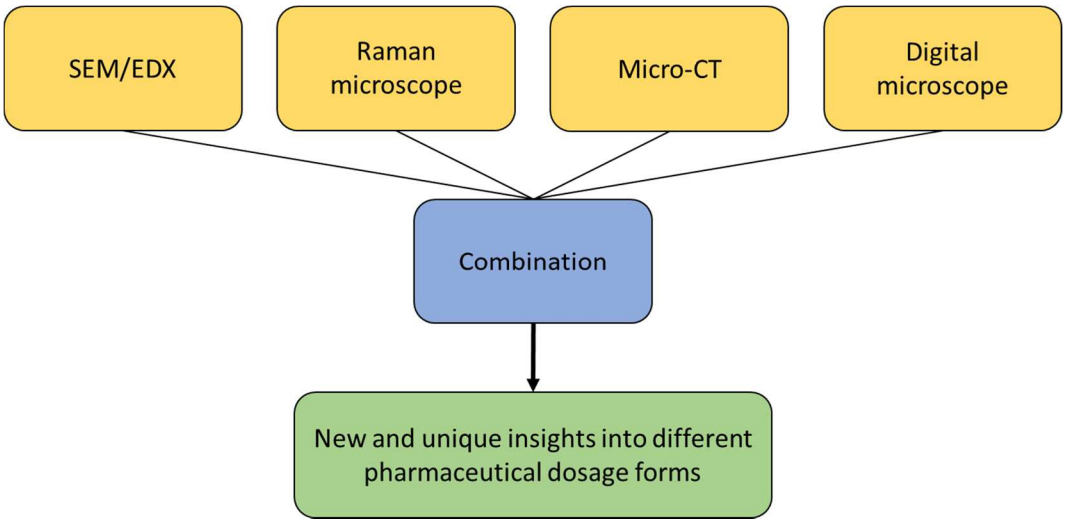

Figure 1: Strategic outline for the implementation of imaging techniques.

The first step is the assessment of the current implementation of standard (SEM/EDX and digitally enhanced light microscopy), established (Raman microscopy) and emerging (micro-CT) measuring instruments in the pharmaceutical industry and comparable fields of application. Next is the development of suitable procedures for the combination of multiple instruments. Here particular attention will be paid to the sample preparation and measurement parameters required for the connection of different analytical techniques. After successful data collection, linking the information to get results that are larger than the

sum of its parts and enabling completely new visualization possibilities on the scale of microns will be the focus. After this, the methods are used for a variety of different applications in the pharmaceutical field such as the deformulation of innovator products, identification of reasons for faulty batches, assistance with study batch selection and further combination with standard analytical tools such as dissolution testing.

3 Methods

3.1 Micro Computed Tomography (micro-CT)

3.1.1 History

Micro-CT is a measuring technique, where a three-dimensional image of the relative density distribution of a sample is created using X-rays and computing power.

With the discovery of a new type of radiation by *Röntgen* in 1895, X-rays laid the foundation for the development of micro-CT systems, as we know them today.[1] The important feature of X-rays is the ability to penetrate material, which opens possibilities to generate images from throughout the sample without the need of prior cutting or other ways of destructive preparation. This is beneficial, when dealing with life samples, valuable objects or when further measurements on the same sample are desired.

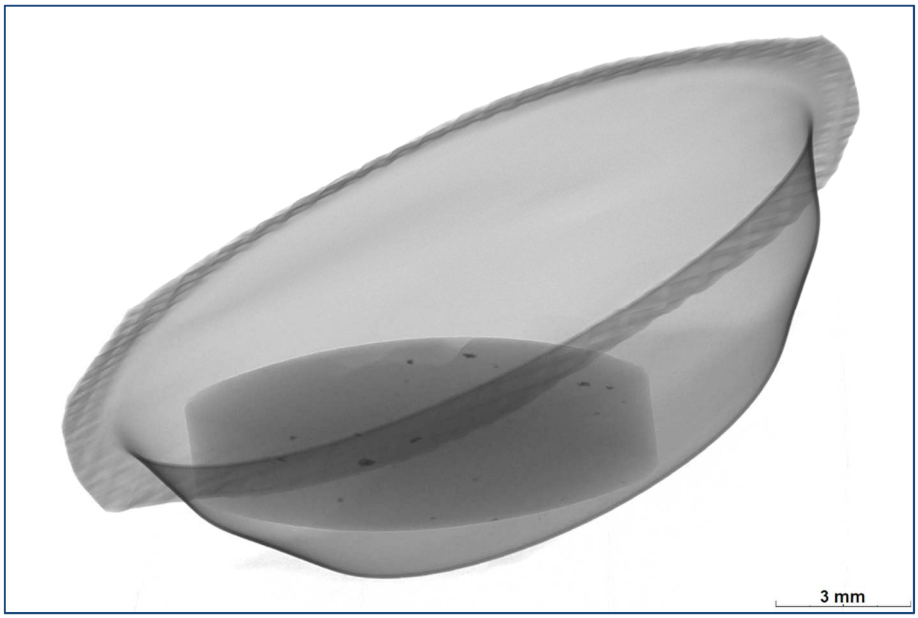

Figure 2: Radiograph of a pharmaceutical tablet sealed in a blister cup.

This feature quickly led to adoption of the new technique for use in medical applications, in the form of medical radiography.[2,3] This is an imaging technique where radiographs or sometimes called “shadow images”, projections of 3D objects on 2D detector planes, are collected (Figure 2). This approach is useful as a fast way to see, for example if a bone is broken, but due to the lack of depth information, it is not applicable in systems that are more

complex. To improve on this and to gain true 3D images, computerized transverse axial tomography was developed and pioneered by *Hounsfield* in 1973. The achievable resolutions were in the range of 10 mm to 250 µm.[4] The broad idea was to collect projection images of a sample from different angles and then ,in a second step, use dedicated computer algorithms to reconstruct a 3D image.[5] In the 1980s, the first micro-CT instruments for laboratory use were introduced and a spatial resolution of ~10 µm could be achieved.[6,7] The first reported usage of micro-CT in the pharmaceutical context came from *Farber et al.* in 2003 studying the porosity and morphology of granules.[8] Later in the same year, *Ozeki et al.* were first to utilize micro-CT to investigate entire pharmaceutical dosage forms. Imaging was used for the comparison of compression characteristics of differently dry-coated tablets.[9]

3.1.2 Recent Examples – State of the Art

Due to its non-destructive nature and possibility to visualize the internal structures of samples, micro-CT imaging is emerging as a powerful tool for the analysis of a variety of different pharmaceutical applications. Such as:

- Mapping the spatial distribution of different components
- Process control of manufacturing
- Length, area and volume measurements
- Layer thickness analysis
- Improvement of 3D printed tablet systems

Solid dispersions are a method used for poorly water-soluble drugs to improve oral bioavailability. The visualization of the 3D microstructure and spatial distribution of different phases was performed with micro-CT. When compared to dissolution testing, a correlation between patches with bad phase separation and poorer dissolution performance was found.[10]

The manufacturing of systems for controlled release of API is an important field of research in the pharmaceutical field. A novel way to produce hollow spherical granules (HSGs) was developed and different techniques used for characterization. The inner structure of different granule formulations was analyzed using micro-CT. Shell thickness, diameter and volume percentage of hollow spheres was determined for n=10 granules and gave insight into the content uniformity of the manufactured products.[11]

3D printing is an emerging new technology for the manufacturing of drug products, making it possible to create tailor-made, structurally complex tablets for different fields of

application. Micro-CT imaging is used in this context to control the dimensional accuracy of the printed tablets by comparing them to the computer-aided design (CAD) models.[12]

Understanding the influence of different manufacturing parameters on tablet properties is an integral part of a functioning QbD approach. The tendency for fracturing or tablet lamination was analyzed in a design of experiment (DoE) study varying formulation and process variables. Micro-CT was used to quantify fractures and internal structure changes.[13]

A way to regulate the dissolution of APIs from tablets is via functional coating. The specific location of the drug release can be influenced, for example with coatings only soluble at certain pH ranges. Another desirable attribute of coatings can be the protection against degradation during storage. Micro-CT can be employed to analyze the homogeneity and thus the functionality of film coating of entire tablets.[14]

3.1.3 Setup

A micro-CT setup consists of three main components (see Figure 3). The first is an X-ray source, in this case an x-ray tube producing a conic beam. Depending on the sample material, different acceleration voltages and filters can be employed to fine-tune the energy arriving at the sample.

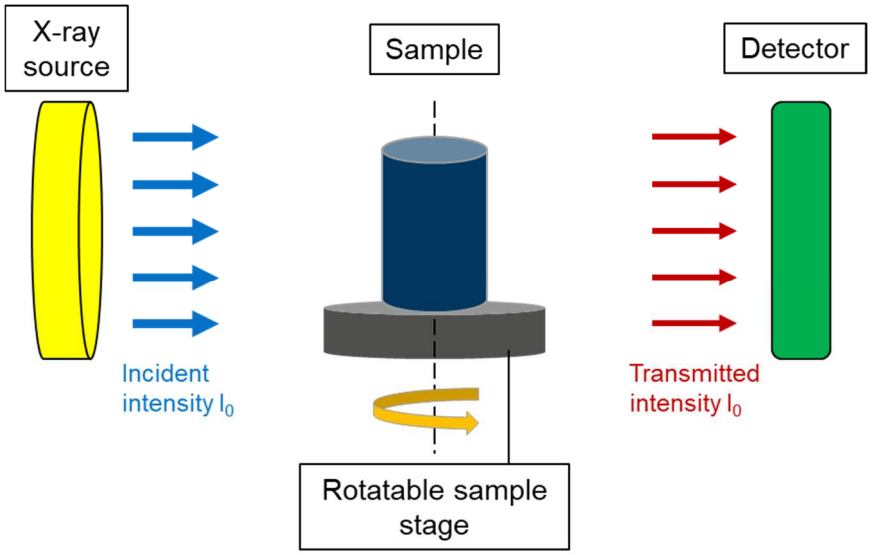

Figure 3: Illustration of a micro-CT setup.

Synchrotron radiation can be used as well but requires a much more complex system, not attainable in a standard laboratory setup and is therefore not discussed further. The specimen is fixed on a rotatable sample stage, which sits between the source and the

detector. This allows for the recording of images from different angles. The intensity of the attenuated x-rays transmitting through the sample is measured at the detector. In a first step, the scintillator converts the incoming radiation to visible light photons, which are then recorded on a 2D CCD sensor producing the radiograph. The device used is Bruker Skyscan 1272 (see Figure 4), equipped with an x-ray source producing 20 - 100 kV, 10 W, a maximum scanning space of 75 mm in diameter and 70 mm in length and a 11 mega pixel (4032x2688 pixels) cooled CCD x-ray detector fiber-optically coupled to a scintillator. The nominal resolution (pixels on the object at maximum magnification) is according to the manufacturer < 0.45 µm.

Figure 4: Micro-CT model Bruker Skyscan 1272

Data acquisition, reconstruction, analysis and visualization in 2D and 3D was performed using Bruker developed software.[15-19] Depending on the chosen parameters, measurement durations can range from roughly one hour to one day.

3.1.4 Theoretical Background

The underlying physical principle in micro-CT used to generate images is that materials of different chemical composition and density absorb different amounts of nuclear radiation. These differences in absorption then generate the grey scale radiographs. The absorption of monochromatic x-rays by matter can be described by the Beer-Lambert law:

$$I = I_0 e^{-\int \mu(s) ds} \tag{1}$$

where intensity of the source is denoted by I_0, the linear attenuation coefficient by μ and the raypath by s.[5] By rearranging equation (1) it can be shown, that the integrated linear attenuation coefficient can be derived at each point of the radiograph from:

$$\int \mu(s) ds = -\ln\left(\frac{I}{I_0}\right) \tag{2}$$

To approximate the ability of a material to absorb x-ray photon energy the linear attenuation coefficient μ can also be described as:

$$\mu = \rho \cdot \frac{Z}{A} \cdot N_{AV} \cdot \left(a + b \cdot \frac{Z^{3.8}}{E^{3.2}} \right) \quad (3)$$

where ρ is the material density, Z is the effective atomic number, A is the atomic weight, N_{AV} is Avogadro's number, a is the Klein-Nishina coefficient describing the scattering cross-section, which is weakly dependent on the x-ray photon energy, b is a constant and E is the photon energy.[5] In practical terms, the absorption of a sample depends on the chemical composition, the density of the compound and the used x-ray photon energy.[20] To reconstruct the 3D dataset, from the recorded 2D radiographs, a Fourier transform-based Feldkamp reconstruction algorithm is used to calculate the local value of μ for each point inside the scanning volume.[21]

3.1.5 Workflow

From receiving the sample to completed data evaluation, four main steps have to be performed:

1. Measurement setup
2. Data reconstruction
3. Segmentation
4. Evaluation of processed images

3.1.5.1 Measurement setup

The first step in setting up a micro-CT measurement is to find a suitable way to fixate the sample. This is of great importance since minimal movement during the rotation process can render the entire measurement blurry and in most cases unusable.

Another point to consider is sample size. When using the cone-beam geometry for measurements the magnification is:

$$Magnification = \frac{source-to-sample\ distance}{source-to-detector\ distance}. \quad (4)$$

For large samples, this means either measurement of only parts of the sample, small magnification or sample preparation that leads to a reduction in size.[22]

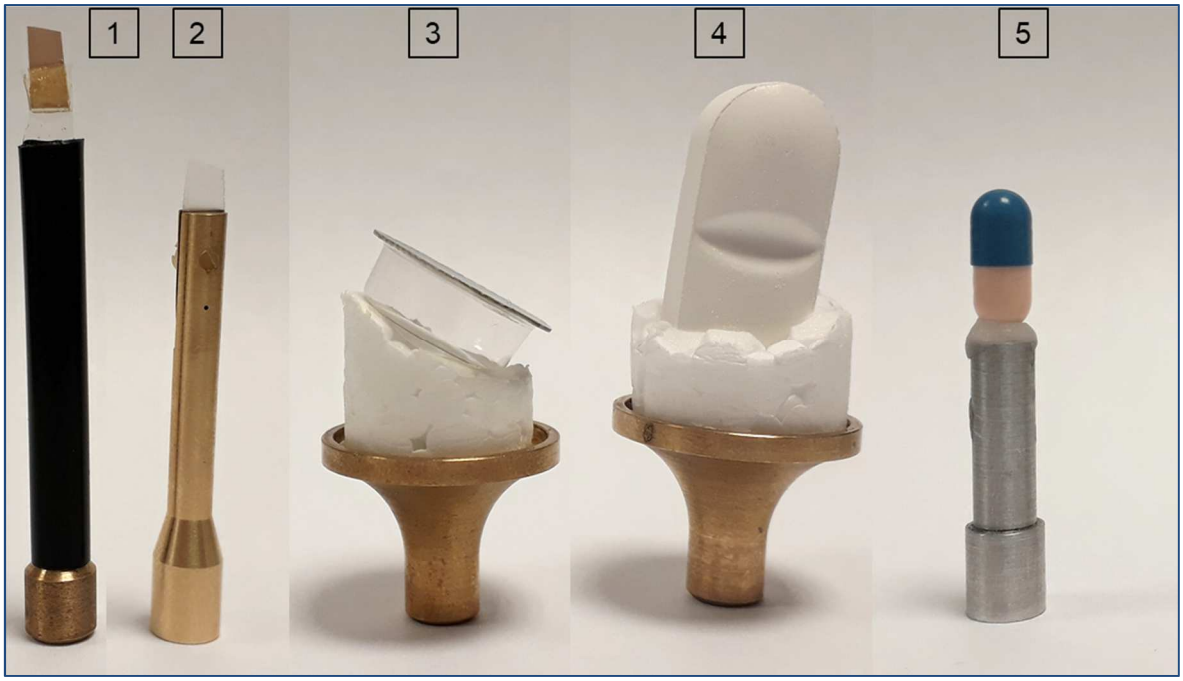

Figure 5: A variety of samples and sample holders.

In Figure 5, different approaches to sample preparation are shown. Due to the large number of diverse samples and the entailing tasks, the fixation of samples can require a little bit of creativity. For example, a cutout of transdermal therapeutic system (1), for stability reasons attached to a piece of glass, fixated in a straw, which was then mounted on the actual sample holder. In picture (3), an empty blister cup, used for packaging of tablets, was mounted with double-sided adhesive tape on an angled piece of Styrofoam. This was done due to the fact, that the aluminum sealing foil has a substantially higher relative density compared to the plastic cup itself. With a perfectly horizontal sample preparation, the x-ray beam arriving horizontally would have to travel for its entire length through the aluminum, which would artificially increase the level of absorption. Preparation of samples with a more homogeneous spatially distribution of relative density, samples that are not prone to movement and samples that need no trimming down before measurement are more straightforward. For example a pellet-filled capsule (5), can be easily mounted on a sample pin by using small amounts of plasiticine. Next, the pixel size of the measurement has to be chosen. As mentioned above, the magnification is dependent on the distance of source to sample and sample to detector, the final voxel size of the reconstructed image is obtained by dividing the pixel size of the detector by the magnification.[22] With the sample in place, source voltage, filters and exposure time are selected to get well-illuminated images. As a rule of thumb, the minimal image brightness should not fall under 15%; otherwise, information on areas with high relative density can be lost.[23] With the sample removed

from the beam-path, two correction factors have to be determined. Firstly, the so-called dark field *D*, an image captured by the detector without x-ray illumination, is collected to measure the dark current as well as the digitization offset. Secondly, a so-called flat field *F*, an image captured with x-ray illumination, is collected to measure and correct for detector response and inhomogeneities in the x-ray beam intensity profile. These steps have to be performed to determine the normalized intensity I_j:

$$I_j = \frac{P_j - D}{F - D} \tag{5}$$

where P_j are the images collected during measurement of the sample.[22]

Frame averaging, the number of images taken at the same position, to reduce noise and enhance contrast is chosen empirically and is typically between one and five. The rotation step determines the difference in angle where images are taken and should be chosen smaller for inhomogeneous samples. Lastly, a measurement can be performed rotating the sample 180 ° or 360 °, the latter should be chosen for inhomogeneous samples. It should be kept in mind that every parameter, which influences the image quality has beyond that, direct consequences for the data size and the measurement duration. Larger data size leads to longer computational times during reconstruction and segmentation. Especially for computationally intensive algorithms, the difference between an image taken at 2k and 4k resolution can be up to several hours for a single step.

3.1.5.2 Data reconstruction

With the measurement completed, a number of 2D radiographs is received. Depending on the chosen parameter, image resolution and rotation step, file sizes can range up to 70 GB and the number of individual radiographs taken can be up to 3600. To produce a 3D data set, data reconstruction has to be performed. During the measurement, two main categories of artifacts may arise that can be corrected in the software during the reconstruction process. Since Eq. 5 is only valid for monochromatic radiation, the usage of polychromatic radiation generated from a normal x-ray tube leads to imaging artefacts called beam hardening. This is caused by the energy dependency of the linear attenuation coefficient μ. X-rays of lower energy have a higher probability to get absorbed than high energetic x-rays. This leads to an overestimation of μ at the outer regions of the sample (see Figure 6, top). This problem can be often solved with software corrections (see Figure 6, bottom), but these can fail with spatial complex samples or the presence of to many different components.

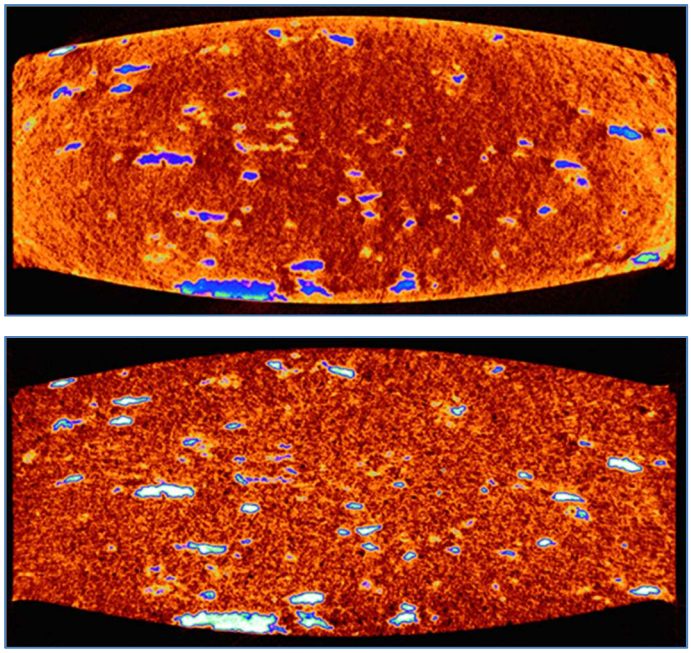

Figure 6: Example of beam hardening in a cross section of a tablet, without correction (top) and with the correct parameters (bottom)

Ring artifacts originate from temporal variations of the source intensity, slightly different response functions of individual pixels on the detector and non-linear dependency of pixels on the energy of the photons. They manifest themselves as circular rings centered on the axis of rotation (Figure 7).

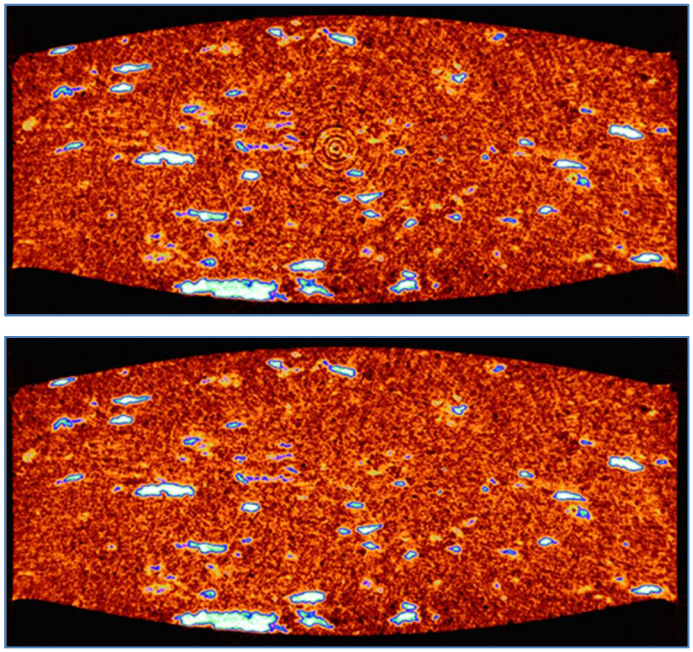

Figure 7: Example of ring artifact correction in a cross section of a tablet: with wrong parameters (top) and correct parameters (bottom)

Slight movements of the sample during measurement can be also corrected in software. Additionally to reduce the size of the file, a region of interest (ROI), the area of the measurement that should be reconstructed, can be selected.

3.1.5.3 Segmentation

The reconstructed data are received as stack of 8-bit, grey scale, 2D images. The aim of this stage is to classify, the areas or structures of the measured sample that are of interest. As with all imaging techniques, micro-CT measurements are subject to noise. In most cases, as an upstream process, a form of noise filtering is performed to improve data quality. Dependent on the condition of the data at hand, a variety of different methods can be employed. Ranging from simple uniform, Gaussian and median denoising procedures to more complex approaches like anisotropic diffusion, a variety of methods is available.[24] In Figure 8, an untreated micro-CT image, a micro-CT image with a strong Gaussian filter and a micro-CT image with an anisotropic diffusion filter, of a tablet encapsulated in a blister are shown.

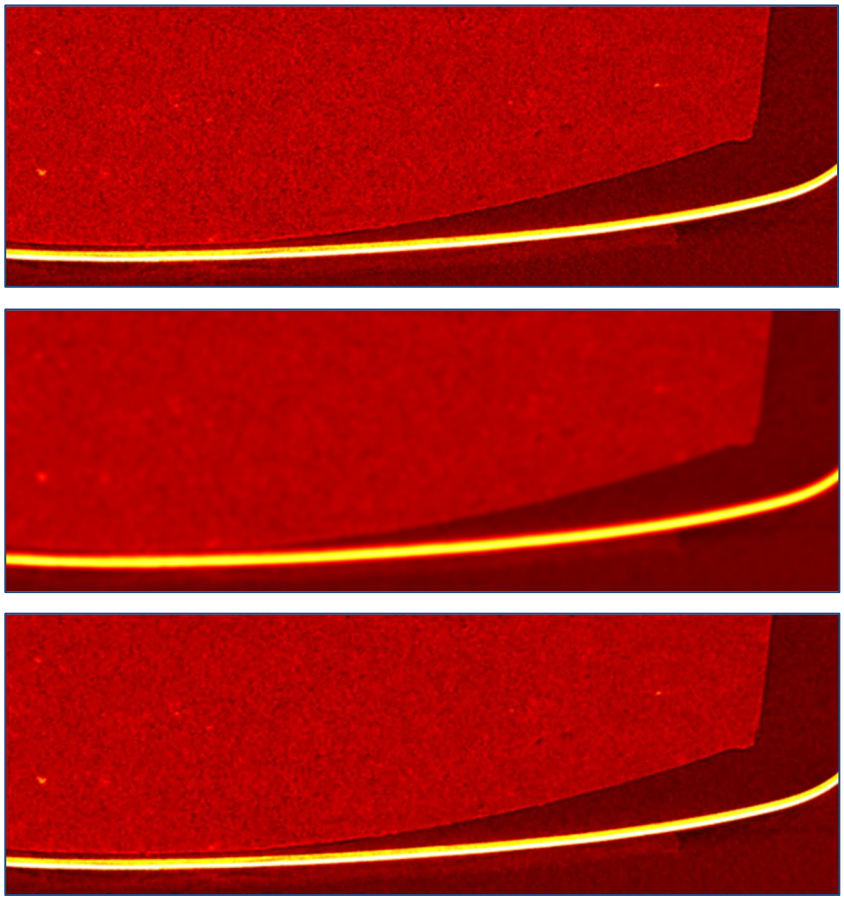

Figure 8: Untreated micro-CT image (top), micro-CT image with strong filtering (middle), micro-CT image with proper filtering (bottom).

With the Gaussian filter, details, especially on the borders of structures, are lost. Application of the anisotropic diffusion filter retains the sharpness around the edges but evens out background areas for better contrast.

As a first step, the data set has to be binarized for further processing. This means that the images, with 255 discreet colors, are reduced to a file where each pixel is either white or black. In the best case, white exclusively represents the structure of interest and everything else, including background, pockets of air, pores and other structures, is black. Although, there is multitude of automatic threshold selection algorithms available in the context of this work, only manual thresholding was used.[25] Detailed explanations for each example are given in the appendix. In Figure 9, the exemplary threshold selection for the range of 80-255 is shown. With the chosen threshold, only the areas with high relative density corresponding to the aluminum blister are retained. As can be seen in the image with the applied threshold, additionally several small dense particles contained in the tablet are visible.

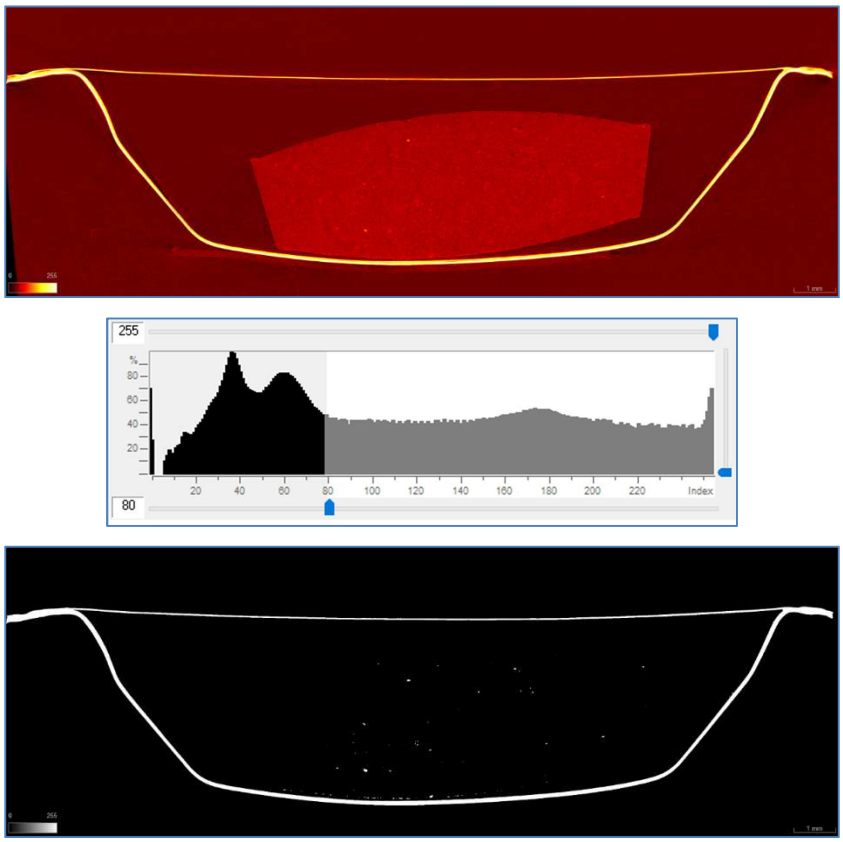

Figure 9: Full-range micro-CT image (top); relative density histogram with the range of 80-255 marked (middle); Binarized image utilizing only pixels in the 80-255 range

Due to residual noise or the fact that individual phases are spread around a mean grey value, thresholding leads to the misclassification of certain voxels, which often makes

cleaning-up steps necessary. Going back to the example of Figure 9, when only information about the blister itself should be extracted, removal of the stray particles contained in the table has to be performed. (Figure 10) Several techniques such as the removal of isolated pixels, as well as dilation and erosion algorithms can be employed prior to the next step. Additionally, watershed algorithms can be performed to separate connected structures.

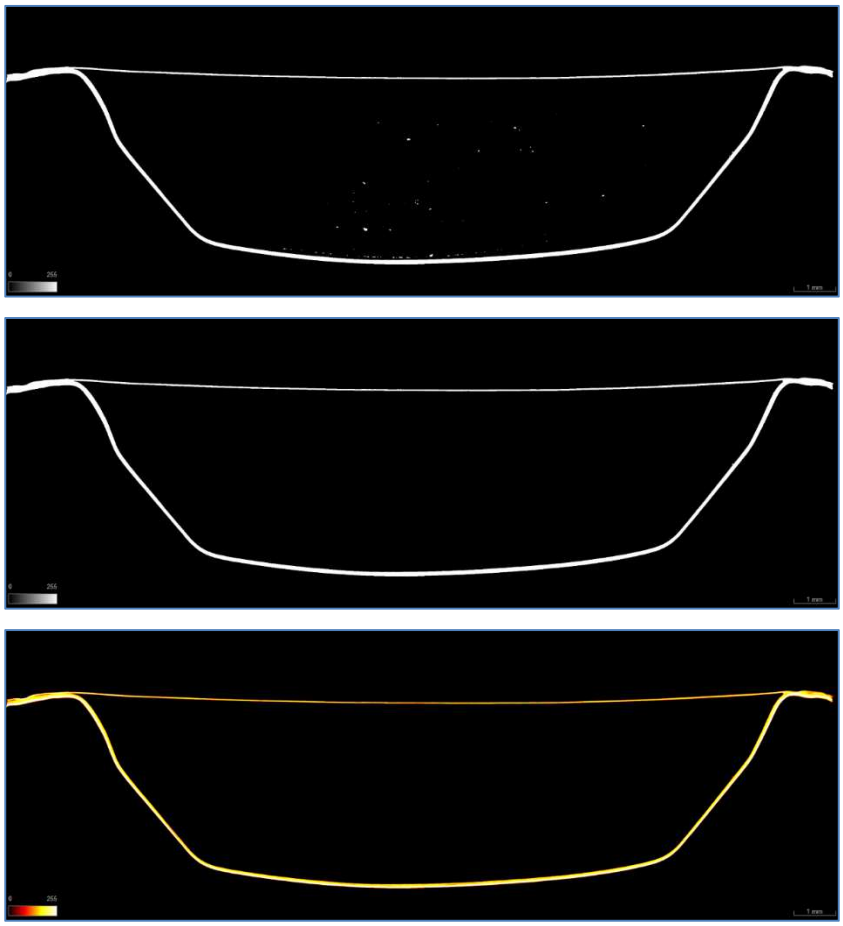

Figure 10: Binarized Image in the range of 80-255 (top), image after the removal of stray pixels (middle), image of just the blister with relative density information (bottom)

3.1.5.4 Evaluation of processed images

The final step is the analysis of the segmented images. This is normally performed on the entire sample in 3D. In specific cases, analysis can also be employed only in 2D, on selected image layers (see paragraph 4.4.5). There is a multitude of output parameters for example, particle size descriptors, overall surface area, overall volume, average distance between particles, particle orientation, etc. Which parameters are of interest has to be chosen individually for each project and will be discussed in detail in the project specific paragraphs of this work.

3.1.6 Concluding remarks

Since micro-CT is used for many different types of samples in many different scientific fields, each requiring specific measurement parameters, no generally accepted protocols exist. Adding to this, exact comparison between two different micro-CT setups is not possible due to the lack of generally accepted calibration phantoms. Another challenge is observer-bias. *Baveye et al.* showed that different experts analyzing the same images chose very different approaches concerning thresholding and thusly receiving different results. The implementation of common automatic thresholding algorithms yielded outcomes that were comparable in variability to those of the experts.[26] To make sure that errors are kept to a minimum, for each series of measurements each parameter that might have an influence on the outcome was locked in at the start of the series. This includes all measurement parameters, segmentation parameters and analysis steps to keep sample results comparable. In the context of this work, micro-CT imaging is used to gather 3D information of the relative density distribution of samples. Without further knowledge or the combination with other measuring techniques, a statement of the chemical composition of the sample is not possible. However, due to the mostly non-destructive nature of measurements, a combination with different analytical tools is possible.

3.1.7 References

[1] W.K. Röntgen, *Science*, **1895**, 726-729.

[2] E.B. Frost, *Science*, **1896**, 235-236.

[3] D.C. Miller, *Science*, **1896**, 516-517.

[4] G.N. Hounsfield, *Br. J. Radiol*, **1973**, 1016-1022.

[5] V. Cnudde, M. N. Boone, *Earth Sci Rev.*, **2013**, 1-17.

[6] J.C. Elliott, S.D. Dover, *J. Microsc.*, **1982**, 211-213.

[7] J.C. Elliott, S.D. Dover, *J. Microsc.*, **1985**, 329-331.

[8] L. Farber, G. Tardos, J.N. Michaels, *Powder Technol.*, **2003**, 57-63.

[9] Y. Ozeki, Y. Watanabe, S. Inoue, K. Danjo, *Int. J. Pharm.*, **2003**, 69-77.

[10] M. Alhijjaj, S. Yassin, M. Reading, J.A. Zeitler, P. Belton, S. Qi, *Pharm. Res.*, **2017**, 971-989.

[11] T. Asadaa, M. Kobikia, Y. Ochiaia, Y. Iwaob, S. Itaib, *Int. J. Pharm.*, **2017**, 617-175.

[12] C. I. Gioumouxouzis, O. L. Katsamenis, D.G. Fatouros, *J. Microsc.*, **2019**, 1-5.

[13] E. Yost, P. Chalus, S. Zhang, S. Peter, A.S. Narang, *J. Pharm. Sci.*, **2019**, 1818-1830.

[14] A. Ariyasu, Y. Hattori, M. Otsuka, *Int. J. Pharm.*, **2017**, 282-290.

[15] Bruker *SkyScan1272* (1.1.15.) [Software].

[16] Bruker *NRecon* (1.7.3.1.) [Software].

[17] Bruker *CT Analyser* (1.18.4.0+) [Software].

[18] Bruker *DataViewer* (1.5.6.2) [Software].

[19] Bruker *CTvox* (3.3.0 r1403) [Software].

[20] A.M. Miguélez-Morán, C. Wua, H. Dong, J.P.K. Seville, *Eur. J. Pharm. Biopharm.*, **2009**, 173-182.

[21] L.A. Feldkamp, L.C. Davis, J.W. Kress, *J. Opt. Soc. Am. A*, **1984**, 612-619.

[22] S. Brisard, M. Serdar, P.J.M. Monteiro, *Cem. Concr. Res.*, **2020**, 105824.

[23] J. Feil, *SkyScan Tutorial (v1.0)*, RJL Micro & Analytic GmbH, Karlsdorf-Neuthard, **2016**.

[24] A. Buades, B. Coll, J. Morel, *MMS by SIAM,* **2010**, 90-530.

[25] M. Sezgin, B. Sankur, *J. Electron. Imaging*, **2004**, 146-165.

[26] P.C. Baveye, M. Laba, W. Otten, *Geoderma*, **2010**, 51-63.

3.2 Raman microscopy

3.2.1 History

In 1928, “A New Type of Secondary Radiation” was discovered by *Raman*, the first experimental observation of inelastic light scattering by molecules in liquid phase.[1] Although of high scientific interest, the usability of Raman spectroscopy was, in the beginning, limited by the missing of an appropriate excitation source. This changed with the discovery of “light amplification by stimulated emission of radiation” devices (Lasers).[2] Lasers are perfectly suited for light scattering experiments because they are a strong monochromatic and coherent source.[3] This led to a widespread use of Raman spectroscopy in different fields like medicine, engineering and material sciences.[4,5] In the pharmaceutical sector, Raman spectroscopy is used extensively for the characterization of active pharmaceutical ingredients (APIs), mainly for the investigation of identity, purity and polymorphism.[6] The coupling of Raman spectroscopy with a microscope followed. The so-called “Raman microprobe” was used to obtain images using a characteristic Raman frequency. Identification and surface mapping of different substances in an inhomogeneous sample became possible by choosing suitable spectral bands.[7] The next big advancement came with the development of the charge-coupled-device (CCD). Raman spectroscopy was still suffering from the inherently weak Raman scattering signals. With the first application of the CCD by *Dierker et al.* in 1987, Raman sensitivity improved and new areas of application were opened.[8] Further improvement came with the increase of processing power, which opened new possibilities for software-aided solutions. For example, the usage of principal component analysis (PCA) for the denoising of Raman spectra that significantly reduced the data collection times.[9] In recent times, Raman imaging gained a lot of interest in the context of quality by design (QbD), as mentioned in the introduction.

3.2.2 Recent examples – State of the art

In the pharmaceutical industry, Raman microscopy has become a useful tool for a variety of different tasks such as:

- Mapping of APIs
- Detection of impurities
- Characterization of the physical state of the API
- Investigation of the dissolution process and pathway of drug release
- Quantification of components

To give an overview of the areas of application, in the following short examples of the usage of Raman imaging on different dosage forms are provided.

The API distribution as well as the distribution of both excipients on drug-eluting stents was determined by Raman imaging. Additionally, using a linear regression model the API content was determined with an accuracy of 1 wt% when compared with the laboratory assay.[10]

With the help of a band-target entropy minimization (BTEM) algorithm, the components of ternary-phase biodegradable double-walled microspheres (DWMS) were investigated. Besides the expected three components, trapped solvents, degradation products and contaminants were found and could be characterized.[11]

Solid dispersions prepared using different heating temperatures and amounts of water were investigated. Two different diastereomer-pairs of the crystalline API as well as amorphous components could be distinguished with Raman microscopy. Additionally the spatial distribution of amorphous API could be correlated with the presence of polyvinylpyrrolidone (PVP), supporting the theory of API undergoing physical transformation during dissolution in PVP.[12]

The physical properties of three-layered matrix tablets were investigated to elucidate the pathway of drug release. Tablet components were mapped before and after the addition of water and differences in thickness of layers could be observed. The pathway of drug release indicated by Raman imaging was in good accordance with the drug dissolution tests.[13]

Raman imaging was used to for the analysis of falsified medicines. The distribution of the components was mapped and the composition of each tablet compared with the originals. Additional quantification of the components was performed and found to be acceptable for the detection of falsified drugs.[14]

Ongoing research is done in the field of chemometrics, to improve the extraction of chemical and physical information from Raman images.[15]

3.2.3 Setup

The term Raman microscope is used for devices that combine Raman spectroscopy with optical microscopy. The main components are a sample stage that is moveable in in the xy- as well as the z-direction; an objective, a laser source and a spectrograph (see Figure 11).

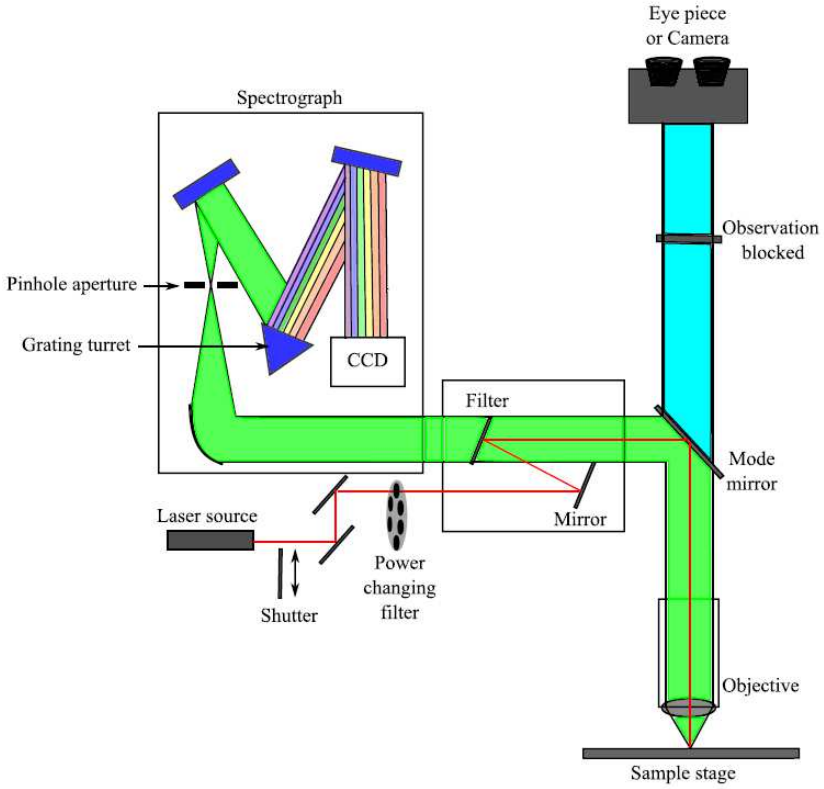

Figure 11: Schematic of the components and beam path of a Raman microscope.[16]

The microscopy component is used to generate white light images of the sample. During spectroscopy the excitation laser travels through the objective onto the sample, the ensuing Raman scattering is then collect in the same objective and the excitation wavelength is removed with a notch filter. A diffraction grating is used for the separation of the wavelengths, which finally reach the CCD detector. To ensure confocality a pinhole aperture is placed in the beam path. Each recorded spectrum is linked to a point on the sample surface. Through the scanning of the entire sample surface or specific regions, a spectroscopic map is generated. In Figure 12, the Raman microscope, from the Renishaw inVia line, that was used throughout this work is depicted.

Figure 12: Raman microscope, Renishaw inVia.

This setup is equipped with three different laser sources, a 785 nm line laser (300 mW), 633 nm point laser (18 mW) and 532 nm point laser (100 mW). Six different objectives, four with narrow focusing range (5x, 20x, 50x and 100x) as well as three with long focusing range (20x, 50x and 100x) are available. For controlling measurements and data handling, the Renishaw proprietary software was used.[17] Depending on the chosen parameters, especially region of interest and point mapping vs. line mapping, measurement durations can range from a few minutes to several days.

3.2.4 Theoretical background

Light scattering occurs when electromagnetic radiation is generated via the induction of oscillating dipoles in molecules, by the electromagnetic field of an incident radiation. There are several different types of scattering (see Figure 13). Rayleigh scattering describes the elastic scattering of light, where the incident and scattered photons have the same energy. Stokes scattering is an inelastic process, where upon scattering, photons lose energy and undergo a red shift. This is measured in classic Raman spectroscopy. When photons gain energy during a scattering process, undergoing a blue shift, the process is called Anti-Stokes scattering. Here the transition occurs not from the ground state but from an excited vibrational state.[18]

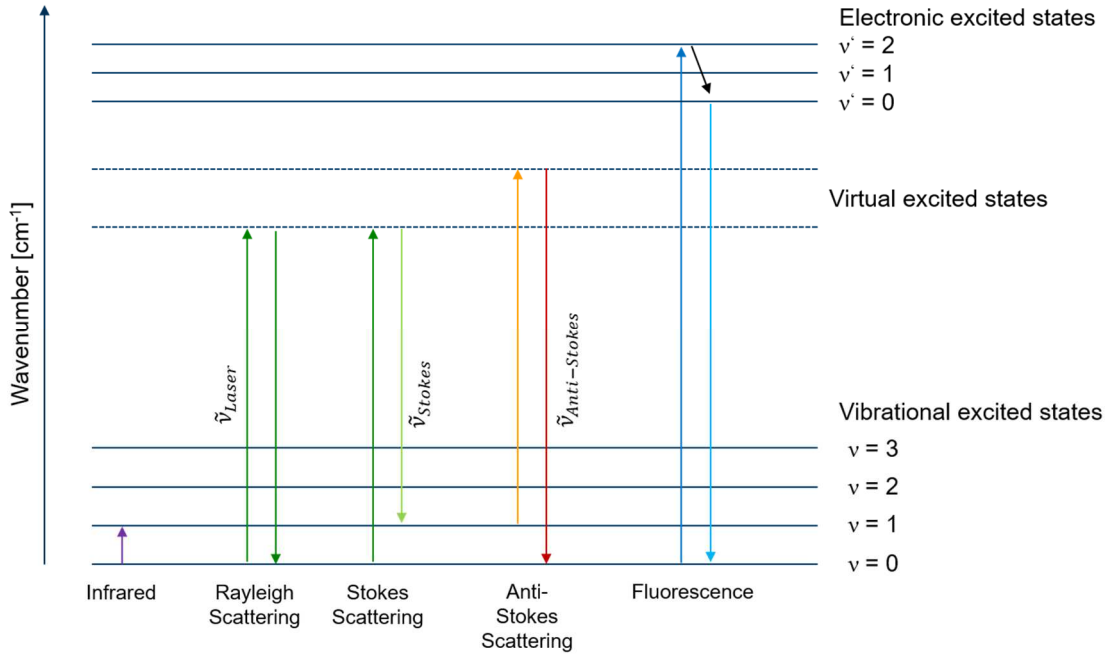

Figure 13: The different light scattering pathways

Scattering is a phenomenon that does not have a high probability to occur. The intensity of Rayleigh is in the range between 1:10 and 1:100 compared with the incident beam. Raman scattering is occurring with a probability of about $1:10^7$.[16] The pattern of the scattered light, its wavelengths and intensities is strongly dependent on the chemical groups in the sample molecule. Vibrations that are more easily polarizable are more responsive to the incident beam and generate more Raman intensity. In contrast to Raman scattering, which requires a change in polarizability, IR spectroscopy can be observed for molecules, which undergo a change in dipole moment upon vibrational excitation. One of the major implications of this is that water, even small amounts, is measured in IR spectroscopy, often times overlaying other sample signal. In Raman measurements water is inactive.[19] Another phenomenon that can occur and interfere with Raman spectroscopy is fluorescence. This is a resonant interaction of light with electronic states of the sample. When a sample shows fluorescence during a measurement due to its higher efficiency compared to Raman scattering, often the Raman signal is overlapped and cannot be detected.[18] The reduction of fluorescence background can be achieved in two ways. Either by the change of excitation wavelength, through the application of a different laser or by the reduction of detection volume. When the lasers at hand do not produce sufficient suppression of the fluorescence signal, a confocal detection setup is employed. This is a setup, were only photons emitted from the focal plane can reach the detector thus limiting the collection of fluorescence photons (see Figure 14).[19]

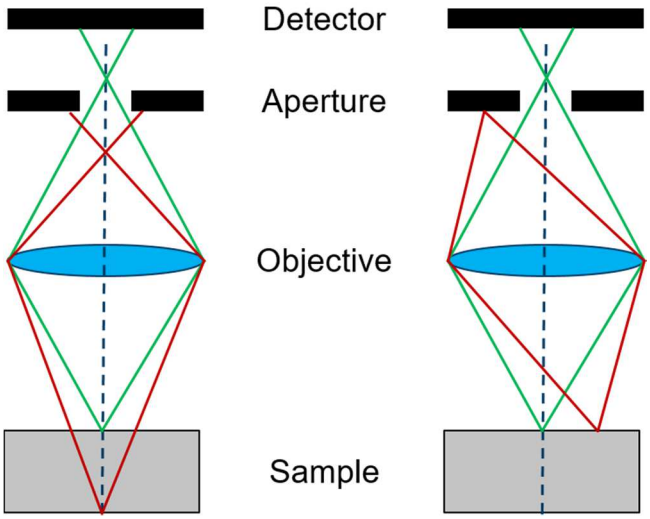

Figure 14: Confocal measurement setup: Raman scattering from the focal point (green) is passing through the aperture to the detector, out of focus scattering (red) is blocked by the aperture (left side axially right side laterally).

Besides the fluorescence suppression, measuring in confocal geometry improves the lateral and axial resolution of measurement. As a simplified descriptor of the lateral resolution, the focused spot diameter *d*:

$$d = \frac{1.22\,\lambda}{NA} \tag{6}$$

with the laser wavelength λ and the numerical aperture *NA* of the objective, can be used. For the measuring of a sample using a laser with 785 nm excitation wavelength and a 100x objective with NA = 0.9, this yields a spot size of 1.06 µm.[20]

An assessment of the axial resolution can be obtained using the formula for the depth resolution (DR):

$$DR = \frac{4.4n\lambda}{2\pi(NA)^2} \tag{7}$$

where *n* is the refractive index of the material, λ is the laser wavelength and *NA* the numerical aperture of the objective. For the same measuring setup as described above and a refractive index *n* of 1.5, a theoretical DR of 1.02 µm is calculated.[21]

In less than ideal systems, these theoretical values can often not be achieved. Surface irregularities and partial absorption of light as well as scattering and refraction at the sample surface will influence the quality and the dimension of the laser spot at focus and thusly yield different results than the predicted.[22] In Raman microscopy, a spatial component is added to the spectral information this is then referred to as a hyperspectral data set. For

opaque substances, the sample surface area provides 2D information, for transparent or semi-transparent samples volume measurements are possible, yielding 3D information.

3.2.5 Workflow

From receiving the sample to completed data evaluation, four main steps have to be performed:

1. Measurement
2. Pre-processing
3. Data analysis
4. Evaluation

3.2.5.1 Measurement

Since Raman microscopy of opaque specimens, such as tablets and pellets, is recording information on the surface, preparation is needed when information on the interior of the sample is desired. For example for tablets, the specimen is cut in half using a scalpel, fixed on a sample holder an milled with a micro-plane to obtain a surface that is as even as possible (see Figure 15).

Figure 15: Sample tablet (left) and the same tablet after sample preparation for Raman microscopy.

Prior to the Raman measurement, white light images of the sample surface are taken, combined in an overview micrograph and used for navigation during the Raman measurement. First, the area of data collection is chosen. Secondly, a multitude of parameters has to be chosen. Laser wavelength, exposure time and laser power are selected to give the best signal-to-noise ratio, the least fluorescence, the shortest scan duration and the lowest risk of sample damage. The scanning step size, the distance between two recorded spectra, is chosen according to the expected particle size of the components in the sample. Utilizing the fact that CCDs are matrix detectors, two different

methods for the scanning of samples, referred to as point mapping and line focus mapping, can be used. With point mapping, the laser is focused on a spot, a Raman spectrum is collected, then the sample is moved and another spectrum is recorded, mapping the entire sample. With line focus mapping, the laser illuminates a line on the surface and multiple spectra are recorded simultaneously. This second method has the advantage of shorter illumination times, reducing risk of sample damage, but also suffers from weaker signal strength.[16]

3.2.5.2 Pre-processing

After the measurement, several pre-processing steps have to be performed to remove unspecific information from the data. Cosmic Rays are high-energy particles originating from the sun and from outside of the solar system. They create a sharp, false signal when hitting the CCD detector and are several orders of magnitude stronger than the Raman signals. This can be filtered out, using the fact that regular Raman signals usually possess a natural line width of > 3 cm^{-1} and can therefore be separated from the very sharp cosmic ray signals.[19] As with every imaging technique, Raman microscopy is subject to noise. The utilized software supplies a way of noise filtering using principle component analysis (PCA). Although the baseline in Raman spectra may contain useful information, for example about the crystallization process, it is advisable to remove it in most applications.[16, 23] Baseline subtraction is performed using the Renishaw patented “intelligent fitting” function which uses polynomial algorithms to fit a new baseline.[24]

3.2.5.3 Data analysis

There are different methods for data analysis. The simplest approach to generate Raman mapping is to use univariate methods. Since each Raman signal correlates to a chemical bond mapping the intensity of a peak at a certain wavenumber or the integration of the area under the peak can reveal the distribution of a compound. For this method, it is required to know the composition of the sample beforehand to choose the correct signal. It is not possible to detect unanticipated substances. Additionally, spectral overlap between spectra of different compounds as well as low concentrations can lead to failure.[25]

For analysis that is more complex, multivariate methods, which take the complete spectral information contained in the data cube into account, can be used. A variety of different analysis methods exists, three are used in the scope of this work and will be discussed in the following.

Principle component analysis (PCA) is a frequently used algorithm for effective data reduction. It is aimed at the reduction of matrix dimensionality by removing the correlation between variables. The data matrix is rotated onto a new coordinate system:

$$X = T \cdot V + E \tag{8}$$

with two matrixes, where *T* describes the scores and *V* the loadings and the residual noise *E*. The principle components are iteratively calculated, with the first component explaining the greatest possible variance of the data, the second (orthogonal to the first) explains the greatest amount of the remaining variance and so on.[24,25] The resulting principle component mapping shows a distribution of data variance but does not have chemical meaning. Spectra may contain negative values and do not allow conclusions on the spectra of pure substances. It the context of this work PCA is used for noise reduction.[19]

Another method where no prior knowledge is need is “Empty Modelling”, the implementation of multivariate curve resolution – alternating least squares (MCR-ALS). The data matrix *X* is decomposed into concertation images *C* and pure spectra *S:*

$$X = C \cdot S^T + E \tag{9}$$

with *E* being the matrix of residuals not explained by the chemical species in *C* and *S*. The aim is the determination of the true matrices of *C* and *S*. After initial estimations of *C* and *S*, equation (10) is solved iteratively using alternating least squares optimization. The results are the pure species spectra.[26]

A third method is direct classical least squares (DCLS). For this technique, knowledge of the sample composition and the pure species spectra of the included components are needed. This method is often used for process control of tablets or other pharmaceutical products were the formulation is known. Since the pure spectra matrix S^T is available, distribution maps can be generated minimizing $\|X - C \cdot S^T\|^2$ from equation (10), *C* can be estimated using the pseudoinverse [25]:

$$C = X \cdot S \cdot (S^T \cdot S)^{-1} \tag{10}$$

In this work, a dual approach is chosen. Raman maps are generated using MCR-ALS, as a method requiring no user input and DCLS to show the components distribution. Both maps are compared and if identical or very similar, Raman mapping can be seen as successful in giving detailed chemical information about the sample. This method reduces the possibility for false positives that can be generated by using only DCLS:

3.2.5.4 Evaluation

With the generated maps, the composition of unknown samples can be elucidated. It is possible to detect foreign particles (contaminations). The distribution of components can be visualized and the homogeneity of the sample determined. A rough quantification of the contained substances can be performed. Within the limitation of this 2D technique, particle size distributions can be calculated. The main task of Raman mapping in this work, was the combination of gathered chemical distribution with the relative density mapping of micro-CT images. For each case study, a paragraph on the combination of information will be provided.

3.2.6 Concluding remarks

Raman microscopy is used to gather information on the chemical composition of a sample. One of the main issues is the problem of subsampling. Since only one layer of a sample is analyzed, measurements may not be representative of the entire sample. This effect is increased for inhomogeneous samples.[27] To circumvent the problem, measurements on more than one layer are performed and compared. Another problem is that sample preparation most often leads to the destruction of the specimens.

3.2.7 References

[1] C.V. Raman, K.S. Krishnan, *Nature*, **1928**, 501-502.

[2] T.H. Maiman, *Nature*, **1960**, 493-494.

[3] S.P.S. Porto, D.L. Wood, *J. Opt. Soc. Am.*, **1962**, 251-252.

[4] L.-P. Choo-Smith, H.G M. Edwards, H.P. Endtz, *Biopolymers*, **2002**, 1-9.

[5] A. Cantarero, *Procedia Mater. Sci.*, **2015**, 113-122.

[6] K. Moriyama, *Curr. Pharm. Des.*, **2016**, 4912-4916.

[7] M. Delhaye, P. Dhamelincourt, *J. Raman Spectrosc.*, **1975**, 33-43.

[8] S.B. Dierker, C.A. Murray, J.D. Legrange, N.E. Schlotter, *Chem. Phys. Lett.*, **1987**, 453-457.

[9] S. Šašić, D.A. Clark, J.C. Mitchell, M.J. Snowden, *Analyst*, **2005**, 1530-1536.

[10] K.M. Balss, G. Llanos, G. Papandreou, C.A. Maryanoff, *J. Biomed. Mater. Res. A*, **2007**, 258-270.

[11] E. Widjaja, W.L. Lee, S.C.J. *Loo, Anal. Chem.*, **2010**, 1277-1282.

[12] N. Furuyama, S. Hasegawa, T. Hamaura, *Int. J. Pharm.*, **2008**, 12-18.

[13] D.H. Choi, K.H. Kim, J.S. Park, *J. Control Release*, **2013**, 763-772.

[14] H. Rebiere, M. Martin, C. Ghyselinck, *J. Pharm. Biomed.*, **2018**, 316-323.

[15] H. Mitsutake, S.R. Castro, E. de Paula, R.J Poppi, *Int. J. Pharm.*, **2018**, 119-129.

[16] G.P.S. Smith, C.M. McGoverin, S.J. Fraser, K.C. Gordon, *Adv. Drug Deliv. Rev.*, **2015**, 21-41.

[17] Renishaw, *Wire 4.4* (build 6602) [Software].

[18] W. Demtröder, *Laserspektroskopie 2*, Springer-Verlag, Berlin Heidelberg, **2013**.

[19] J. Toporski, T. Diening, O. Hollricher, *Confocal Raman Microscopy*, Springer-Verlag, Berlin Heidelberg, **2018**.

[20] K.C. Gordon, C.M. McGoverin, *Int. J. Pharm.*, **2011**, 151-162.

[21] C.B. Juang, L. Finzi, C.J. Bustamante, *Rev. Sci. Instrum.*, **1988**, 2399-2408.

[22] R. Tabaksblat, R.J. Meier, B.J. Kip, *Appl. Spectrosc.*, **1992**, 60-68.

[23] A. Hédoux, L. Paccou, Y. Guinet, J.-F. Willart, M. Decamps, *Eur. J. Pharm. Sci.*, **2009**, 156-164.

[24] Renishaw Handbook for Wire Software.

[25] C. Gendrin, Y. Roggo, C. Collet, *J. Pharm. Biomed. Anal.*, **2008**, 533-553.

[26] R. Tauler, A. Smilde, B. Kowalski, *J. Chemometr.*, **1995**, 31-58.

[27] J. Johansson, S. Petterson, S. Folestad, *J. Pharm. Biomed. Anal.*, **2005**, 510-516.

3.3 Scanning electron microscopy with energy-dispersive X-ray spectroscopy

3.3.1 History

3.3.1.1 Scanning Electron Microscopy

At the beginning of the development of scanning electron microscopy (SEM) are two discoveries. In 1926, *Busch* found that magnetic fields could be used as lenses causing electron beams to converge to a focus. This laid the foundation for geometrical electron optics.[1] Around the same time *de Broglie*, introduced the concept that all matter has a wave-like nature. This meant that charged particles, for example an electron could be associated with a wavelength. This marked the start of wave electron optics.[2] In 1931, *Ruska* and *Knoll* experimentally proved the concept of *Busch's* lens formula. By the combination of two primitive lenses, the first transmission electron microscope, with a magnification of 16x, was constructed.[3,4] The first "scanning microscope" was realized in 1935, but the resolution was limited to about 100 µm because no demagnifying lenses where used.[5,6] The recommendation for the use of demagnifying lenses to obtain a fine electron probe was proposed by *von Ardenne* in 1938. This described the theoretical basis for the scanning microscope, as we know it today.[7] In later published experimental work, focus spots of 50 – 100 nm in diameter were realized.[8] Because transmission electron microscopy (TEM) at this time had a better resolution for the analysis of thin samples, the development of SEM was directed towards the study of the surface of opaque specimens, where the preparation of thin slices was not possible.[9] With the inclusion of an electron multiplier tube as a preamplifier of the secondary electrons emission current, *Zworykin* developed the first true SEM in 1942. He demonstrated that secondary electrons can be used to provide topographic contrast and achieved a resolution of 50 µm.[10] In the following decade, *Smith* improved the existing systems by implementing nonlinear signal amplification and stigmators to correct imperfections of the lens.[11-14] The introduction of a new style of detector by *Everhard* and *Thornley* greatly improved the detection of secondary electrons. The design incorporated a light pipe carrying the signal from the scintillator inside the evacuated sample enclosure to the photomultiplier located outside the vacuum.[15] In 1965, with all new developments at hand, the first commercial SEM, still very similar to instruments used today, was introduced.[16]

3.3.1.2 Energy-dispersive X-ray spectroscopy

Development of Energy-dispersive X-ray spectroscopy (EDX or EDS) began with the first scanning microanalyser by *Duncumb* in the 1959. This instrument combined an x-ray diffracting spectrometer with a SEM setup. The detection limit at this time was about 1 part per 1000 in mass fraction.[17] Following the introduction of fully focusing linear-track diffracting spectrometers with high collecting power the limits of detectability were improved.[18] In the 1960s, with the development of semiconductor x-ray detectors the collecting efficiency was improved by a factor of 100 or more. Additionally, it was now possible to record the full spectrum of x-rays at the same time. Later improvements of condenser lenses and electron guns led to spot diameters of about 20 nm.[19]

3.3.2 Recent examples – State of the art

SEM/EDX systems are used for a wide variety of tasks and on different types of samples in the pharmaceutical environment. The two main areas of application are the mapping of the spatial distribution of different components and the investigation of sample morphology.

A pellet formulation with water-soluble and water-insoluble polymers is used to get modified release characteristics for drugs. SEM gave novel insight into the internal structure of poly(vinyl acetate) (PVAc) and polyvinyl alcohol–polyethylene glycol graft copolymer (PVA-PEG) film coated pellets. With the addition of EDX-mapping, it was possible to visualize the distribution of the atomic composition of the layered structure of the pellets.[20]

The detection and measurement of nanoparticles is an important part of experimental nanotoxicological studies. Commonly used nanoparticles such as zinc oxide (ZnO) and titanium dioxide (TiO_2) have the tendency to form agglomerates in suspensions. Visualizing the influence of bovine serum albumin (BSA) on the agglomeration was performed using SEM. Particle size, morphologies and particle distribution were studied for raw nanoparticle suspensions and compared to samples with added BSA.[21]

Melt granulation is a manufacturing technique in the pharmaceutical industry, where the final dosage form is prepared without the addition of water or organic solvents. An important component in the making of granules, containing materials with poorly compactible materials, is the binder material. Binder distribution in different granule formulations was analyzed using SEM/EDX mapping.[22]

Application of solid lipid nanoparticles (SLN) and solid lipid microparticles (SLM) as API carriers for local cutaneous treatment is another field of interest in pharmaceutical research. EDX-mapping of the outermost human *stratum corneum*, after the application of SLNs and

SLMs gave insight into their penetration depths and locations where degradation took place.[23]

Ultrafine fibers are a promising candidate as a soft porous scaffold for wound healing and tissue regeneration. On the one hand, as a physical protection layer and secondly as a potential carrier for the delivery of antibacterial agents. SEM was used to monitor the effect of different formulations, the impact of aging and the influence of drug loading on fiber morphology.[24]

3.3.3 Setup

The main components of a SEM equipped with an EDX detector are shown in Figure 16. The electron beam produced by the electron gun is converged and collimated into a parallel stream by the condenser lenses. Apertures in the beam path are used to suppress scattered electrons and to reduce spherical aberrations. Deflection coils are used to deflect the beam in the x- and y-axes to raster the samples surface. Three different types of detectors collect either backscattered electrons, secondary electrons or x-ray photons. The specimen is mounted on a controllable sample stage.[25]

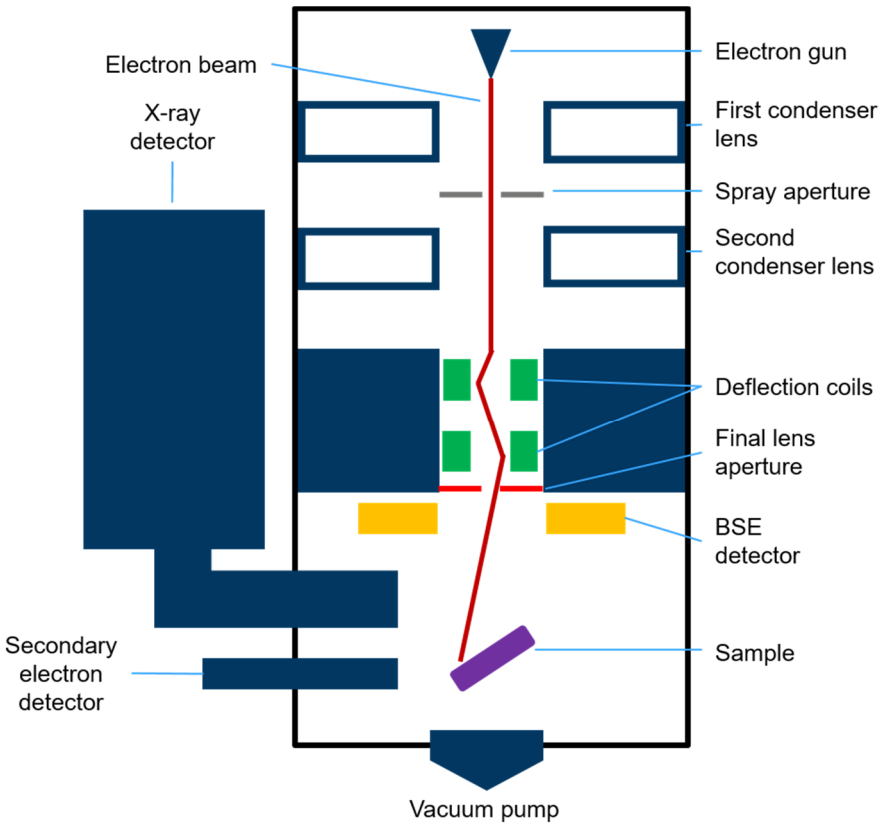

Figure 16: Schematic diagram of a scanning electron microscope with EDX detector.

The machine used throughout this work was a Hitachi TM3030Plus equipped with a Quantax70 energy dispersive X-ray spectrometer.

3.3.4 Theoretical background

SEM/EDX is used for the analysis of sample microstructure morphology and chemical composition. With *de Broglie's* groundwork that all matter possesses wave-like properties, Abbe's equation can be used to estimate the limit of resolution *d* using [2]:

$$d = \frac{0.612 \cdot \lambda}{NA} \tag{11}$$

where, λ is the wavelength and the *NA* numerical aperture. This of course, is only true for a perfect optical system. In the real world, diffraction and interference are responsible for lower attainable resolutions. During measurements, the surface of the sample is scanned systematically using a focused electron beam. Interactions of the beam with the specimen result in the emission of a variety of signals:

- Backscattered electrons
- Secondary electrons
- Characteristic x-rays
- X-ray continuum

One of the main sources used for imaging are backscattered electrons (BSE). They are generated through elastic collision of incident electrons with electrons of the outer shell with similar energy or the atomic nucleus. Differences in signal intensities are caused by differences in atomic species. The amount of backscattered electrons is dependent on the positive charge of the nucleus; thusly elements with higher atomic numbers have a higher backscattered yield (for example ~6% for carbon and about 50% for gold). The recorded images therefore contain information on the topography and the atomic composition of the sample. Due to their high energy, BSE are recorded form different depths of the sample, this as a deteriorating effect on the lateral resolution (about 1 µm). A second source for imaging are secondary electrons. The interaction of the incident beam with the sample causes ionization of atoms and the subsequent emission of loosely bound electrons, which are then detected. Due to their low energy, signals detected originate from only a small area of the samples surface (lateral resolution up to 10nm). Using secondary electrons the surface characteristics of samples can be visualized. The addition of an EDX-detector enables the detection of characteristic x-rays. Inner shell electrons can be ejected from their shell by the collision with electrons of the incident beam, creating an electron hole. An electron from a higher-energy shell fills the hole. The energy difference between the higher-

energy and lower-energy shell may be released in the form of an x-ray photon. The energy released is characteristic for each atomic species, thusly enabling mapping. During this process, due to the interaction of high-energy electrons with the electron cloud a continuous background is created, which is also referred to as continuous x-ray signal. This presents itself as background noise and can be discarded from the spectrum before analysis.[25]

3.3.5 Workflow

Compared to micro-CT and Raman microscopy the SEM/EDX image generation is simpler and more akin to standard digitally enhanced digitally enhanced light microscopy. Since SEM/EDX has to be performed in vacuum, only the imaging of solid samples is possible. Depending on, if information on the outside or inside of the sample is requested, the cutting or otherwise preparation of the specimen is required. As mentioned in paragraph 0, backscattered and secondary electrons can be detected. Since image generation occurs nearly immediately, a quick cycling through the parameters is a suitable method to get the desired image quality. For improvement of the contrast charge-up reduction can be implemented. For EDX, a region of interest has to be defined where the analysis is performed. This way either the entire image or only specific areas are taken into account. Besides the spatial distribution, the quantitative distribution of individual types of atoms can be recorded. Due to the generation of x-ray photons in different samples depth, this is more a representation of multiple layers of sample and not just the surface.

3.3.6 Concluding remarks

Compared to micro-CT and Raman microscopy SEM/EDX permits for a quick scanning of the sample. Morphological information as well as to a certain point, chemical information can be extracted from a sample. Depending of the necessary magnification this information is spatially limited. Chemical information gathered, is only derived from the specific types of atoms. It cannot discriminate between different molecules with the same atomic composition, this becomes a problem when a sample contains only organic substances.

3.3.7 References

[1] H. Busch, *Ann. Phys.* **1926**, 974-993.

[2] L. de Broglie, *Optique Electronique et Corpusculaire*, Hermann, Paris, **1950.**

[3] E. Ruska, M. Knoll, *Z. Tech. Phys*. **1931**, 389-400 and 448.

[4] E. Ruska, M. Knoll, *Z. Physik* **1932**, 318-339.

[5] E. Ruska, M. Knoll, *Ann. Physik* **1932**, 607-640 and 641-661.

[6] M. Knoll, *Z. Tech. Phys.* **1935**, 467-475.

[7] M. von Ardenne, *Z. Phys*. **1938a**, 553-572.

[8] M. von Ardenne, *Z. Tech. Phys.* **1938b**, 407-416.

[9] A. Bogner, P.-H. Jouneau, G. Thollet, D. Basset, C. Gauthier, *Micron*, **2007**, 390-401.

[10] V.K. Zworykin, J. Hillier, and R.L. Snyder, *ASTM Bull. No. 117* **1942**. 15-23.

[11] K.C.A. Smith and C. W. Oatley, *Br. J. Appl. Phys.* **1955**, 391-399.

[12] K.C.A. Smith, "*The scanning electron microscope and its fields of application*" Ph.D. dissertation, **1956**, Cambridge Univ., England.

[13] K.C.A. Smith, *Pulp Pap. Mag. Ca*n. **1959**, T366-T371.

[14] K.C.A. Smith, "*Scanning*," in Encyclopedia of Microscopy, edited by G. L. Clark (Reinhold, New York **1961**, p. 241-251.

[15] T.E. Everhart and R.F.M. Thornley, *J. Sci. Instrum*. **1960**, 246-248.

[16] P.J. Breton, *Scanning Microscopy*, **1999**, 1-6.

[17] P. Duncumb, *Br. J. Appl. Phys.* **1959**, 420-427.

[18] T.A. Hall, *Micron and Microscopica Acta,* **1986**, 91-100.

[19] T.A. Hall, B. L. Gupta, *Q. Rev, Biophys*. **1983**, 279-339.

[20] S. Ensslin, K.P. Moll, K. Paulus, K. Mäder, *J. Control Release*, **2008**, 149-156.

[21] R. Tantra, J. Tomlins, P. Quincey, *Colloids Surf. B*, **2010**, 275-281.

[22] K. E. Steffens, K.G. Wagner, *Int. J. Pharm.*, **2019**, 118649.

[23] V. Iannuccelli, G. Coppi, M. Romagnoli, S. Sergi, E. Leo, *Int. J. Pharm.*, **2013**, 204-212.

[24] S.S. Said, A.K. Aloufy, O.M. El-Halfawy, N.A. Boraei, L.K. El-Khordagui, *Eur. J. Pharm. Biopharm.*, **2011**, 108-118.

[25] W. Zhou, Z.L. Wang, *Scanning Microscopy for Nanotechnology*, Springer, New York, NY, **2006**.

3.4 *In vitro – in vivo* correlation (IVIVC)

As defined by the FDA, in vitro – in vivo correlation is understood as a "*predictive mathematical model describing the relationship between the in vitro property of an oral dosage form and relevant in vivo response*".[1] The in vitro properties are dissolution and release rates of the API and the in vivo response is the concentration of the drug in the plasma or the amount absorbed. The main objective of IVIVC is to have a reliable testing method for batch release that is easy to perform, cheap and fast.[2] During the development of a pharmaceutical product, *in vitro* testing is used to get information on the influence of physical properties of the API, excipients and the manufacturing process.[3] Correlation between *in vitro* testing and *in vivo* behavior has to be shown for one trial batch that is used in a study on humans, to demonstrate that the employed dissolution and release methods are suitable to differentiate between good and insufficient samples. After a successful correlation with *in vivo* data, these methods can be used for quality control of content uniformity, batch conformity and the detection of physical or chemical changes occurring during storage or stability testing. The dissolution method can be used for subsequent batch release, when it is able to detect defective batches.[4-5]

3.4.1 References

[1] U.S. Department of Health and Human Services Food and Drug Administration, *Guidance for Industry: Extended Release Oral Dosage Forms: Development, Evaluation, and Application of In Vitro/In Vivo Correlations*, **1997**.

[2] Y. Lu, S. Kim, K. Park, *Int. J. Pharm.*, **2011**, 142-148.

[3] K.H. Bauer, K.-H. Frömming, C. Führer, *Lehrbuch der pharmazeutischen Technologie*, Wissenschaftliche Verlagsgesellschaft, Stuttgart, **2002**.

[4] U.S. Department of Health and Human Services Food and Drug Administration, *Guidance for Industry: Nonsterile Semisolid Dosage Forms Scale-Up and Postapproval Changes: Chemistry, Manufacturing, and Controls; In Vitro Release Testing and In Vivo Bioequivalence Documentation*, **1997**.

[5] The European Agency for the Evaluation of Medicinal Products, *Note for guidance on development pharmaceutics*, **1998**.

4 Transdermal therapeutic systems

4.1 Introduction

Transdermal therapeutic systems (TTS) are drug-loaded adhesive patches that are placed on the skin for controlled release of medication through the skin into the bloodstream.[1] The most commonly known example of this category is the nicotine patch. Alongside, TTS for the treatment of pain (fentanyl), angina pectoris (nitroglycerin), hypertension (clonidine) and several other systems, for a variety of different applications, are available.[2] The administration of medicine through the skin has several advantages compared to the more prevalent oral route. Transdermal drug delivery (TDD) can be used when the active ingredient would be subjected to a significant first-pass effect in the liver, where premature metabolization of the drug could occur.[3] Compared to hypodermic injections the application of patches has a lower risk for the transmission of diseases by needle re-use and does not generate dangerous medical waste.[3,4] Another advantage is that through the removal of the patch the administration of medicine can be stopped at any time, when drug input is no longer desirable.[5] Additional positive effects are achieved through long periods where the drug level in the patient is held constant.[2] The main drawback for TDD is that most APIs cannot be absorbed through the skin and/or lead to irritation or sensitization of the skin.[6] The TTS investigated in this work is a patch for the treatment of Parkinson's disease (rotigotine).

4.2 Motivation

In comparison to tablets, ointments and the intravenous application of drugs TTS are a relatively new way of drug delivery, with first publications only during the 1970s.[7] FDA approval of the first commercially available prescription patch occurred in 1979.[2] To this day, only a small portion of all available pharmaceutical products is TTS. In the year 2020, just fifteen different APIs were FDA approved for the use in patch formulations.[8] The Patches analyzed here have unique properties such as a very small profile (~150 µm) and the semi-transparent, semi-solid constitution of the API/adhesive matrix. For these reasons, many existing and well-established methods (HPLC, infrared spectroscopy, powder diffraction) cannot be used at all or only to a limited extent for the characterization of patch systems. As with all pharmaceutical dosage forms a broad scientific understanding of the

sample is demanded by the authorities. Localization and characterization of the API in the final product is of great interest to fulfill this goal. Conventional methods like powder diffraction for the elucidation of chemical composition of the specimen and laser scattering for particle size analysis are not applicable for semi-solid samples like TTS. Methods implemented for the classification of patches during the development stages include dissolution testing for the compilation of API release rates, HPLC analysis for the determination of composition of contents and digitally enhanced light microscopy for visual inspection. These methods have in common that they do not offer the possibility to collect information about the 3D spatial structure of the sample. This is particularly important for patches, as the spatial distribution of the API can have a major influence on the release. Depending on whether it is located directly at the interface between patch and skin or in deeper layers, where diffusion through the adhesive layer is necessary, it is released at different rates. To the knowledge of the author, no 3D localization methods for API in patches are known in the literature. To bridge this knowledge gap, a novel combination of analytical imaging methods is developed and implemented, to obtain in-depth information and statistical data to deliver distribution information to support patch development.

4.3 The Patch

4.3.1 The API: Rotigotine

Rotigotine is a selective dopamine agonist for the treatment of Parkinson's disease (PD), first approved in Europe in 2006 and reapproved with new API polymorphic form in 2012.[9]

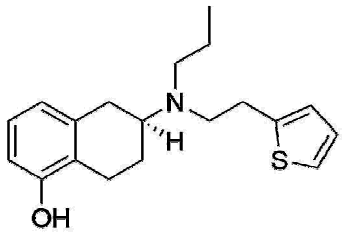

Figure 17: Chemical structure of rotigotine.

Structurally, rotigotine is (-)-(*S*)-6-[Propyl(2-thiophen-2-ylethyl)amino]-5,6,7,8-tetrahydro-naphthalen-1-ol (see Figure 17). It is the first drug that was developed from the start for TDD and not previously approved in another dosage form.[2]

4.3.2 Schematic composition

The product of interest is a patch in the form of a typical single layer matrix design, with backing foil, API-loaded adhesive matrix and release liner. The schematic of the structural composition is shown in Figure 18. This type of design can be found for a variety of different APIs.[5] The release liner is detached before administering the API-loaded adhesive matrix directly onto the skin. The backing foil provides a layer of physical protection and rigidity.

Figure 18: Schematic of the rotigotine transdermal therapeutic system; with backing foil (red), API-loaded adhesive matrix (orange) and release liner (grey)

The size of a patch with manually measured thickness of 140 µm is shown in Figure 19 (left side). To illustrate the dimensions of the patch, a micrograph of the edge of a 1-euro coin, taken with the same magnification, is provided for reference (right side). With digitally enhanced light microscopy, the different layers of the TTS are hardly discernible.

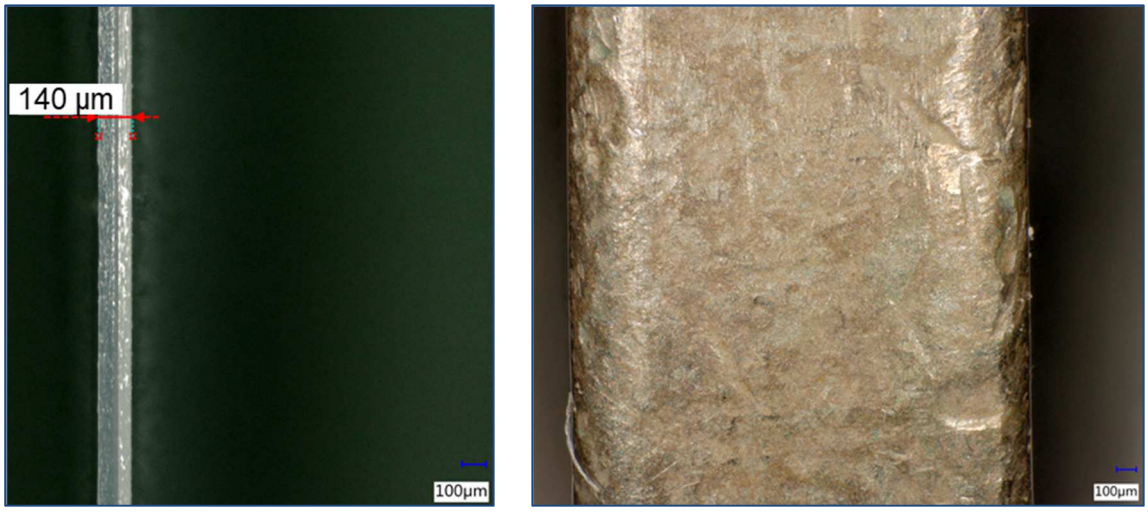

Figure 19: Micrographs in z-axis recorded with 100x magnification of a patch (left) and a 1-euro coin for comparison (right)

A top-down view of a development patch sample, with a diameter of about 36 mm, is shown in Figure 20. A 1-euro coin is again used as scale.

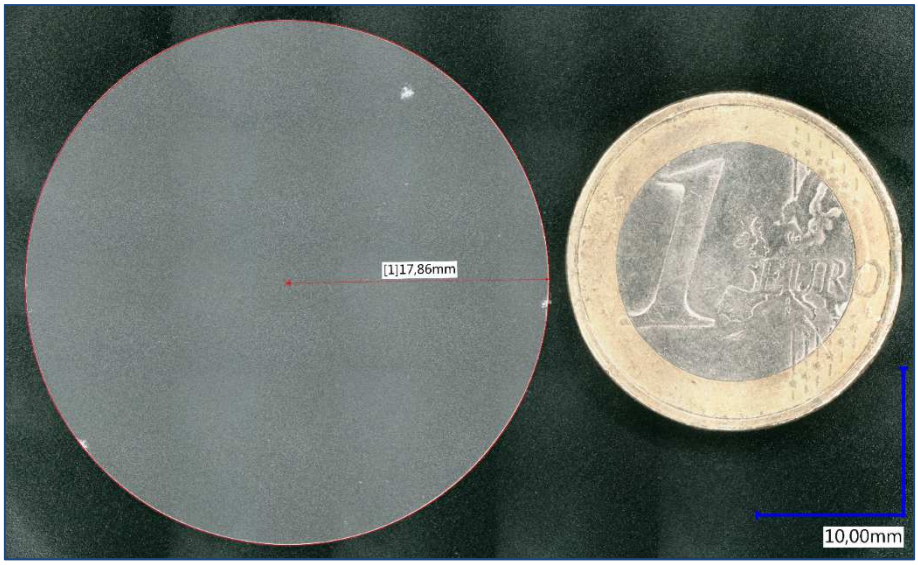

Figure 20: Micrograph of a development patch with radius measurement (left) and 1-euro coin as scale (right).

4.4 Where is the API located?

4.4.1 Digitally enhanced light microscopy

To get a first visual overview of the sample microscope images were recorded, using polarized light and anti-reflection settings for best quality (see Figure 21). Due to the reflectiveness of the release liner, it has to be removed prior to image generation. In the micrograph, several circular structures or zones of varying size can be seen. An automatic detection of the zones is not possible due to the achievable contrast being insufficient. This and the overall poor resolution of the structures is due to the small size of the circular zones and their axial and lateral distribution. Zones from deeper within the sample naturally seem smaller and more obscured by overlying layers. With manual measurements, only a small fraction of the structures can be captured. In this case, digitally enhanced light microscopy is useful for a quick first glance at the sample, but does not provide in-depth information about the patches composition. Beyond that digitally enhanced light microscopy can be used for the detection of crystallization of API and other large physical problems.

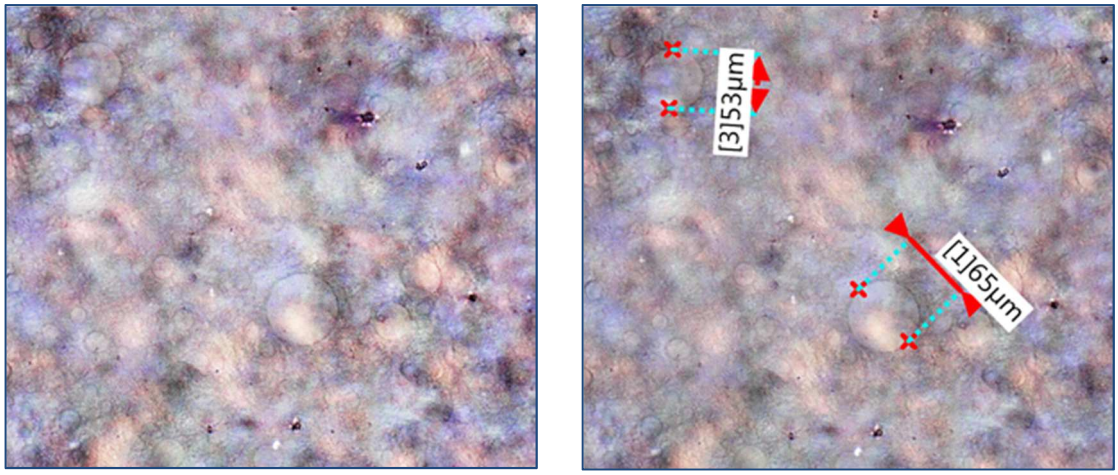

Figure 21: Contrast-enhanced micrograph taken with a digital microscope and polarizing filter, with manual measurements of the structures (right).

4.4.2 2D Raman microscopy

To gain information about the chemical composition in 2D, with special attention to the localization of the API, Raman microscopy was performed. Prior to Raman analysis, the release liner has to be removed, because it interferes with focusing on the adhesive matrix surface. The three main components of the API-loaded adhesive matrix (API, adhesive and the excipient polyvinylpyrrolidone) show characteristic Raman spectra with characteristic peaks without overlap (see Figure 22).

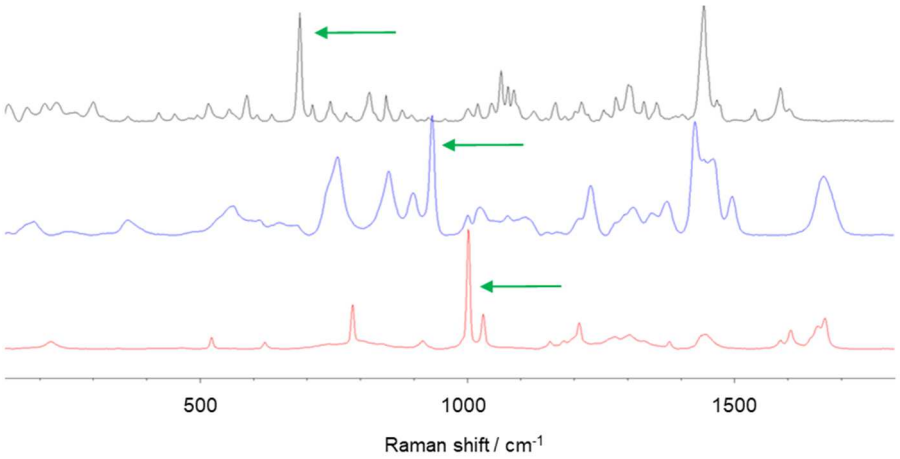

Figure 22: Overlay of the three main components: API (top); cross-linked polyvinylpyrrolidone (middle) and adhesive (bottom).

With the help of Raman microscopy, the composition of the circular structures could be illuminated. In Figure 23, Raman mapping using the MCR-ALS algorithm is depicted. It shows two distinctly different structures, complementary to each other.

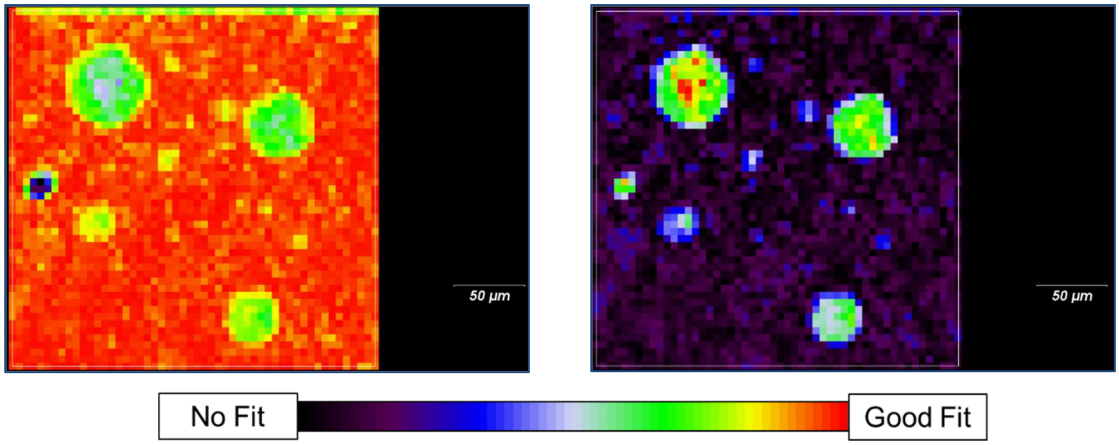

Figure 23: MCR-ALS Raman mapping of the two calculated components.

Using the DCLS algorithm, the circular structures can be attributed to API co-located with the excipient cross-linked polyvinylpyrrolidone. Their distribution is in good accordance with the structures visible in the microscope image as well as with the distribution of the second component found with MCR-ALS. Additionally the surrounding spectra are in good accordance with the adhesive reference spectrum (see Figure 24).

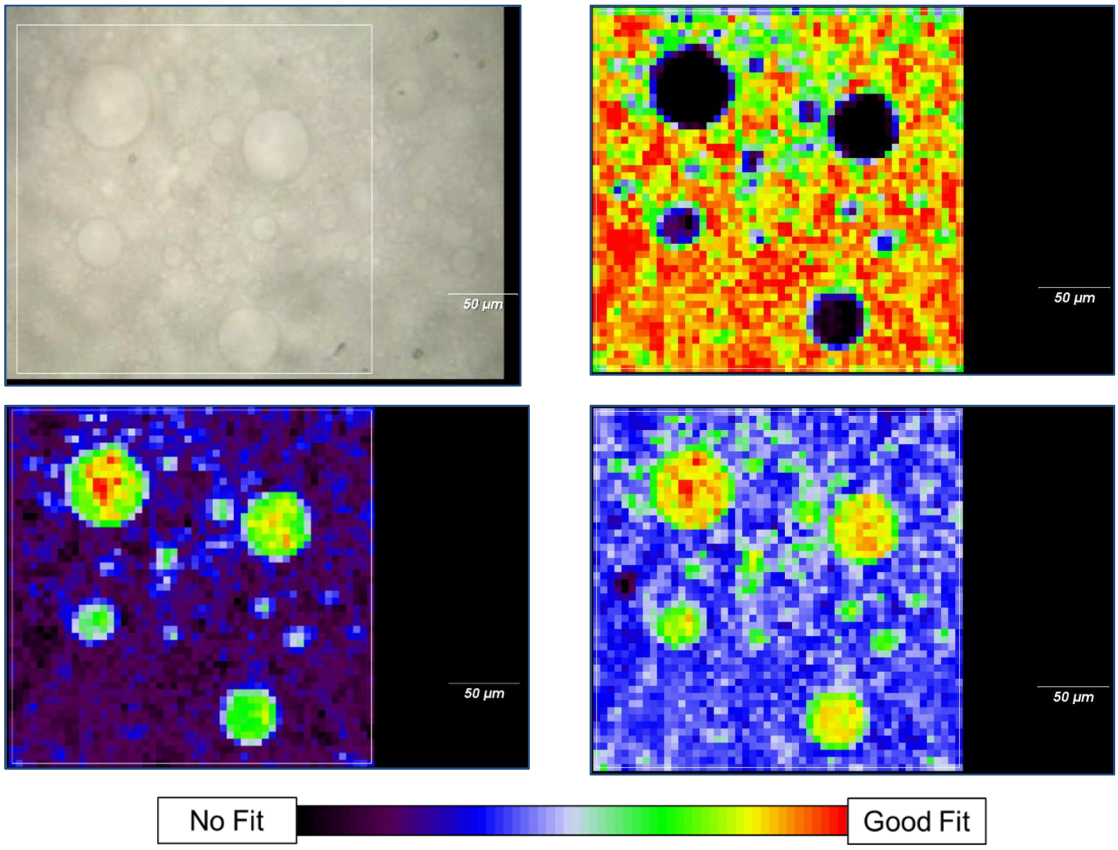

Figure 24: Microscope image of a patch section (top, left); 2D Raman microscopy DCLS mapping of the same area for the adhesive (top, right) the API (bottom, left) and polyvinylpyrrolidone (bottom, right).

Mapping of small areas (approximately 260 x 260 µm) of the specimens is achievable. Mapping of larger areas leads to damage of the measured regions. This is because of the semi-transparent nature of the adhesive layer and the opaqueness of the backing foil. Laser light can partly travel through the API matrix, is then reflected at the backing layer and is passing again through the API matrix, increasing the time the laser beam interacts with the sample. Additionally, due to the small nature of the structures, very small scanning steps (5 µm) have to be chosen, which increases the number of spectra taken per area. Finally because of fluorescence with the line laser (785 nm) point mapping had to be used, which additionally extends laser time on the sample. These factors combined lead to high-energy input into the sample, which results in damaged patch areas and unusable spectra, when larger areas are investigated.

4.4.3 SEM/EDX

As with light and Raman microscopy, for SEM/EDX analysis the release liner has to be removed prior to measurement.

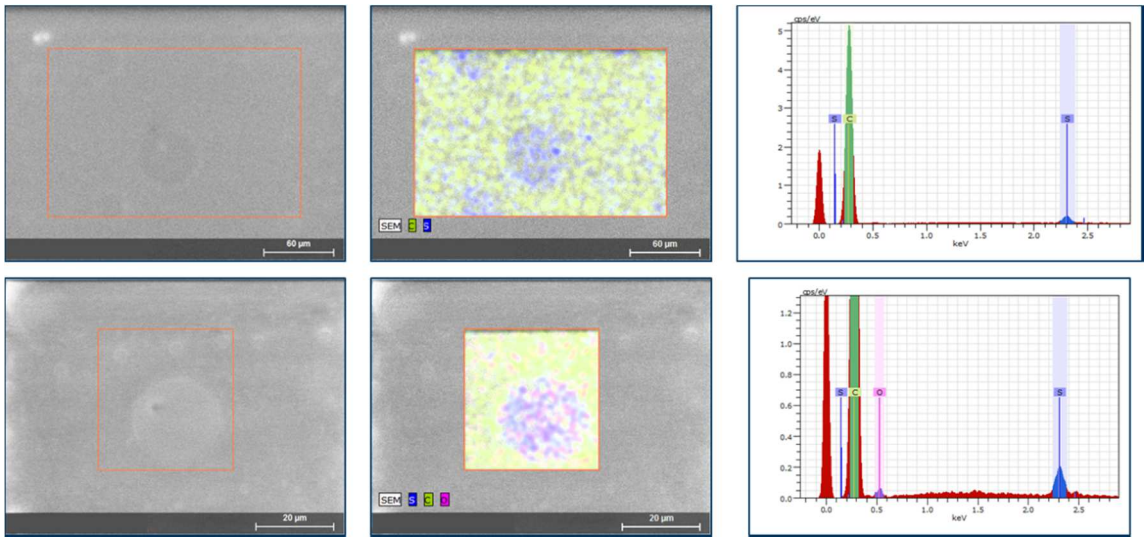

Figure 25: SEM/EDX images: SEM-Image with 600x magnification (top, left), with 2000x magnification (bottom left); corresponding EDX-mapping (middle) and EDX spectra (right).

In Figure 25, SEM/EDX images of rotigotine patches are shown in 600x and 2000x magnification. The 600x magnification is chosen to show the largest possible area with useable contrast, with less magnification the zones cannot be detected. Using magnifications larger than 2000x increases the sample damage making the recorded images unusable. Circular structures already known from light and Raman microscopy can be detected. Since the API is the only component of the patch formulation containing a sulfur atom, mapping of sulfur reveals the site of API molecules. Mapping of the sulfur signal

(blue) for 600x magnification and the sulfur and oxygen (also contained in the API molecule) signals (purple) for the 2000x magnification, show localization of API inside the circular structures. This confirms the findings of the 2D Raman microscopy results. For this type of sample, SEM/EDX suffers from bad contrast and exhibits noticeable blurriness. This is partly due to the semi-solid nature of the patch. A fraction of the adhesive matrix is seemingly not completely stable in vacuum. Another factor is that the high beam intensity necessary for EDX is damaging the surface of the sample over time.

4.4.4 3D Raman microscopy

Due to the semi-transparent nature of the patch samples, Raman mapping in 3D is possible. To the collection of Raman spectra in x- and-y direction found in 2D Raman microscopy, for volume measurements additional spectra in z-direction are recorded. This is achieved using a highly confocal measurement setup, thus only allowing information from a very narrow focal plane to reach the detector. The scanned sample volume is then composed of individual voxels (3D pixels) each with its corresponding Raman spectrum. Data treatment and analysis proceeds analogous to measurements in 2D. The problems illustrated for 2D Raman (sample damage with larger measurement areas) do even more apply for volume mapping that is why only small regions can be mapped.

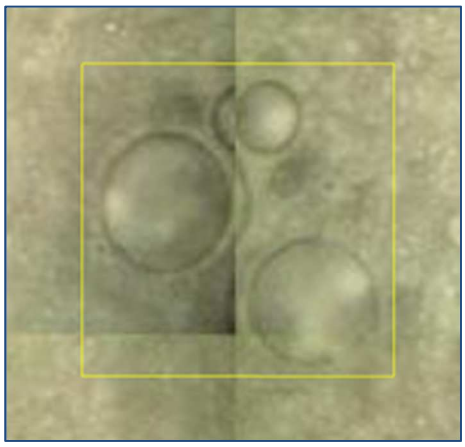

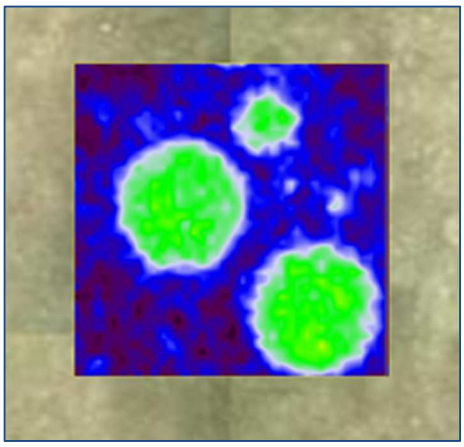

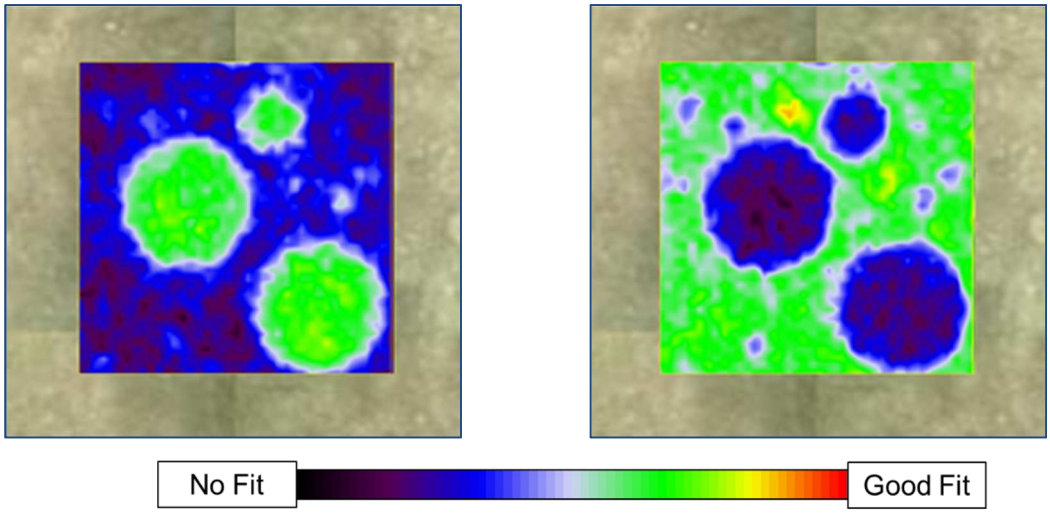

Figure 26: Raman-Volume measurement, top down view. DCLS mapping of API (top, right), polyvinylpyrrolidone (bottom, left), adhesive (bottom, right).

In Figure 26, a top down view of the analyzed patch area, with DCLS mapping of the API, the excipient cross-linked polyvinylpyrrolidone and the adhesive is shown. As with 2D mapping, API and cross-linked polyvinylpyrrolidone are co-located in the same areas – the circular structures – and are surrounded by the adhesive. To improve clarity for the 3D Raman microscopy images different substances are assigned colors. Areas where the measured spectra are in good accordance with the reference spectra (green and yellow in Figure 26) are color-coded red for the API, cyan for the adhesive matrix and blue for the backing foil. To achieve a 3D image, the adhesive matrix is displayed with 95% transparency (see Figure 27).

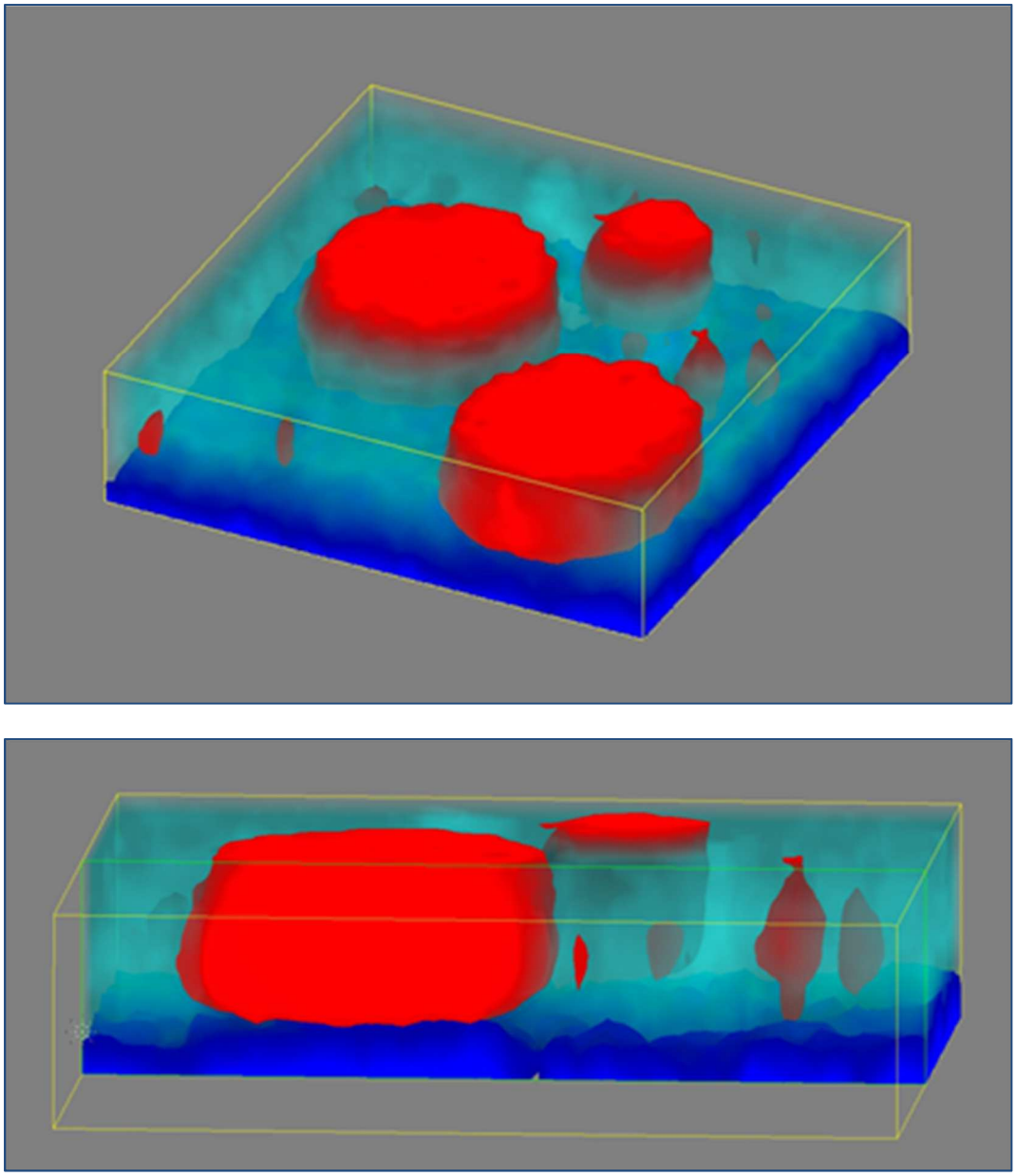

Figure 27: 3D Raman images: Isometric view (top) and vertical cut through the sample (bottom) with DCLS mapping of API (red), adhesive matrix (cyan) and backing foil (blue).

API reservoirs of different shapes, sizes and relative localization in respect to the sample-air interface, can be found. Especially the larger zones display structures similar to spheres, which seem to be wedged between the backing foil and the (for the measurement removed) release liner, which would be found on the top. This shows that large surface areas of API would be in contact with the skin, once the patch is applied. Smaller API zones show drop-shaped patterns and are fully enclosed by the adhesive matrix.

4.4.5 Micro-CT

4.4.5.1 Sample preparation

As seen with the other analytical methods, the structures of interest have sizes in the range from < 1 µm to ~50 µm. The entire patch has a diameter of about 36 mm. As mentioned in paragraph 3.1.5, the combination of a large sample and very small structures makes a reduction in sample size necessary. Therefore, 2 mm by 3 mm areas of patch were cut out and mounted on a special precision clamp sample holder (see Figure 28). In contrast to the other implemented analytical methods, for micro-CT measurements the removal of the release liner is not necessary.

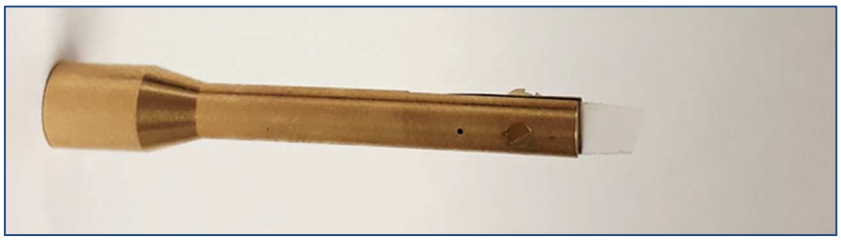

Figure 28: Patch cutout mounted on a precision clamp sample holder.

4.4.5.2 Measurement and Data treatment

In Figure 29, radiographs of two different viewing angles of a patch sample are shown. In the picture on the right side, the patch composition with release liner, adhesive layer with API and backing foil (from left to right) can be seen.

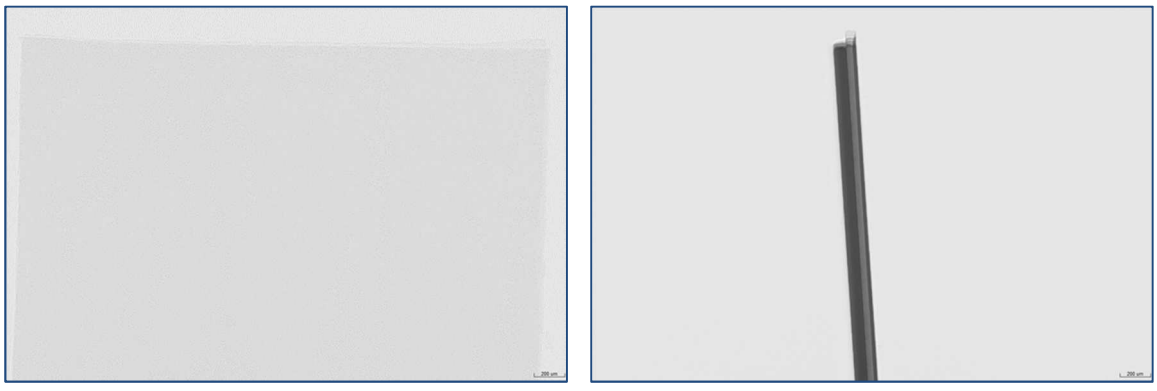

Figure 29: Radiographs of a patch sample coronal view (left) and sagittal view (right).

Since small structures down to the maximum resolution of the method should be investigated, the collected images are recorded using the highest possible quality (4032 x 2688 px and pixel size of 0.9 µm), which leads to large files (1900 individual images; with a total size of 39 GB), resulting in long computational times (multiple hours). After the

measurement is completed, a suitable region of interest (ROI) is chosen (see red rectangle in Figure 30). This is achieved by the digital removal of areas entirely without sample, sample edges and areas of the release liner and backing foil. Thus, the file size can be reduced and computational times shortened, without losing useful information.

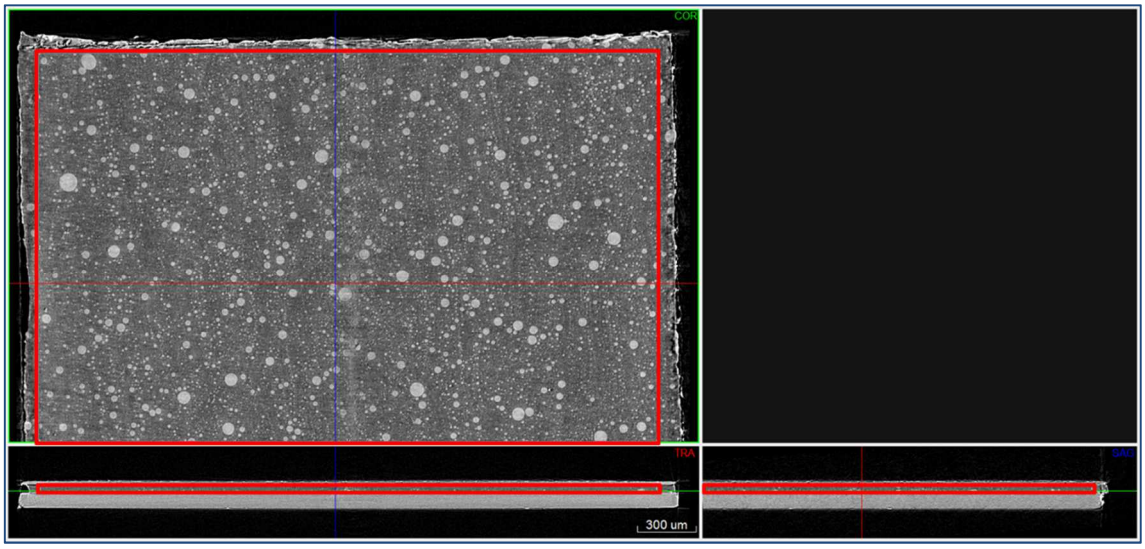

Figure 30: Coronal (top), transverse (bottom, left) and sagittal (bottom, right) grey scale micrographs with the ROI in red.

With the combined findings of microcopy, SEM/EDX and 2D/3D Raman microscopy, it can be assumed that the API is located in the circular zones, which correspond to areas of high relative density (white and light grey) in the micro-CT pictures shown in Figure 30 and Figure 31. For an in-depth comparison between micro-CT and Raman imaging, see paragraph 4.4.6. A custom-made task list (TL_RGT_01) was developed and the stepwise process of the digital isolation of structures with high relative density is shown in Figure 31. For a clearer representation, the steps are shown in 2D, while the actual data processing takes place in 3D. The first image shows the 2D greyscale image of the plane closest to the release liner, the area later in contact with the patients' skin, of the chosen ROI from Figure 30. For the second image, a density threshold was chosen to isolate the circular structures from the surrounding sample material. This converts the image to a binary file, which is necessary for the implementation of further digital protocols and data analysis. The last step, the removal of stray particles originating from noise, yields the final image, which is used for the analytical data acquisition.

(1)

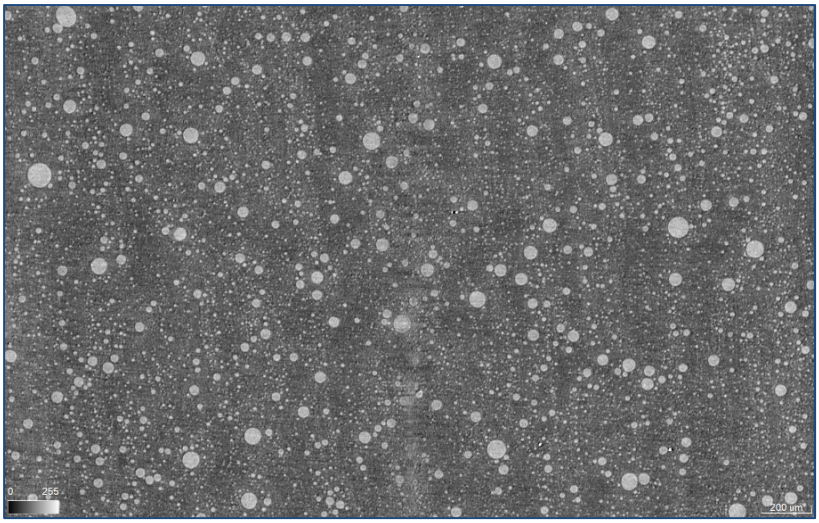

(2)

(3)

Figure 31: Stepwise treatment of the micro-CT images: Raw image of the chosen ROI (top); image after thresholding (middle); image after thresholding and the removal of stray particles (bottom).

Following the data treatment steps explained above, the data set can be used to visually augment the greyscale image to show the spatial particle distribution in the patch with high contrast. The isolated areas with high relative density are colored red; areas of low relative density are colored cyan and set to 95% transparent to enable true 3D view of the spherical structures (see Figure 32). In the top down view, circular zones with varying sizes can be seen randomly distributed throughout the sample. When looking at the isometric and cross-sectional view, the large structures are hemispherical with the section plane facing outwards. This is the interface area between patch and environment/skin. The same is true for small areas of high relative density, when bordering the release liner. When smaller particles are located in a way that they are surrounded by the adhesive matrix, they are mostly spherical in shape.

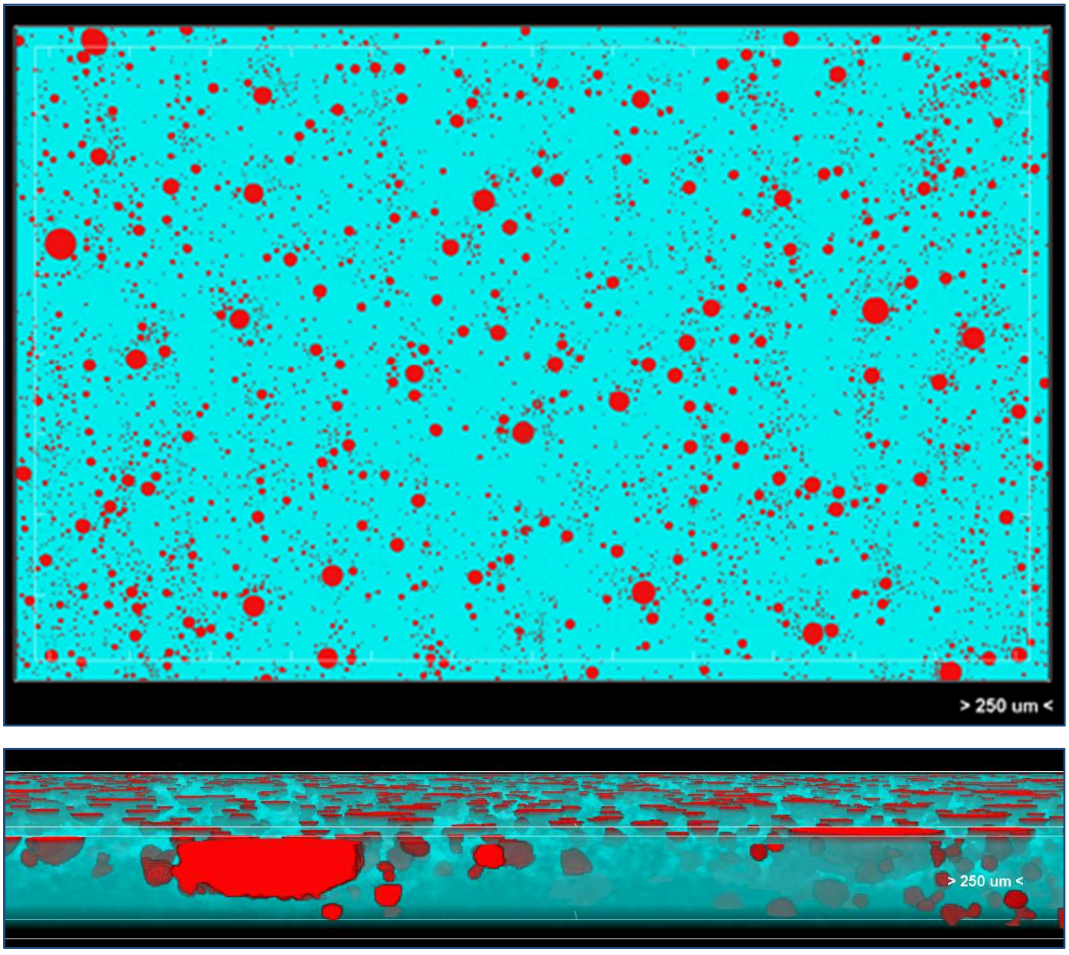

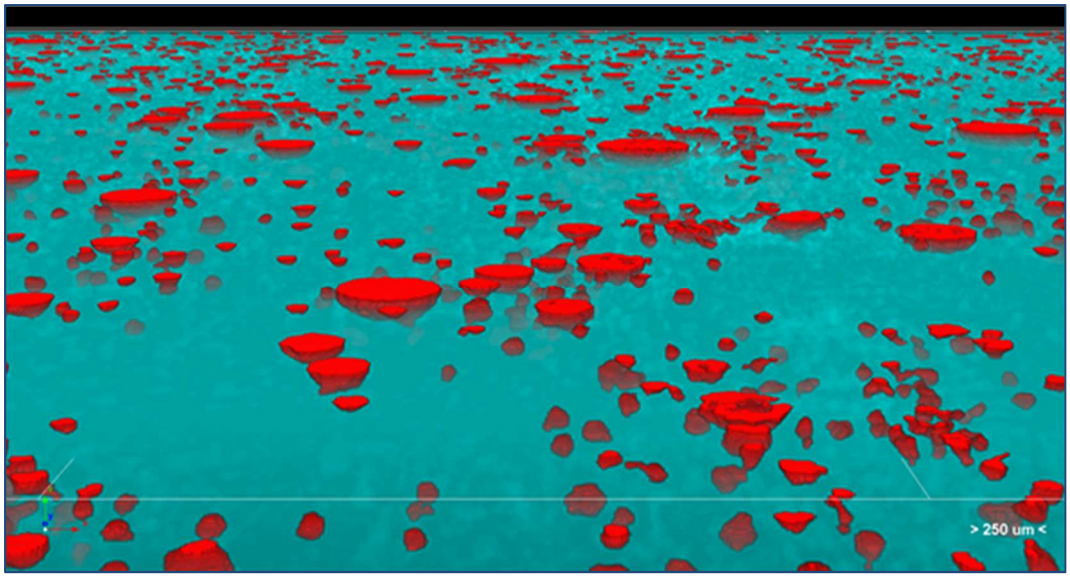

Figure 32: 3D view of micro-CT Data with the circular structures colored in red and the surrounding adhesive matrix in cyan with a high opacity value: top down view (top), vertical cut through the adhesive matrix (middle) and isometric view (bottom).

The 3D micro-CT images give the impression that the large areas of high relative density are impacted in shape and expansion by the release liner they are bordering. This is plausible from a manufacturing standpoint, since the coating-mixture is applied directly onto the release liner and particles of higher density should sink to the bottom of a semi-solid framework.

4.4.6 Combination of information – Localization of the API

In Figure 33, comparison of 3D Raman mapping and 3D micro-CT imaging of a singular zone is shown. With both techniques, similar structures can be found. With Raman imaging, the API can be located in the – with microscopy visible – spherical structures. The main drawback of this testing method is its spatial restrictions, explained in sections 4.4.2 and 4.4.4. Additionally the removal of the release liner is necessary prior to measurements, which could have an influence on the topology. Micro-CT measurements on the other hand lack in chemical information but enable the analysis of larger sample areas and do not require the removal of the release liner. Finding of the same structures, in both 3D methods and supporting evidence in SEM/EDX analysis, enables linking of chemical information – localization of API in the spherical structures – to the areas of high relative density in the micro-CT data and thereby a comprehensive understanding of the patch system. This led to the application of micro-CT analysis as a tool for the root cause investigation of an occurred out-of-expectation (OOE) quality event.

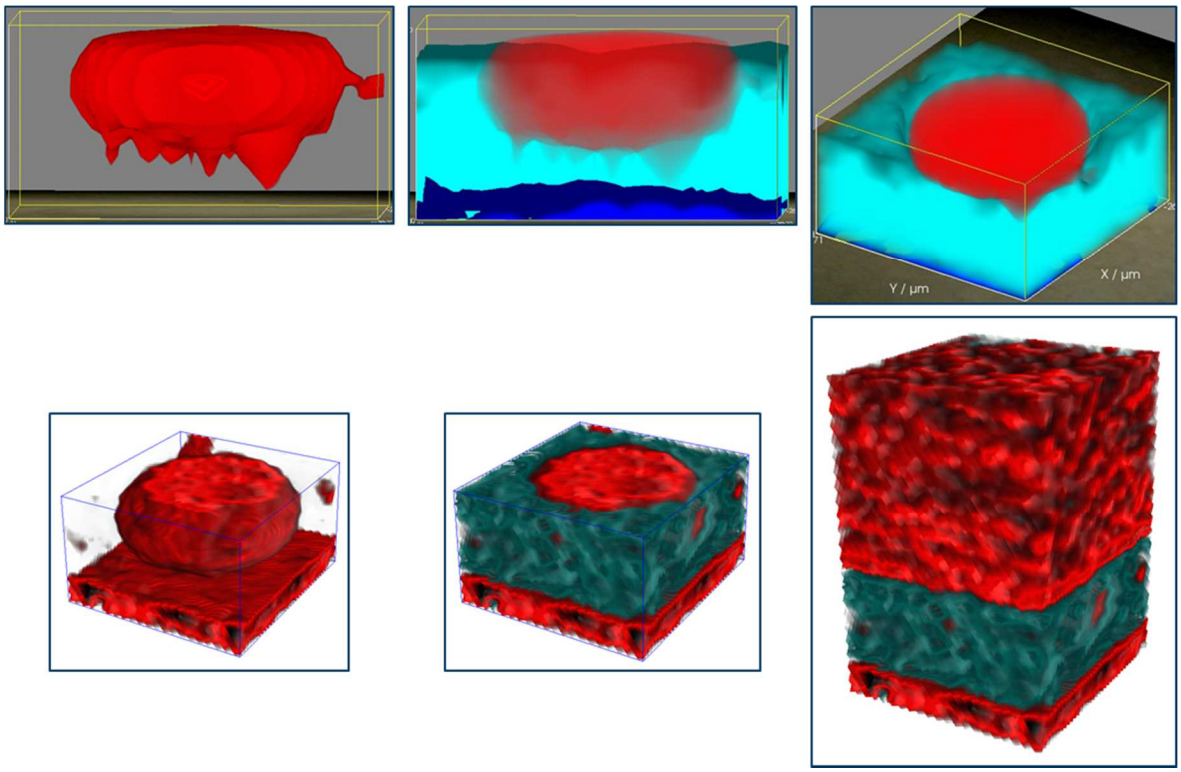

Figure 33: 3D Raman images with the mapping of API (red), adhesive matrix (cyan) and backing foil (blue) (top row), and 3D micro-CT images of the release liner, a spherical structure and backing foil; all areas with high relative density in red and the adhesive matrix as areas of low relative density in cyan (bottom row).

4.5 Analysis-guided process improvement

4.5.1 The challenge

In patch development, dissolution testing is used to evaluate the extent and rate of the release of API from the patch sample. Even though *in vitro – in vivo* correlation (IVIVC) is generally not guaranteed for TTS products, dissolution testing can be used to detect differences in the production flow. Following the “Guideline on quality of transdermal patches” published by the EMA, *in vitro* release tests are “a critical quality attribute to be specified in the finished product release and shelf life specification”.[10]

During development of the patch manufacturing process, unexpected dissolution results were found during batch testing, causing an out-of-specification quality event. One of the batches showed unexpected differences in dissolution rates between samples taken from the start of production (Start) and later sampling points. Samples taken at the end of the manufacturing process (End) display a noticeable shift towards a slower dissolution rate (see Figure 34).

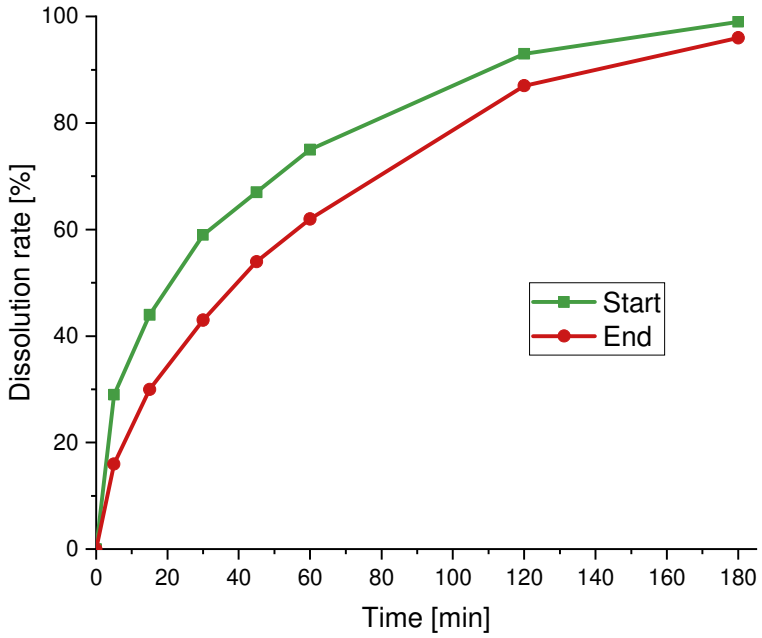

Figure 34: Dissolution profiles of samples taken at the start (green) and at the end (red) of the manufacturing of the faulty batch.

Upon first investigation with digitally enhanced light microscopy, it was found that the circular/spherical zones, which were demonstrated to contain API, reduced in size during the manufacturing process (see Figure 35). Due to the relative poor contrast, the overall image quality of the microscope images and the lack of automated zone size determination it was only possible to analyze small sample sections in 2D. To enable analysis of larger areas of sample, data collection in 3D and automatable size determination, micro-CT imaging was chosen for further patch characterization.

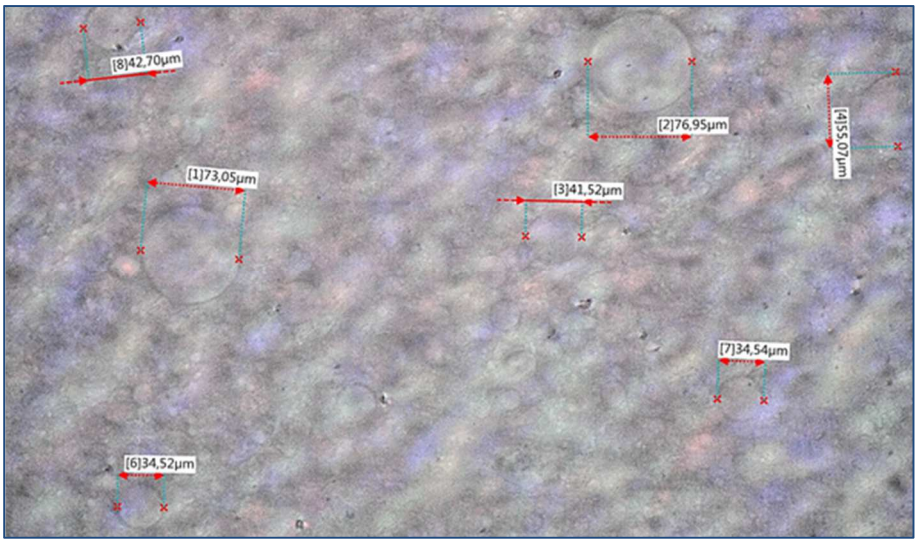

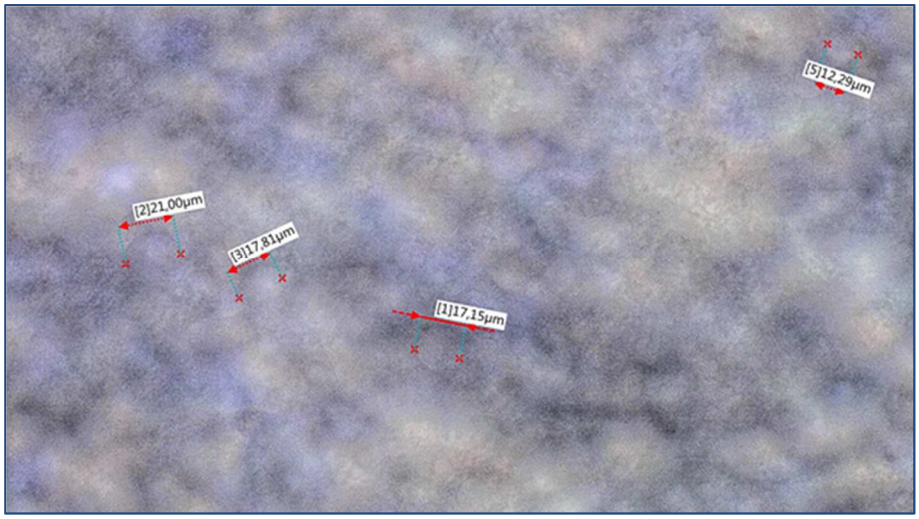

Figure 35: Microscope images of samples taken at the beginning (top) and the end (bottom) of the manufacturing process, with manual size measurements.

In the following paragraphs, the stepwise troubleshooting process will be outlined following the detection of an erroneous batch. An overview of the performed steps is given in Figure 36.

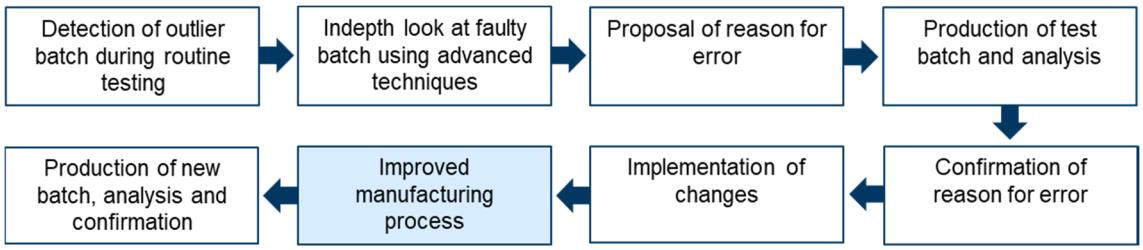

Figure 36: Strategy outline for the troubleshooting process.

4.5.2 Analysis Parameters

Prior to sample comparison, analysis parameters have to be selected. In the prior paragraphs, it was shown that the API measurement with micro-CT is possible. Particle detection is realized using the steps described in paragraph 4.4.5. Of special interest is the API particle size (distribution) and its localization within the adhesive matrix. A 2D and a 3D analytical approach was used to illustrate differences between the samples.

3D analysis parameters

For full 3D particle size analysis, the structure thickness parameter was employed. This is a way of obtaining a particle size values independent of the structures' type (for further detail see Hildebrand 1997). This is necessary since the zones especially in the edge regions are no longer of pure spherical nature. Furthermore, this provides a method of API size

measurement, which is independent from the location within the API-matrix. The entire particle is used for size measurement. For the graphical representation, histograms are plotted. For the x-axis, particles are binned according to size, with size classes being double the measurement resolution of 0.9 µm. The y-axis is plotted as fractional volume density distribution, which is a way of weighing particles according to their contribution to the total volume of all detected particles, instead of the pure count of particles in a size bin, since API distribution is desired and not numerical particle count.[11]

2D analysis parameters

Because the interface between the release liner and the adhesive matrix is the area later in contact with the dissolution medium (and the skin), a 2D analysis method of the sample was implemented to better understand changes in this area. Additionally, it offers the possibility of comparison with the microscope images. For the analysis, only 2D information from a singular data layer bordering the release liner was used. The extracted values are presented as major diameter, which describes the largest possible diameter that can be fitted to a particle. The amount of particles in a certain size range is counted and normalized to count per mm² to ensure comparability between samples. This is necessary because sample preparation is done manually, resulting in specimen with slightly different sizes. For a clearer visual presentation, particles from this layer are color-coded according to particle size (see Table 1).

Table 1: Color-coding according to particle size, for 2D micro-CT analysis with particle sizes referring to the major diameter.

Range [µm]	0.0 – 1.8	1.8 – 3.6	3.6 – 7.2	7.2 – 14.4	14.4 – 28.8	28.8 – 57.6	57.6 – 115.2
Color	Light blue	Blue	Cyan	Green	Yellow	Orange	Purple

As a supplementary measure for API characterization in 2D, the total area of zones is calculated summing the individual surfaces of all API zones and converting it to area per mm², to ensure comparability between samples.

4.5.3 Characterization of the initial faulty batch

A histogram of the structure thickness distribution of API zones in 3D, of samples from the erroneous development batch, is depicted in Figure 37.

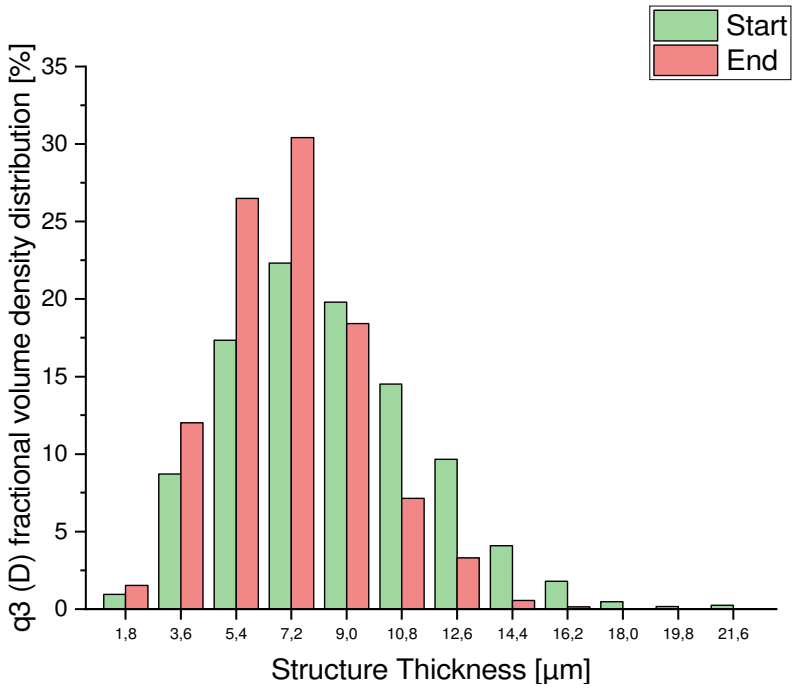

Figure 37: Structure Thickness distribution of API zones in the samples from the start and end of the manufacturing process of the faulty batch.

A shift from larger API-particles at the beginning of the production, to smaller particles at the end of the manufacturing process can be seen with a decrease in average structure thickness from 8.5 µm at start to 7.0 µm at the end. Particles with a structure thickness > 18 µm are completely missing at the end of production. 2D Micro-CT images of the interface between the API/adhesive matrix and the release liner also show a decrease of large particles (orange) from the start to the end of manufacturing (see Figure 38).

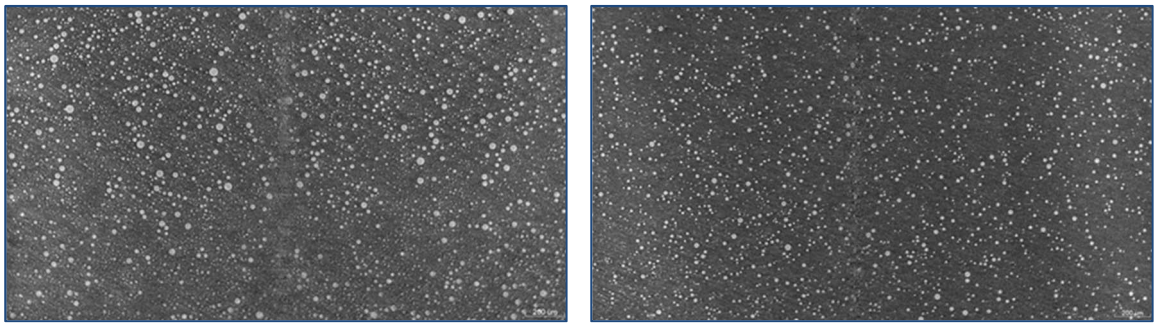

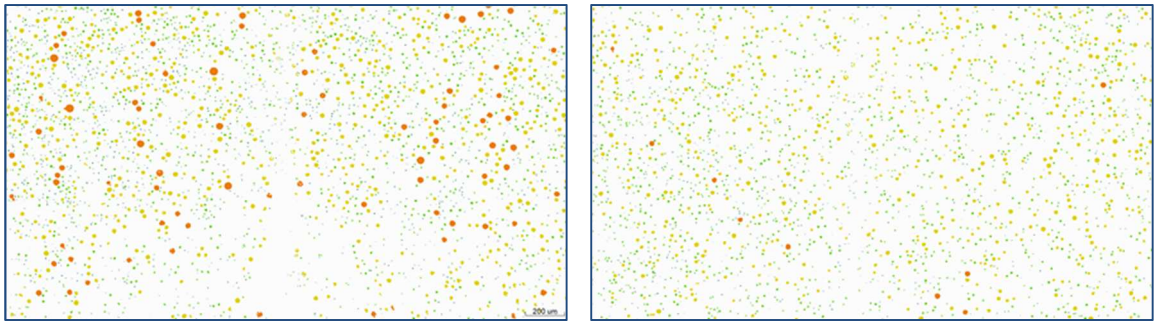

Figure 38: Top row: Grey scale micro-CT images of the patch layer closest to the release liner for sampling points at the start (left) and the end (right) of the manufacturing process. Bottom row: Corresponding images with color-coding according to zone size.

The histogram of the corresponding particle size measurements supports the visual impression. The sum of all measureable particles is decreasing by 26%. Additionally the amount of the largest zones (> 57.6 µm) – zones with the largest surface-to-surface contact – are mostly missing at the end (see Figure 39).

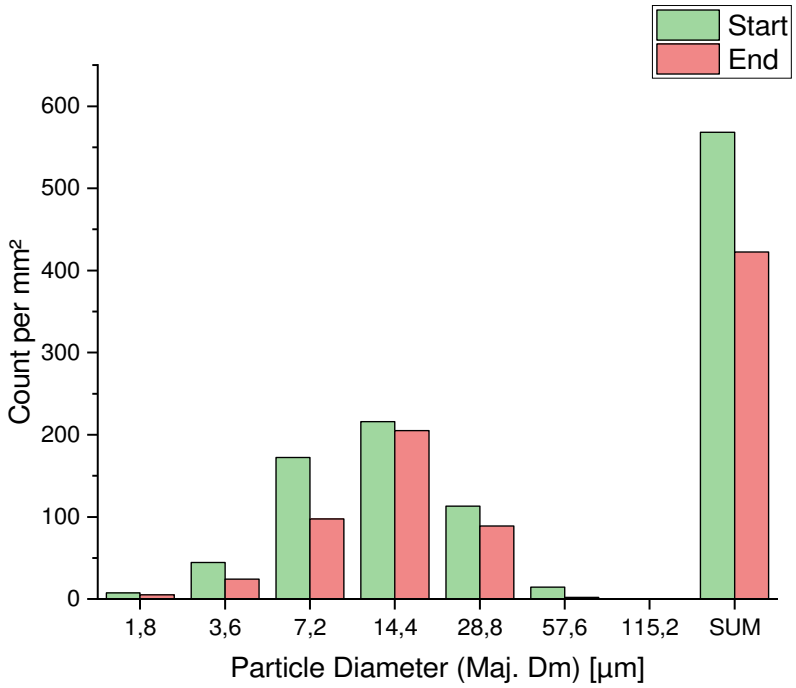

Figure 39: 2D particle analysis of the layer bordering the release liner of the faulty batch.

When adding up the area of each individual API zone, a similar difference between the start and the end of the manufacturing process can be found (see Table 2). The total area of zones reduces by 37%.

Table 2: Total area of zones in the layer bordering the release liner of the faulty batch.

Sampling point	Start	End
Total area of zones per mm² [µm²]	55039	34550

All three metrics point to a reduction in size of individual API particles as well as an overall decrease of API in the layer bordering the release liner. With the reduction of API area in the layer bordering the release liner for samples taken later in the manufacturing cycle, more API from deeper layers in the adhesive matrix has to migrate to the interface, which is a slowing factor. It is likely that this is responsible for the slower dissolution performance for samples taken later in the manufacturing cycle.

4.5.4 Assumed and investigated reason for error – Test batch A

To ensure homogeneity of the API, it is dissolved in a sensitive mixture of four different solvents. Because of the volatility of some of these solvents, the coating mixture has to be contained in an environment as stable as possible. If at any time during the manufacturing process a leak would occur, solvents could evaporate leading to a change in mixture composition and thus API solubility, subsequently affecting the patch performance. To test this hypothesis, a new batch (called test batch A) was manufactured simulating the occurrence of a leak, an untight seal or otherwise compromised manufacturing system, with an intentionally untight vessel.

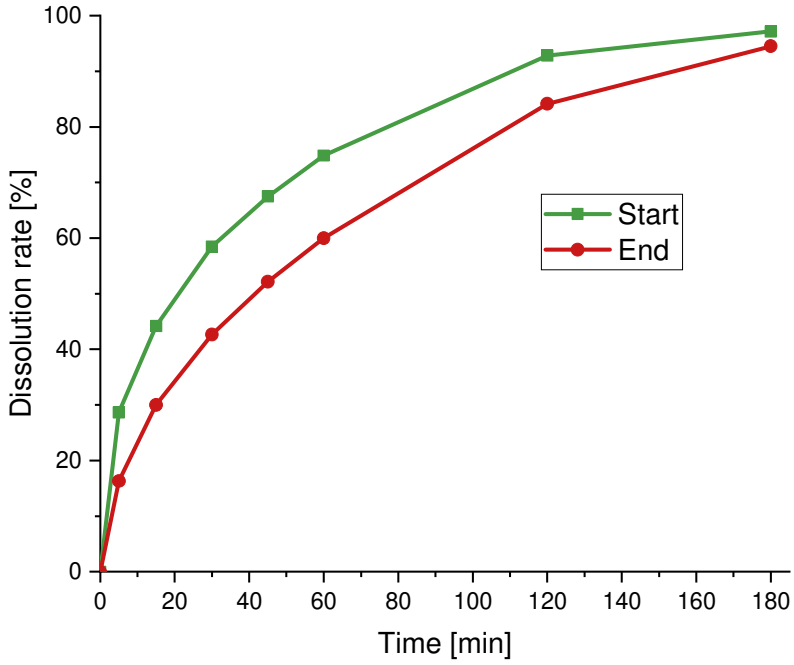

Figure 40: Dissolution profiles of samples taken at the start and end of the manufacturing of test batch A.

The dissolution results for test batch A show a similar trend of reduced dissolution rate for samples taken at the end of production. The curve progression is comparable to the initial faulty batch (see Figure 40). The histogram of the structure thickness distribution of API

zones is depicted in Figure 41. This batch also shows a decline in the amount of large zones from the start to the end of the manufacturing process with the average structure thickness decreasing from 12.8 µm to 8.3 µm. It is noticeable that a higher proportion of large zones can be identified and that generally the particles size distribution is broader compared to the initial faulty batch at the start.

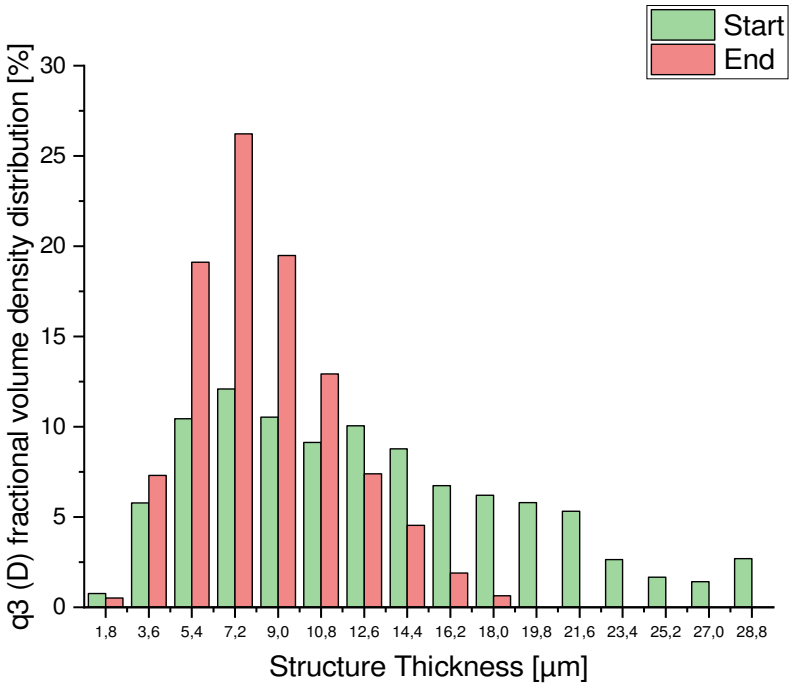

Figure 41: Structure Thickness distribution of API zones in the samples from the start and the end of the manufacturing process of test batch A

2D Micro-CT images of the interface between the API/adhesive matrix and the release liner also show a decrease of large particles (orange) from the start to the end of manufacturing. Unlike the initial faulty batch, very large particles (purple) are present at the start, which are entirely missing at the end (see Figure 42).

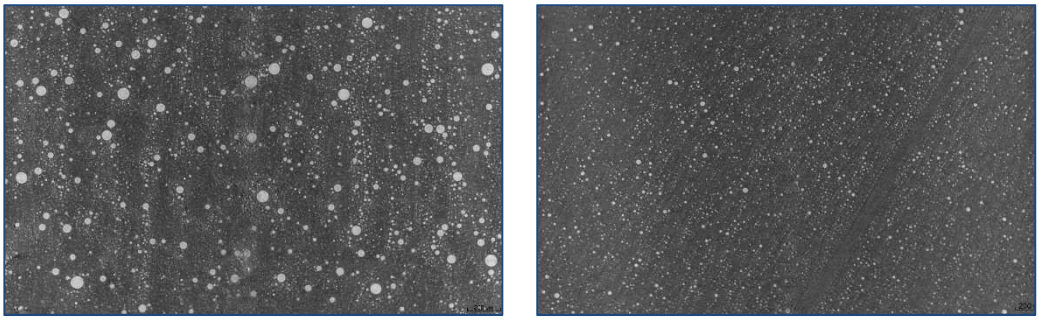

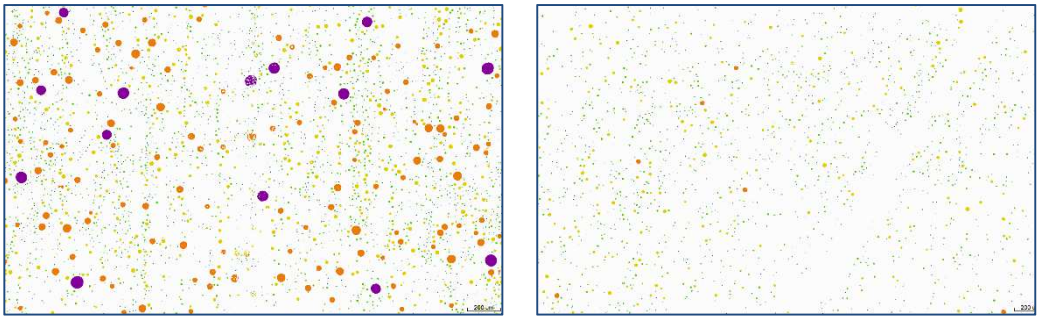

Figure 42: Top row: Grey scale micro-CT images of the patch layer closest to the release liner for sampling points at the start (left) and the end (right) of the manufacturing process. Bottom row: Corresponding images with color-coding according to zone size

The histogram of the corresponding particle size measurement follows the visual findings. There are about 50% less particles per mm² overall. Particles > 28.8 µm are missing and the number of smaller particles has also decreased considerably at the end of production (see Figure 43).

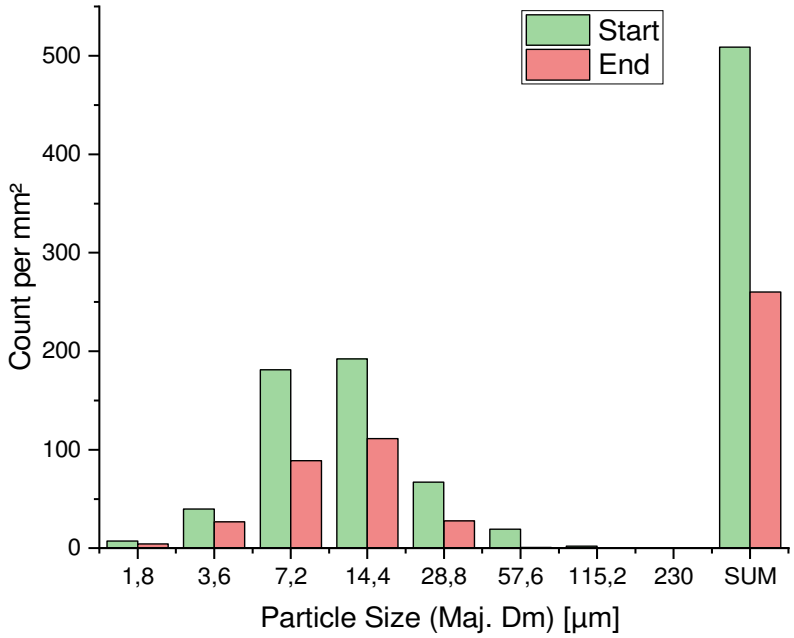

Figure 43: 2D particle analysis of the layer bordering the release liner of test batch A

When adding up the area of each individual API zone, a similar difference between the start and the end of the manufacturing process can be found (see Table 3). The total area of zones reduces by 74%, which is double the amount of the faulty batch.

Table 3: Total area of zones in the layer bordering the release liner of test batch A.

Sampling point	**Start**	**End**
Total area of zones per mm² [µm²]	56790	14890

Conclusion

Test batch A also shows reduction in particles sizes (2D and 3D), particle count and total area of zones per mm², from the start to the end of production. However, the effects are more pronounced. This indicates that a leak in the manufacturing system was indeed the cause for the error. The difference in the strength of the impact could be caused by a smaller leak in the initial faulty batch resulting in a less severe influence on the measured API metrics.

4.5.5 Improved manufacturing process – Test batch B

Following the findings in the above paragraphs, additional precautions were implemented to ensure a properly sealed manufacturing system. A new batch (test batch B) produced after the implementation of these changes is analyzed in the following. The dissolution rates for samples taken at the start and at the end of manufacturing are nearly identical (see Figure 44).

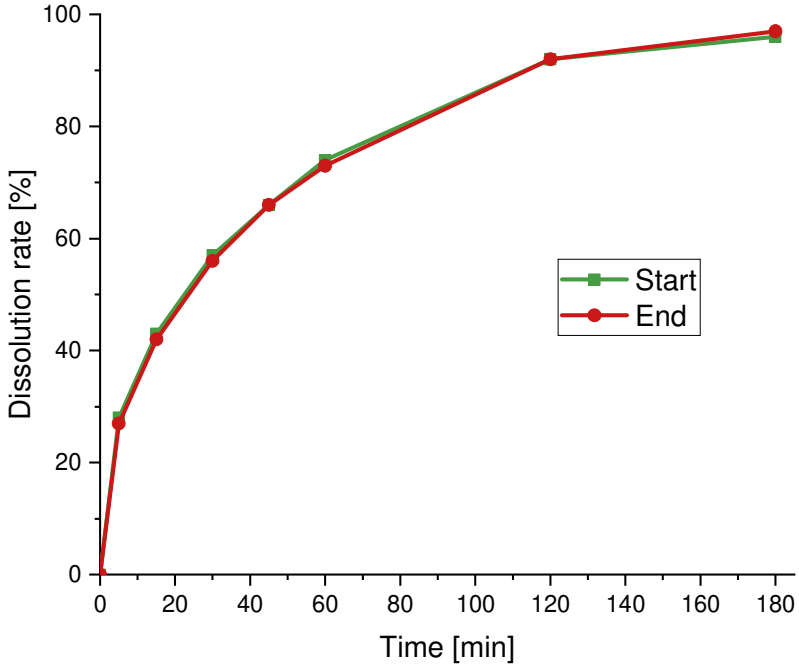

Figure 44: Dissolution profiles of the samples from the start and the end of manufacturing process of test batch B.

In Figure 45, the structure thickness distribution of the API zones is shown. From the start to the end of production, the particle size is shifting to smaller values, but the shape of the distribution remains comparable. The largest particles are again completely missing at the end of the manufacturing cycle and the average structure thickness is decreasing from

11.4 µm to 8.8 µm. Overall there is still a measurable difference between the samples but to a lesser extent.

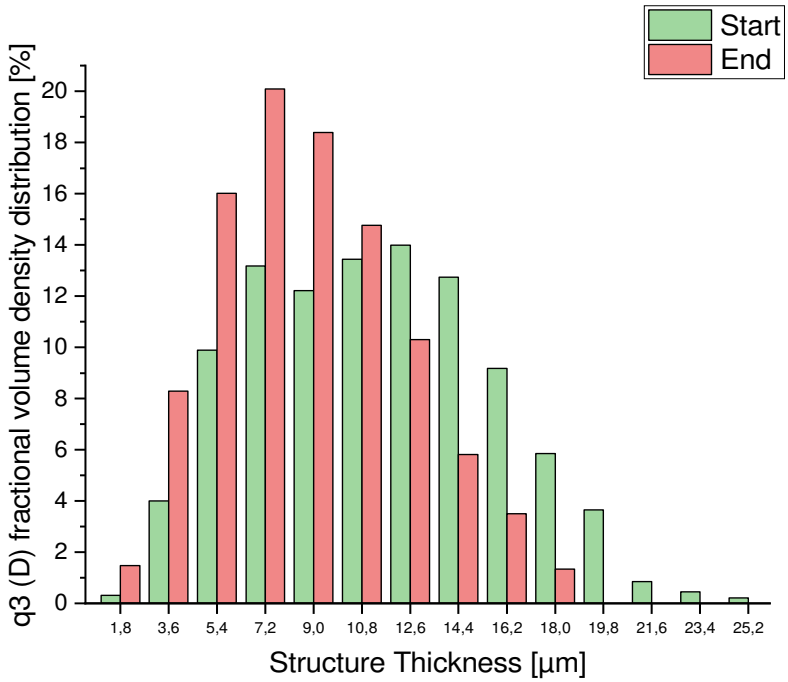

Figure 45: Structure Thickness distribution of API zones in the samples from the start and the end of the manufacturing process of test batch B.

A similar behavior can be found in images of the layer bordering the release liner. Disappearing of the largest particles (purple) and a small reduction in large particles (orange) at the end of production can be seen (see Figure 46)

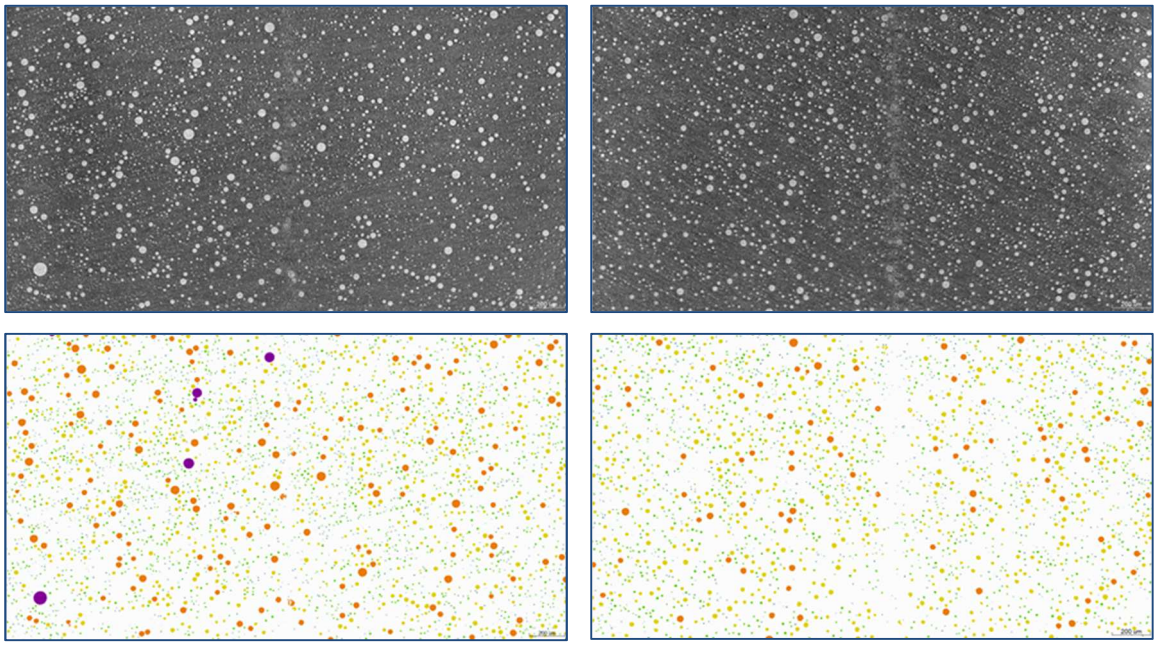

Figure 46: Top row: Grey scale micro-CT images of the patch layer closest to the release liner for sampling points at the start (left) and the end (right) of the manufacturing process. Bottom row: Color-coded images according to zone size of the patch layer closest to the release liner for sampling points at the start (left) and the end (right) of the manufacturing process.

Analysis of this region is graphically presented in Figure 47. The histogram shows a small reduction of large particles and a reduction in overall particle count by about 9%.This is similar to the trend found in the two faulty batches, but in a much weaker manifestation.

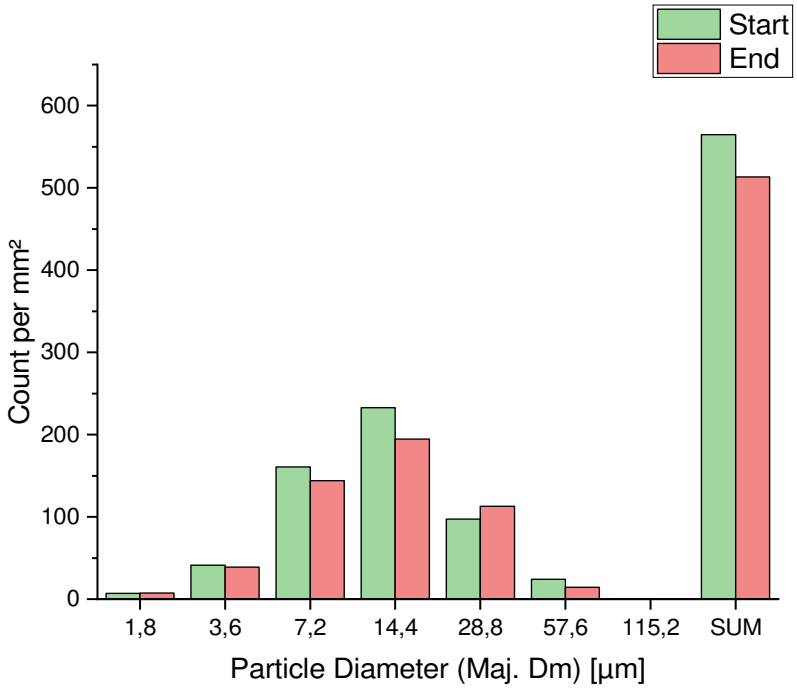

Figure 47: 2D particle analysis of the layer bordering the release liner of test batch B.

The difference between the total area of API zones per square millimeter patch surface is 18%, again a considerably smaller reduction compared to the faulty batch and batch A (see Table 4).

Table 4: Total area of zones in the layer bordering the release liner of test batch B.

Sampling point	**Start**	**End**
Total area of zones per mm² [µm²]	65940	54006

4.6 Inter-batch comparison

An overlay graph of all dissolution results discussed in the previous paragraph is depicted in Figure 48. Samples from the start of all three batches and from the end of test batch B show nearly identical dissolution performance. Samples from the faulty batch and test batch A, taken at the end of production, show noticeable slower dissolution rates, with the sample from test batch A being the slowest.

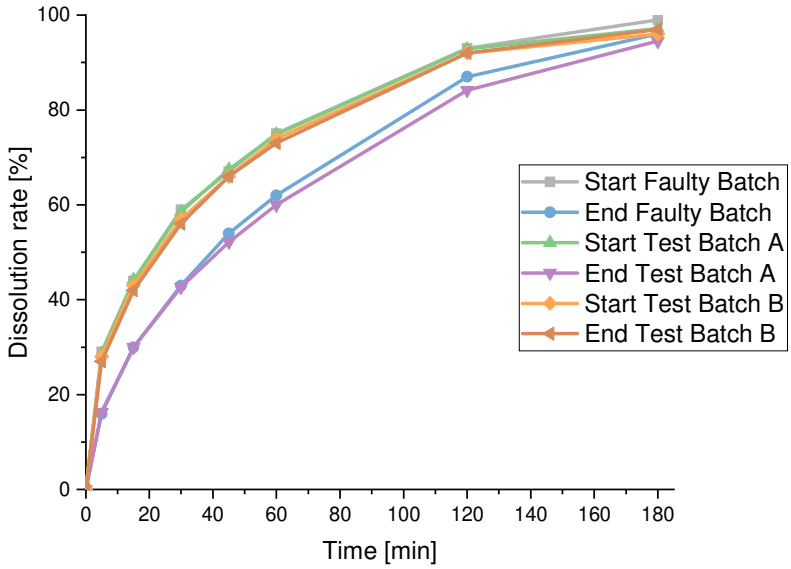

Figure 48: Dissolution rates of the faulty batch and test batches A and B for samples from the start and end of the manufacturing process.

When comparing micro-CT data for all three batches with the dissolution results, several trends can be derived. Samples taken at the start, display very similar dissolution behavior but have differences in average particle size, amount of large particles and total area of zones. There is an upper limit, which seems to be close to the measured parameters of batch B, where an increase of these values is no longer reflected in the measured dissolution rate. It is likely that large particles at the interface between sample and dissolution medium are released rapidly upon entering the testing vessel. Because the first sampling point of the dissolution method is only after five minutes, changes in the sector of instant and very fast release are not detected with this method. This is best illustrated by the difference in micro-CT values for test batch B. Here micro-CT data for the samples taken at the start show larger values compared to all other samples, but have an almost identical measured dissolution rate. Micro-CT values slightly decrease for the sample taken at the end of production, down to levels comparable to samples taken from the start of the other two batches with similar dissolution rates, but the dissolution performance remains nearly unchanged (see Table 6). Similarly, there is a lower limit, where differences in particle size and total particle area can be linked to the dissolution performance. The faulty batch and test batch A show noticeable differences in the micro-CT data, but only a small shift in dissolution rate. Assay data of the API show comparable values for samples taken at the start and end. This means that in samples taken at the end of production the same amount of API is present. The reduction in measureable API zones is therefore not connected with a decrease of API content (see Table 5).

Table 5: API assay values for samples from the start and end of the faulty batch and test batch B. (Measurements for the test batch A have not been performed).

Sample	Faulty batch start	Faulty batch end	Test batch B start	Test batch B end
Assay API [%]	101.0	100.6	101.1	100.9

There are two possible, not mutually exclusive, explanations for this behavior. It cannot be ruled out that a certain amount of API is dissolved in the adhesive matrix. The adhesive itself is a solid compound, which when received from the manufacturer is mixed with a solvent to enable processability. Since the API is soluble in the present solvent it cannot be conclusively determined to which extend the API is dissolved in the adhesive matrix. The second possibility is that the API is located in submicrometer-sized zones, which are below the detection limit of the micro-CT and can therefore not be measured. It is plausible that the influence of these two factors on the dissolution is increased at the later sampling point, where the amount of large particles has decreased and therefore has a reduced impact (see Table 6). The total particle area per mm² is the measured parameter that is most predictive of the dissolution behavior, illustrating best the importance of numerous, large API zones in the layer bordering the release liner for a fast release rate.

Table 6: Average structure thickness, count of large particles, decrease in particle count and total particle area for three batches at sampling points at the start and end of manufacturing.

Sample	St. Th. Avg. [µm]	Particles with major diameter > 57.6 µm	Decrease in total particle count per mm² [%]	Total particle area per mm² [µm²]
Faulty batch start	8.5	14	22.2	55039
Faulty batch end	7.0	2		34550
Test batch A start	12.8	21	48.9	56790
Test batch A end	8.3	1		14890
Test batch B start	11.4	25	9.3	65940
Test batch B end	8.8	15		54006

4.7 Conclusion

Through the unique combination of SEM/EDX, Raman microscopy and micro-CT imaging, a formerly impossible, 3D localization of API in a pharmaceutical patch formulation was achieved. This enabled observation of various API parameters on a micrometer scale in this transdermal therapeutic system, such as particle size, surface area and particle shape. Furthermore, the analysis of only specific regions of patch samples, for example the interface between API/adhesive matrix and dissolution medium, was made possible.

This information was implemented into the day-to-day business when a newly manufactured development batch showed irregularities during routine dissolution testing. A reduction in release rate was found for samples taken at the end of a manufacturing cycle. When analyzing and comparing samples from the start and end of production with micro-CT, a reduction of API particle size and API surface area was found. Together with the dissolution results, this indicated that a manufacturing error, in conjunction with API handling, might be the cause of the out-of-expectation results. A leaky manufacturing device was proposed as a reason for the irregularities found. To test this hypothesis a batch with an intentionally faulty system was produced. For this test batch, the shift in dissolution rate and trends for API particle size and surface area were comparable to the initial batch, confirming the leaky device theory. Based on the results additional steps were implemented to ensure the tightness of the manufacturing system. To verify the effectiveness of the improvements, a batch produced with the updated system was analyzed. This batch showed satisfactory dissolution results and only small differences in the micro-CT measurements. This project showed that the implementation of new analytical technologies are able to produce previously inaccessible information about complex pharmaceutical drug delivery systems and can be very useful tools for root-cause investigations, speeding up the process of troubleshooting. Additionally, it was shown that conventional testing methods such as dissolution testing and novel imaging analysis are complementary, with each method improving on the limitations of the other.

4.7.1 References

[1] J. Hadgraft, M. E. Lane, *Am. J. Drug Deliv.*, **2006**, 153-160.

[2]M.N. Pastore, Y.N. Kalia, M. Horstmann, M.S. Roberts, *Br. J. Pharmacol.*, **2014**, 2179-2209.

[3] M.R. Prausnitz, R. Langer, *Nat. Biotechnol.*, **2008**, 1261-1268.

[4] M.A. Miller, E. Pisani, *Bull. World Health Organ.*, **1999**, 808-811.

[5] S. Wiedersberg, R.H. Guy, *J. Control Release*, **2014**, 150-156.

[6] F.B. Hofmann, *Handbook of Experimental Pharmacology*, Springer-Verlag, Berlin Heidelberg, **2010**.

[7] J. Hadgraft, M.E. Lane, *Int. J. Pharm.*, **2005**, 2-12.

[8] U.S. Department of Health and Human Services Food and Drug Administration, *Approved Drug Products*, **2020**.

[9] *https://www.ema.europa.eu/en/medicines/human/EPAR/neupro* (accessed **04.11.2020**).

[10]The European Agency for the Evaluation of Medicinal Products, *Guideline on quality of transdermal patches*, **1998**.

[11] H.G. Merkus, *Particle Size Measurements*, Springer, **2009**.

5 Film-coated tablet

5.1 Introduction

There are different routes for the enteral (absorption via the gastrointestinal tract) administration of drugs. Due to its ease of use and convenience, oral administration is the most common way of taking medicine. Tablets, capsules, granules and powders fall into the category of solid formulations for oral application. The solid dosage form mentioned in this example is a film-coated tablet (FCT).[1] Film-coatings can have different purposes, ranging from functional (i.e. gastro-resistance) to protective to decorative.[2] The film coating of the here analyzed samples is applied to give color, to simplify recognition and distinction between different drug products. To be effective tablets have to disintegrate to release the drug, which then has to dissolve in the surrounding medium migrate through mucosa, stomach or colon tissue and finally be absorbed into the bloodstream to become bioavailable. The dissolution and absorption characteristics can be influenced by the pH value of the surrounding medium, molecular size and shape of the API or functional coatings, which delay release.[1] Since the mid-1990s, a system to correlate the *in vitro* dissolution performance and *in vivo* bioavailability of drug products, the biopharmaceutics drug classification scheme (BCS), is used.[3] The central assumption is that drug absorption is mainly governed by drug dissolution and gastrointestinal permeability. This results in four classes:

- BCS I: High solubility and high permeability
- BCS II: Low solubility and high permeability
- BCS III: High solubility and low permeability
- BCS IV: Low solubility and low permeability

The API used in this project is ticagrelor, classified as a BCS class IV substance with an overall mediocre bioavailability of 36%.[4] The combination of low solubility and low permeability can result in problems in the oral administration route.[5] Especially the particle size and shape of the API has to be closely monitored, since it can have direct influence on the *in vivo* and *in vitro* performance of the final product. Depending on the desired characteristics, tablets can be designed to release the entire contained API immediately after application or to release with a build-in delay time. This can be of use when therapeutic plasma concentrations are needed in the early morning hours, for example for the treatment

of arthritis or Parkinson's disease.[6] The tablet under investigation is a dosage form containing 90 mg of ticagrelor as an immediate release formulation (see Figure 49).

Figure 49: Ticagrelor tablet and 1-euro cent coin as reference.

5.2 Motivation

A batch, manufactured at the same site and under the same manufacturing conditions as fully functional batches before, showed deficient dissolution performance, resulting in an out of specification quality event (OOS). The dissolution specification requires that 85% or more of the API be released at the 15- and 20-minute mark. This mark was not reached by one batch. This prompted an in-depth investigation into possible reasons for the error. The manufacturing process parameters were found to be consistent with previous batches and are therefore not further analyzed. Because the API is a poorly water-soluble substance, particle size will have an impact on the dissolution behavior (see paragraph 5.5.6). Therefore, a possible change in particle size distribution is a major focus point in the investigation. Particle size analysis on film-coated tablets is difficult and with established techniques requires invasive sample preparation. The standard method is performed by manual removal of the film coating, suspension of the sample in a medium where the API is insoluble, but most of the excipients are soluble and following visual inspection under the microscope. This is a relatively rudimentary method and only limited information can be gained (see paragraph 5.5.2). Additionally, laser diffraction is used to gather information

about the particle size distribution of the combined insoluble components. A reliable differentiation of the individual components is not possible in this case. Because of these drawbacks, Raman microscopy is used for the chemical identification of tablet cross-sections. Since this method still requires the destruction of the samples integrity, micro-CT imaging is additionally implemented. This method enables 'looking into the tablet' without prior sample preparation, but yields only information about the relative density distribution in the tablet. The novel combination of both methods allows for a true 3D mapping of the API.

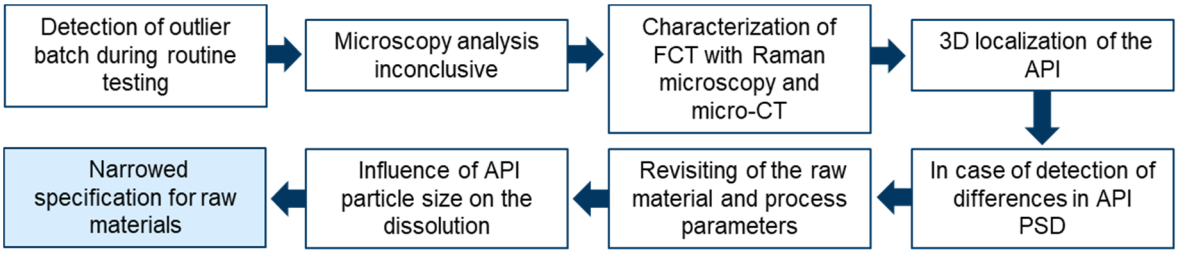

Figure 50: Strategy outline for the troubleshooting process.

5.3 The FCT

The 90 mg FCT of ticagrelor is comprised of the components shown in Table 7. The three main components API, mannitol and MCC add up to 93% of the tablet. Mannitol is used as sweetener, MCC as filler, Hypromellose (hydroxypropyl methylcellulose) as a binder, pregelatinized starch as disintegrant and magnesium stearate as lubricant for improved powder flow during the manufacturing.[6]

Table 7: Composition of the FCTs.

Ingredient	Amount per tablet [mg]	Percent per tablet [%]
Ticagrelor	90.00	30.00
Mannitol	126.00	42.00
Microcrystalline cellulose (MCC)	63.00	21.00
Hypromellose	9.00	3.00
Pregelatinized starch	9.00	3.00
Magnesium stearate	3.00	1.00
Sum	300.00	100.00

5.3.1 The API: Ticagrelor

Ticagrelor is a platelet aggregation inhibitor used for the prevention of heart attacks and strokes. It is an antagonist of the diphosphate P2Y12 receptor on thrombocytes and reduces their coagulability.[7,8] Structurally ticagrelor is (1S,2S,3R,5S)-3-[7-[(1R,2S)-2-(3,4-

Difluorphenyl)cyclopropylamino]-5-(propylthio)-3H-[1,2,3]triazolo[4,5-d]pyrimidin-3-yl]-5-(2-hydroxyethoxy)cyclopentan-1,2-diol (see Figure 51).

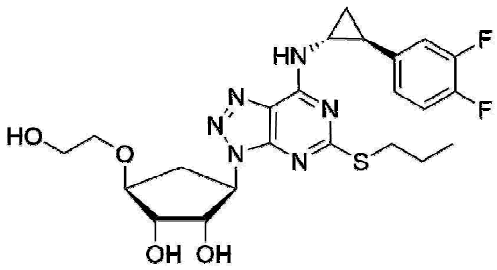

Figure 51: Chemical structure of ticagrelor.

5.4 Characterization of the FDF

5.4.1 Raman microscopy

5.4.1.1 DCLS-Analysis

In Figure 52, a micrograph of the cut and milled cross-section of a ticagrelor FCT, with the chosen region of interest (red rectangle), and DCLS mapping of the, based on mass, largest excipient, mannitol is shown. The ROI was selected to cover as much of the tablet surface as possible. The measured spectra are in very good accordance with the reference spectrum. A matrix-like distribution can be found, where large areas of interconnected regions of mannitol (green, yellow and red) can be found, only interrupted by mostly circular zones (blue and black). These circular zones can be attributed to the API (see Figure 53, top left).

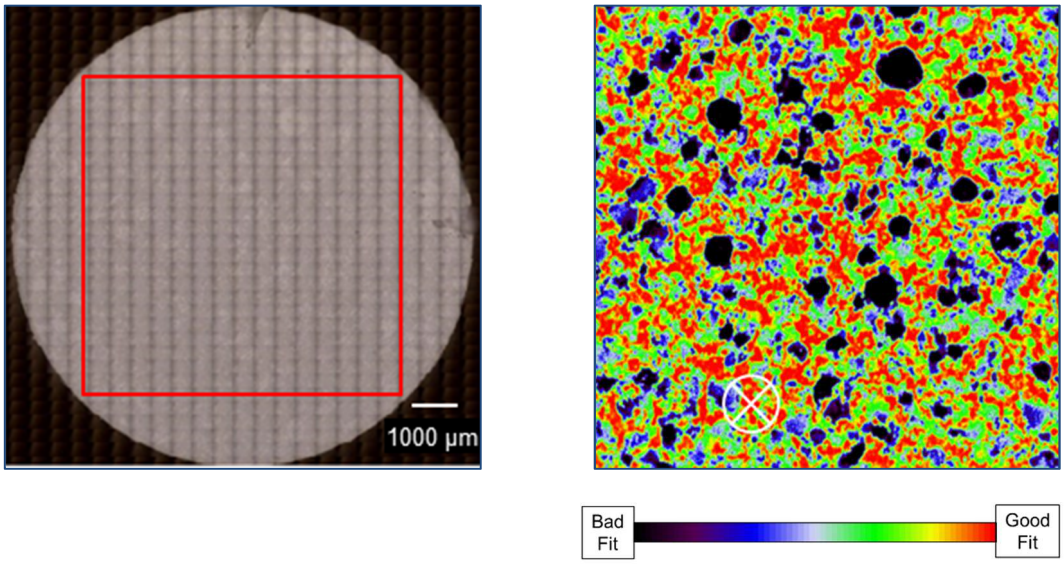

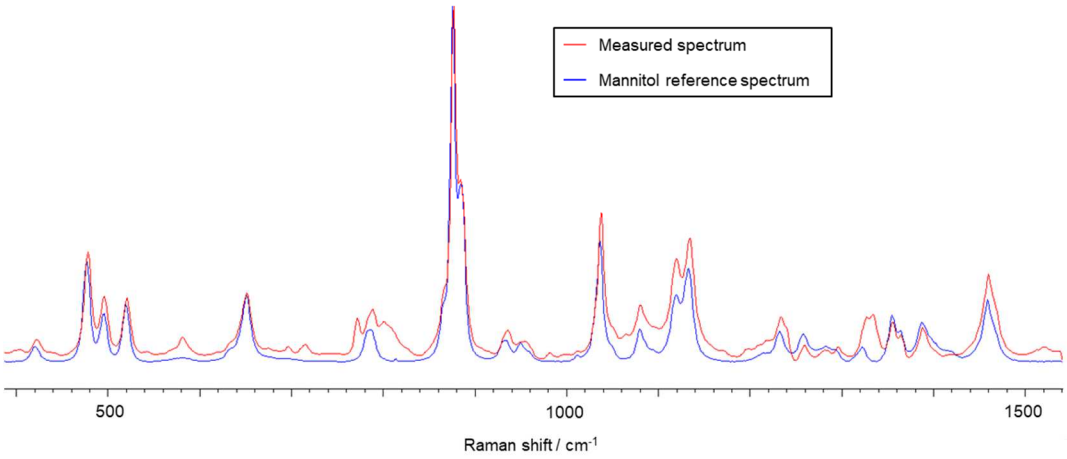

Figure 52: White light image of tablet cross section with ROI (top left), DCLS Raman mapping of mannitol (top right) and Raman spectrum at the crosshair.

The measured spectra are in very good accordance with the API reference spectrum. The API is located in mostly circular and off-shape particles, homogenously distributed throughout the sample surface. Microcrystalline cellulose (MCC) is distributed in the form of round and off-shape particles throughout the tablet surface. Being a substance with relative low Raman intensity, the measured spectra show significant overlap with spectral components of the API as well as mannitol, but identification using the characteristic peaks at about 1200 cm^{-1} is possible (see Figure 53, top right).

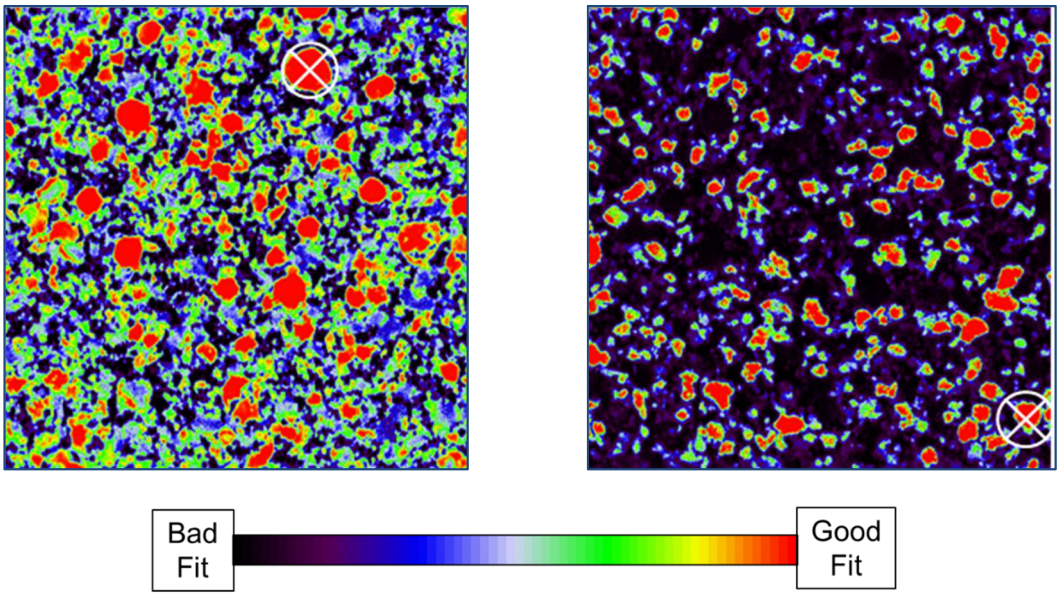

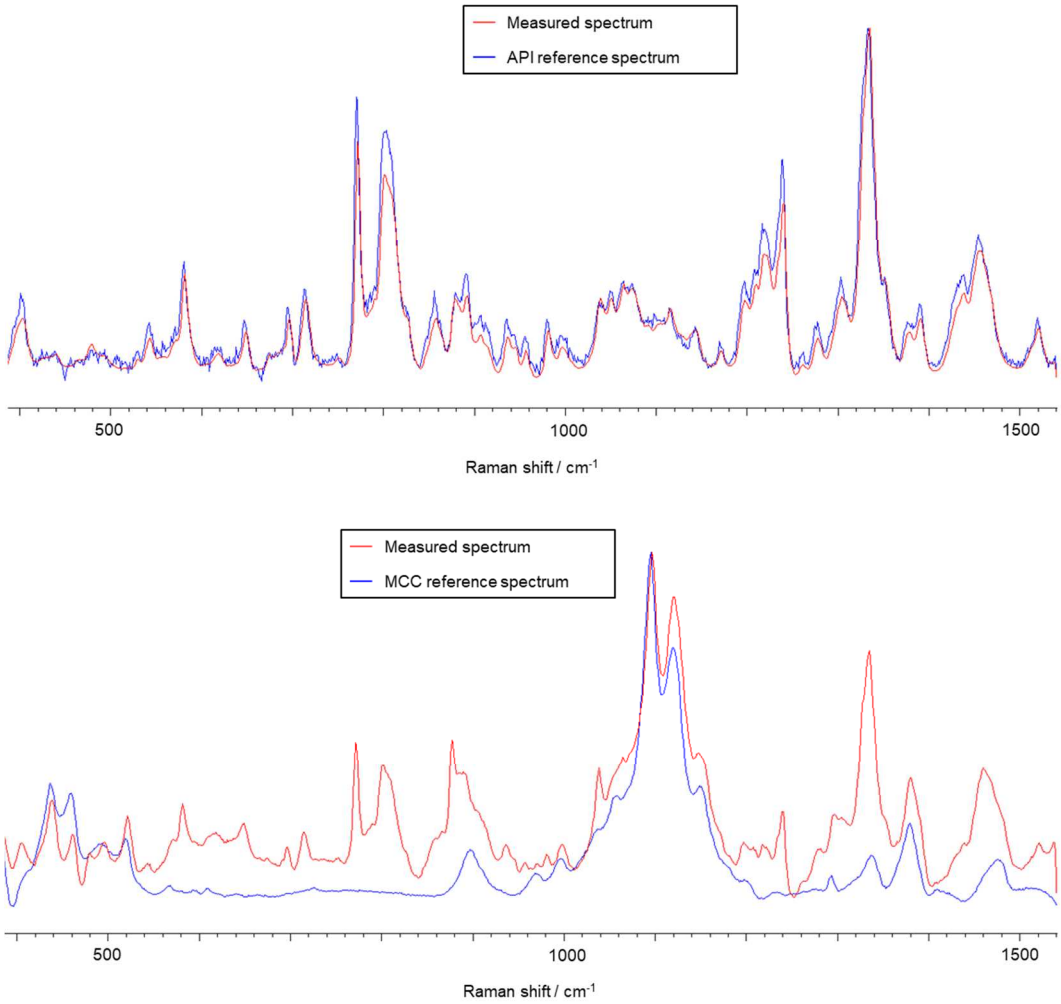

Figure 53: DCLS Raman mapping of the API (top left), DCLS Raman mapping of MCC (top right), Raman spectrum at the crosshair in red and the API reference spectrum in blue (middle) and Raman spectrum at the crosshair in red and the MCC reference spectrum in blue (bottom).

5.4.1.2 MCR-ALS analysis

The MCR-ALS method is used as a complementary tool to verify the findings of the DCLS method, because no user input is needed to perform the analysis and thus it being not as perceptible to human error. Because of the heavy spectral overlap in the MCC spectra, mapping using the MCR-ALS analysis method results in only two components (see Figure 54). The first component (left) is very similar to the distribution of mannitol; the second component is very similar to the distribution of API (right).

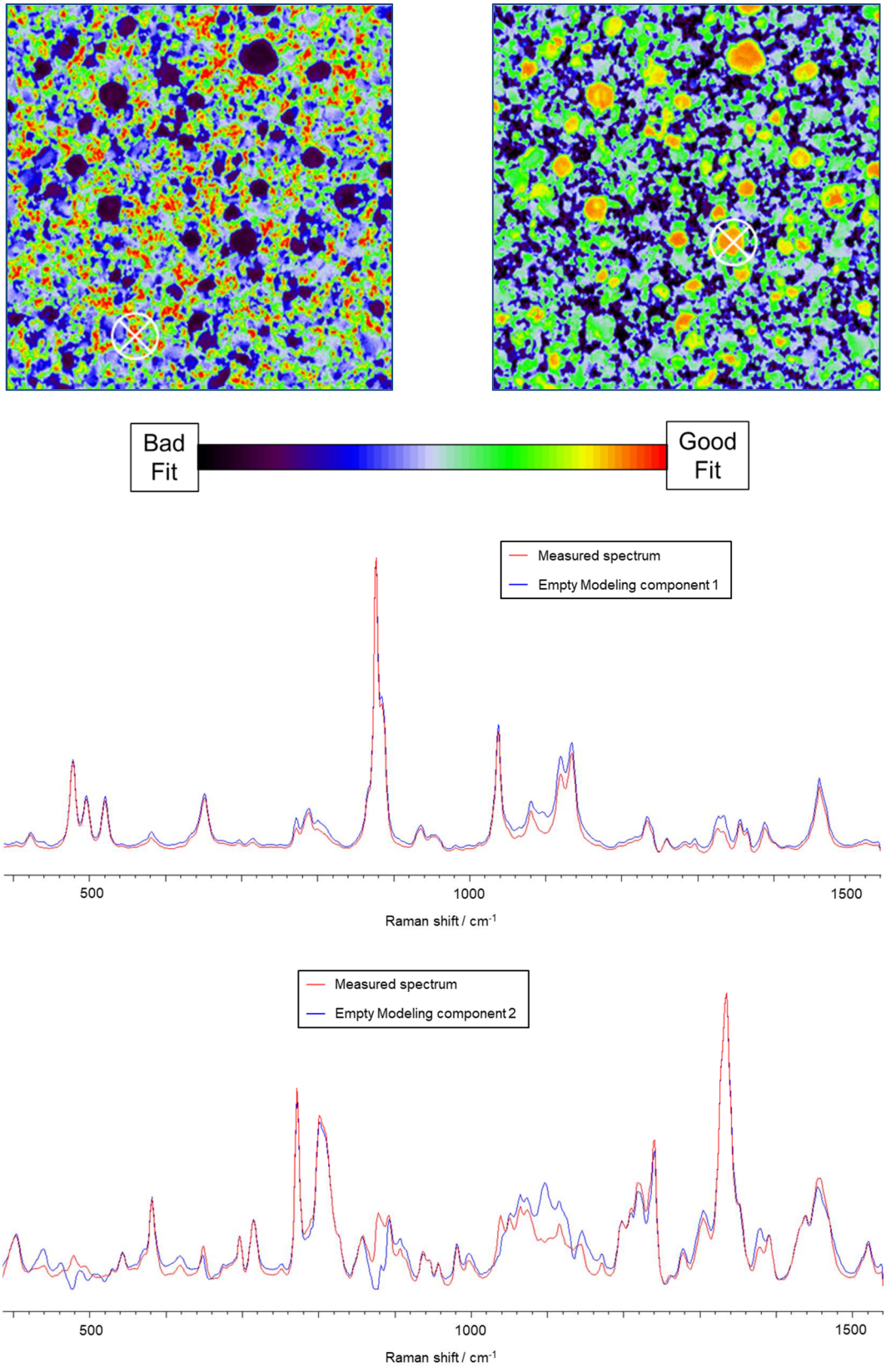

Figure 54: MCR-ALS results for the two found components with corresponding calculated spectra (blue) and spectrum at the crosshair (red).

5.4.1.3 Summary

With DCLS and MCR-ALS, the localization of API in mostly circular particles embedded in a matrix of mannitol can be shown. Detection of the other excipients was not possible using Raman microscopy. This is due to a combination of small quantities used in the formulation and relative weak Raman scattering efficiency of the substances.

5.4.2 Micro-CT

Tablets are fixed to the sample holder pin with plasticine, no further preparation is necessary. In the grey scale micro-CT images in Figure 55, the relative density distribution of a ticagrelor tablet is shown.

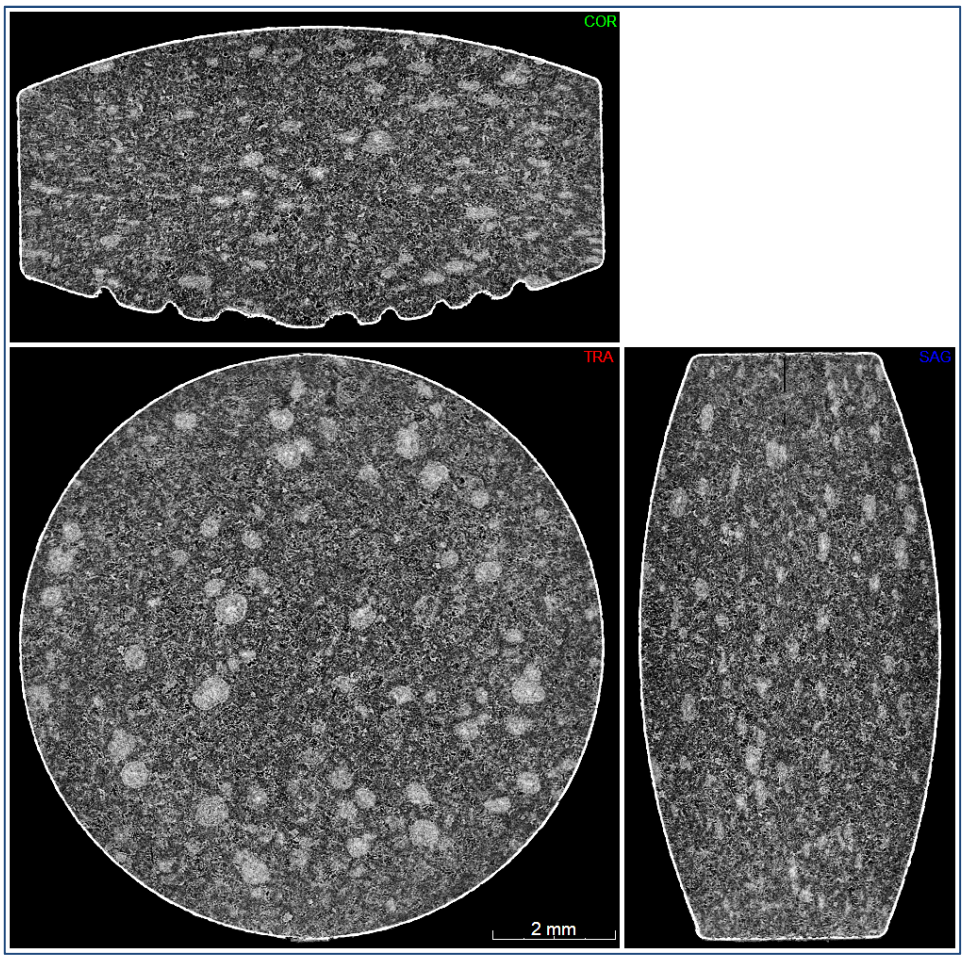

Figure 55: Coronal (top), transverse (bottom, left) and sagittal (bottom, right) grey scale micrographs of a FCT batch 1. Bright areas are correlated with areas of higher relative density.

The film coating has a high relative density (white), enclosing the tablet core. This is to be expected, because the pigment component of the coating is titanium dioxide an inorganic substance with high density. Since the coating is only applied for identification/coloring

purposes and has no pharmaceutical function it is removed digitally. Physical removal of the coating with a scalpel is possible but bears the risk of damaging or altering the tablet core, which is the main region of interest. Within the tablet, distinct structures with higher relative density (white and light gray) can be found. Especially in the transverse plane (TRA in Figure 55), those structures are circle-like and similar to the API structures found with Raman microscopy. Their shape in the coronal and sagittal images is more elongated and oval shaped which points to deformation of spherical API particles during the tableting step. To perform analysis on the areas of higher relative density, particles have to be isolated and the image binarized. Three custom-made task lists are developed for the tablet isolation (TL_TIC_01), digital removal of the film-coating (TL_TIC_02) and particle analysis (TL_TIC_03). The multi-step process is displayed and described in Figure 56.

1	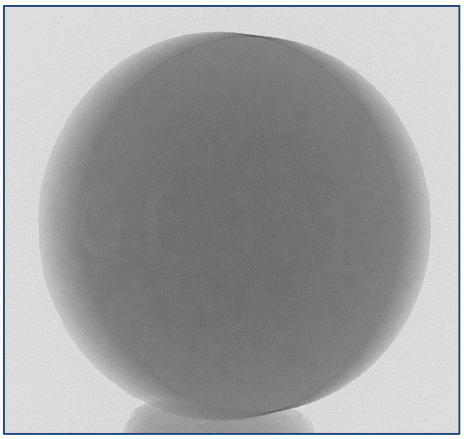	One of 3600 radiographs, taken during the measruement, showing the entire tablet and plasiticine on the bottom with which the tablet is mounted on the sample holder.
2	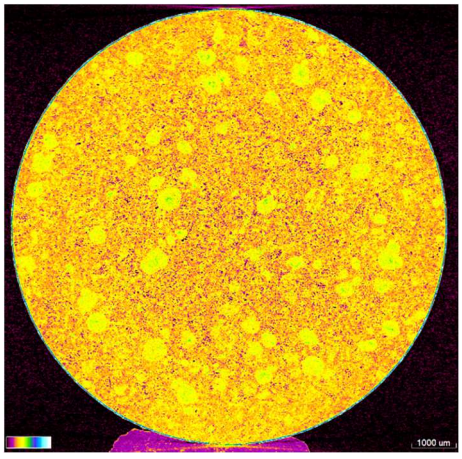	Reconstructed image, the tablet with medium relative density (green/yellow/orange), plasticine with minimal relative density (purple) and small fluctuations in the black background area.

3	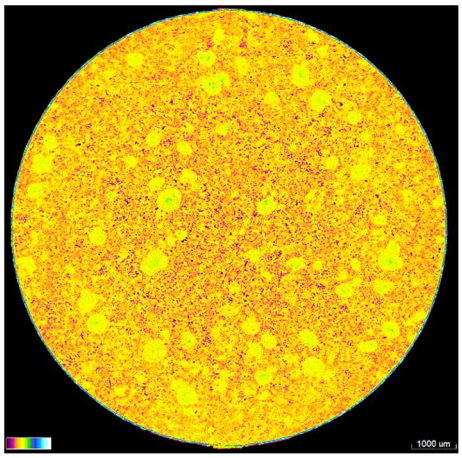	Because the background fluctuations and plasticine area might interfere with the analysis later on, the tablet is digitally isolated and placed on a completely black background
4	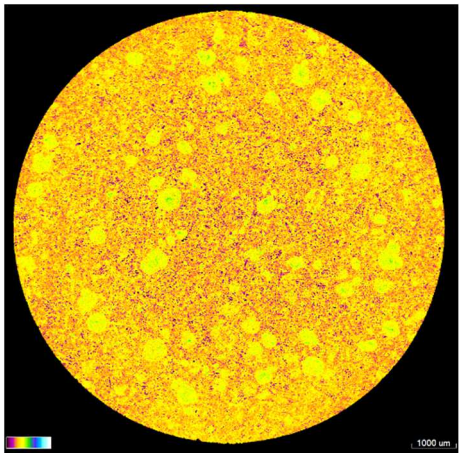	The film coating is not of interest when analyzing the particle structures within the tablet and is digitally removed. 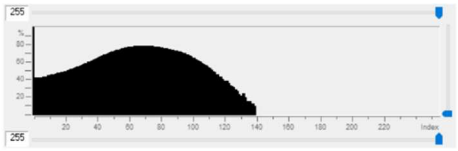
5	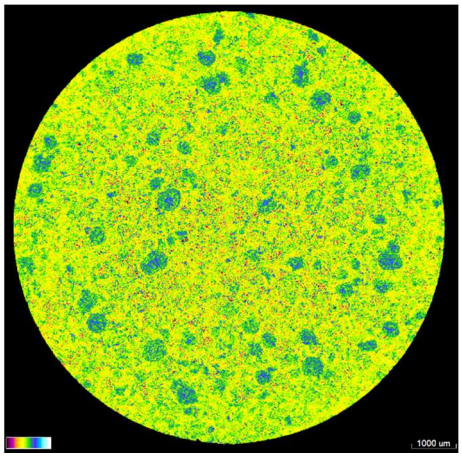	After removal of the film coating (formerly the areas of the sample with the highest relative density), the histogram only uses half of the available gamut and is therefore stretched for a finer distribution of relative densities. 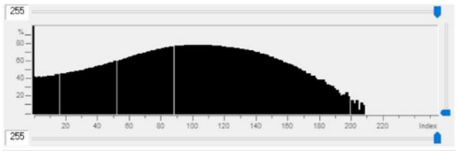

6	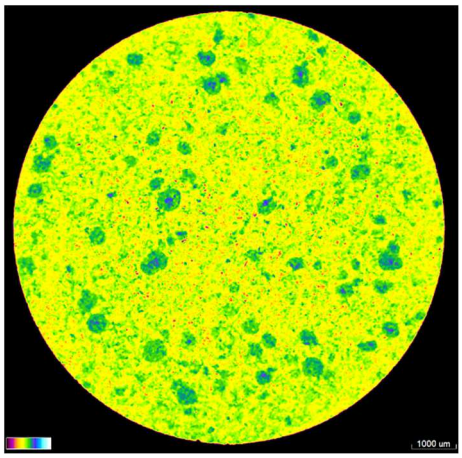	An algorithm to reduce noise (anisotropic diffusion) is implemented to smooth out small density fluctuations within the regions of lower relative density (light-green and orange) to help isolating particles with high relative density (blue and dark-green).
7	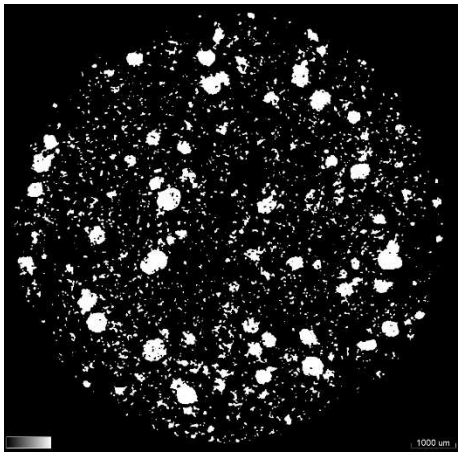	After manually thresholding the dataset, a binarized image is received.
8	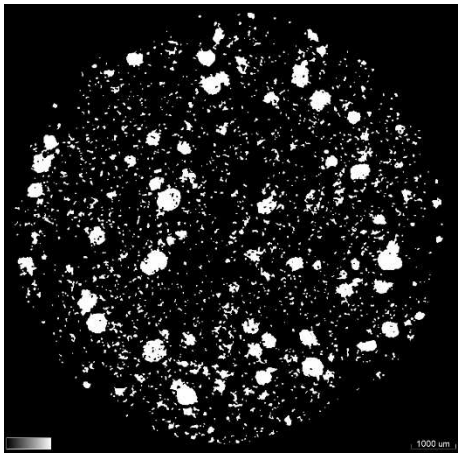	The final image for analysis is received after a despeckle step, to remove pixels with sizes of the resolution or smaller, thus not containing information.

Figure 56: Stepwise procedure of particle isolation.

5.4.3 The combination of micro-CT and Raman microscopy

To confirm that areas of high relative density in micro-CT images are closely related to the API distribution, comparative measurements are performed. A tablet is prepared for Raman microscopy (cutting and milling a smooth surface) and marked with a scalpel on the sides for easier alignment (light blue arrows, Figure 57). Raman microscopy and afterwards micro-CT is conducted on the same sample. For the overlay in Figure 57 (bottom left), the micro-CT images is color-inverted for better contrast.

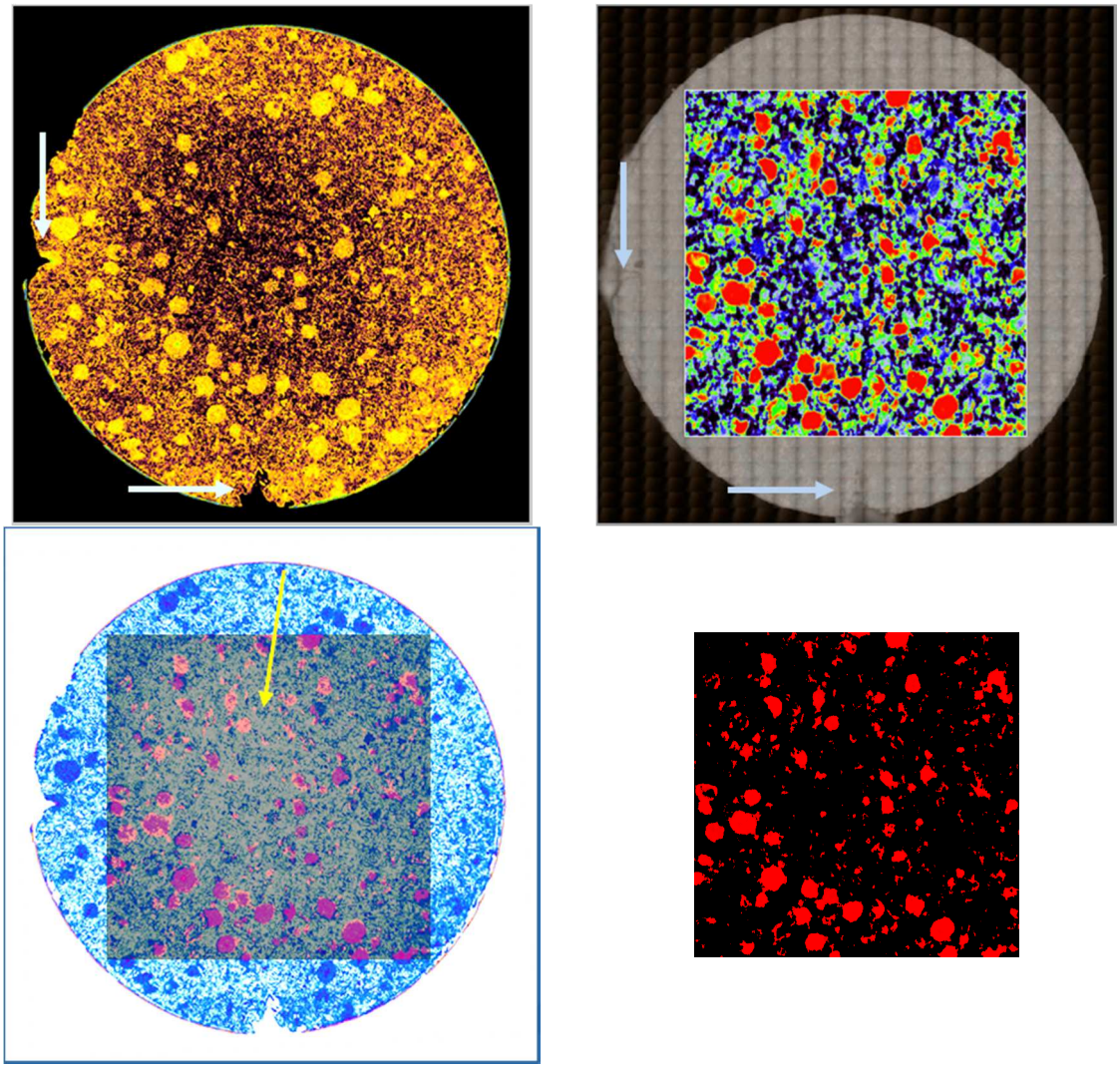

Figure 57: Micro-CT image (top left) and Raman API mapping (top right) of the same tablet from batch 1. Color inverted micro-CT image with API-Raman mapping overlay with 60% transparency (bottom, left), API-Raman mapping with regions of good fit (bottom right).

Raman mapping was reduced to areas where the measured spectra are in good accordance with the API reference spectra, indicated by red coloring. Areas displaying good accordance with the API reference spectrum, in the Raman microscopy image, can be found as areas with higher relative density and similar shape in the micro-CT image. Despite

the good comparability, certain differences between the images can be seen. Discrepancies can be explained by the different recording methods and sample preparation. Raman microscopy scans the sample surface from the top and compresses differences in sample height into one 2D image, while also including spectral information from a few micrometers deep. Smaller differences in height are reduced but not completely removed during sample preparation. The result is a 2D image with information from several layers arranged horizontally above and below the actual, uneven sample surface. Micro-CT on the other hand x-rays the sample and captures the entire volume of the specimen. The reconstructed image is composed of individual 2D layers where the topographic information is preserved. This is further enhanced by the fine resolution (pixel size: 4 µm) of the measurement. These problems are most apparent in the top part of the middle (see arrow), where API particles are found in the Raman measurement but do not have counterparts in the micro-CT images. This is caused by a height difference in the sample at this spot, where the micro-CT measurement recorded air (regions colored white) and the averaging effect of the Raman, with the laser not being disturbed by air above the sample, is recording deeper lying information. Aside from the measurement type specific variations, there is good evidence that particles with high relative density are API.

5.5 Analysis-guided error investigation

5.5.1 The challenge

A batch manufactured at a different site, showed an out of specification (OOS) quality event during routine dissolution testing. The required release rate was not achieved for the faulty batch (batch 1). In Figure 58 the dissolution rate of an in-specification batch (batch 2) and the out of specification batch (batch 1) is plotted against time. The dissolution curve of batch 1 is noticeable lower than the benchmark batch 2. At the 60-minute mark, both batches reach the same release rate.

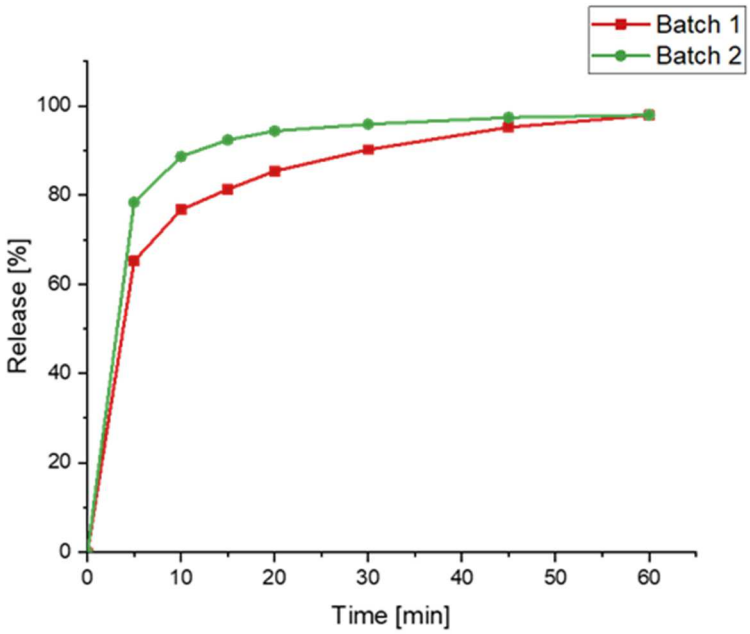

Figure 58: Dissolution profiles of the faulty batch (batch 1) and the reference batch (batch 2).

The dissolution medium was selected to replicate the environment in the stomach, because this is the region were the tablet dissolves in the body and the API is absorbed. Deficiencies in dissolution tests can indicate problems of the products bioavailability; this is especially problematic for BCS class IV substances such as ticagrelor.

5.5.2 Investigation using microscopy

As the first standard method, digitally enhanced light microscopy measurements were performed on both batches (see Figure 59). The film coating was removed using a scalpel, the tablet suspended in water and the suspension treated with a vortex mixer. This way the water insoluble substances, API (55%), MCC (38.2%), starch (5.5%) and magnesium stearate (1.8%) can be analyzed under the microscope. With digitally enhanced light microscopy, only visual classification is possible. The needle like shapes are in good accordance with the shapes found for the unprocessed API. The larger, spherical particles are similar to MCC raw material, but no unambiguous allocation of individual particles is possible. Additionally a major drawback is the extensive sample preparation needed which might alter particle size and shape. With microscopy, no clear differences between the two batches can be found.

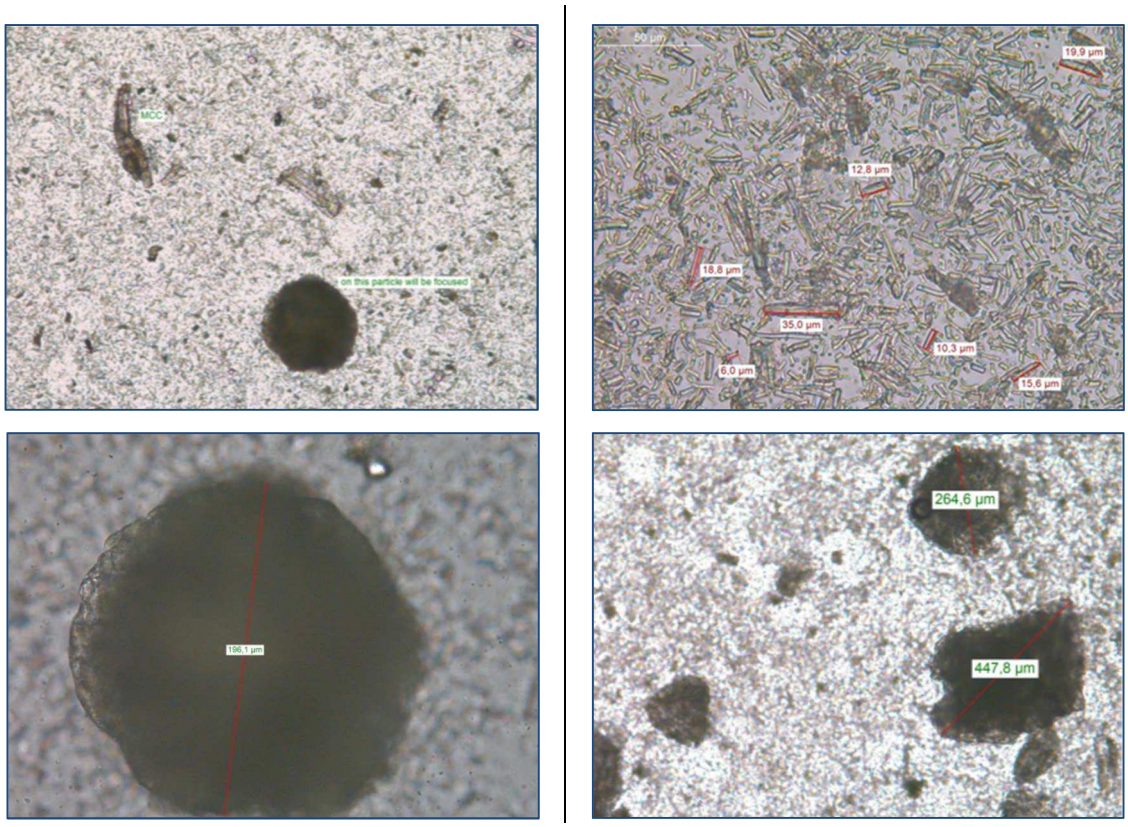

Figure 59: Microscope images of the insoluble components of the faulty batch (left) and the reference batch (right)

5.5.3 Investigation using Raman microscopy

To see if the spatial distribution and particle size of the three main components of the tablet formulation remains constant between the faulty batch and the reference batch, Raman mapping was carried out. Comparison between API and the two excipients mannitol and MCC for two tablets of the faulty batch and one tablet of the reference batch are displayed in Figure 60. Both tablets of the faulty batch show very similar Raman mapping results for all three substances. Raman mapping of MCC for both batches shows comparable results, of isolated particles evenly distributed throughout the milled tablet cross section. In contrast mapping of API and mannitol shows noticeable differences.

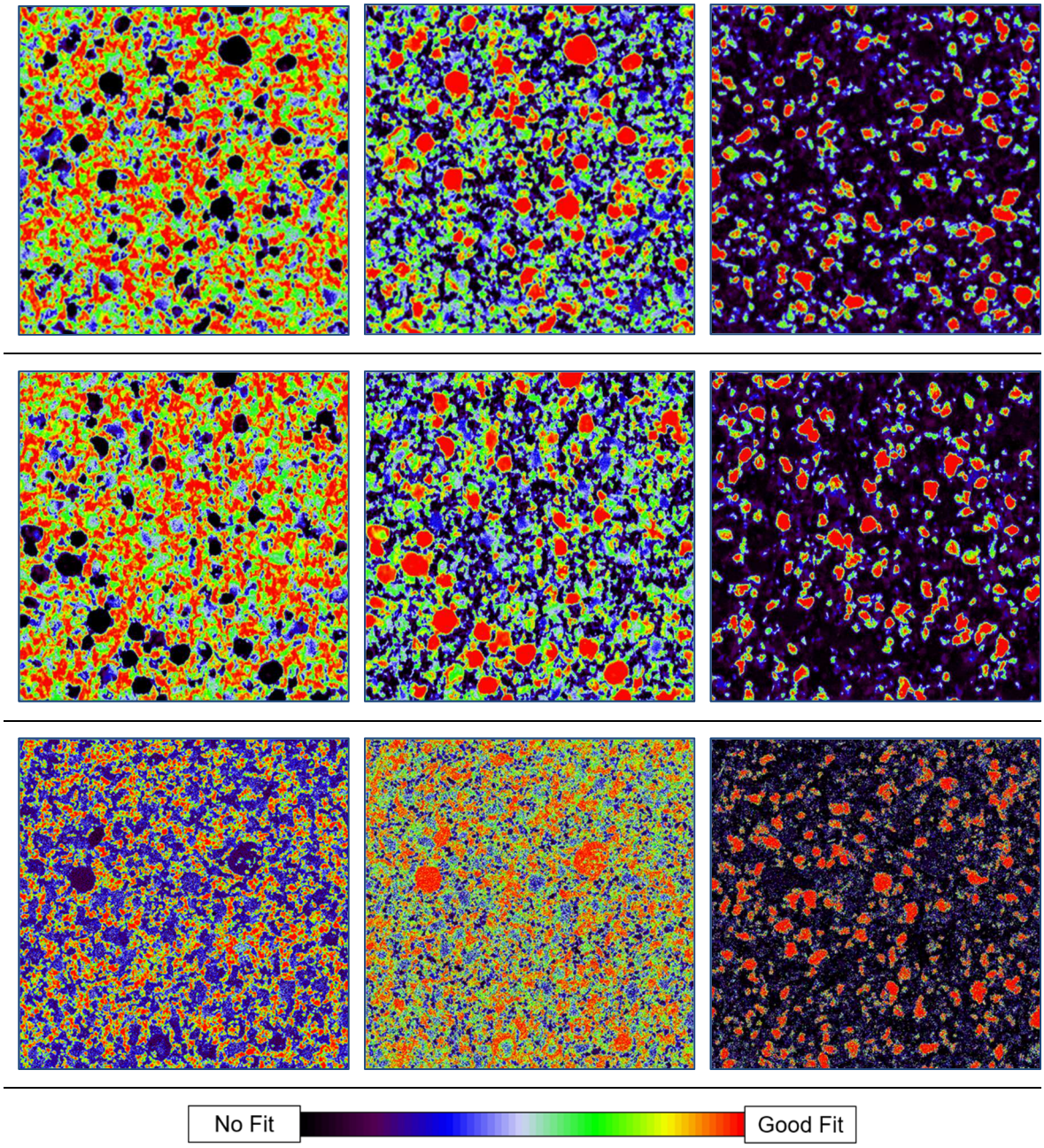

Figure 60: Raman mapping of mannitol (left column) API (middle column) and MCC (right column) for the faulty batch tablet 1 (top row), faulty batch tablet 2 (middle row) and the reference batch (bottom row)

API in the faulty batch is located in large discrete particles, whereas in the reference batch, only a few discernable particles can be found and the overall API distribution is much more diffuse. This has impact on the distribution of mannitol, which is more finely distributed in the reference batch compared to the faulty batch. The used laser for the measurements had to be changed from a 785 nm line laser for the faulty batches to a 633 nm point laser for the references batch. This was necessary to suppress high amounts of fluorescence,

most likely generated by the smaller particle size of the API and the resulting finer distribution. Tests with other tablet formulations showed that a change in laser has no noteworthy influence on the gathered data. The main difference is a slight visual change in the appearance of the point laser maps looking more “grainy”. The largest drawback is the considerable longer acquisition times needed with point laser measurements. Although, only small 2D areas can be analyzed by Raman microscopy, differences in the API PSD can be recognized and are investigated more in-depth using micro-CT in following paragraphs.

5.5.4 Investigation using micro-CT

5.5.4.1 Combination of micro-CT and Raman microcopy – Batch comparison

To get detailed insights into the composition of the FCT, micro-CT and Raman microscopy comparative measurements were performed. In Figure 61, Raman and micro-CT images of the same tablet surface are shown for the faulty batch and the reference batch. To achieve the best possible contrast, a binary color scheme was chosen for the micro-CT images. Raman color-coding gamut is identical for both measurements. The arrows indicate scalpel cuts for easier alignment of the images.

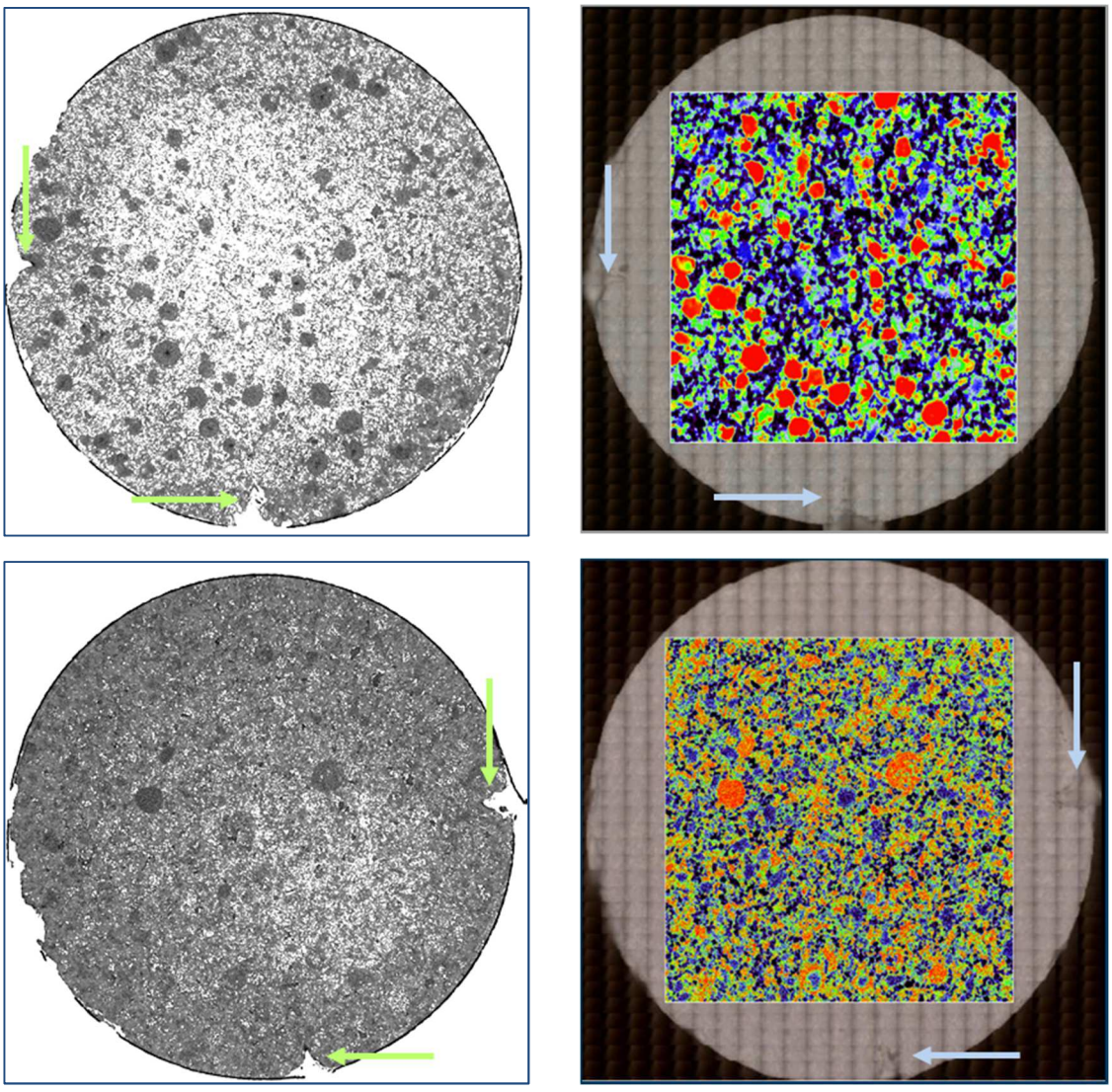

Figure 61: Micro-CT image and Raman API mapping of the same tablet for the faulty batch (top) and the reference batch (bottom).

API areas in the reference batch look more finely dispersed with only a few distinct particles. In the faulty batch, a larger number of individual particles, mostly circular in shape, are

present. Raman microscopy and micro-CT images are in good accordance, displaying the same trends. On these grounds, micro-CT is implemented for the analysis of API particle size distribution for both batches.

5.5.4.2 Batch homogeneity – Intra-batch comparison

To reduce the risk of subsampling, micro-CT measurements are carried out on six samples of each batch. Sample preparation, measurement and reconstruction parameters as well as steps for particle isolation, using the procedure described in paragraph 5.4.2., are kept identical for each individual tablet. To demonstrate intra-batch homogeneity, six tablets of the faulty batch are investigated using three different properties. PSD of the API, total porosity of the tablet and tablet volume are selected to be monitored for possible changes and drifts during the manufacturing process. Particle size is reported as volume-equivalent sphere diameter (ESDv), which is obtained by measuring the volume of a particle and calculating the diameter of a sphere with the same volume. This is a common description of size for particles, also used in laser diffraction and sieving analysis. Furthermore, particle size distributions will be weighted by volume, because the volume (and related surface) play an important role in the dissolution processes. All graphs are plotted with a binning of 5 µm on the x-axis with the cumulative volume undersize on the y-axis.[9]

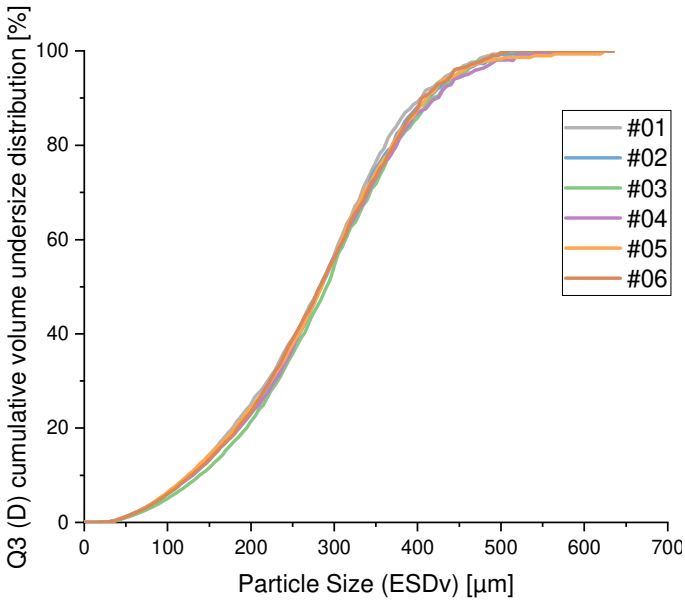

Figure 62: Cumulative volume undersize particle size distribution of six tablets of the faulty batch.

All samples of the faulty batch show nearly identical curve progressions with an overall mean D(0.5) of 286 µm, indicating a homogenous particle size distribution and constant manufacturing parameters with no relevant changes during the batch manufacturing

process (see Figure 62). To further investigate intra-batch homogeneity, the percentage of porosity for each tablet was measured. Larger variations in this parameter would indicate differences in chemical composition or changes in molding pressure during tablet compaction. Only minimal variations can be found, confirming stable manufacturing conditions (see Table 8).

Additionally the sample volume (volume of the entire tablet) was determined. Fluctuation in this parameter would be caused by problems with powder flow or the filling unit. With minimal differences, unobstructed production can be assumed (see Table 8).

Table 8: Total porosity and tablet volume for six samples of batch 1

Sample	**#01**	**#02**	**#03**	**#04**	**#05**	**#06**	**Avg. ± SD**
Porosity [%]	1.76	1.82	1.51	1.78	1.48	1.79	1.69 ± 0.15
Tablet volume [mm³]	299.28	299.49	295.80	298.44	298.58	297.13	298.12 ± 1.41

The data processing steps and manual thresholding values chosen for the analysis of particle size distribution, porosity and total tablet volume yield comparable and comprehensible results. This confirms that micro-CT imaging can be used for the detection of differences in manufactured ticagrelor tablets.

5.5.4.3 API particle size – Inter-batch comparison

In Figure 63, the average particle size distribution (n = 6) of the faulty batch and reference batch are plotted as cumulative volume undersize (bold lines) and fractional volume density distribution (bars).

The batches differ strongly in both mean particle size as well as particle size distribution. The faulty batch has a considerably higher mean particle size of about 285 µm compared to 150 µm of the reference batch. In the histogram it is clearly visible that the reference batch has a larger percentage of particles < 200 µm with its maximum at about 100 µm, whereas the faulty batch has its maximum at about 300 µm with a significantly larger percentage of particles > 200 µm. Both batches contain particles with sizes > 500 µm.

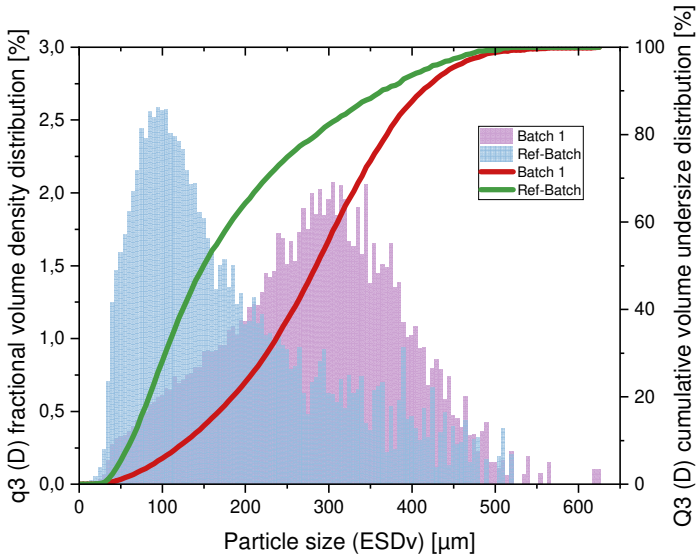

Figure 63: Fractional volume density distribution and cumulative volume undersize distribution of the faulty batch (batch 1) and a reference batch.

These particle size values are used to generate color-coded images (see Figure 64 and Figure 65). Large particles are colored in red and orange and smaller particles in yellow, green, blue and purple. It is apparent that in the faulty batch large particles are more frequent compared to the reference batch.

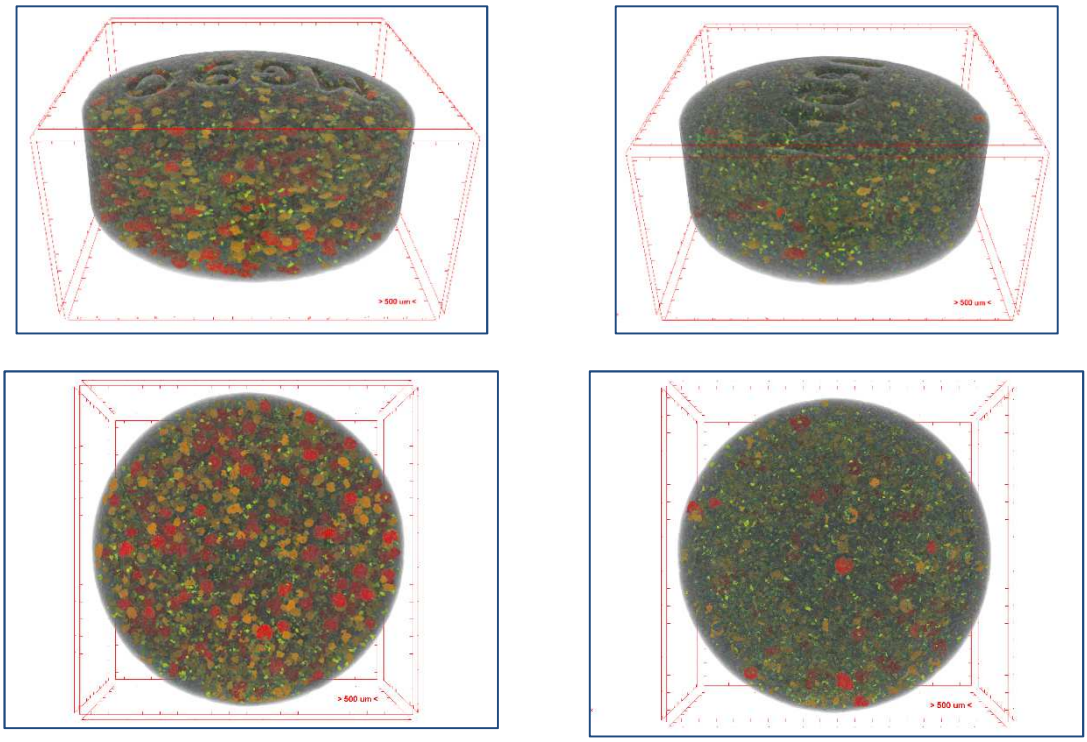

Figure 64: Isometric (top) and top-down (bottom) view of batch 1 (left) and reference batch (right), with particles colored according to size and sample outline in translucent grey.

Additionally it can be seen, that the large particles are distributed randomly throughout the tablets of both batches. This suggests that the difference in particles size existed before the tableting process and that raw materials with different PSDs were used to manufacture the two batches.

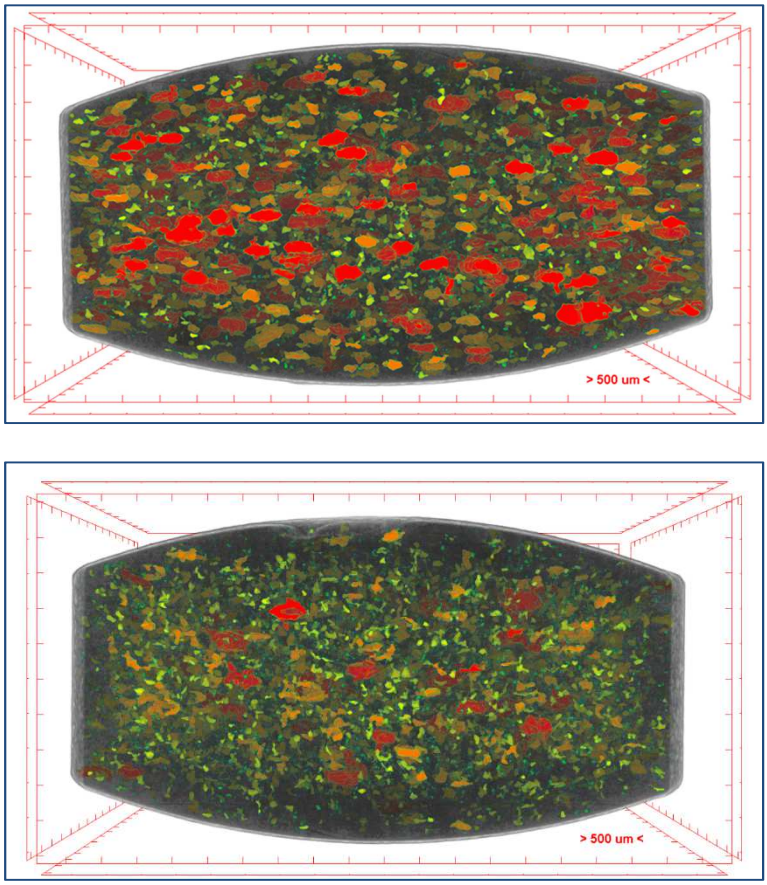

Figure 65: Digital cut through a sample of batch 1 (top) and reference batch (bottom) with particles colored according to size.

5.5.5 Inspection of the raw material

To investigate possible reasons for the differences, the manufacturing reports were checked and it was found that different raw material API batches were used for the FDF batches. Additionally, due to only small quantities available, multiple API batches were combined for making individual FDF batches (see Table 9). This triggered an in-depth look at the used API batches, including particle size measurements using laser diffraction analysis.

Table 9: Composition and particle size values for the API raw material of the faulty and reference batch.

Sample	Faulty batch	Reference Batch
API batches used	65% API batch A	50% API batch C
	35% API batch B	25% API batch D
		25% API batch E

Particle size measurements were obtained from the API manufacturer and compared to measurements done in-house (see Table 10). Particle size determination between the in-house method and the information from the manufacturer show clear differences for all three values, which are especially drastic for the D(0.9) value (see Table 10). Upon further inspection of the measurement parameters, it was found that the manufacturers' procedure included a sample preparation step using ultra-sonication.

Table 10: Particle size measurements with laser diffraction for API batches used in the faulty batch (A and B) and reference batch (C, D and E) from the API manufacturer and in-house analysis.

Source	**API manufacturer**			**In-house**		
Particle Size	**D(0.1) [µm]**	**D(0.5) [µm]**	**D(0.9) [µm]**	**D(0.1) [µm]**	**D(0.5) [µm]**	**D(0.9) [µm]**
API batch A (65%)	2.64	11.12	62.59	5.97	32.3	467.0
API batch B (35%)	2.95	11.24	56.39	7.65	30.2	370.0
API batch C (50%)	3.07	10.24	42.56	6.05	16.3	47.4
API batch D (25%)	3.38	12.01	54.21	7.76	23.1	170.0
API batch E (25%)	2.17	7.47	34.01	5.81	15.5	143.0

Using microscope analysis of the raw material it was discovered that the API exists in two different shapes, small needles and large spherical agglomerates that resemble particles found in the micro-CT and Raman microscopy measurements (see Figure 66). It is most likely that the ultra-sonication step is responsible for the disintegration of the agglomerates and therefore yielding smaller particle size values. The in-house method is discriminatory against the presence of agglomerates.

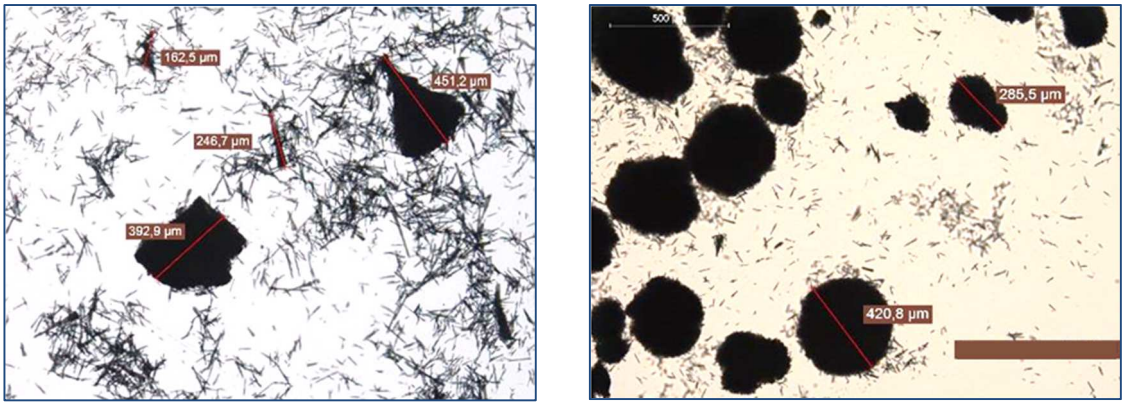

Figure 66: Microscope image of API raw material in water with needle-shaped API and less amount of agglomerates (left) and large amount of agglomerates (right).

To demonstrate the influence of the API particles size on the solution rate, two batches with different amounts of agglomerates were procured from the manufacturer. Characterization of the raw material was done using laser diffraction without sonication. The sample with a higher amount of agglomerates and a D(0.9) value of 368 µm shows a slower solution rate compared to the sample with low amounts of agglomerates and a D(0.9) value of 207 µm (see Figure 67). This shows direct influence of the particle size distribution of the API on the *in vitro* performance. This is expanded on in paragraph 5.5.6.

This led to a change in measurement protocols at the manufacturer and an adjusted particle size specification to exclude large amounts of agglomerates.

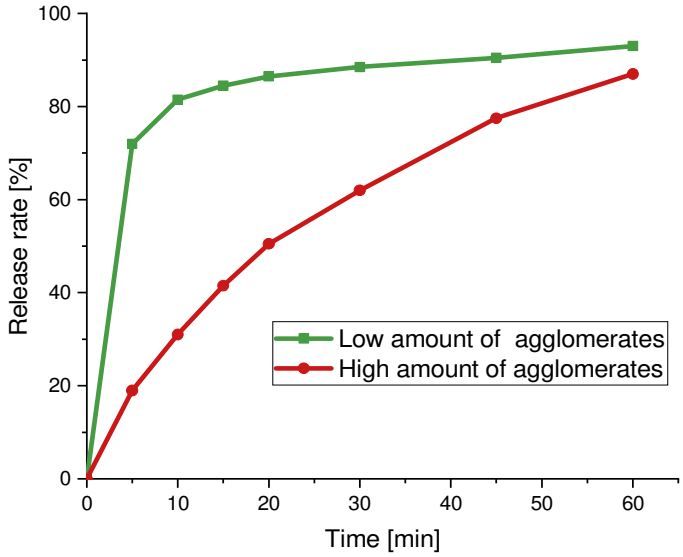

Figure 67: API raw material solution rate of sample with high (red) and low (green) amount of agglomerates.

5.5.5.1 Comparison of micro-CT and laser diffraction data

When comparing the laser diffraction data of unprocessed API with micro-CT data of API PSD in the tablets similar trends, but also some differences can be found (see Table 11). Micro-CT data shows much larger values for D(0.1) and D(0.5) as well as larger values for the D(0.9) of the reference batch. Several factors come into play, when comparing these two analytical methods. For laser diffraction, the API is suspended in water, spatially isolating individual particles. This can lead to the disintegration of agglomerates, even without sonication and is insensitive to adhesion between particles, which could play a role during the mixture and tableting of powders. Furthermore, the detection limit is roughly an order of magnitude more accurate compared to micro-CT, thus smaller particles are detected.

Table 11: Particle size statistics form the micro-CT data (ESDv) for the faulty batch and the reference and the calculated mixtures of raw material measured with laser diffraction.

Sample	D(0.1) [µm]	D(0.5) [µm]	D(0.9) [µm]
Faulty batch (micro-CT)	129.1	284.9	412.2
Ref-Batch (micro-CT)	62.5	149.5	363.3
Faulty batch (Raw)	6.56	31.7	433.1
Ref-Batch (Raw)	6.42	17.8	102.0

For powders with high amounts of fines this can lower the D(0.1) and D(0.5) values. Micro-CT on the other hand, is sensitive to agglomerates within the finished product because no sample preparation is needed and the gathered information is in 3D. In addition, singular particles being in close proximity or in contact are measured as one particle, leading to larger values. A major difference between the two methods is that with laser diffraction the raw, chemically pure substance is measured. In micro-CT, the chemical information has to be introduced, with the help of other analytical tools by the user and particle isolation is performed by manual thresholding.

In conclusion, although micro-CT and laser diffraction are quite different techniques for different fields of application, making a direct comparison difficult, similar trends between the two batches can be found.

5.5.5.2 Visual comparison of raw material with FDF

When comparing digitally enhanced light microscopy images of unprocessed API particles with micro-CT images of the tablet, particles of similar shapes and sizes can be found (see Figure 68). From this, it can be concluded that agglomerates are not destroyed during the production of the FDF and the specification during raw material testing is of high importance.

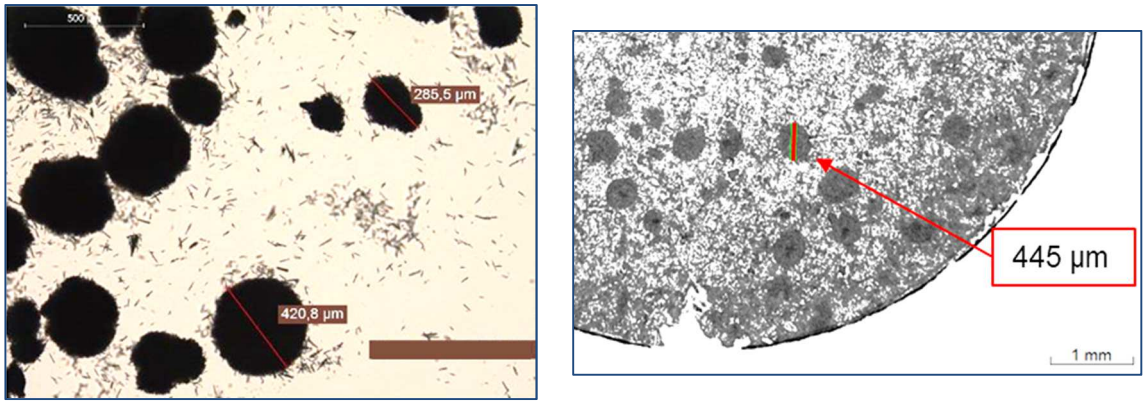

Figure 68: Particle size measurement of raw API with digitally enhanced light microscopy (left) and particle size measurement with micro-CT (right).

5.5.6 Correlation between particle size and dissolution

The standard method to explain the dissolution rate is to use the Noyes-Whitney equation:

$$\frac{dC}{dt} = \frac{DS}{Vh}(C_s - C_t) \tag{12}$$

where *dC/dt* is the solute dissolution rate, *D* is the diffusion coefficient of the substance in solution (partly related to the viscosity of the solvent), *S* is the surface area of the solute particles, *V* is the volume of the solution, *h* is the thickness of the diffusion boundary layer, C_t is the concentration of the dissolved substance at a given time *t* and C_s is the concentration of the substance required to saturate the solvent.[10]

Equation 13 can be simplified, when $C_t << C_s$, so that the dissolution rate is directly proportional to the saturated concentration:

$$\frac{dC}{dt} = KSC_s. \tag{13}$$

When *D*, *V* and *H* can be assumed constant, which is given when the experiment is setup correctly, they can be summarized to *K*. This is called ‘sink conditions’ and met if the concentration of the solute does not exceed 10% of the amount required for equilibrium saturation. This can be facilitated when the solute is removed faster from the medium than it dissolves (or when the volume of the medium is very large). If these conditions apply the dissolution rate is directly proportional to the interfacial surface area (or particle size) and to the equilibrium solubility. *In vivo*, these conditions are met when a poorly water soluble API is administered orally and faster absorbed from solution in the gastrointestinal fluids than it is dissolved.[11] The influence of particle size of poorly water-soluble drug molecules on the dissolution rate is well documented in the literature. The dissolution rate of ibuprofen,

itraconazole and ketoconazole was improved using novel crystallization techniques yielding smaller API crystals. Particle size measurements were performed using laser diffraction.[12] *Kyung et al*. showed for four different poorly water-soluble model drugs that dissolution rate strongly relates to the particle size distribution. Measurements were performed on the raw materials, which were fractionated based on their particles size. Sizing was performed using SEM, digitally enhanced light microscopy and specific surface area determination using a gas adsorption method.[13] Although particle size is often described in the form of sphere equivalent diameter, micro-CT offers other options, which are of advantage when the particle surface is of interest. The Sauter diameter (SD) is the diameter of a sphere with the same volume to surface area ratio as the measured particle. It is defined by the surface diameter d_S:

$$d_S = \sqrt{\frac{A_p}{\pi}} \tag{14}$$

and the volume diameter d_V:

$$d_V = \left(\frac{6V_p}{\pi}\right)^{1/3} \tag{15}$$

which results in:

$$SD = \frac{d_V^3}{d_S^2} \tag{16}$$

The surface area A_p and volume V_p are measured with micro-CT and the equation can be written as:

$$SD = 6\frac{V_p}{A_p} \tag{17}$$

or with the specific surface area S_V:

$$SD = \frac{6}{S_V} \tag{18}$$

Therefor the Sauter diameter is a form to describe the particle size (distribution) using the specific surface areas of particles, making it suitable for the comparison with dissolution rate. When looking at the particle size distribution using the Sauter diameter, the differences between the references batch and the faulty batch are accentuated, compared to the description as equivalent sphere diameters (see Figure 69). Particles of the faulty batch have a broad distribution with similar frequencies between 35 µm and about 200 µm with the largest particles reaching 350 µm. Particle size distribution of the reference batch is a

monomodal distribution with a maximum at 55 µm and the vast majority of the particles being smaller than 100 µm. Although, large particles up to 350 µm can still be found.

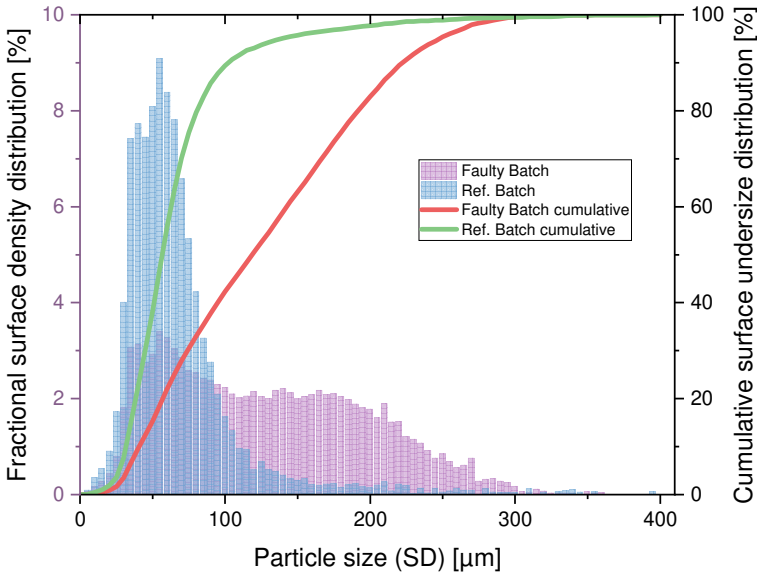

Figure 69: Particle size distribution according to the Sauter diameter for the faulty and reference batch.

5.6 Conclusion

Tablets are the most common dosage form for the delivery of drugs. Advantages include ease of manufacturing, high dosage accuracy, simplicity of usage, good storability and transport.[6] The main problem with analyzing tablets is that most measurement methods require extensive sample preparation, which result in the destruction of the specimen. Often the spatial distribution of individual components is altered prior to analysis and thus not available for interpretation.

To improve on this problem, novel imaging techniques are used and combined with established techniques to enable an in-depth characterization of intact pharmaceutical tablets. Raman microscopy is implemented for the chemical identification and localization of the three main components of the tablet, API, mannitol and microcrystalline cellulose, in 2D tablet cross-sections. 3D mapping of the relative density distribution of entire tablets, without the need of invasive sample preparation, is realized using micro-CT imaging. Through measurements on the same sample, it is possible to link chemical information from Raman data with selected relative density values of the micro-CT dataset. Combining information from both techniques enables an unprecedented look into a film-coated tablet. After the development of a custom-made, multistep task list for particle isolation, it is possible to locate the API contained in the tablet in 3D. This provides detailed information

about the drugs' particle size, shape and spatial distribution. The robustness and repeatability of measurement results is demonstrated by analyzing multiple tablets per batch yielding matching results. The capability of measuring the particle size distribution of API without altering the specimen proved to be of use when a batch showed out-of-specification (OOS) dissolution results. For conventional methods, the tablet has to be dissolved in a medium where the API is insoluble. The remaining suspension is analyzed using digitally enhanced light microscopy or laser diffraction. Differentiating between individual insoluble components was not entirely possible due to visual similarities between API and one excipient. When comparing results of the faulty batch with samples from the reference batch no clear differences were found. Raman mapping of tablet surfaces from the OOS and reference batch showed similar particle size and shape of one excipient, but noticeable differences for the API. To expand on this, Raman enhanced micro-CT measurements of both batches are performed. Spherical API particles with diameters of up to 500 µm, homogenously distributed throughout the tablet, are discovered. The faulty batch, with slowed dissolution rate, possesses a distinctly broad particle size distribution with a large amount of particles > 200 µm. In contrast, the reference batch has a PSD resembling a normal distribution with considerable fewer large particles. A subsequent look at the raw materials revealed large spherical API particles to be agglomerates of smaller API crystals. This led to an in-depth look at the product specification received from the API manufacturer. Standard particle size measurement of raw materials is performed using laser diffraction of API suspensions in water. After checking the measurement procedure, a preceding sonication step was found to be problematic, possibly disintegrating agglomerates before the start of the analysis. Upon skipping this step, laser diffraction was able to reveal the presence of agglomerates in several API raw material batches, some of which were used for production of the faulty FDF batch. It is well documented in literature that particle size distribution of poorly water-soluble drugs can have a major influence on the *in vivo* and in *vitro* performance.[14] Ticagrelor, the API of this project, is a BCS IV class drug (low solubility and low permeability) with mediocre bioavailability. The different results for the particle size distribution of the API in the finished product and the different amounts of agglomerates found in the corresponding raw materials suggest that this factor is responsible for the unsatisfactory dissolution behavior of the OOS-batch. This led to a change in raw material testing and narrower specification for sourcing. This project showed that Raman enhanced micro-CT can play an important role in the error detection of faulty solid dosage forms in the pharmaceutical context and is able to contribute to fast and robust solution finding.

References

[1] S.K. Bardal, J.E. Waechter, D.S. Martin, *Applied Pharmacology*, Elsevier, St. Louis, Missouri, **2011**.

[2] L.A. Felton, S.C. Porter, *Expert Opin. Drug Deliv.*, **2013**, 421-435.

[3] G.L. Amidon, H. Lennernäs, V.P. Shah, J.R. Crison, *Pharm. Res.*, **1994**, 413-420.

[4] R. Teng, J. Maya, *J. Drug Assess.*, **2014**, 43-50.

[5] The European Agency for the Evaluation of Medicinal Products, *Assessment Report For Brilique*, **2011**. At: https://www.ema.europa.eu/en/documents/assessment-report/brilique-epar-public-assessment-report_en.pdf

[6] K.H. Bauer, K.-H. Frömming, C. Führer, *Lehrbuch der pharmazeutischen Technologie*, Wissenschaftliche Verlagsgesellschaft, Stuttgart, **2002**.

[7] K.A. Jacobson, J.-M. Boeynaems, *Drug Discov. Today*, **2010**, 570-578.

[8] R.F. Storey, S. Husted, R.A. Harrington, *J. Am. Coll. Cardiol.*, **2007**, 1852-1856.

[9] H.G. Merkus, *Particle Size Measurements*, Springer, **2009**.

[10] E. Brunner, **1903,** *Z Phys Chem.*, **1904**, 56-102.

[11] M. Mosharraf, C. Nyström, *Int. J. Pharm.*, **1995**, 35-47.

[12] N. Rasenack, B.W. Müller, *Pharm. Res.*, **2002**, 1894-1900.

[13] K.R. Chu, E. Lee, S.H. Jeong, E.-S. Park, *Arch. Pharm. Res.*, **2012**, 1187-1195.

[14] M.E. Aulton, K.M.G. Taylor, *Aulton's Pharmaceutics: The design and manufacture of medicines*, Elsevier, **2018**.

6 Pellet formulations

6.1 Introduction

The present project is a capsule formulation filled with gastro-resistant pellets (GRC), where a multitude of homogenous pellets is contained in a hard gelatin capsule. After oral administration, the capsule dissolves in the stomach and releases the pellets into the surrounding medium. In the case of gastro-resistant pellets, the migration into the intestines and subsequent drug release follows.[1] There are several advantages to pellet formulations and multiparticulate formulations in general. Due to the small nature of pellets, they can easily pass from the stomach to the gastro-intestinal tract. This reduces the intra- and inter-subject variability. Arriving in the gastro-intestinal tract as multiple small units also reduces the risk of localized dose dumping, which could lead to peak plasma fluctuations and localized irritations on gastro-intestinal mucosa. Lastly, multiparticulates enable the mixing of the drug with food, improving its application for pediatric and geriatric patients.[2] In Figure 70, the dimensions of the samples are shown in comparison with a 1-euro cent coin.

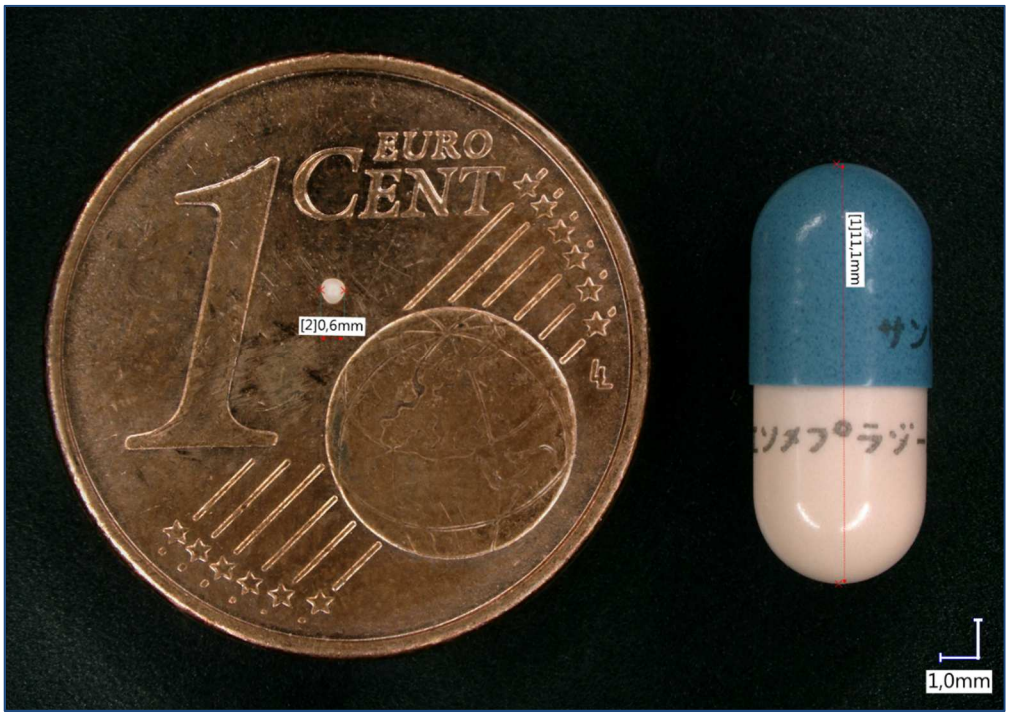

Figure 70: Pellet-filled capsule (right), singular pellet (middle, on top of the coin) and 1-euro cent coin as scale (left).

The pellets contain a sucrose sugar core, a digestible, pharmacological inert material, which is used to regulate the overall particle size. This is of importance because the dissolution rate is governed among other factors by the pellet diameter.[1] The sugar core serves as the initial building block of the pellet on which the API is applied.[3] The employed API, esomeprazole {(S)-5-Methoxy-2-[(4-methoxy-3,5-dimethylpyridin-2-yl)methylsulfinyl]benz-imidazole} belongs to the class of proton-pump inhibitors (PPIs) (see Figure 71).

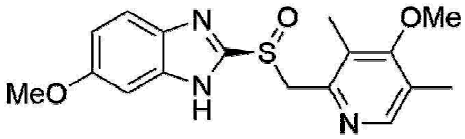

Figure 71: Chemical structure of esomeprazole.

This drug type is used for the treatment of several acid-related disorders, such as gastro-esophageal reflux disease (GORD)[4], *Helicobacter pylori*-associated duodenal ulcer [5], Zollinger-Ellison syndrome [6] and nonsteroidal anti-inflammatory drug (NSAID) associated gastric ulcer.[7] After absorption, PPIs are transported via the bloodstream to the parietal cells of the stomach. Here after protonation, the activated API binds irreversible to a cysteine unit of the H^+/K^+ - ATPase and thereby suppresses the secretion of stomach acid. [8] PPIs are acid-labile and mostly absorbed in the small intestine. Therefore, esomeprazole has to be protected, for example through coating, with an acid-resistant layer to ensure functionality when administered orally.[8] Materials such as methacrylate co-polymers, cellulose acetate phthalate, and polyvinyl acetate phthalate are used as enteric coating agents to provide protection from stomach acid and ensure API stability until release in the small intestines. Because of the acid groups inherent to these substances, a direct contact with the API has to be avoided.[9] For this reason an intermediate layer consisting of talcum and binders, isolating the API from the gastro resistant layer has to be employed. This leads to the composition schematically shown in Figure 72. A number of other excipients can be taken from the patient information leaflet. These perform different tasks as stabilizers, binders or manufacturing process supporting material (see Figure 72 right side).

Due to the more complex manufacturing process, pellet-dosage forms are more expensive and not as common as standard tablet formulations.[10]

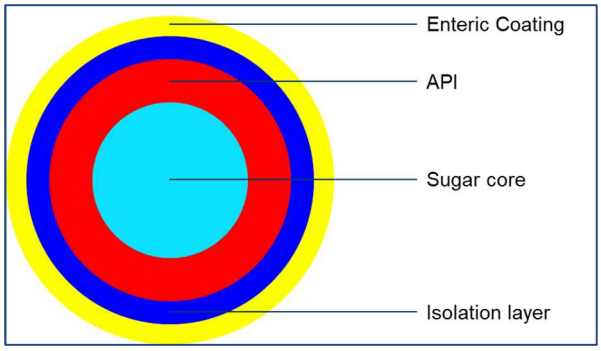

Excipient	Purpose
Glyceryl monostearate 40-55	Surface-active emulsifying agent
Hydroxypropyl cellulose	Thickener, binder, emulsion stabilizer
Hypromellose (hydroxypropyl methylcellulose)	Binder
Magnesium stearate	Lubricant
Methacrylic acid copolymer	Enteric coating
Polysorbate 80	Surfactant, Stabilizer
Sugar spheres	Starter pellets
Talc	Isolation layer
Triethyl citrate	Stabilizer, plasticizer

Figure 72: Schematic composition of an esomeprazole pellet in this project (left). List of excipients from patient information leaflet with common intended purpose.[11]

6.1.1 Motivation

The aim of a generic pharmaceutical company is to produce a product that is bioequivalent to the innovator. To facilitate this requirement, comprehensive understanding of the chemical and physical composition as well as the factors governing *in vitro* and *in vivo* behavior of the product to be copied are necessary. In Figure 73, the strategy outline is shown.

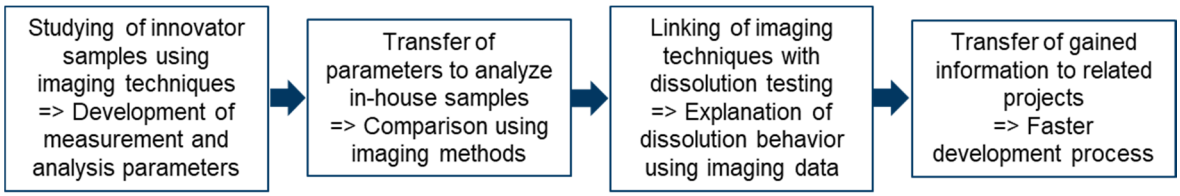

Figure 73: Strategy outline for the selection of suitable batches for BE-study and transferability of measurement/analysis procedures.

In a first step, several established and new imaging techniques are implemented to characterize the innovators pellet composition. At this stage, the measurement and analysis parameters are refined and the critical quality attributes (CQAs) identified. Through the unique combination of analytical tools, parameters such as pellet count per capsule, individual layer thickness of each layer or pellet surface can be extracted with the help of custom-made multistep analysis algorithms. Of special interest is the development of a new method to investigate the stability of the API until the location of release is reached. For this reason, detailed information about deficiencies in the layer isolating the API from the enteric coating should be collected. With standard methods, detection of a broken or insufficient isolation layer is done indirectly via stability testing and HPLC-guided search for API

degradation products. Depending on the severity of the defects, problems of the product can only be detected after several days or weeks, when the concentration of the degradation products is high enough for detection. An additional drawback of HPLC analysis in this case, is the destructive nature of the measurement method, preventing subsequent analysis on the same sample. For this purpose, a novel Raman enhanced micro-CT method is implemented to get destruction-free insights into the intermediate layers structure without prior sample preparation. In a second step the gained information about how the methods are optimally implemented and which information can be gathered, comparisons between innovator samples and in-house samples are performed. In the process of BE-study batch selection, differences in the dissolution rate between the innovator and in-house capsules were found. The third step is to use the newly developed imaging techniques to find explanations for the variations. In the last step, it is shown that the developed measurement and analysis methods can be modified to be used in similar projects, thus shortening development time.

6.2 Characterization of the innovators FDF

For the 2D analysis methods, digitally enhanced light microscopy, Raman microcopy and SEM/EDX, pellets are removed from the capsule embedded in epoxy resin and cut to receive cross sections through several pellets.

6.2.1 Digitally enhanced light microscopy

In Figure 74, digitally enhanced light microscopy images of the pellet selection and of a singular zoomed-in pellet are shown. The layered structure of the pellets is easily recognizable. The sugar core seems to be molten during the milling process and solidified afterwards. Due to the necessary sample preparation steps, it cannot be ruled out that possible pellet defects are caused by the milling process itself. To get a quick first look at the pellet layer proportions digitally enhanced light microscopy is a suitable method, requiring minimal effort.

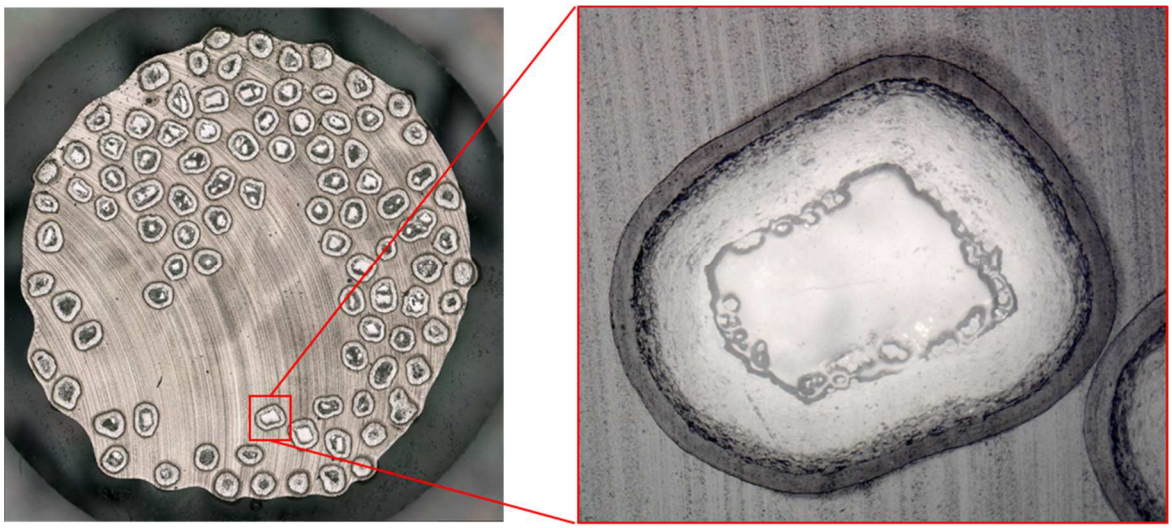

Figure 74: Digitally enhanced light microscopy images of the entire pellet selection (left) and detail image of a singular pellet (right).

6.2.2 Raman microscopy

Using the image composition function of the Raman microscope, the same pellet that is used for digitally enhanced light microscopy can be selected. The red rectangle describes the area where Raman spectra are recorded. First, the MCR-ALS algorithm is used to analyze the entirety of the measured spectra without additional input. In a second step, the calculated components are compared to reference spectra of pure substances using DCLS, yielding the chemical distribution of the sample surface.

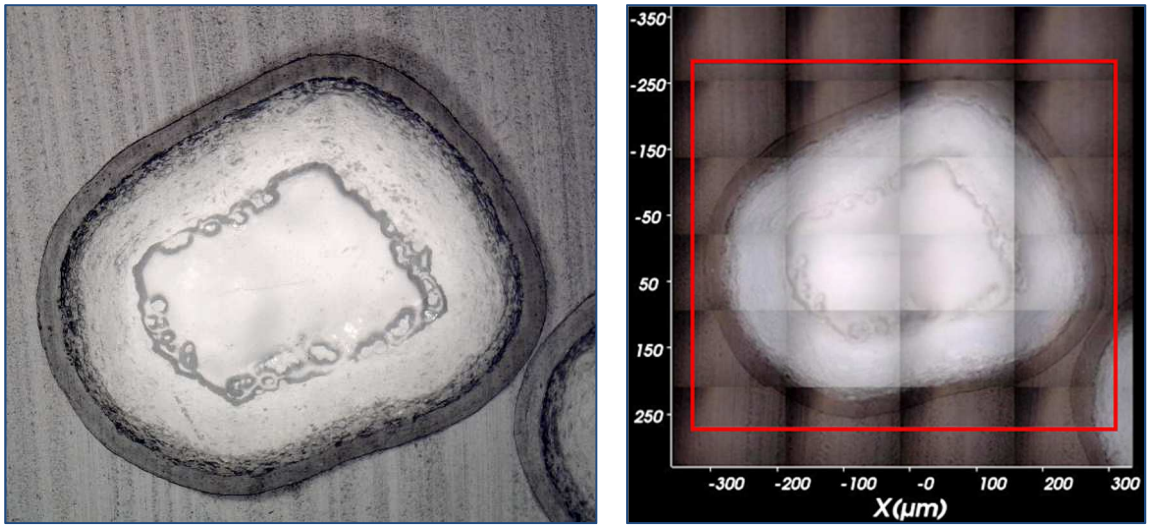

Figure 75: White digitally enhanced light microscopy image (left) and composite white light image recorded with the Raman microscope unit (right).

6 Pellet formulations

A

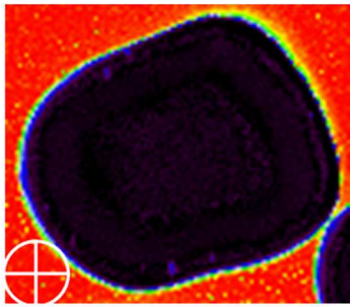

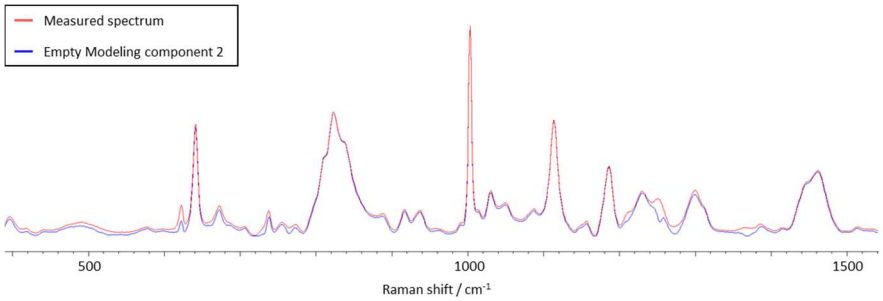

B

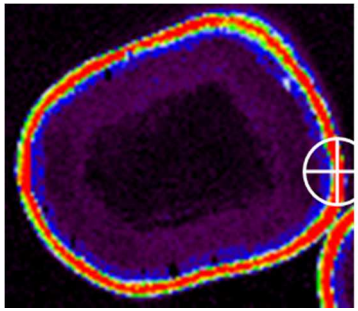

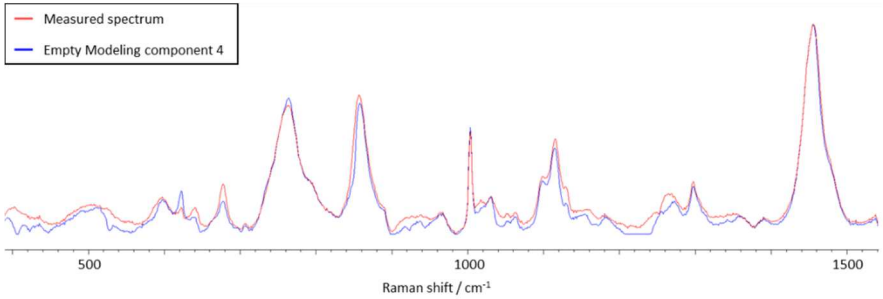

C

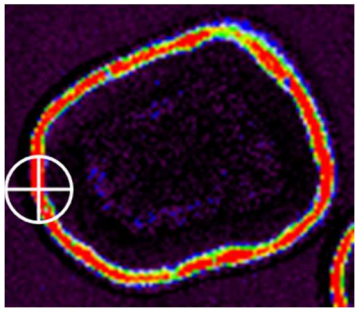

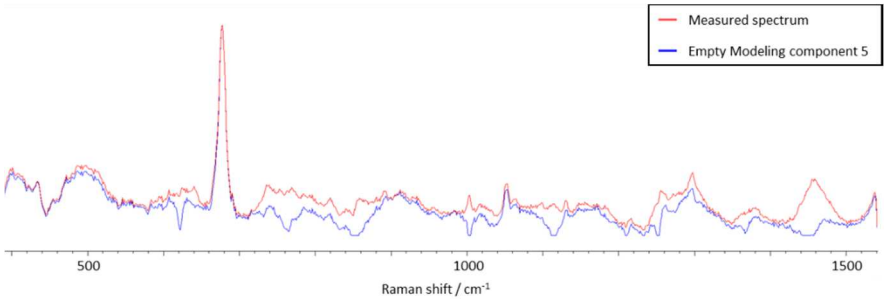

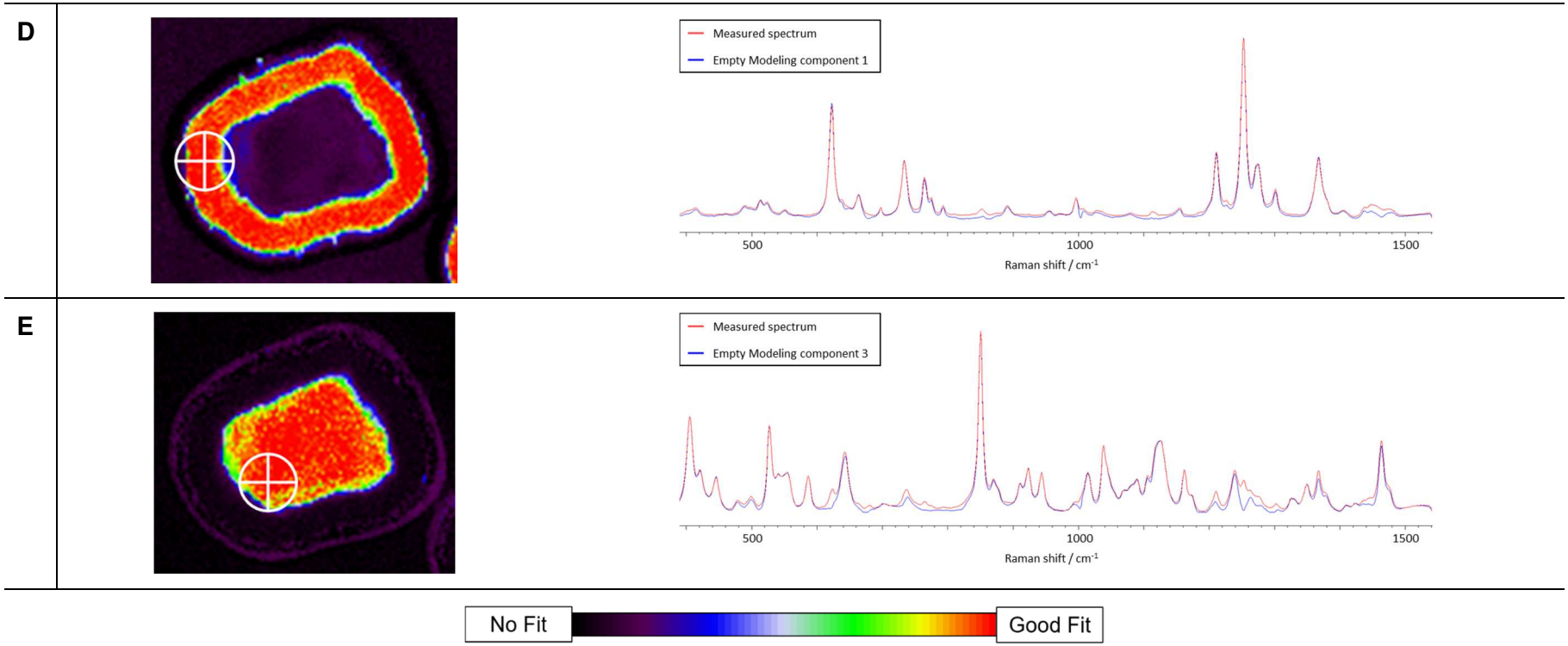

Figure 76: MCR-ALS mapping of five calculated components (left) and measured Raman spectra in red, at the point of the crosshair and the calculated components spectra in blue (right)

The MCR-ALS algorithm is calculating five different pure spectra to explain the entirety of the gathered spectral information. Raman mapping shows a composition of a core, three chemically different layers and the surrounding epoxy resin used to fixate the pellets. Measured spectra from red areas of the mapping are in very good accordance to the calculated components (see Figure 76). In order to assign the calculated components to spectra of pure spectra of reference substances the DCLS chemometric method is used.

6 Pellet formulations

A*	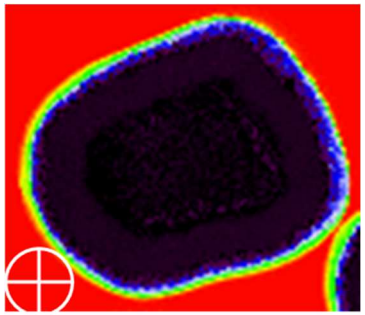	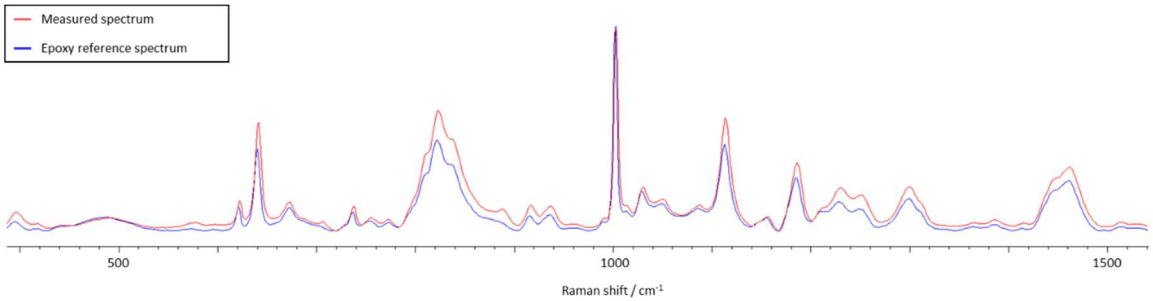
B*	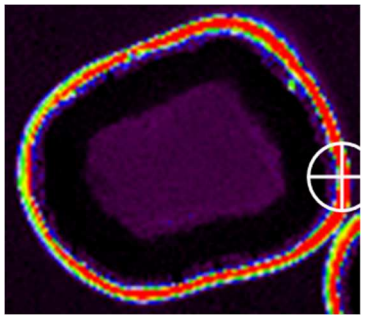	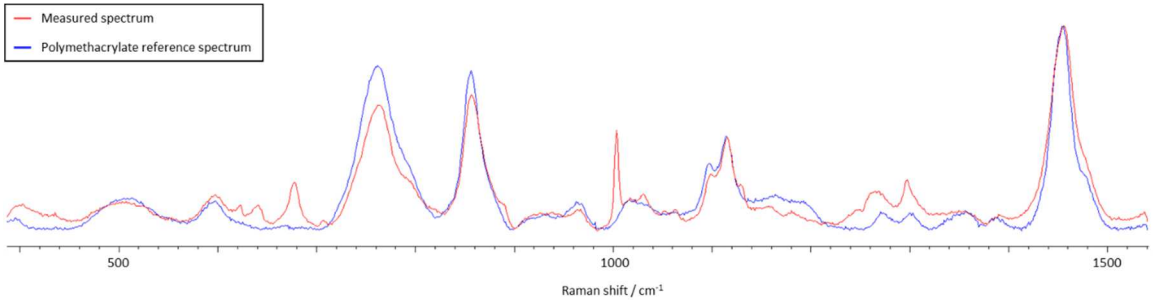
C*	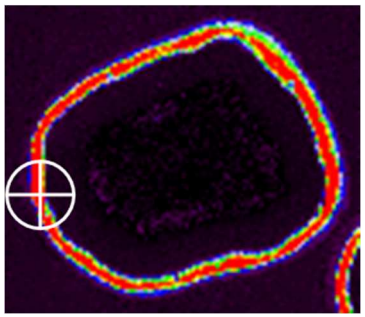	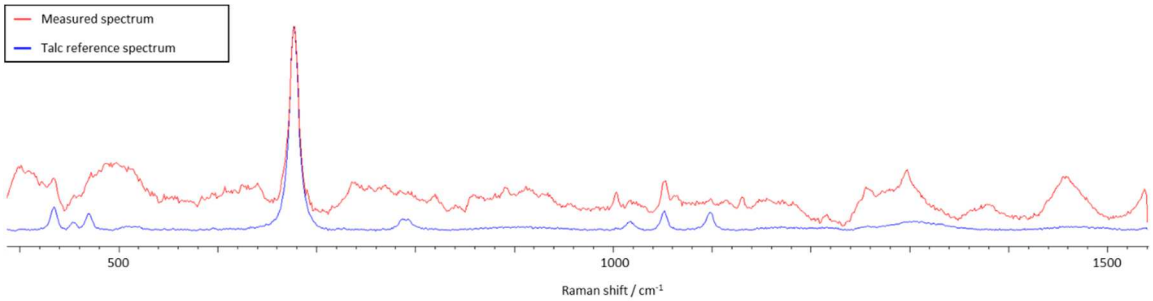

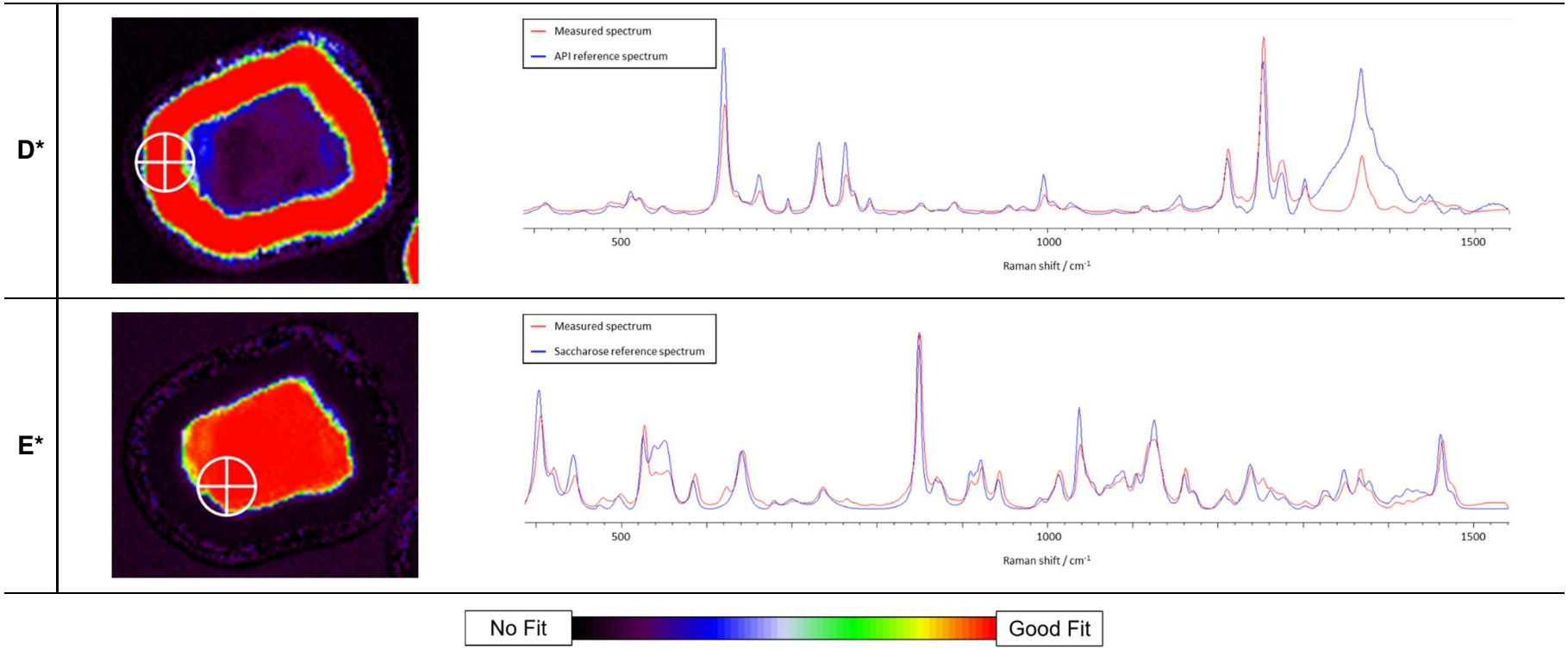

Figure 77: DCLS mapping of epoxy resin (A*), polymethacrylate (B*), talc (C*), API (D*) and saccharose (E*) (left) and measured Raman spectra at the point of the crosshair (red) and the reference spectra of pure substance (blue) (right).

The DCLS algorithm compares the measured spectra with reference spectra and outputs a color-coded mapping according to the fit of the comparison (see Figure 77). The epoxy resin surrounding the pellet is as expected in very good accordance to the reference spectrum of pure epoxy (A*). The spectra measured at the outermost layer of the pellet are in good accordance with a copolymer of methacrylic acid and methyl methacrylate, a commonly used substance for enteric coatings (B*). The intermediate layer, in direct contact with the API can be identified as talc.

Due to its small cross-section (~30 µm) spectral overlap from the API at 1250 cm^{-1} and 1295 cm^{-1} as well as from the outer layer at 1460 cm^{-1} is found (8) (see also paragraph 3.2.4). Due to its small cross-section (~30 µm) spectral overlap from the bordering talcum layer can be found at 675 cm^{-1} and from the epoxy resin at 1000 cm^{-1} (C*). The API is located in a layer, surrounding the core region. The measured spectra are in good accordance to the reference spectrum. The broader peak of the reference spectrum at 1370 cm^{-1} might be caused by an amorphous fraction in the reference sample and a pure crystalline substance in the pellet-formulation (D*). The core region is in very good accordance to the reference spectrum of saccharose (E*). The casing of the pellets in epoxy prevents proper heat dissipation. For this reason, it is not possible to measure more than one pellet at a time. Large measurement areas have too much heat input from the laser, which results in sample damage. Raman mapping can be used for the chemical identification of the main components of the pellet-formulation from the innovator. It is apparent that the manufacturing process leads to a clear separation of components into different layers with no mixing between substances. Several excipients found in the patient information leaflet, primarily binders, stabilizers and manufacturing process-supporting materials are not detected with Raman microscopy. A possible reason might be their very low concentration and/or lower Raman efficiency compared to the main components. To confirm these results SEM/EDX analysis is performed.

6.2.3 SEM/EDX

With SEM/EDX, the atomic species distribution of a pellet can be analyzed. Of special interest is the API, which exists both as sodium and magnesium salt. In Figure 78, SEM/EDX mapping of the same pellet analyzed by digitally enhanced light microscopy and Raman microscopy is displayed. The SEM image shows the pellet composition consisting of the core region and three layers. To capture the entire pellet, a relatively low magnification of 200x has to be used. Because of this and the small structural features of the specimen, mapping can only be seen as a rough overview.

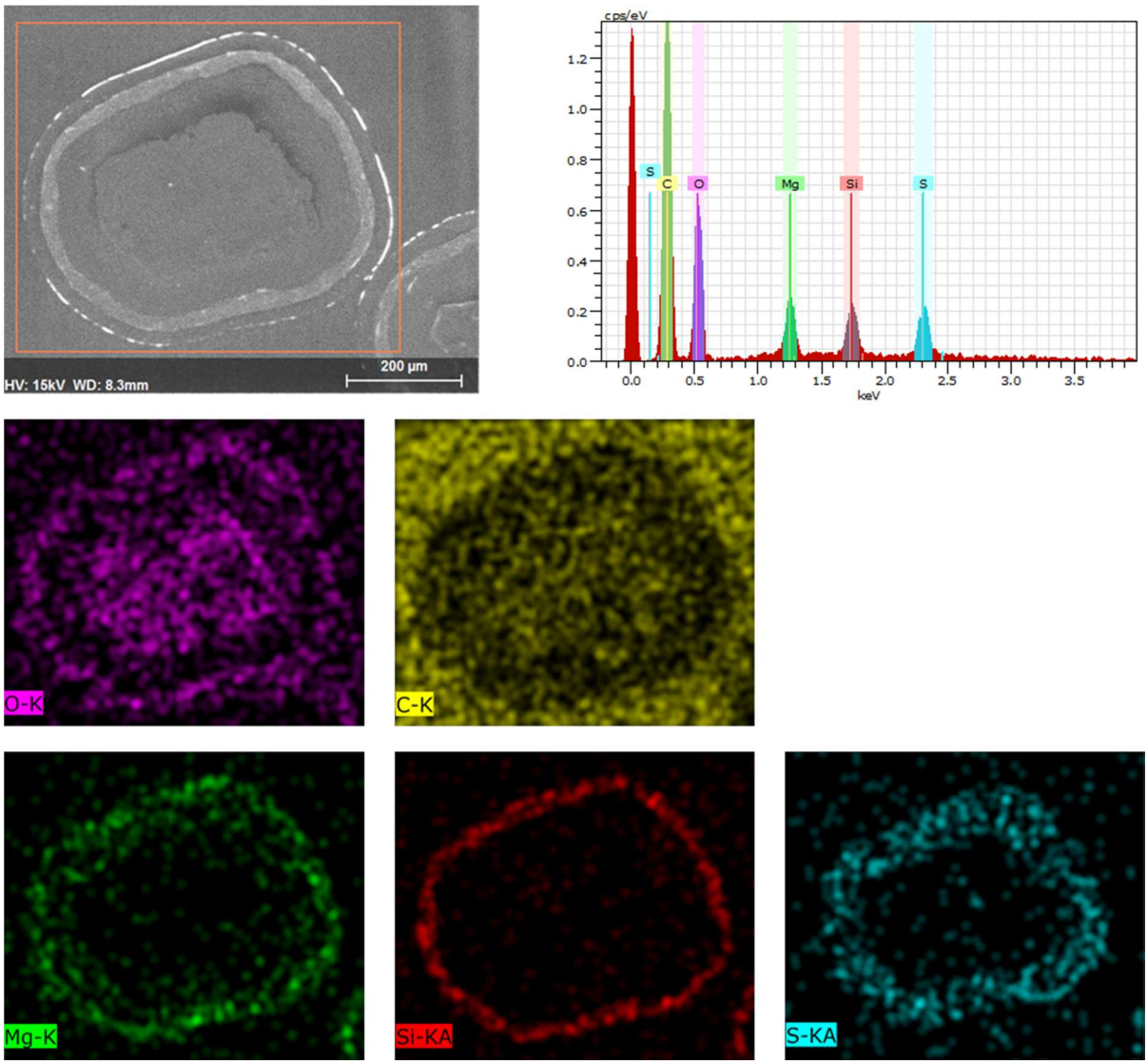

Figure 78: SEM/EDX Overview: SEM image (top left) with region of interest (orange rectangle), spectral composition (top right) and mapping of the individual atom species.

With EDX analysis, five different atom species are found in the sample. It is of note, that no sodium is present in the sample, which points to the use of the magnesium salt form of esomeprazole. Carbon can be found throughout the sample, with the exception of the isolation layer, which can be expected for mostly organic compounds. To get a better resolution, a measurement with 1000x magnification of the left side of the pellet is shown in Figure 79. Oxygen being part of the sugar core, the API, talcum and polymethacrylate can be found in each part of the pellet. The core region being comprised of saccharose shows high amount of oxygen and no heteroatoms. In the API-layer, sulfur and magnesium can be found which is consistent with the magnesium salt formulation of the drug. The isolation layer shows silicon and magnesium, which supports the Raman findings of talcum, a

mineral with the formula $Mg_3Si_4O_{10}(OH)_2$. The GR-layer shows no heteroatoms, which is also consistent with the organic copolymer polymethacrylate.

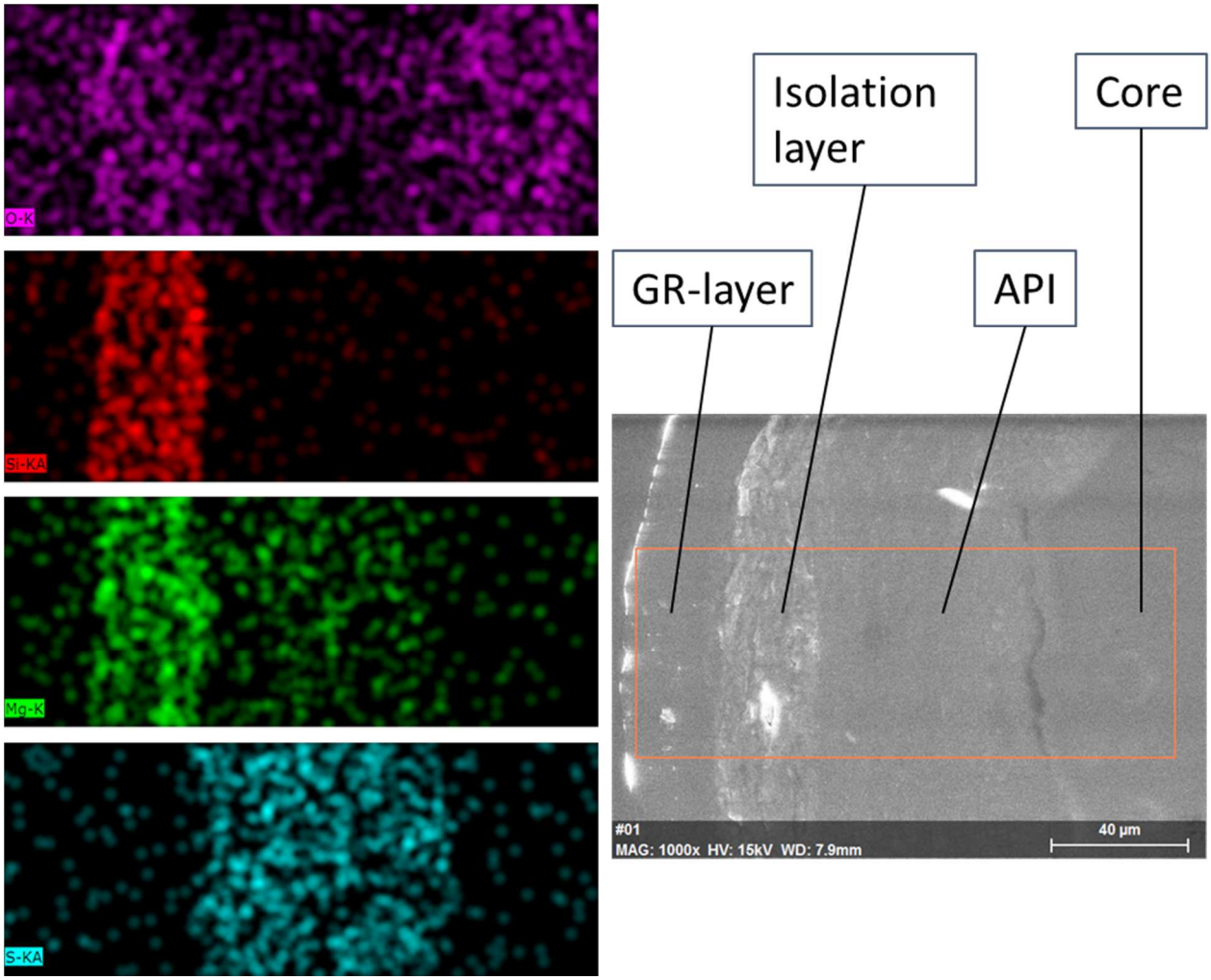

Figure 79: SEM/EDX detailed view: SEM image with region of interest (right), EDX mapping of four different kinds of atoms (left).

Because of their pure organic compositions, several excipients found in the patient information leaflet, primarily binders, stabilizers and manufacturing process supporting materials cannot be assigned beyond doubt with SEM/EDX.

6.2.4 Micro-CT

In contrast to digitally enhanced light microscopy, Raman microscopy and SEM/EDX, micro-CT analysis enables measurement of the entire, unaltered pellet-filled capsule. In Figure 80, a radiograph of the sample is displayed, showing the hard gelatin capsule three-quarters filled with pellets and the plasticine, with which the capsule is fixed on the sample pin, at the bottom.

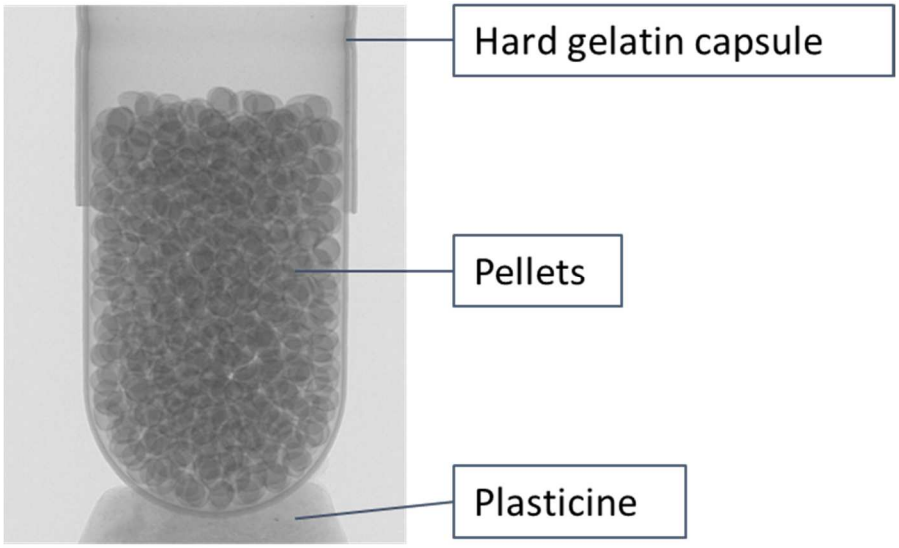

Figure 80: Radiograph of a pellet filled capsule sample from the innovator.

The sequential steps needed to get from the radiographs to images fit for data analysis are depicted in Figure 82. All data processing and analysis takes place in 3D, but is depicted in 2D for ease of understanding. First, a zoomed-in picture (of **1** in Figure 82) of the marked area to highlight individual pellet composition is shown in Figure 81. Here the core and layer composition of the pellets is visible. Because of the minimal differences between the relative density values of the sugar core and the surrounding API-layer, separation is hardly possible. In the following, the combined region will be referred to as “core+”.

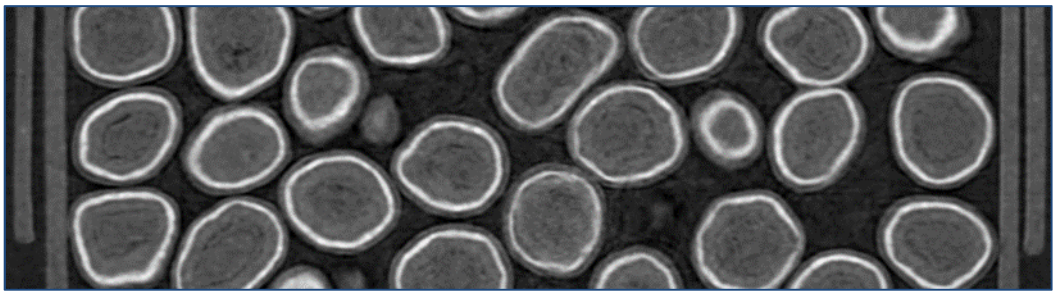

Figure 81: Enlarged image of the marked area of picture **1** in Figure 82.

After the reconstruction of the 2400 radiographs taken (pixel size 7.0 µm), **1** is obtained as grey scale image with the full relative density distribution.

The first goal is to isolate individual pellets. Because the capsule is not of interest for this project, it is digitally removed. The same is done to the background, which because of its relative density fluctuations might interfere with particle analysis. Additionally, pellets that are in contact with each other have to be detached. Through multiple step task list (TL_ESO/GRC_01), including binarization, despeckle and a watershed algorithm for the

separation, the binary mask **2** is received. This mask is then applied to **1** to yield the individual pellets with density information seen in **3**.To separate and analyze the individual components of the pellets two custom-made task lists (TL_ESO/GRC_02 and TL_ESO/GRC_03) were implemented. Because the isolation layer has the highest relative density, it can be separated using manual thresholding and stray particle removal, yielding the binarized image **4**. The core+ region and the gastro enteric layer share relative density values, therefore thresholding is not sufficient for separation. The hollow spheres of the isolation layer in **4** are digitally filled, resulting in spheres consisting of the core+ and the isolation layer. From this transition image, the isolation layer is subtracted yielding only the core+ (see **5**).

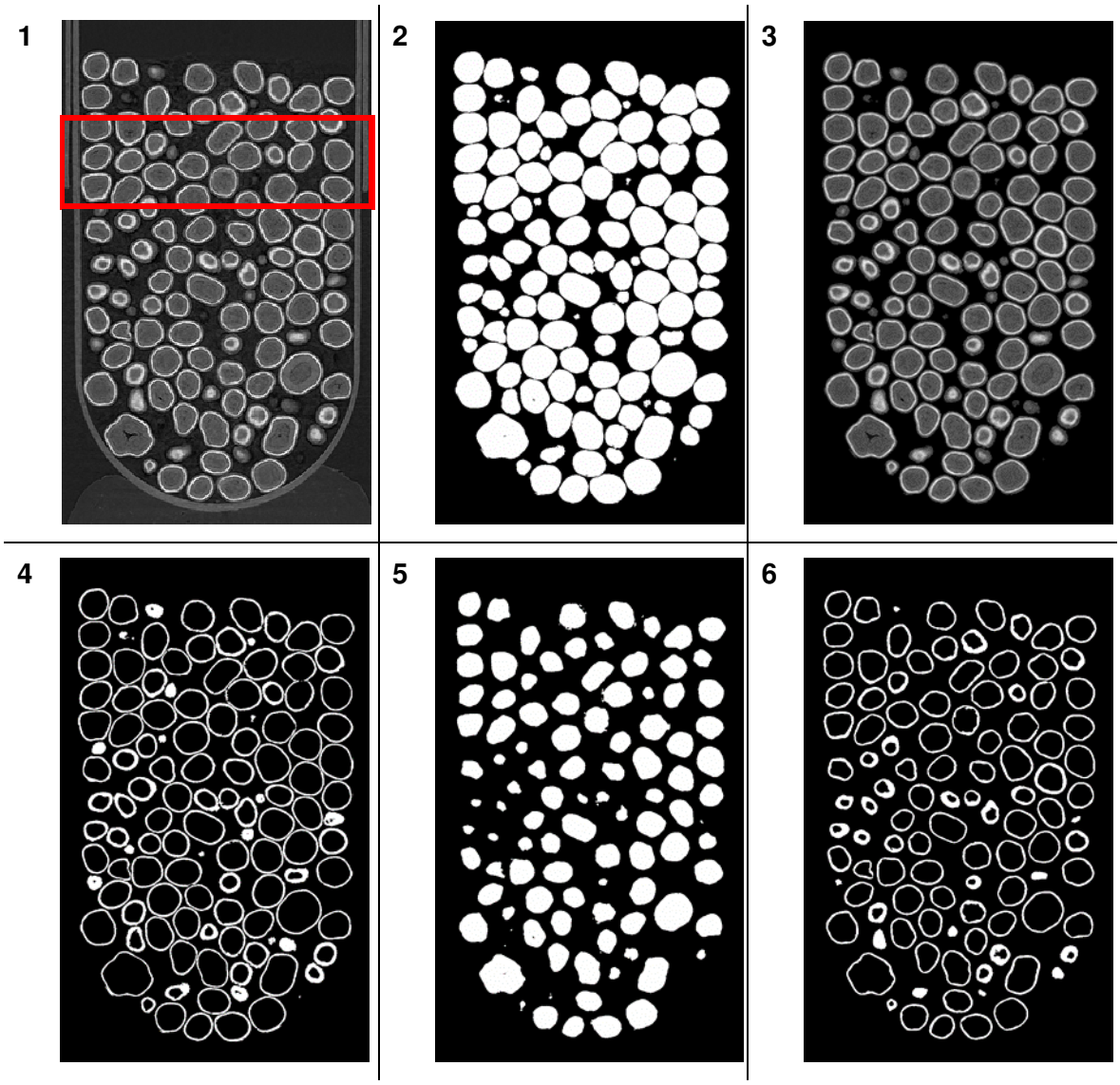

Figure 82: Reconstructed grey scale image (1), isolated pellets, binarized (2), isolated pellets, grey scale (3), isolation layer (4), core region (API + sugar core) (5), GR-layer (6).

For the GR-layer, the isolation layer and the core+ is subtracted from the whole pellets resulting in image **6**. Several noise reduction and stray particle removal steps have to be incorporated to get clean images for the core+ and enteric coating layer (see paragraph 3.1.5.3 for more details).

Using the 3D visualization software, the individually obtained components can be integrated into one 3D-model. With the help of the binarized images of the core+ (red), isolation layer (blue) and GR-layer (yellow) a detailed view of the sample can be exhibited. This can help with the manual detection of easily recognizable errors and the overall orientation within the sample (Figure 83).

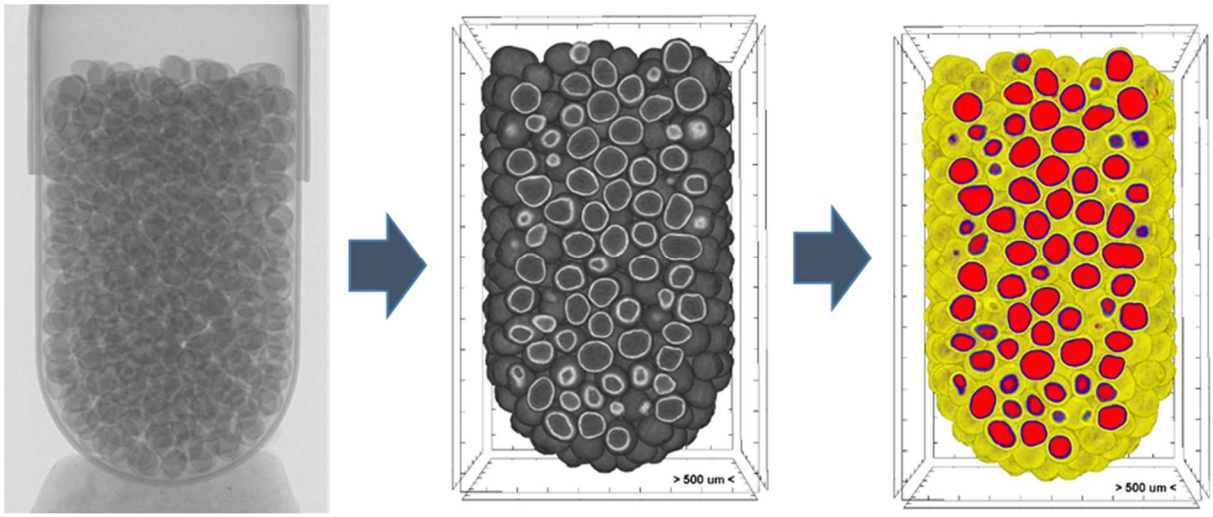

Figure 83: Raw image (left), reconstructed model (middle), composite image of three binarized regions, with the core in red, isolation layer in blue and the GR-layer in yellow (right).

6.2.4.1 Damaged Pellets

For this project damaged pellets are defined as pellets that have a broken or otherwise flawed isolation layer. Depending on the cause, damages can occur in different forms. In Figure 84, two comon examples are shown. In the left micro-CT image the pellet is broken in half, a possible reason is the porrous sugar sphere and the local occurance of mechanical force during the manufacturing process. In the image on the right, a not so obvious deffect of the isolation layer is shown. Here the possible reason might be a problem during the coating process. Several possible root-causes for this include: innsufficient coating solution, sticking and afterwards inhomogeneous separation of particles, coating process too slow and/or too slow drying. Both kinds of damages will be captured during micro-CT analysis.

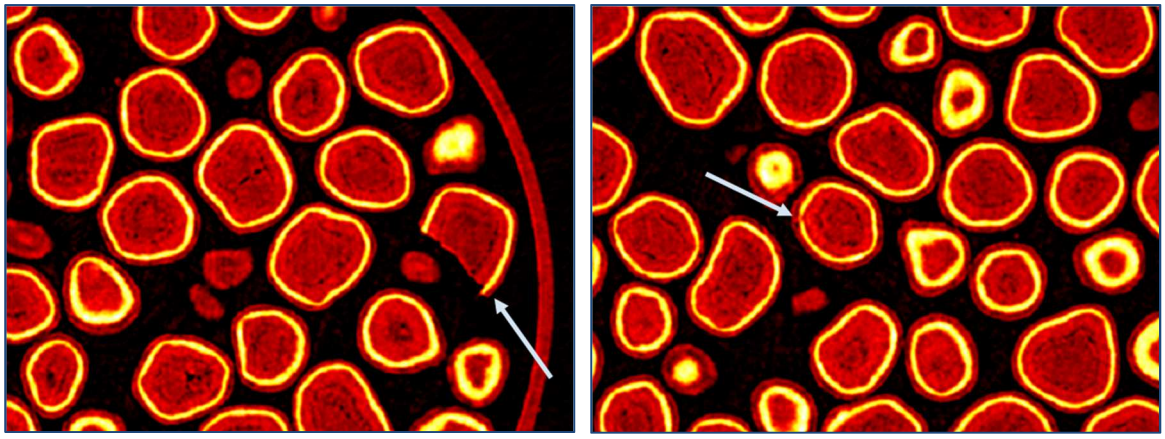

Figure 84: Micrographs of damaged pellets (marked with arrows).

Since there is no standard procedure for the detection of pellets with defective isolation layer, a custom-made task list (TL_ESO/GRC_04) had to be developed (see Figure 85). When performing an individual particle analysis on the newly prepared data set, treated as explained in Figure 85, the volume of each pellet can be plotted against its corresponding sphericity to show the number of defective pellets. Sphericity is the ratio of the surface of a sphere of the same volume as the measured particle and the actual surface area of the measured particle.[12]

1	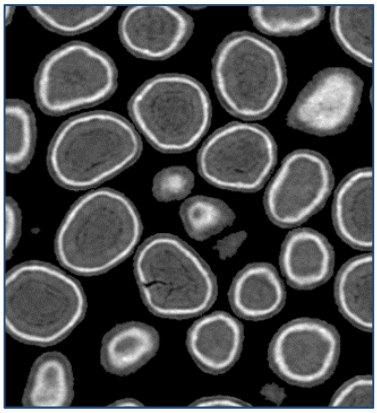	Grey scale image of isolated pellets.
2	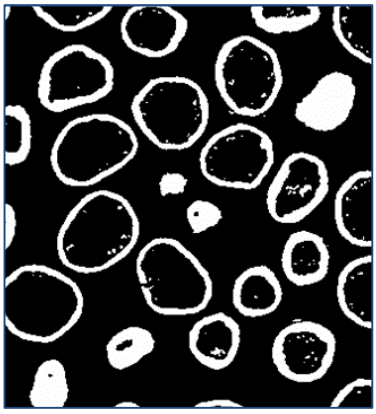	Manual thresholding of the isolation layer and stray particles of the same relative density range

3	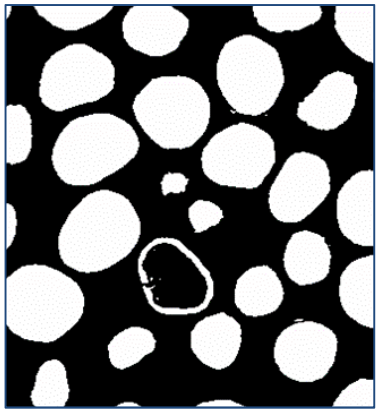	Digital removal of pores. This results in completely white circles (spheres in 3D) where the isolation layer is intact; leaving pellets with broken isolation layers as interrupted circles (hollow but defective spheres in 3D).
4	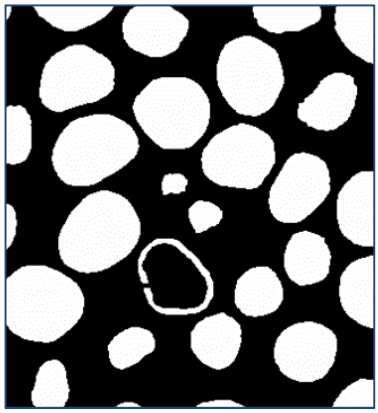	The multi-step process of stray particle removal yields a data set, where each particle is either a white circle (2D)/ white sphere (3D) or for broken pellets, an interrupted circumference (2D)/hollow sphere (3).

Figure 85: Stepwise procedure for the detection of pellets with damaged isolation layer.

Due to the prior data handling, pellets with a defective isolation layer are transformed into hollow spheres, intact pellets into normal spheres. This has consequences for the volume and the sphericity of the particles. In the plots in Figure 86, damaged pellets can be found in the bottom left corners as particles with low sphericity and small particles volumes. This way for capsule #04 of innovator batch 1 four of 673 defective pellets can be found.

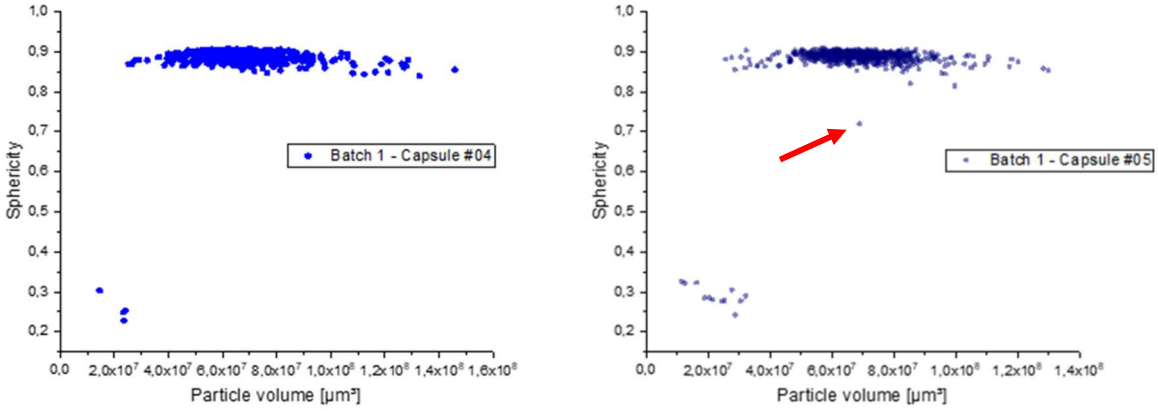

Figure 86: Plotting of sphericity against the particle volume after the custom-made task list (TL_ESO/GRC_04), for capsules #04 (left) and #05 (right) of originator batch 1.

For capsule #05, twelve of 667 pellets with defective isolation layer and one additional outlier pellet (arrow) can be found.

The visualization of the detected faulty pellets is shown in Figure 87. It can be seen that the damaged pellets are randomly distributed across the capsules. Additionally, in the zoomed-in image the type of damage can be identified.

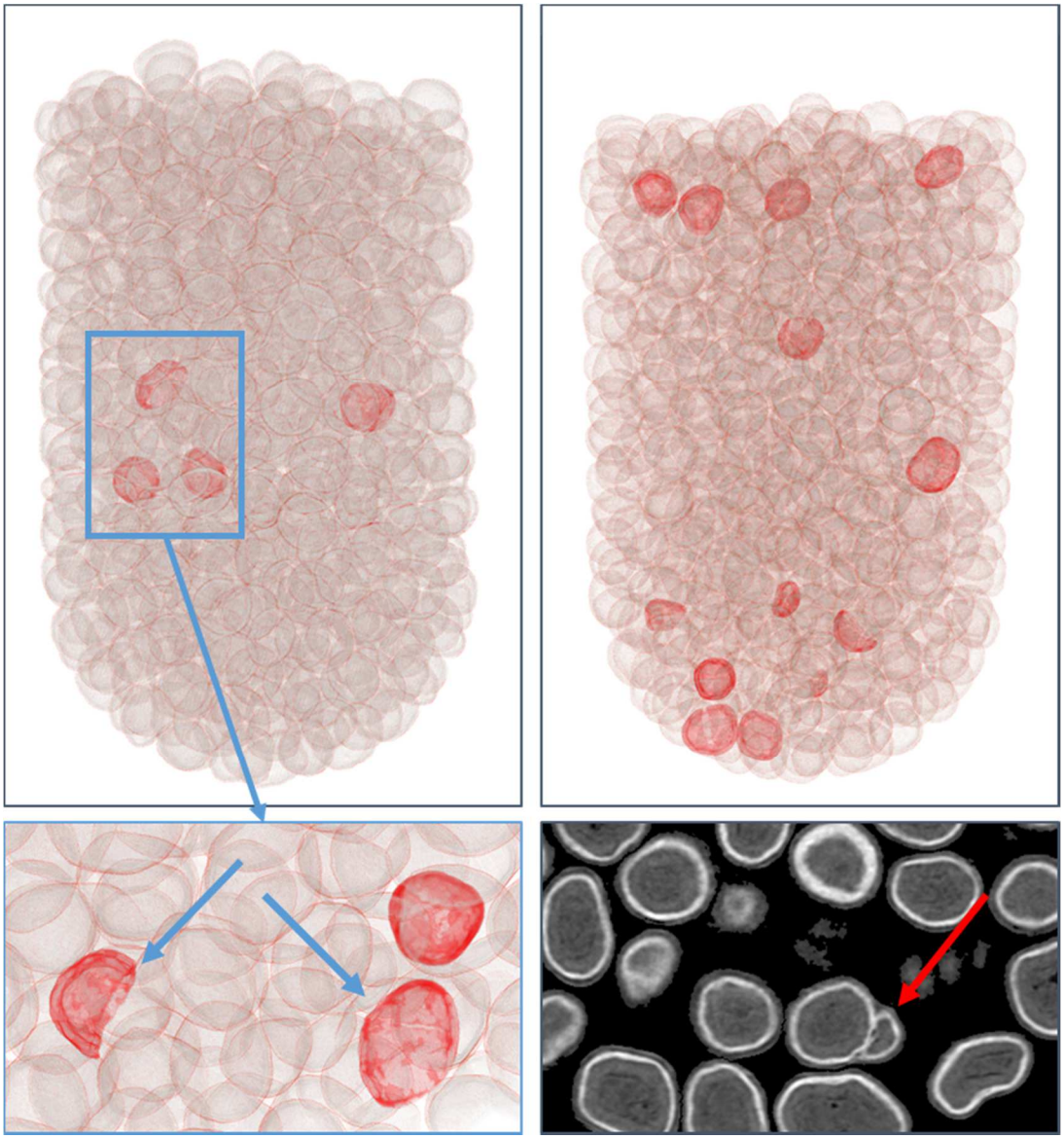

Figure 87: Micro-CT presentation of capsule #04 (top left) and capsule #05 (top right) with the defective pellets marked in red. Rotated detail image of the marked area of capsule #04 (bottom left) and the outlier pellet of capsule #05 (bottom right).

Upon closer investigation, the outlier pellet of capsule #05 can be identified as a large pellet conjoined at the isolation layer with a very small pellet, explaining the observed decrease in sphericity (see Figure 87, bottom right). Development stability tests, for related substances (primarily degradation products) using HPLC-UV, on originator and in-house

batches showed no direct connection between API degradation and the percentage of defective isolation layers. Analysis after storage at 25°C / 60%rH revealed no stability issues after 12 months for in-house or innovator batches. It is possible that the degradation effect of the whole pellet during stability testing has a much stronger influence of the deterioration of the API compared to the defects in the isolation layer found with micro-CT imaging. The amount of damaged pellets can therefore be more seen as a measure of uniformity and process stability (i.e. coating homogeneity).

6.2.5 Combination

In Figure 88, the results of the different imaging techniques are shown for esomeprazole pellets. In the top left, an overview image of pellets incased in epoxy and milled to halved pellets is shown. Aside is an SEM image for a detailed look at a singular pellets structure. On the top right a Raman microscopy image with saccharose (cyan), API (red), talcum (blue), polymethacrylate (yellow) and epoxy (white) shows the chemical composition of the same pellet. On the bottom left a comparative micro-CT image of the same specimen is shown, because of the very similar relative densities of polymethacrylate and epoxy, the GR-layer cannot be resolved. The other two micro-CT images, of complete pellet-filled capsules, show the relative density distribution of isolated pellets as grey scale (middle) and color-coded according the binarization of the core, isolation layer and GR-layer (right). The comparison shows that each imaging technique delivers a unique view of the GRC formulation with the possibility to answer specific analytical questions and only the combination gives an in-depth view of the sample that allows solving of additional more complex questions.

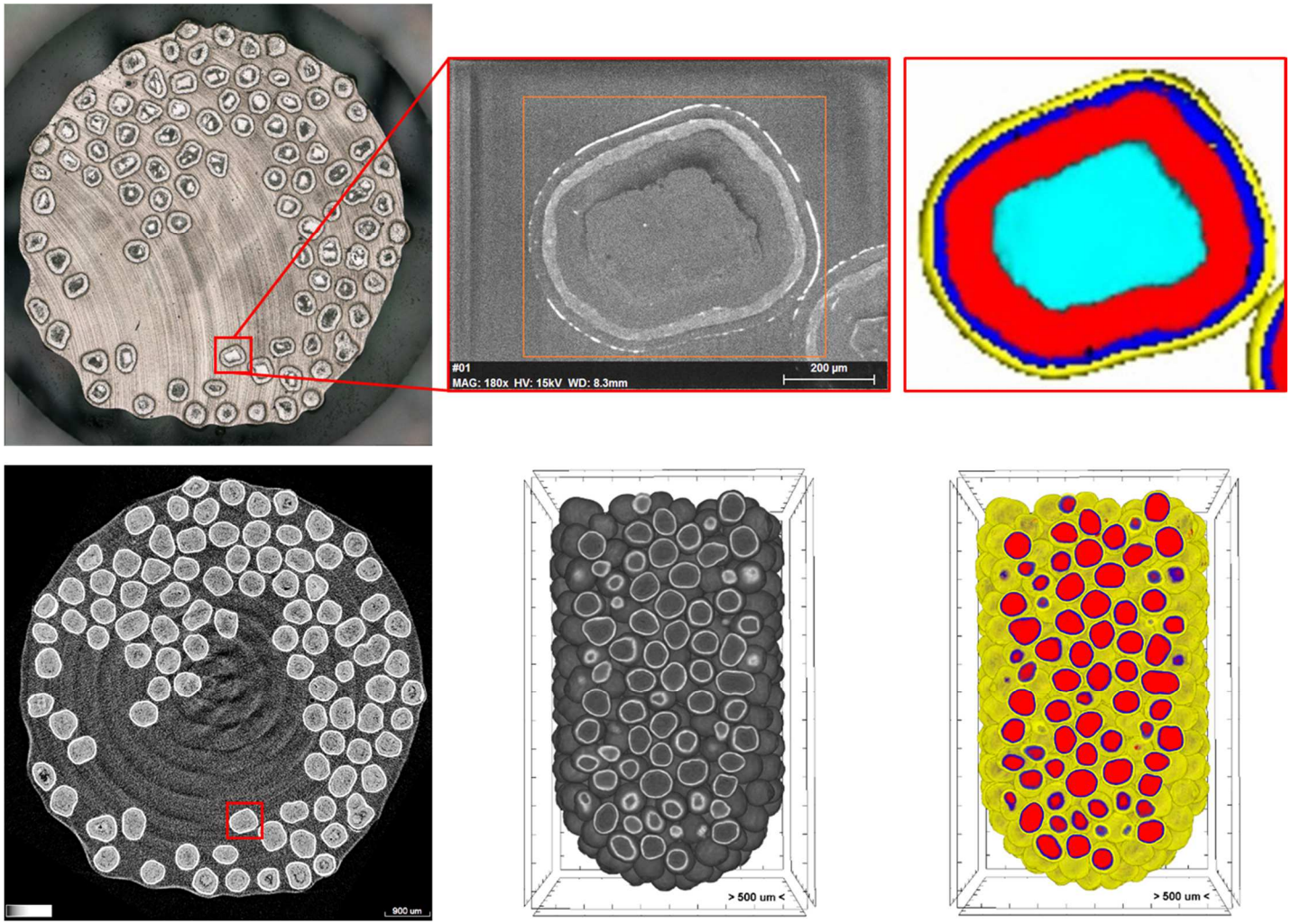

Figure 88: Digitally enhanced light microscopy overview (top left), singular pellet recording with SEM (top, middle) and with Raman microscopy (top right), comparative measurement with micro-CT (bottom left), micro-CT measurement of complete pellet-filled capsule as grey-scale image (bottom, middle) and with layer structure color-coded (bottom, right).

6.3 Bioequivalence study – Batch selection

6.3.1 Introduction

For a bioequivalence (BE) study, a promising in-house and innovator batch needs to be found. With a successful BE study, no further studies are necessary. This lowers the number of study subjects involved, therefore reducing health risks, and leads to an overall reduction in development expenses. Due to the high BE risk of gastro resistant formulations in general, the classification of esomeprazole as a BCS II compound and the lack of pilot BE data, analytical imaging was employed to explain differences in dissolution results and support batch comparison. Three innovator batches and three in-house batches are screened to find the most similar pair of batches. For sake of information gain, an additional in-house test batch Z from earlier in the development cycle (with slightly altered composition) was co-analyzed, to further explain the influence of certain parameters on dissolution result. To minimize the influence of sub-sampling, six capsules of each batch (about 4000 pellets in total) are analyzed and average values used for comparison. To get a well-founded comparison between the three innovator (1, 2, 3) and three in-house batches (A, B, C) initially the chemical identification and localization of the different functional components in 2D is performed using Raman microscopy (see paragraph 6.2.2). After the exclusion of major chemical and/or structural differences, micro-CT imaging is used to gather in-depth 3D information (see paragraph 6.2.4). The following parameters are measured:

- Pellet count per capsules
- Amount of damaged pellets per capsule
- Average particle size of whole pellets
- Average particles size of the core+ region
- Total volume and total surface area of all pellets contained in a capsule
- Isolation layer and GR-layer thickness

The information gathered investigating the innovator could now be used for additional measurements on in-house batches and to perform batch comparisons. The main goal is to give a recommendation, which in-house batch might perform closest to the innovator batch.

6.3.2 Raman comparison

2D Raman mapping of pellets from originator and in-house batches show very similar spatial distribution of the four main components, API, saccharose, talc (isolation layer) and polymethacrylate (GR-layer).

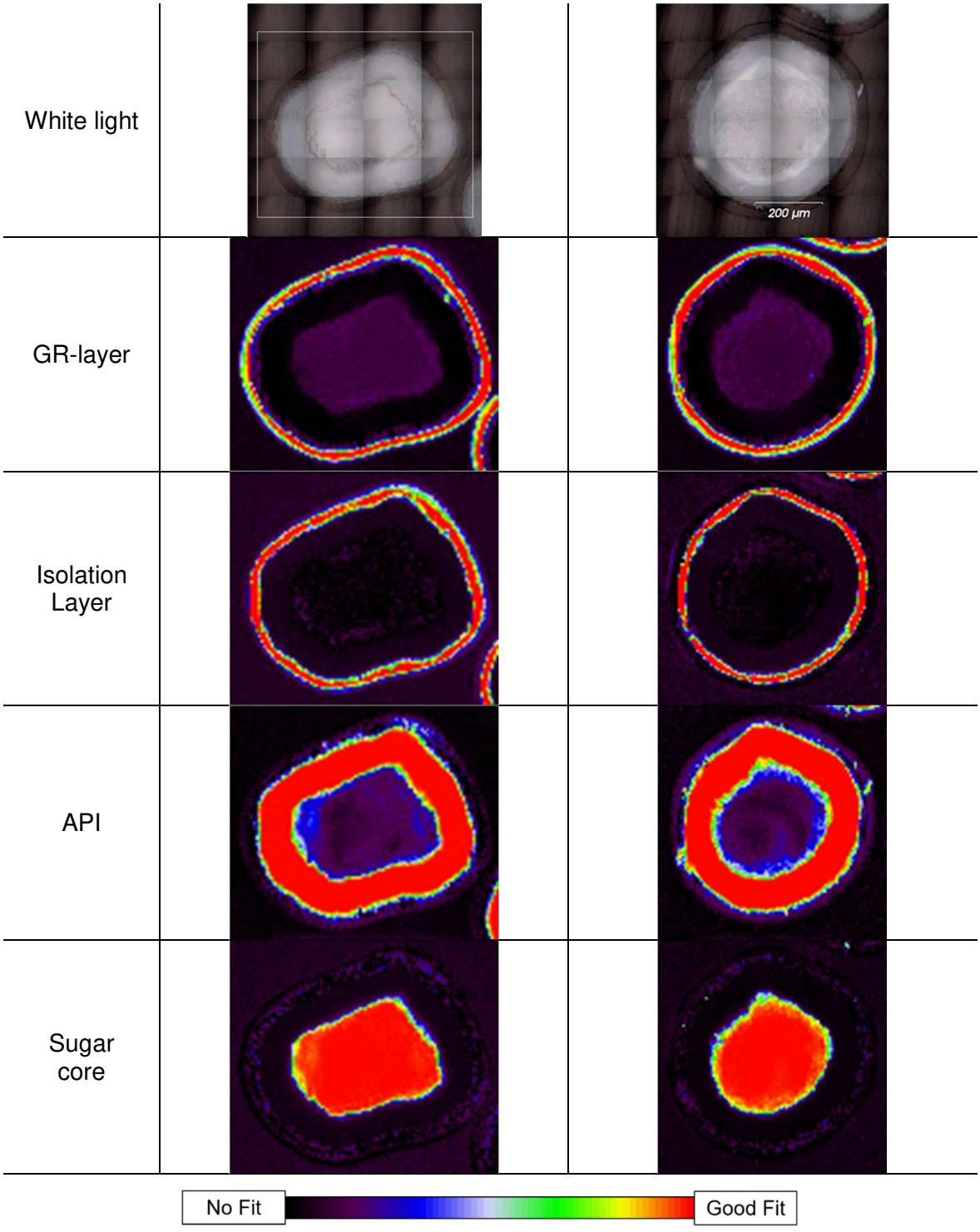

Figure 89: Micrograph and Raman mapping of the four main components of a pellet of the originator batch 2 (left column) and the in-house batch A (right column).

Layer thickness for the API, isolation and gastro-resistant layer look very similar concerning size and shape (see Figure 89). With these findings, in-depth comparison of the pellets was started using micro-CT imaging.

6.3.3 Micro-CT comparison

With micro-CT analysis, several small differences can be observed. When looking at the particles size distribution of the three in-house batches and the three innovator batches each set has one outlier batch but display overall similar monomodal distributions. Batches 3 and C show an increased particle size compared to the other batches (see Figure 90). The test batch Z has a bimodal distribution, which is the result of deficient sugar core starting material. Due to a production malfunction or subsequent incorrect handling, a certain amount of sugar spheres were broken, resulting in a visible peak at smaller particles sizes (~400 µm) and an overall lower average size. When looking at the overview plot at the bottom right corner, it can be seen that the curve progression of batches 1-3 and A-C is comparable with a shift to slightly higher values for the in-house batch.

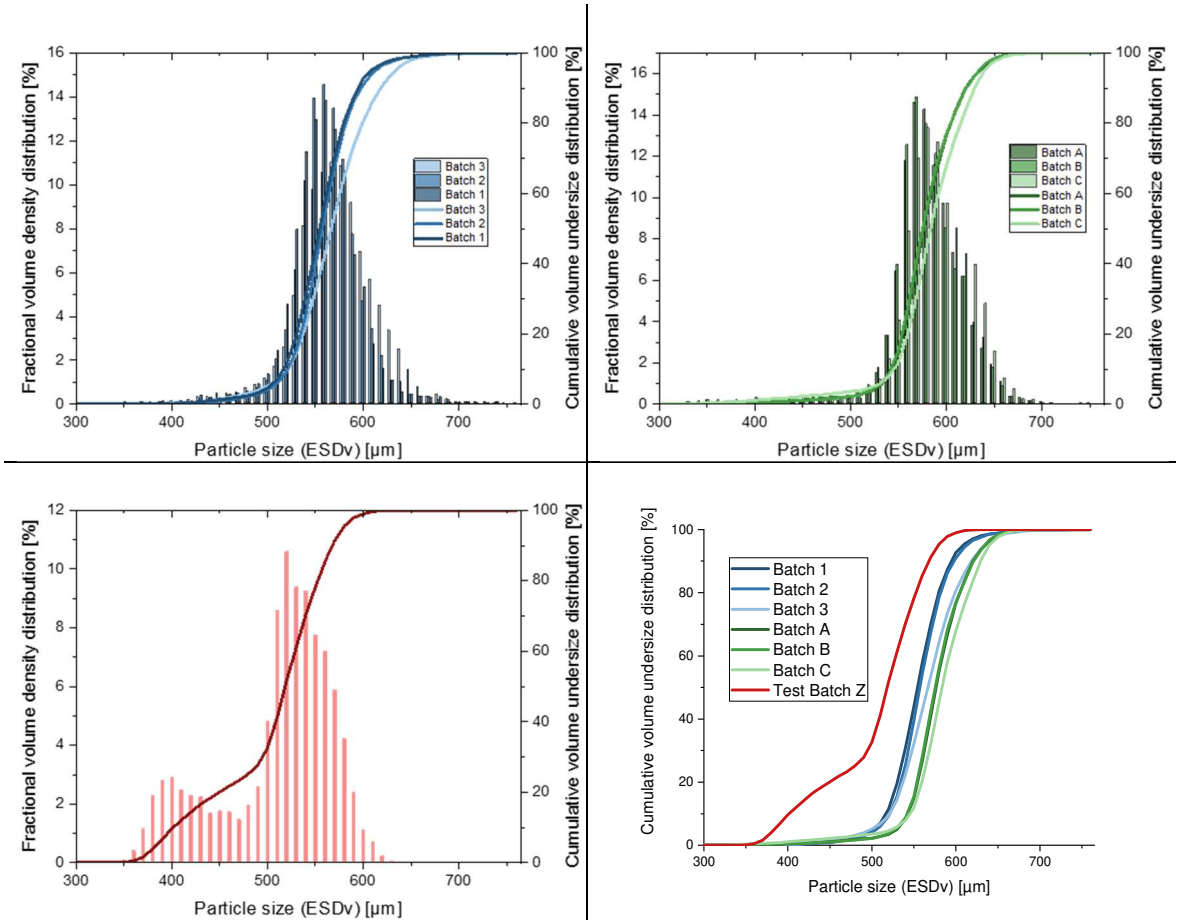

Figure 90: Overview of particle size distribution of three innovator batches (top left), three in-house batches (top right), one test batch Z (bottom left) and a comparison plot (bottom right).

In the following, a discussion based on the parameters shown in Table 12 is carried out. When looking at average and total pellet count, batches A and B are similar, as well as batches 1 and 2. Batches C and 3 show differences to their respective sets. Overall pellet count is slightly increased for the in-house batches. The same is true for the amount of damaged pellets, while the overall counts are in the low single digits. The test batch Z is showing considerably higher values for pellet count and damaged pellets, indicating difficulties early in the development process. The average isolation thickness is very similar between all measured batches. The layer thickness of the GR-layer is about 18% larger in the in-house batch set compared to the innovator batch set, while the intra-set values are very similar. Test batch Z is similar to the innovator. Batches A and B have very similar total surface areas with C being again the outlier with a slightly smaller value. Values for the innovator batches are comparable to each other and about 7% smaller than the in-house batches. The test batch Z has a considerably higher total surface area. Batch Z shows the largest differences to the other samples, this is caused by an erroneous sugar core batch and un-optimized manufacturing procedures earlier in the development cycle, but can still be used for comparative purposes. The in-house specimen have two very similar batches A and B and one slightly differing batch, batch C. Innovator batches 1 and 2 are also very similar while batch 3 shows small differences. Overall, there are small differences between the in-house and innovator samples.

Table 12: Micro-CT data overview for three in-house batches (A-C), the test batch (Z) and three innovator batches (1-3) with average values for n = 6 capsules per batch.

	Sample	Batch A	Batch B	Batch C	Avg.	Batch 1	Batch 2	Batch 3	Avg.	Test Batch
	Whole pellets									
A	Avg. Count (damaged pellets)	704 (18)	703 (13)	670 (22)	693 (18)	687 (12)	678 (12)	649 (13)	671 (12)	997 (87)
B	Total count (damaged pellets)	4226 (105)	4220 (79)	4020 (129)	12466 (313)	4121 (70)	4066 (71)	3892 (77)	12079 (218)	5983 (524)
C	Avg. particle size with SD [µm]	577.43 ± 35.64	576.50 ± 36.43	582.32 ± 43.17	578.75 ± 38.41	554,42 ± 35,67	557,80 ± 34,96	566,60 ± 42,34	559.61 ± 37.65	504.46 ± 59.02
D	Avg. Total volume [µm³]	71.7 x 10^9	71.3 x 10^9	70.3 x 10^9	71.1 x 10^9	62.0 x 10^9	62.3 x 10^9	62.8 x 10^9	62.4 x 10^9	69.8 x 10^9
E	Total surface area [µm²]	832,931,080	831,397,208	815,384,854	826,571,048	771,015,299	765,672,091	766,301,665	767,663,019	925,508,547
	Core									
F	Avg. particle size with SD [µm]	448.07 ± 34. 81	447.01 ± 35. 07	451.83 ± 41. 26	448.97 ± 37.05	440,90 ± 36,28	443,62 ± 34,90	450,64 ± 42,04	444.88 ± 37.64	396.57 ± 60.99
	Isolation Layer									
G	Avg. layer thickness with SD	30.75 ± 2.83	30.75 ± 2.99	31.03 ± 2.87	30.85 ± 2.89	28,37 ± 2,63	28,24 ± 2,53	28,71 ± 2,70	28.44 ± 2.62	27,28 ± 2.16
	Gastro-resistant layer									
H	Avg. layer thickness with SD	41.32 ± 2.41	41.29 ± 2.45	41.49 ± 2.49	41.37 ± 2.45	33,96 ± 3,54	34,24 ± 3,59	34,14 ± 3,64	34.11 ± 3.59	33.65 ± 10.42

Correlation between pellet characteristics

In Figure 91, individual parameters of the six capsules from each of the three innovator batches (see Table 12) are checked for possible relations. When correlations can be established, the amount of needed test parameters (i.e. for study purposes) could be reduced. In **1** the correlation between the particle size of the whole pellets and the particle size of the core section is shown. The linear fit shows a good correlation between the data points with an R^2-value of 0.98568. This means that the particles size of the sugar spheres is the main impact source on the size of the finished pellet. This is on the one hand because the core makes up the largest part of the pellets and on the other hand because of very homogeneous isolation and GR-layer thickness. To see if there is a correlation between the amounts of damaged pellets and the overall pellet count in a capsule the measured values are plotted (see **2**). It can be seen that the amount of damaged pellets is independent of the pellet count. This is indicating that damages are not occurring during capsule filling but before.

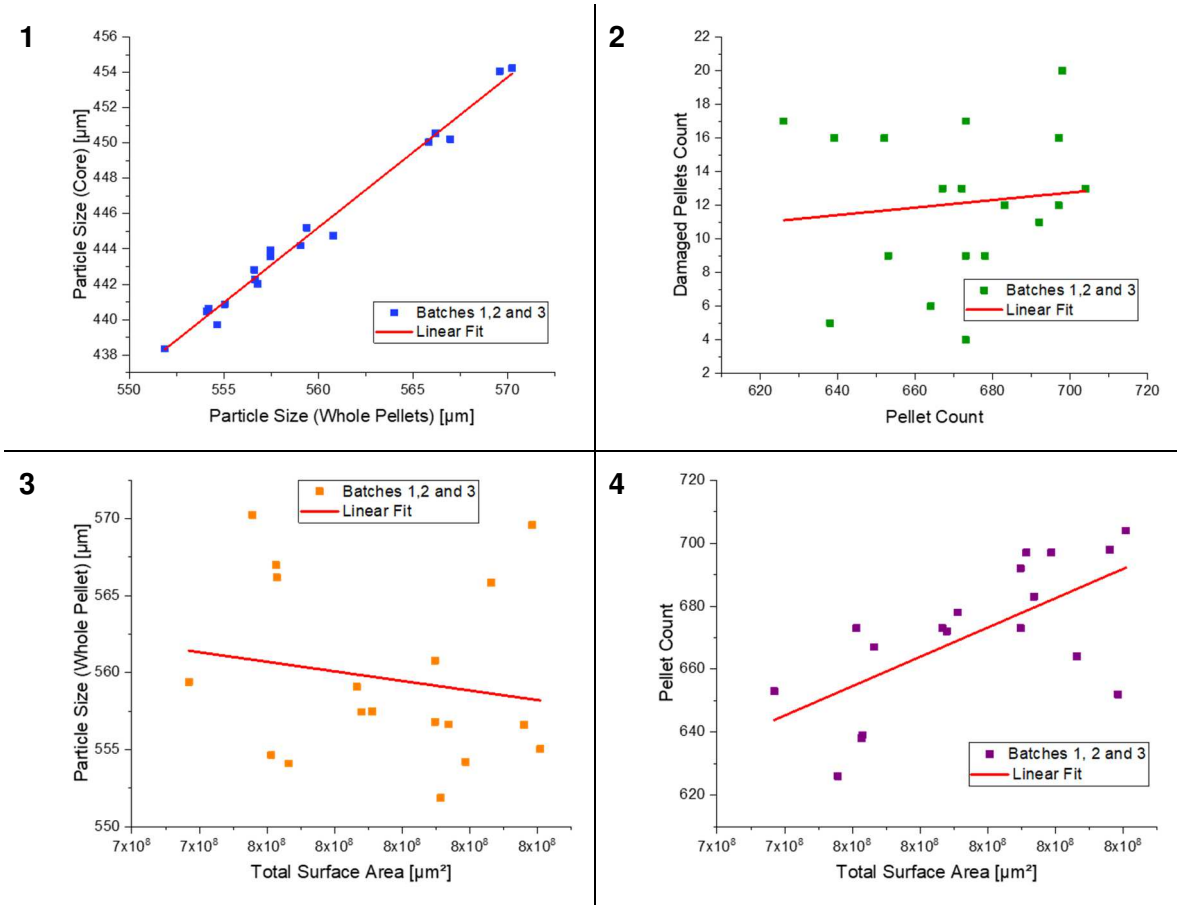

Figure 91: Correlations between pellet characteristics.

An important factor influencing dissolution processes is the surface area of all pellets in a capsule. For this reason, the total surface area of all pellets contained in a capsule are

plotted against the average particle size (**3**) and pellet count (**4**). Because pellets are no perfect spheres and do not possess perfectly smooth surfaces no direct correlations between total surface area, pellet size (R^2 = 0.03051) and pellet count (R^2 = 0.43274) can be found. Therefore, the total surface area has to be evaluated separately when looking at the dissolution rates.

6.3.4 Dissolution results

The dissolution results show noticeable differences between the in-house and innovator batches, which can be correlated with trends found in micro-CT data for individual batches to give possible explanations (see paragraph 6.3.5). To model the dissolution and release behavior of capsules upon oral administration, two different dissolution methods are employed. To ensure bioequivalence independent of the intake of food prior to taking the drug, models for fed and fasten state are implemented. For the fed state, the patient had a meal prior to drug application. This has an influence on the pH in the stomach and is replicated *in vitro* with different pretreatment steps of the FDF. The capsules are first placed in a medium with pH 5 for 30 min, followed by 2 h at pH 3 and 2.5 h at pH 1.7. This simulates pH gradient after meal consumption and the subsequent digestion and emptying of the stomach, leading to pH conditions increasingly dominated by the stomach acid. After the pretreatment steps, the residual content of API in the capsules is measured (see Table 13). Batches produced in-house show overall more retained API. Batch 3 shows the most similar residual assay to the in-house batches. It is noticeable that for in-house as well as for innovator batches, batches identified as being the most different of the sets (see paragraph 6.3.3), retain the most API.

Table 13: Residual assay of fed state model for innovator and in-house batches.

Batch	Batch 1 (Innovator)	Batch 2 (Innovator)	Batch 3 (Innovator)	Batch A (in-house)	Batch B (in-house)	Batch C (in-house)
Residual assay [%]	71	68	**76**	79	77	**83**

For the fasten state, the capsules are pretreated for 1 h in 0.01 M hydrochloric acid with pH 2, to replicate the influence of the stomach acid on the FDF in an empty stomach. Dissolution testing occurs in a gradient between pH 5.6 to pH 6.6 (with 10 min intervals) and carbonate buffer to simulate drug release in the intestines. The dissolution results are presented in Figure 92. Batches manufactured in-house show a lag-time of five to ten

minutes compared to the innovator. The test batch Z shows the fastest release of all samples.

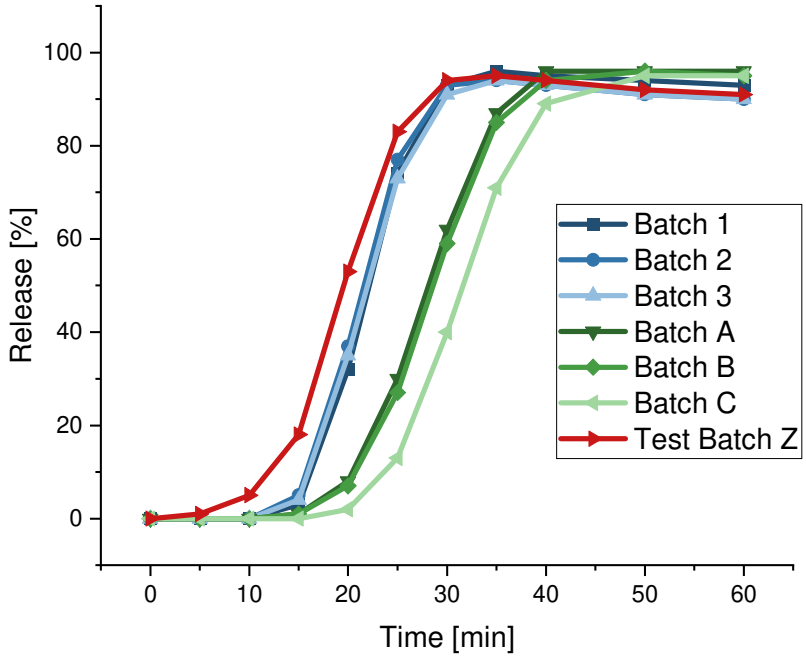

Figure 92: Dissolution profiles of three innovator batches (1-3), three in-house batches (A-C) and test batch Z.

6.3.5 Micro-CT aided explanations

The fact that more API is retained in the in-house batches can be explained by the larger layer thickness of the gastro-resistant layer, providing longer protection from low pH values, compared to the innovator (see row H of Table 12). Batch 3 showing the most similar residual assay results, compared to the in-house batches, cannot be attributed to a larger GR-layer, but this batch has the largest and fewest pellets, known to be slowing factors of dissolution processes, out of the innovator batches.[2] The differences in the dissolution curve behavior can again be explained by the larger gastro-resistant layer of batches A-C, which is most likely more intact after the treatment with hydrochloric acid and thusly delays the release. The fast release of test batch Z, which has very similar GR-layer thickness compared to the innovator batches, can be explained with higher total surface area and pellet count, speeding up the dissolution process. In contrast to the prior micro-CT findings, all three innovator batches perform nearly identical. In-house batch C, with the most pronounced lag time has the smallest total surface area of the in-house batches and the fewest pellets, which can explain the dissolution performance (for more details on the influence of particle size and surface area see paragraph 5.5.6) Two main factors governing the dissolution behavior can be established. The larger GR-layer thickness of the in-house

batches has a slowing impact on the disintegration of pellets in acidic mediums and the total surface area and/or pellet count has an influence on the dissolution rate. Analytical imaging analysis and dissolution testing show that innovator batch 3 is the most similar to the in-house batches; from which batch A and B are nearly identical and either one is a good fit for comparison.

6.4 Transferability of a method – Esomeprazole multiple unit tablet

Besides the pellet-filled capsule formulation, esomeprazole is also available as multiple unit tablets (MUTs). To see if the methods developed for the GRC formulation are transferrable, in-house manufactured MUTs are analyzed. The main differences between these MUTs and the previously discussed capsule samples is, that the multilayered pellets are not loosely contained in a capsule, but embedded in excipients and compressed into a tablet and then film-coated. This can be seen in the first two microscope images (1 and 2) in Figure 93. Chemical mapping of the different pellet layers with Raman mapping (3) and SEM/EDX (4 and 7) was performed as described in paragraph 6.2.2 and 6.2.3 respectively except no epoxy raisin for fixating the pellets is needed due to the embedding in to tablet. Due to a slightly different formulation, the isolation layer (blue) is composed of talc mixed with titanium dioxide. Additionally the tablet filler substance can be identified with Raman as MCC and the strongest Raman active substance in the tablet coating is titanium dioxide, which is further confirmed with EDX mapping (7).

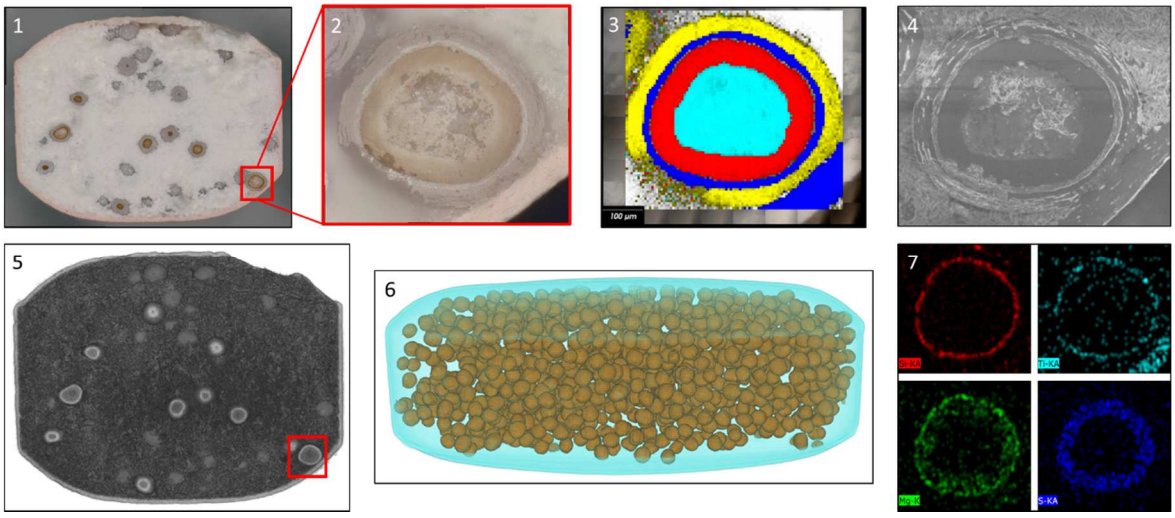

Figure 93: Overview of the different imaging techniques used on esomeprazole MUTs: Digitally enhanced light microscopy (1-2), Raman microscopy (3), SEM (4), Micro-CT (5-6), EDX (7)

For micro-CT analysis (5 and 6), two different measurement setups are necessary. For the detection of pellets with damaged isolation layer, the pellet count per tablet, pellet distribution within the tablet and analysis of the film coating measurements of the entire MUT-tablet can be used. This measurement is performed with a pixel size of 5.5 µm. Because the GR-layer and the tablet excipient show overlapping regions of relative density an isolation of complete, individual pellets is not possible. Both materials are organic substances with a low relative density in orange (see Figure 94). As mentioned in paragraph 3.1, to improve the resolution and pixel size of a micro-CT measurement the sample has to be moved closer to the detector, this leads to a smaller measurement area. In this case, this leads to the restriction that only a section of the tablet can be measured (pixel size: 2.0 µm). Because of the different measurement parameters, the absolute relative density values are different for measurement of whole tablets and sections of tablets, resulting in slightly different color distributions (see Figure 94, Figure 95 and Figure 96).

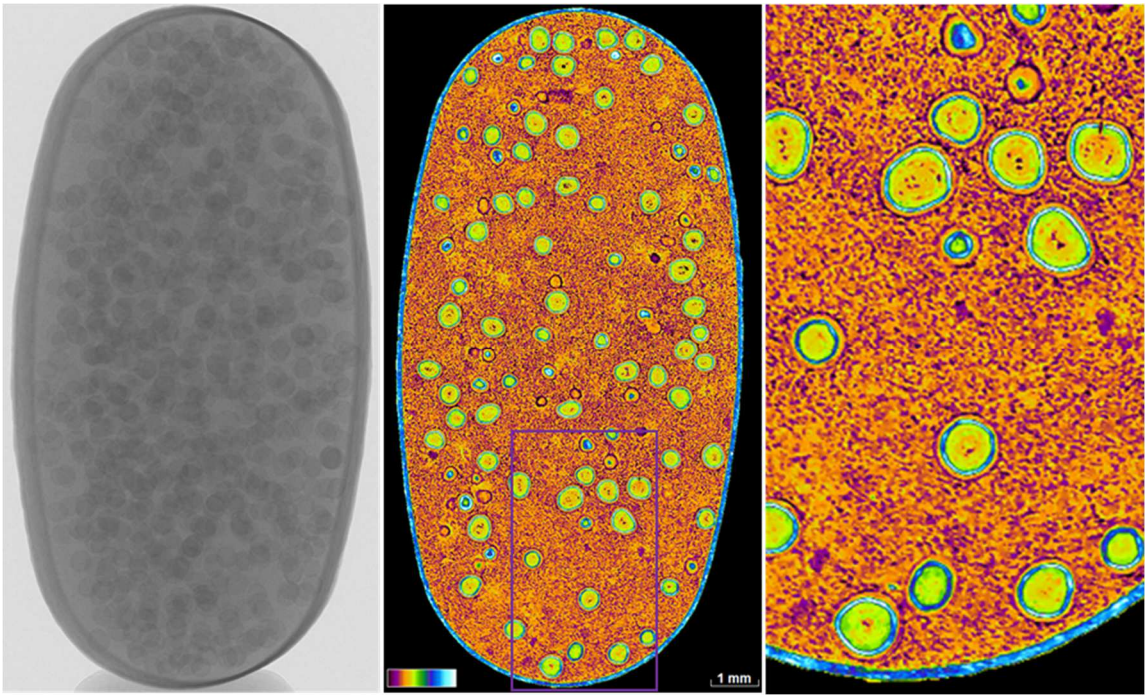

Figure 94: Micro-CT shadow projection, reconstructed image and zoomed-in image of entire tablets.

With this method, it can be seen that the pellets are nearly completely surrounded by a thin layer of air (black) and are only connected sparsely to the tablet filler (green, orange, purple). This is most likely the result of the compaction of the tablet and resulting deformation of MCC around the more rigid pellets.

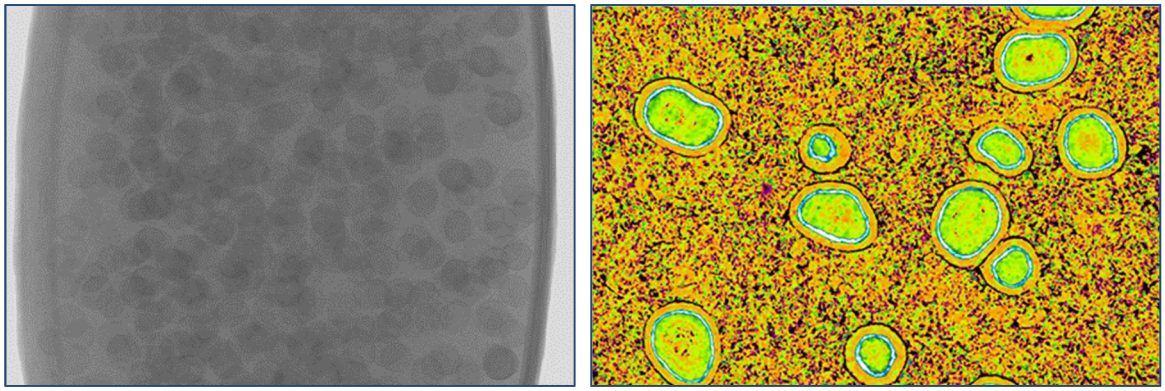

Figure 95: Micro-CT shadow projection and zoomed-in reconstructed images of a tablet section.

Experience gained during the development of the task lists (TL_ESO/GRC_02) for the isolation and analysis of the individual layers of the pellets could partly be used for the MUTs. Due to the different surrounding medium of the pellets, however, some adjustments have to be made for MUTs and custom developed analysis task lists (TL_ESO/MUT_01, TL_ESO/MUT_02 and TL_ESO/MUT_03) are implemented. There are several similarities between the GRC and MUT formulation. The pellet structure is the same, displaying the composition of sugar core, API-layer, isolation layer and GR-layer (see Figure 96). As with the GRC project, due to very similar relative density values for sugar core and API a separation is not possible and both layers together will be referred to as “core+”.

1

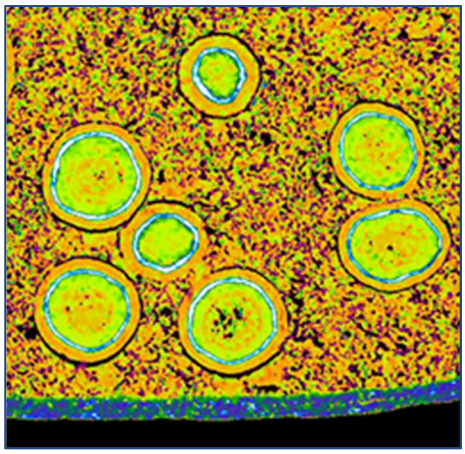

2

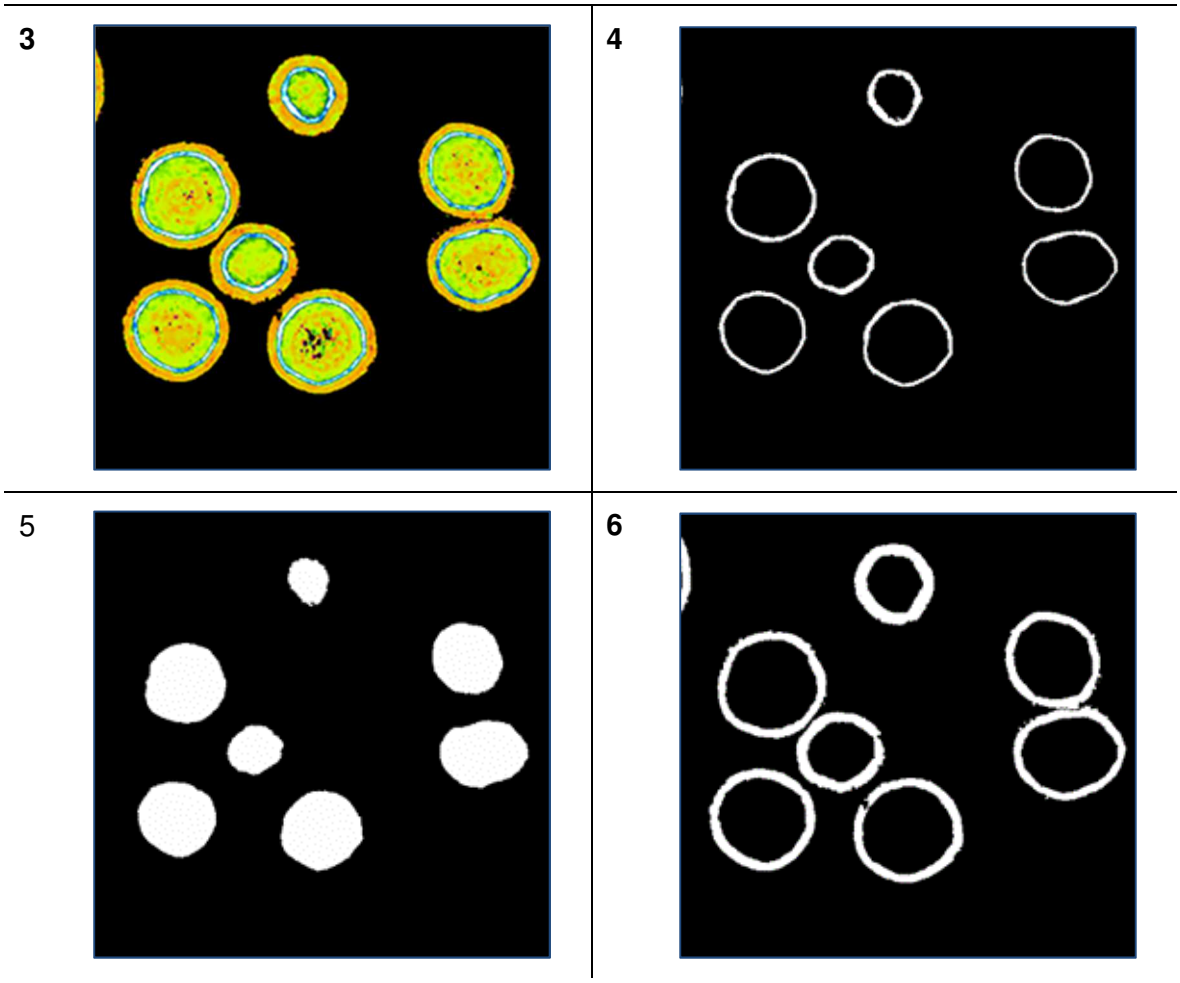

Figure 96: Stepwise isolation of the tablets' film coating (2), pellet core+ (3), whole pellets (4), isolation layer (5) and GR-layer (6).

Of additional interest with MUTs is the homogeneity of the outer film coating of the tablet, which is easily isolated due to the high relative density compared to the tablet filler (**2**). Isolation of the whole pellets is done by manual thresholding of the isolation layer, digitally filling, and gradually increasing the size of the pellets with final containment by the surrounding layer of air (**3**). As mentioned before the isolation layer can be obtained directly by manual thresholding (**4**). Isolation of the core+ region is achieved by digitally filling the isolation layer and its subsequent subtraction (**5**). By subtracting the core and isolation layer from the whole pellets the GR-layer is obtained (**6**).

With the isolation of the individual pellet components, statistical data can be gathered comparable to the GRC project. With MUTs, the breaking or damaging of pellets during the tableting process is of higher concern and micro-CT analysis can be used to quantify pellet damage. The same method explained in paragraph 6.2.4.1 for the detection of damaged pellets can be implemented for MUTs (see Figure 97). On average 48 of 967 pellets showed defects in the form of small cuts and cracks, very few pellets were found to be broken in

half or show similar damages (one or two per tablet). This leads to the conclusion that the chosen compaction pressure is a minor risk factor.

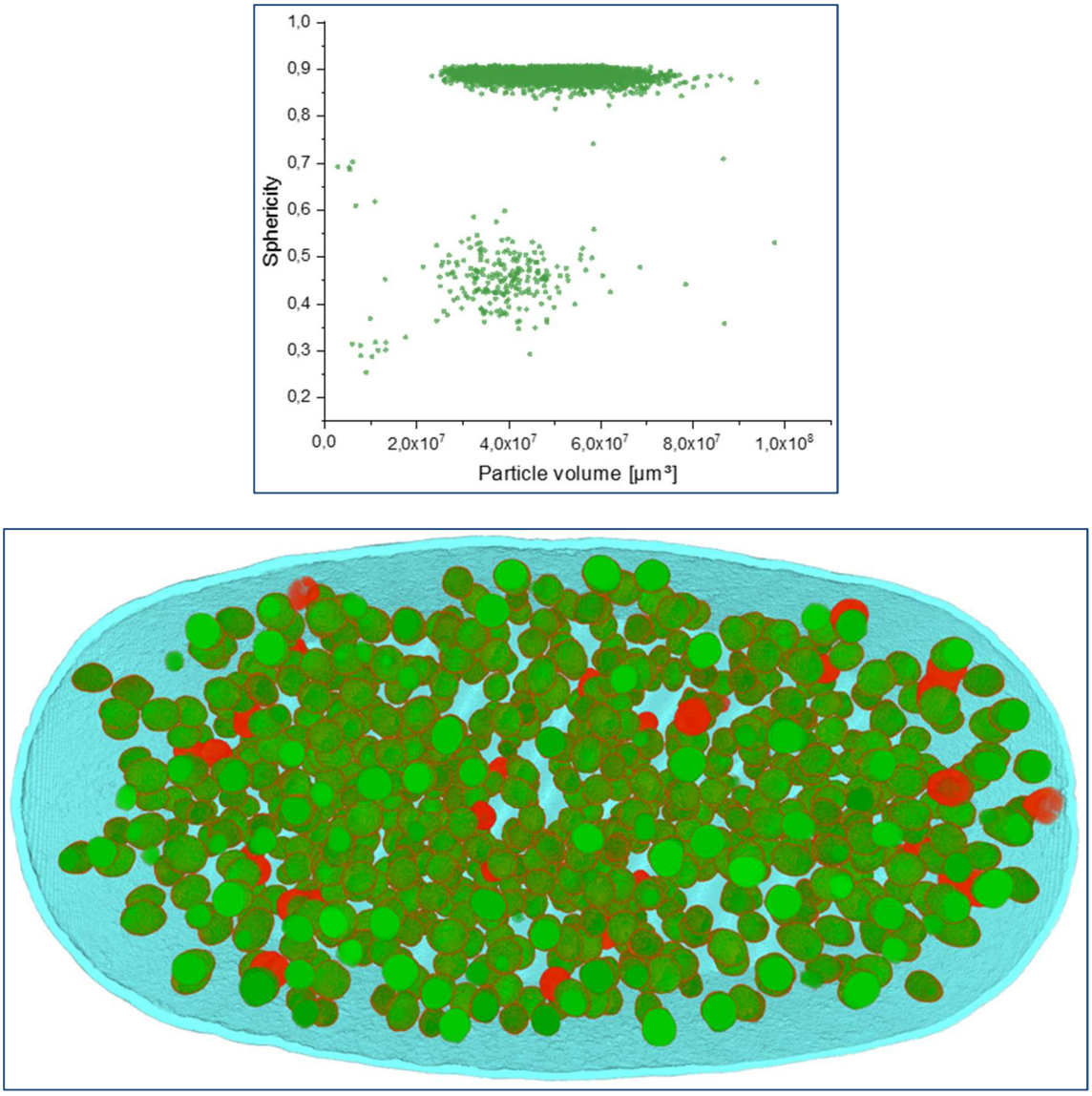

Figure 97: Damaged pellets plot for five measured MUTs (top) and digital cut through a MUT with damaged pellets (red), intact pellets (green) and tablet film coating (cyan).

In Table 14, a small overview of the analysis data gathered with micro-CT is shown. Compared to the GRC formulation of the average of the three in-house (see Table 12), the MUTs contain noticeable more pellets, with smaller pellet size, resulting smaller average total pellet surface area, comparable GR-layer thickness and smaller isolation layers.

Table 14: Micro-CT data overview for five measured MUTs and the average of the three-house GRC batches.

Analysis parameter	Samples (n = 5)	GRC (Avg. of Batches 1-3)
Pellet count (damaged Pellets) for the whole MUT	967 (48)	693 (18)
Avg. pellet size (ESDv) [µm]	506.28 ± 67.05	578.75 ± 38.41
Avg. total pellet surface [µm²]	467,793,007	826,571,048
Avg. pellet core size (ESDv) [µm] with SD	391.8 ± 50.3	448.97 ± 37.05
Avg. layer thickness of isolation layer [µm] with SD	20.8 ± 2.48	30.85 ± 2.89
Avg. layer thickness of GR-layer [µm] with SD	42.6 ± 3.24	41.37 ± 2.45

The analysis of esomeprazole MUTs showed that experience gathered from similar projects could be transferred. By small adjustments on a few measurement and analysis parameters to cater to the different manufacturing processes, it was possible to obtain in-depth information of pellets embedded in tablets without prior sample preparation.

6.5 Conclusion

Pellet-filled capsule formulations offer several advantages such as a reduction of physiological fluctuations of the API concentration in the patient and the possibility for spatial separation of components. This leads to relative complex compositions, requiring more intricate manufacturing processes. In the example at hand, the API is an acid-labile compound, which has to be released in the small intestines. To provide protection from the acidic medium in the stomach, the pellets are coated with a gastro-resistant layer (GR-layer). In this case, the GR-layer is comprised of a polymer, which is due to the presence of carboxylic acids groups insoluble in water at low pH conditions. Because this layers' acidic-groups, it has to be physically separated from the API using an intermediate layer. For the official approval of a new generic product, its bioequivalence compared to the innovator has to be demonstrated. For this reason, suitable in-house and innovator batches need to be evaluated. Because no prior pilot BE-study was performed, no reliable IVIVC results are available and new analytical imaging techniques were employed to expand on the findings of dissolution testing.

Raman microscopy and SEM-EDX were used successfully to identify the main components' spatial distribution and verify comparability between in-house and innovator batches. The linking of these findings with micro-CT enables an in-depth analysis of samples in 3D. With the development of a custom made measurement procedure and micro-CT analysis task

lists it became possible to analyze all pellets contained in a capsule without the need of invasive sample preparation. As a result, a large number of different morphological parameters was made available, such as the number of pellets per capsule, pellet surface area and volume, the dimensions of the individual pellet layers and the amount of pellets with specific damages. With this large number of different measured data, the manufacturing process and the homogeneity of the in-house produced batches can be monitored. Furthermore, after measuring the innovator batches differences found in *in vitro* testing can be explained. A larger GR-layer is measured for in-house batches, which leads to the retention of more API after pretreatment in an acidic medium and delayed dissolution rates compared to the innovator product. Overall, dissolution methods and analytical imaging showed the same trends for outlier batches found in the in-house and innovator batches. This results in the same recommendation for the batch selection process, from the dissolution method interpretation and imaging analysis.

To show the transferability and adaptability of the imaging techniques, an esomeprazole pellet formulation, where the pellets are incased in a tablet – a so-called multiple unit tablet (MUT) – was analyzed. Raman microscopy and SEM/EDX could be used as before, showing the spatial distribution of the components. For micro-CT imaging, a twofold approach had to be used. Measurement of the entire tablet had to be carried out at lower resolutions (pixel size: 5.5 µm), because of the size restriction inherent to the instrument. This led to a non-optimal image quality, which permitted the complete separation of individual pellet layers, due to poor contrast between the GR-layer and the surrounding excipients. To obtain the same in-depth information about the pellet composition as achieved for the GRC samples, a second measurement of only tablet sections with higher resolution (pixel size: 2.0 µm) was performed, resulting in a sufficient contrast and the isolability of full pellets. Thus, a unique look into MUTs was made possible without the need of destructive sample preparation. This revealed prior unobtainable information. With this new method, the influence of the tableting pressure on the breaking of individual pellets can be investigated without potentially sample altering preparation steps. Furthermore, it is possible to reveal each pellets location, within the tablet, in 3D to verify homogeneous distribution. The isolation of the individual pellet components is analogous to the GRC formulation, making the detection of manufacturing errors possible. The most surprising new information was the presence of a thin layer of air surrounding each pellet, a fact prior unknown.

With the new methods developed for GRCs as well as MUTs, the product development process can be improved. First, the link between Raman microscopy/SEM EDX (chemical

information in 2D) and micro-CT (relative density information in 3D) has to be established. With the identification of important sample components, specimens measured with micro-CT can be transferred to dissolution testing, enabling a direct correlation between measured features of the sample and its dissolution behavior. This reduces the amount of dissolution testing necessary to get significant results and thus speeds up the process while also lowering the costs.

6.5.1 References

[1] K.H. Bauer, K.-H. Frömming, C. Führer, *Lehrbuch der pharmazeutischen Technologie*, Wissenschaftliche Verlagsgesellschaft, Stuttgart, **2002**.

[2] A.R. Rajabi-Siahboomi, *Multiparticulate Drug Delivery*, Springer, New York, NY, **2017**.

[3] D. Werner, *Pharm. Technol. Eur.*, **2006**, 35-41.

[4] R. Jones, T. Patrikios, *Int. J. Clin. Pract.*, **2008**, 1844-1850.

[5] H.-B. Yang, B.-S. Sheu, S.-T. Wang, *Am. J. Gastroenterol.*, **2009**, 1642-1649.

[6] https://www.accessdata.fda.gov/drugsatfda_docs/label/2014/021153s049,021957s016

,022101s013lbl.pdf, (accessed 13.11.2020).

[7] C. Scarpignato, R.H. Hunt, *Gastroenterol. Clin. N. Am.*, **2010**, 433-464.

[8] J.R. Horn, C.W. Howden, *Aliment. Pharmacol. Ther.*, **2005**, 20-24.

[9] P. Barmpalexis, A. Grypioti, *Drug. Dev. Ind. Pharm.*, **2018**, 942-952.

[10] G. Kutz, A. Wolff, *Pharmazeutische Produktue und Verfahren*, Wiley-VCH, Weinheim, **2007**.

[11] M.E. Aulton, K.M.G. Taylor, Aulton's Pharmaceutics: The design and manufacture of medicines, Elsevier, 2018.

[12] H. Wardell, *J. Geol.*, **1933**, 310-331.

7 Pyrotechnical strobe formulations

7.1 Introduction

Strobes are pyrotechnical formulations that oscillate between phases of darkness and light emission. The common fields of application are mainly fireworks but also military use as tracers.[1,2] Although the first mentions of strobes emerge at the end of the 19th century, the first theoretical advances did not start until the 1970s by *Krone* and *Wasmann*.[3-6] *Krone* developed his explanatory approach based on a mixture of magnalium as fuel and ammonium perchlorate (AP) as oxidizer. He observed a condition of the reaction mixture, which he called "semi-slag", where a foam composed of solid and partly molten components, containing only trace of magnesium, is formed before a flash. The main concept is that of two competing chemical reactions, the slow oxidation of magnesium – so called "dark" phase – and the fast oxidation of aluminum, in the presence of active gases in the "semi-slag", resulting in the flash.[3,4] In *Wasmann*'s approach, physical parameters play a central role. In the research, formulations containing copolymers of unsaturated monomers with nitrate groups and metal perchlorates as oxidizers were used. During the strobe process, structures comparable to *Krone*'s "semi-slag" were observed. In these formations, heat is accumulated until the ignition point, resulting in the visible flash. In *Wasmann*'s hypothesis, the strobe behavior is due to the low heat conductivity of the involved materials. The delaying factor is the slow transfer of heat from the exterior to the interior of the mixture, which leads to a decrease in reaction speed.[5,6]

Several years later *Shimizu* formulated another theory to explain strobe behavior.[7,8] The main focus point is the presence of two pairs of oxidizer and fuel, resulting in two different reactions, one dark reaction and one flash reaction. The driving factor for the flash reaction is temperature. The ignition of a strobe formulation on the surface triggers a reaction in the dark zone, which has a low activation energy and low heat output. This leads to the formation of hotspots on the surface that increase in size with rising temperature. When the temperature of the dark zones reaches the ignition point, the flash reaction takes place. The cycle continues with small areas of the dark zone that did not reach the ignition temperature. [7,8]

A more recent theory comes from *Davie*s, building on a previous thermokinetic model for cool flames, developed by Sal'nikov.[9,10] Based on the binary system of magnesium and

AP, this model uses chemical and physical parameters to explain the strobe effect. In a first, slow reaction (dark reaction) solid and liquid magnesium react to form intermediate species (gaseous magnesium), which subsequently react in a fast exothermic reaction (flash reaction). There are two variables (the temperature of the mixture and the concentration of the intermediate species) as well as four parameters (ambient temperature, initial concentration of reactants, ratio of activation energies and heat transfer coefficient) involved in this approach. A flash reaction can only occur when the amount of heat and concentration of the intermediate species, generated in the first reaction, are sufficient. This concept underlines the inseparability of the dark and flash reactions.[9]

All the theories mentioned above can be used to explain the strobing behavior of a specific mixture, but are incapable of predicting new strobe formulations.

7.2 Motivation

As seen in the introduction, the standard substance used as oxidizer in strobe formulations is AP. Due to the comparable size of the perchlorate, it can impede the uptake of iodine in the thyroid gland, making the discovery of alternatives desirable.[11] Another drawback is the formation of toxic halogenated degradation products.[12,13] Ceric ammonium nitrate (CAN) with the formula $(NH_4)_2Ce(NO_3)_6$ and an oxygen balance of +35.02 % with respect to formation of CO_2 and CeO_2, belongs to the class of oxidizing agents.[14] Due to its application as catalyst in organic synthesis [15], it is relatively inexpensive (~2 €/gram) [16], making it a fitting candidate for the use as oxidizer in strobe-formulations.

Its main drawback is its high hygroscopicity, as measured with differential thermal analysis (DTA) and thermogravimetric analysis (TGA) (see Figure 98). This is a known factor concerning long-term storability and the reliability of energetic materials.[17]

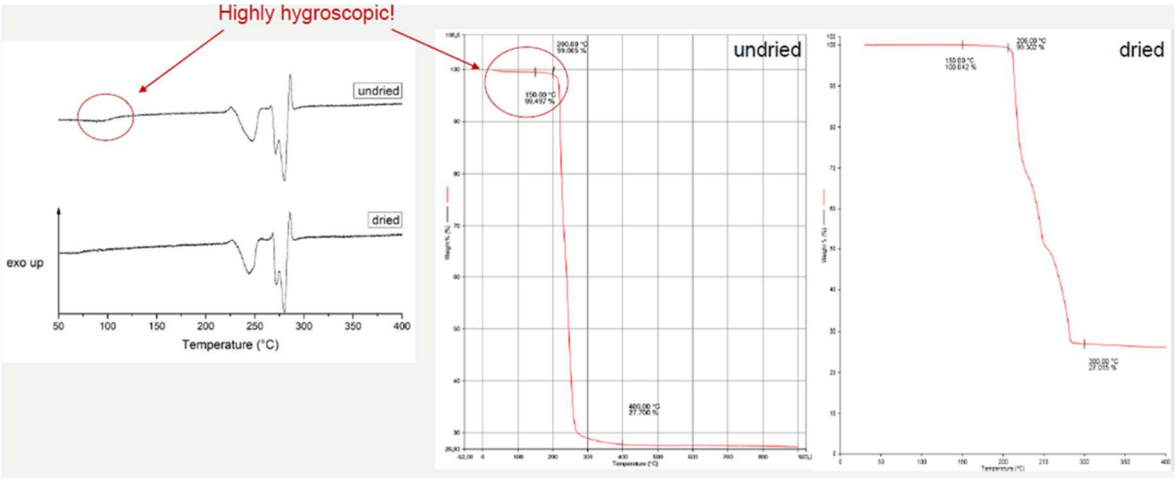

Figure 98: DTA (left) and TGA (middle and right) measurements of the CAN raw material before and after drying.

To solve this problem, small amounts of stearic acid are added to CAN raw material to improve stability upon storage under standard conditions. Here, a balance has to be found between the improvement of stability and the negative influence of SA (reducing agent) on the oxygen balance. A mixture with the ration of 15:1 (CAN:SA) showed the best performance. This project is the first trial to characterize pyrotechnics using advanced imaging techniques. Of big interest is the mechanism with which the addition of stearic acid is reducing the hygroscopicity of CAN. Furthermore, it should be shown which in-depth information about the mixtures could be extracted when employing new analysis techniques. This could be of subsequent use to specifically change manufacturing processes and raw material treatment to enhance the performance of the final product.

This project is a collaboration with Alicia Dufter-Münster of the AK Klapötke at Ludwig-Maximilian University of Munich. Manufacturing of the mixtures, DTA, TGA as well as strobe specific measurements were kindly provided by A. Dufter-Münster.

7.3 Characterization of the mixture

Preparation of the mixture

To prepare the mixtures, SA is dissolved under constant stirring, at room temperature in ethyl acetate. The addition of the insoluble CAN leads to a suspension. The removal of solvent at rotation speeds of 210 rpm yields a powder mixture of white, yellow and orange particles.

7.3.1 Thermal analysis and sensitivity testing

In Table 15, the oxygen balance (Ω_{CO2}), decomposition temperature (T_{dec}), friction sensitivity (FS), impact sensitivity (IS) and electrostatic discharge sensitivity (ESD) of the raw materials and 15:1 mixture are shown. The raw materials do not show any sensitivities to the three tested ignition sources. The mixture on the other hand, shows sensitivities to IS and ESD, which is to be expected when bringing an oxidizer in contact with a fuel. Lastly, the mixtures' decomposition temperature is lowered. The stoichiometry of CAN/SA (15:1) was chosen to receive the desired positive oxygen balance.

Table 15: Sensitivity parameters and oxygen balance of CAN, SA and mixture.

	CAN	SA	CAN/SA (15:1)
Ω_{CO2} [%]	35.02[a]	-292.46	14.55[a]
T_{dec} (onset) [°C]	283	> 400	200
FS [N]	/	/	> 360
IS [J]	/	/	20
ESD [J]	/	/	0.750

[a] Oxygen balance with respect to formation of CeO2.

DTA is used to test the stability of the mixture when exposed to air (see Figure 99). The DTA profile of the mixture is vastly different compared to the raw materials. The exothermic peak at about 200 °C indicates the decomposition point of the mixture (left side). On the right side of Figure 99, it can be seen that the main peak at about 200 °C remains the same over the span of two weeks and no changes at 100 °C (evidence for water) can be found, indicating no degradation or hygroscopicity.

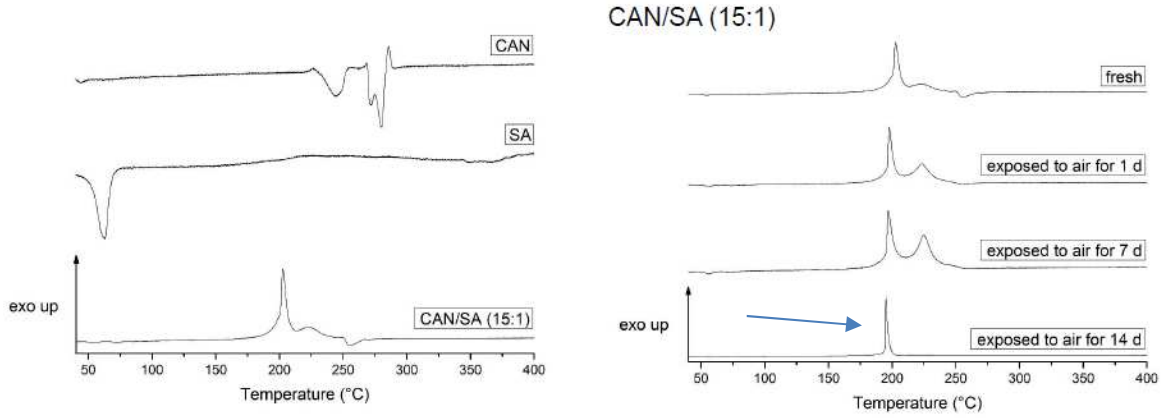

Figure 99: DTA measurements of raw materials, the mixture (15:1) (left) and the mixture after storage (right).

7.3.2 Strobe performance

To investigate the capability of the manipulated material to serve as oxidizer in a pyrotechnic strobe formulation, tests against a standard formulation (control) are performed.[18] Two formulations with different ratios of CAN/SA (15:1) and magnalium (Mg-Al) are used for comparison. CS90M10 is composed of 90 wt% CAN/SA (15:1) with 10 wt% Mg-Al and CS85M15 of 85 wt% CAN/SA (15:1) with 15 wt% Mg-Al.

The standard formulation contains halogen in the oxidizer as well as chromium (very toxic) [19,20] in a substance (K2Cr2O7), which is used to improve the strobing effect of the mixture (see Table 16).[21]

Table 16: Composition of a standard strobe formulation and two formulations based on CAN/SA mixture.

	Control	CS90M10	CS85M15
AP [wt%]	60	/	/
CAN/SA (15:1) [wt%]	/	90	85
Mg-Al [wt%][a]	25	10	15
$BaSO_4$ [wt%]	15	/	/
$K_2Cr_2O_7$ [wt%]	5	/	/
NC [wt%][b]	26.25	/	/

[a] Magnalium with a mesh size -140 (grain size < 106 µm). [b] 10 wt% nitrocellulose in acetone

In Table 17, the measured parameters for the control formulation, CS90M10 and CS85M15 are shown. New pyrotechnical formulations should have better or equal performance as well as lower or equal sensitivity properties, to be considered viable alternatives.[22]

Table 17: Parameter comparison between the standard strobe formulation and two mixtures based on CAN/SA.

	Control	CS90M10	CS85M15
Ω_{CO2} [%][a]		5.36	0.76
T_{dec} (onset) [°C]	320	174	175
***FS* [N]**	64	> 360	216
***IS* [J]**	2	10	5
***ESD* [J]**	0.677	0.750	0.750
λ_d [nm]	567-590	586-575	573-587
***f* [1/s]**	9	4	5

[a] Oxygen balance with respect to formation of CeO_2

It can be seen that the sensitivity values improve for both new mixtures. The decomposition temperatures of the formulations containing CAN/SA are considerably lower, but should be still sufficiently high for safe storage. The strobe frequency of the control is about twice as high, but within the desired range of 1-10 flashes per seconds.[23]

The CS90M10 mixture provides space in the oxygen balance for reducing color imparters substance such as B4C or amorphous boron for the use in green pyrotechnics. For blue strobes copper(II) oxide or copper(II) carbonate hydroxide might be a suitable candidates. Until now only yellow and red are available as chlorine-free strobes.[24,25] CAN-SA mixtures are promising pyrotechnic matrices for the development of differently colored, halogen-free strobe formulations.

7.3.3 Microscopy

In Figure 100, micrographs of the raw materials of stearic acid and CAN are shown. Stearic acid is colorless with shard-like particles. CAN is a yellow to orange substance with spherical particles and rough surface.

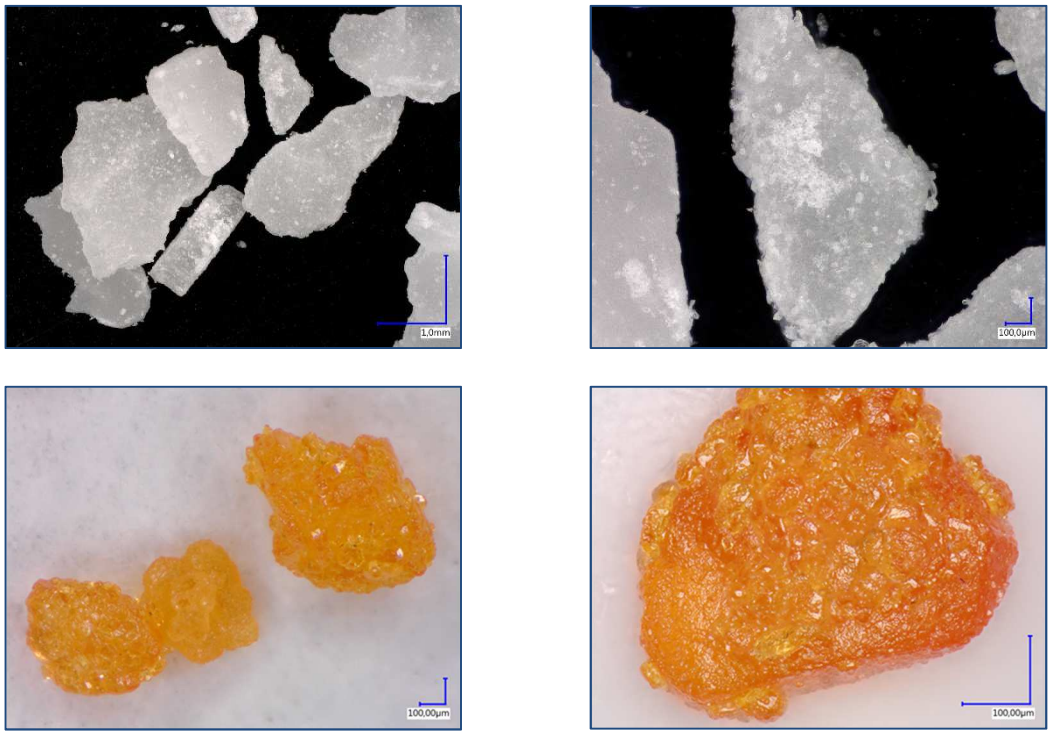

Figure 100: Micrographs of the stearic acid raw material with 50x (top, left) and 200x (top, right) magnification and CAN with 200x (left, bottom) and 500x (right, bottom) magnification.

In Figure 101, micrographs of CAN/SA (10:1) mixture and CAN/SA (15:1) mixture are shown. The increased content of CAN in the 15:1 mixture results in a stronger orange color of the powder (see **5** compared to **1**).

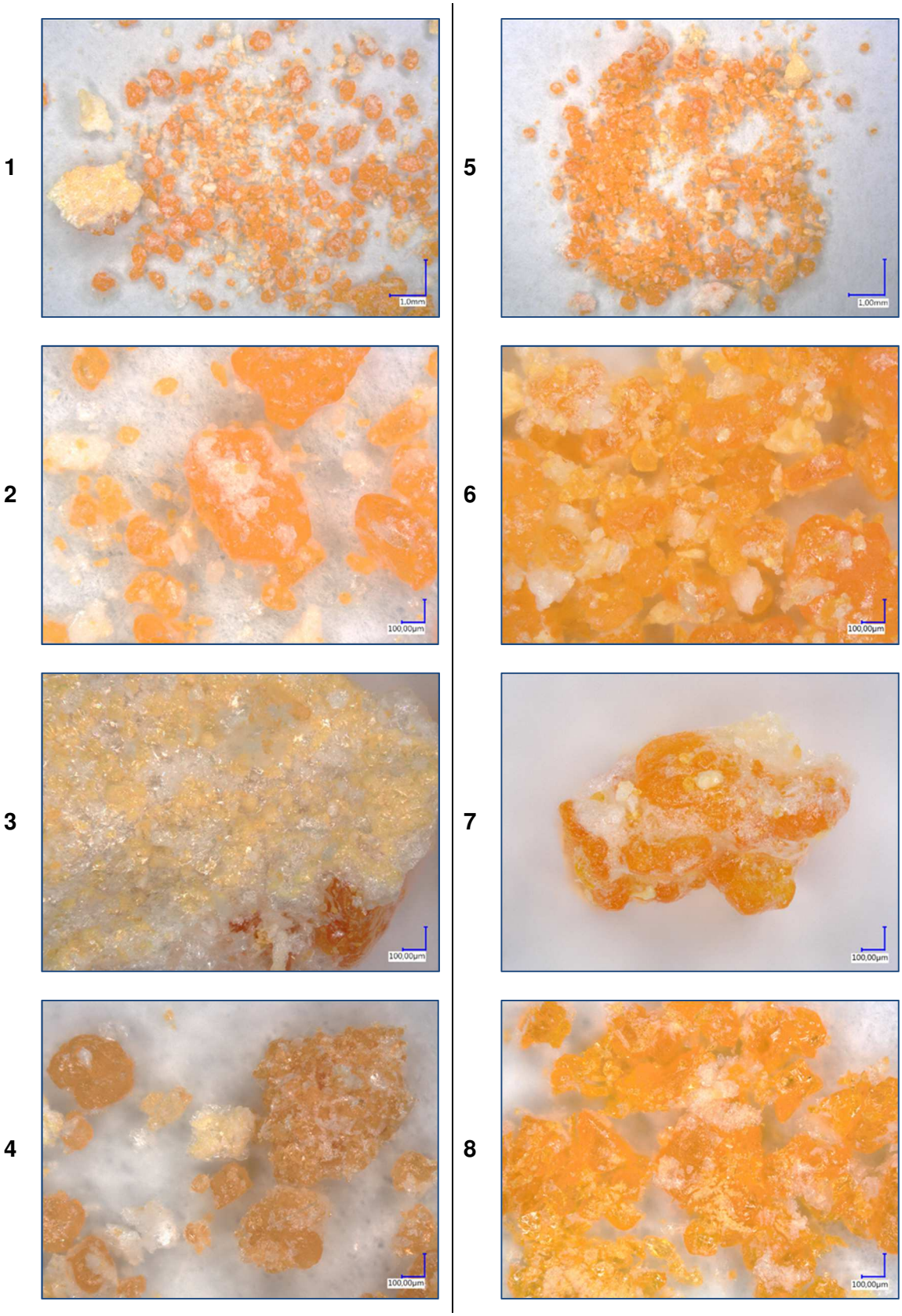

Figure 101: Micrographs of the CAN/SA (10:1) mixture (**1**-**4**) and CAN/SA (15:1) mixture (**5**-**8**). Images **1** and **5** are taken with 20x magnification, all other images with 200x magnification.

When looking at individual particles, cluster-like structures with white, yellow and orange areas can be found. When applying small amounts of force using a spatula to the particle in picture **7**, it disintegrates easily into the fragments shown in **8**. With digitally enhanced light microscopy, there is no evidence for a homogenous coating of SA on CAN particles. To get a 3D look at the raw materials, as well as powder formulations micro-CT was employed.

7.3.4 Micro-CT

7.3.4.1 Sample preparation

For micro-CT measurements, the raw material of CAN, as well as the mixtures are filled into hard gelatin capsules, which are fixed on the sample holder using plasiticine (see Figure 102).

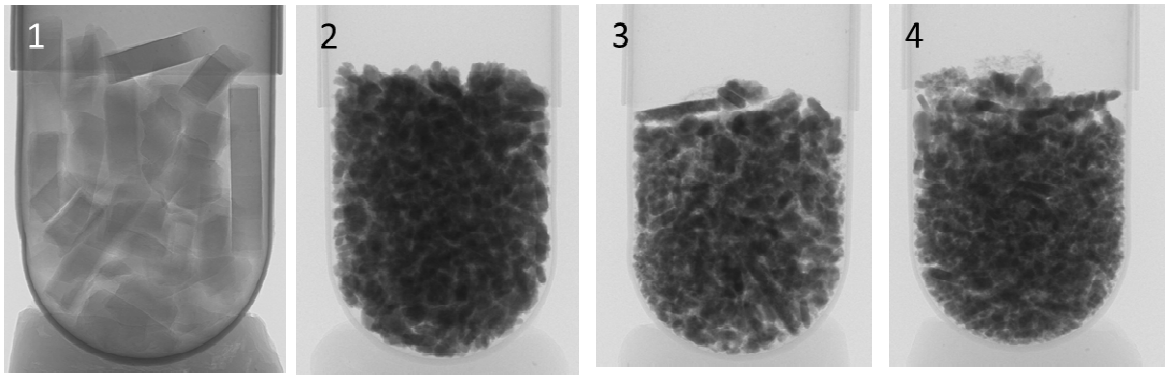

Figure 102: Radiographs of SA raw material, CAN raw material of the CAN/SA (10:1) mixture and 15:1 mixture (from left to right).

7.3.4.2 Visual analysis

Micro-CT analysis should be used to give insight into the spatial distribution of the stearic acid and if coating of CAN particles took place. It should be noted that SA has a considerably lower density as well as relative density compared to CAN. This is already evident in the radiographs where the capsules filling (SA raw material), the capsule and the plasticine all show similar relative density (grey values) (see Figure 102, **1**). For samples containing CAN, the capsule contents are considerably darker (higher relative density) compared to the capsule and plasiticine (see **2**-**4**). For this reason, it was necessary to alter the measurement parameters for SA analysis compared to measurements of samples containing CAN. Therefore exact comparisons of SA raw material and the other sample is not possible, which is not further problematic since the particles are dissolved during the preparations of the mixture and thus losing their prior particles size and shape.

Micro-CT measures the attenuation (also referred to as relative density) of the x-ray beam crossing the sample. This value is dependent on the chemical composition and density of the sample as well as the used x-ray photon energy. When measuring the raw materials homogenous chemical composition and density can be assumed but since a non-monochromatic energy is used, small variations in x-ray photon energy are to be expected and are visible in the form of small differences in the measured attenuation. This leads to slight differences in color, in this example light to dark blue, for chemical homogenous particles. Another peculiarity of micro-CT imaging is shown in Figure 103. Here it can be seen that the interface between the CAN particle (blue) and the surrounding air is not immediate but proceeds over a relative density gradient in pixel steps from the high relative density (blue) of the particles over medium relative density values (green and yellow) to low relative density values (purple and black). This gives each particle the impression of a uniform halo, not to be confused with a perfectly homogenous coating.

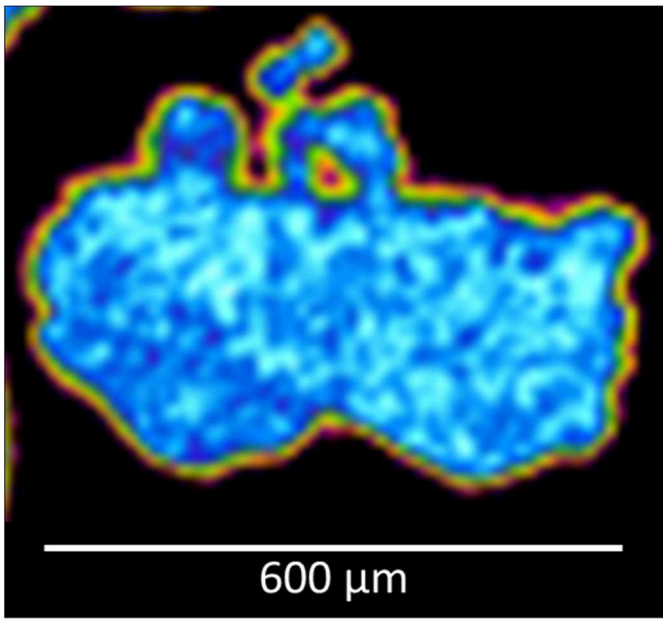

Figure 103: 2D micro-CT image of a singular particle of the CAN raw material

In Figure 104, horizontal, digital 2D slices of the relative density distributions in the CAN raw material, CAN/SA (10:1) and CAN/SA (15:1) mixtures are shown. Visually all three samples are very similar, with the majority of particles being of high relative density (blue) surrounded by air (black). This is comparable for CAN raw materials as well as for both mixtures, therefore it is plausible that the different hues of blue represent CAN.

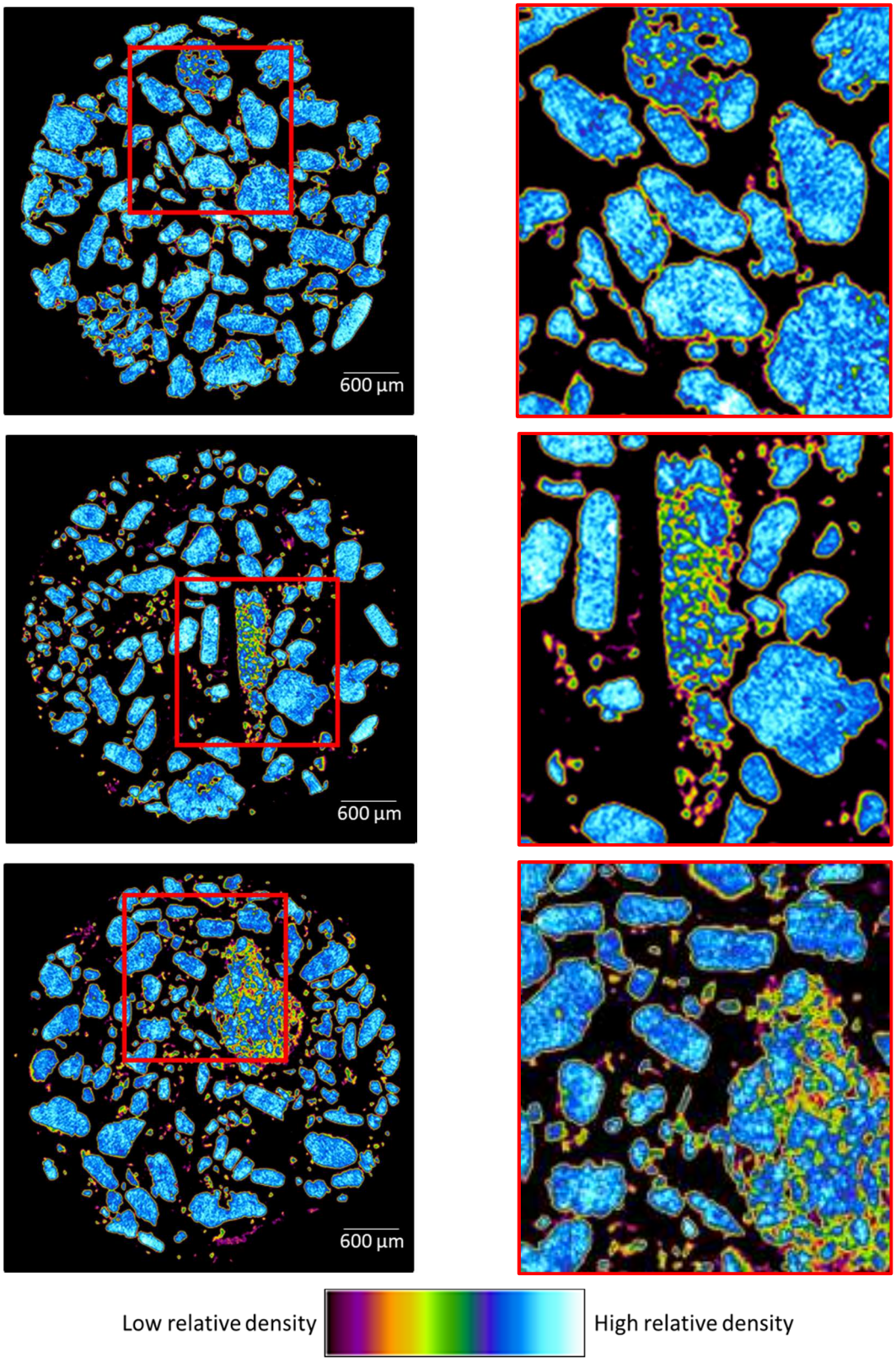

Figure 104: 2D Micro-CT images with detail picture, of the CAN raw material (top), of the CAN/SA (10:1) mixture (middle) and of the CAN/SA (15:1) mixture (bottom).

The main differences between the raw CAN and the mixtures is the higher amount of smaller particles of different relative densities (colors other than blue) and “clustered” areas, where a multitude of small blue particles are surrounded by material of lower relative density, in green and yellow (indicative of SA). A detail image in 3D is shown in Figure 105, where a cluster was digitally isolated. The areas of higher relative density are colored in blue and areas of lower relative density in yellow and green. When digitally removing the low relative density areas, individual blue particles are found (see bottom).

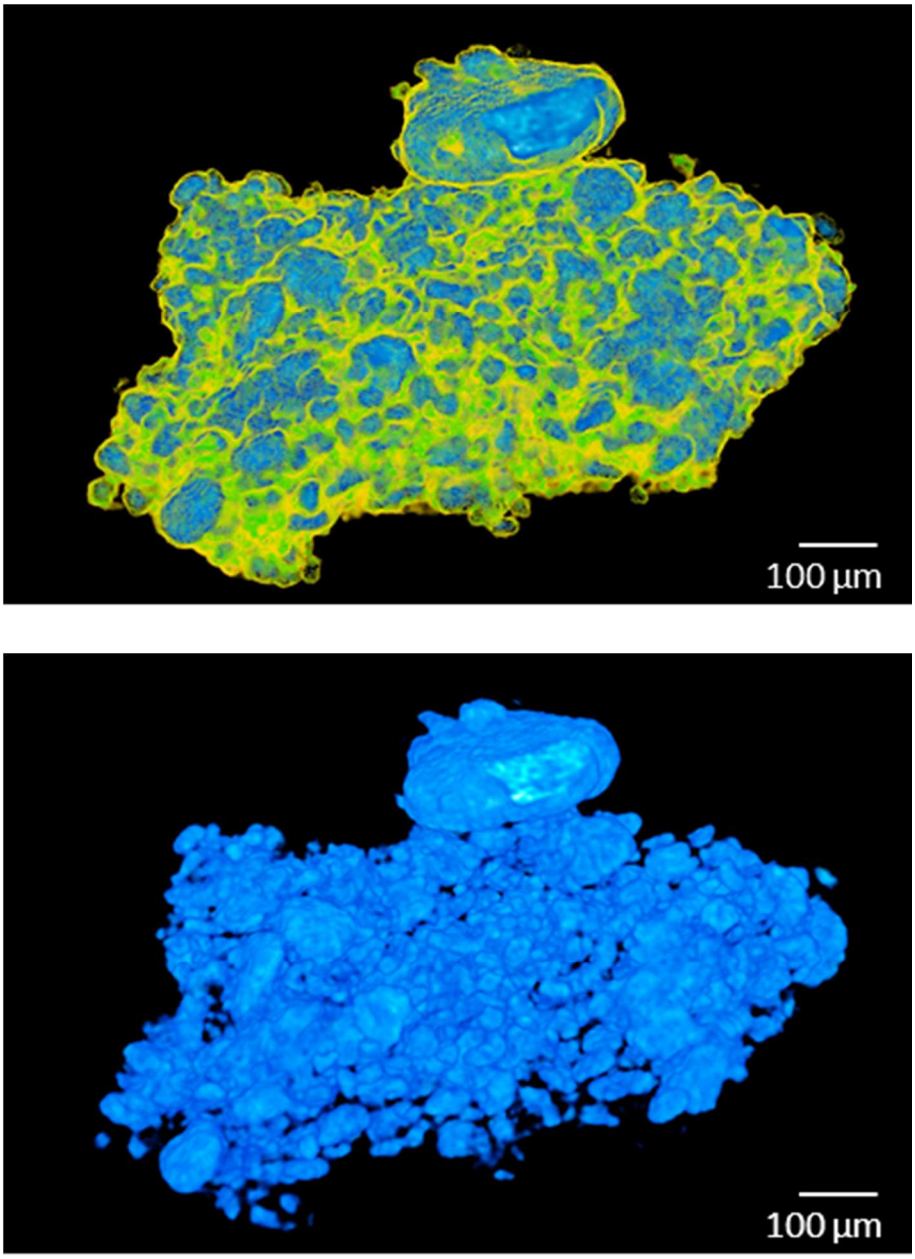

Figure 105: 3D micro-CT image of a digitally isolated cluster in the CAN/SA (15:1) mixture.

When combining the findings of microscopy and micro-CT, it seems plausible that at later stages during the process of solvent evaporation, SA precipitates in small puddles of remaining solvent, as a slurry, encasing finer CAN particles and thus forming clusters.

7.3.5 Particle analysis

For particle analysis, three custom-made task lists, for particle isolation (TL_CAN/SA_01), CAN particle isolation (TL_CAN/SA_02) and particle analysis (TL_CAN/SA_03) are implemented. An overview over the implemented steps is provided in Figure 106. The procedure is comparable to the isolation of API particles in the FCT discussed in paragraph 5.4.2. Because the contrast between (CAN) particles and surrounding medium (air) is very sharp, no filtering steps had to be implemented.

1	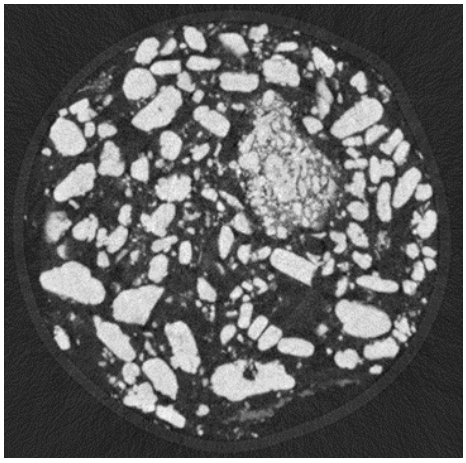	Grey scale image as received after reconstruction of the raw images.
2	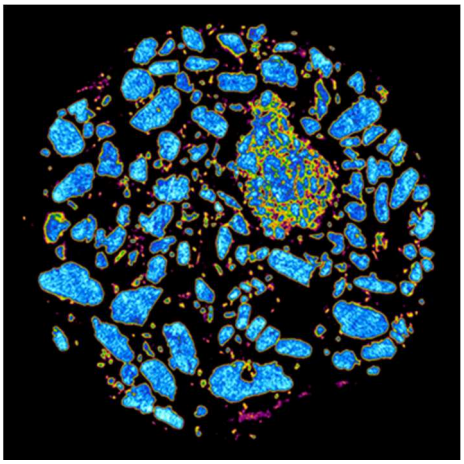	Implementation of a mask using manual thresholding to remove the capsule and background fluctuations.

3	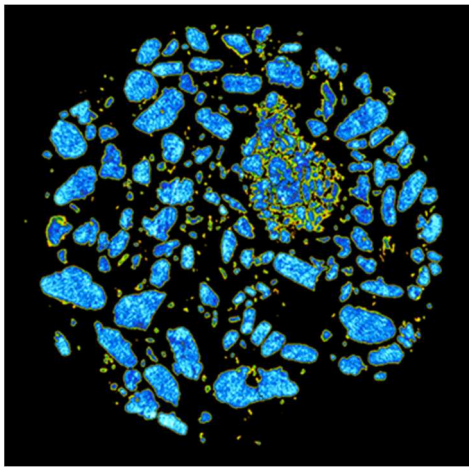	Since the particle size of CAN particles (high relative density in blue) is of interest a pre manual thresholding step followed by an despeckle step to remove particles close to the measurements resolution are implemented to simplify the image for the subsequent, computationally intensive step of particle separation using an watershed algorithm.
4	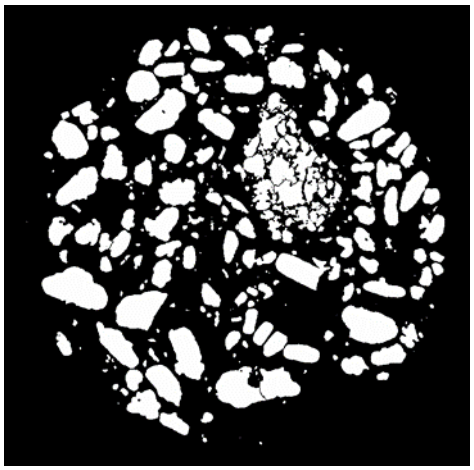	The final binary image for analysis of isolated CAN particles is received via manual thresholding.

Figure 106: Stepwise procedure of CAN particle isolation.

Since the procedure of particle isolation is subject to several manual thresholding steps, which as the name implies are parameters chosen by the operator, the measured values should not be taken as exact values, but as a means to compare samples that have been measured and analyzed using identical parameters. Particle size measurements were carried out using the exact same analysis parameters for raw material and mixtures, ensuring that only CAN particles are registered. In Table 18 as well as in Figure 107 the particle size distributions are depicted. It can be seen that the raw material has overall, larger particles and that both mixtures are comparable. This suggests that the manufacturing process of the mixtures has a size reducing influence on the CAN particles.

Table 18: Particle size distribution of the raw material and the two mixtures.

	ESDv [µm]			
Sample	**D10 [µm]**	**D50 [µm]**	**D90 [µm]**	**Avg. Surface area [µm²]**
CAN	305	442	549	592,784
10:1	194	360	508	70,135
15:1	182	329	510	74,055

Additionally the average surface area is reduced by approximately 10% from the raw material to the mixtures, indicating a smoothing effect of the manufacturing process on the CAN raw materials' rough surface areas.

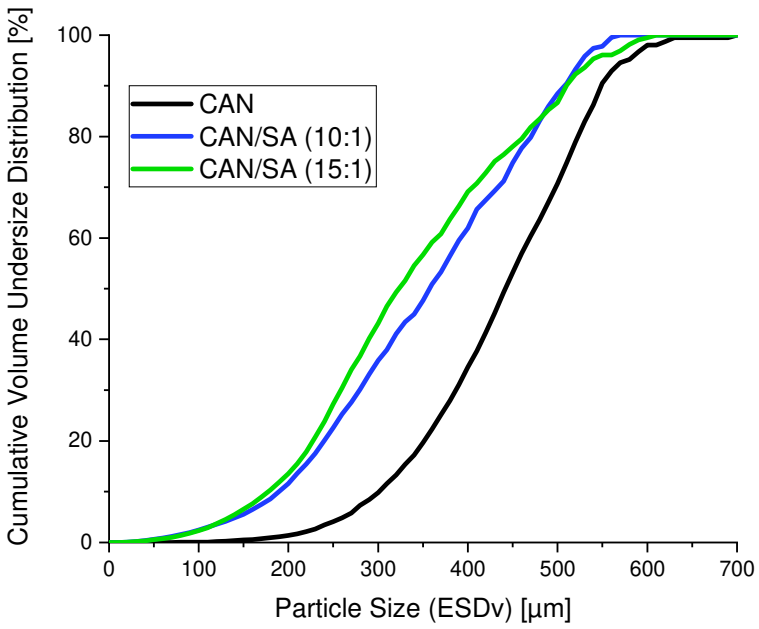

Figure 107: Cumulative particle size distribution (ESDv, volume weighted) for raw material of CAN and mixtures.

7.3.6 Raman-Microscopy

For Raman microscopy, the powder samples are transferred to a microscope slide and individual particles or substructures of agglomerates are measured either with line mapping or with space-resolved point spectra. Reference Raman spectra are taken using the raw materials from which the mixtures were manufactured (see Figure 108).

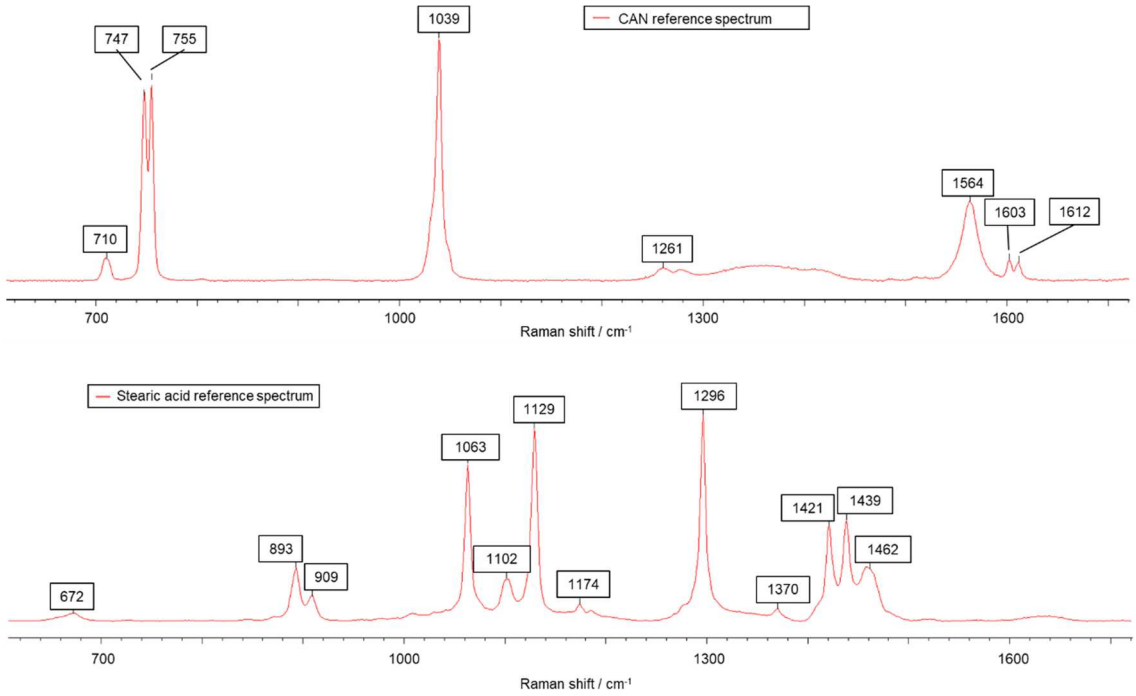

Figure 108: Reference spectra of raw materials CAN (top) and stearic acid (bottom)

In Figure 109, mapping of an area of an orange colored particle was performed using line mapping and MCR-ALS (empty modeling). It can be seen that only one component is found, indicating homogenous chemical composition. The calculated spectrum is nearly identical with the reference spectrum of CAN. From this can be concluded that pure CAN particles are still present in the mixture.

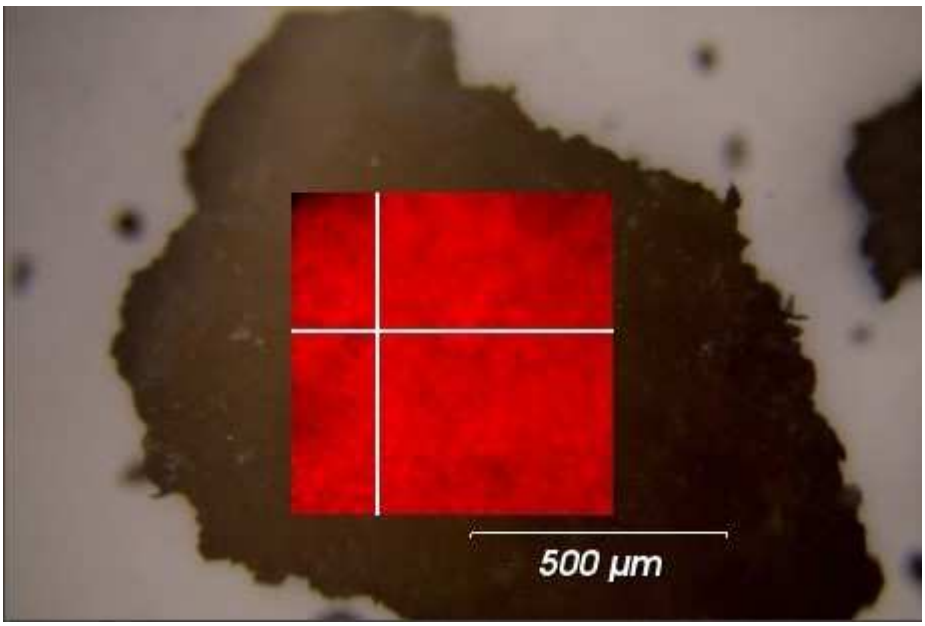

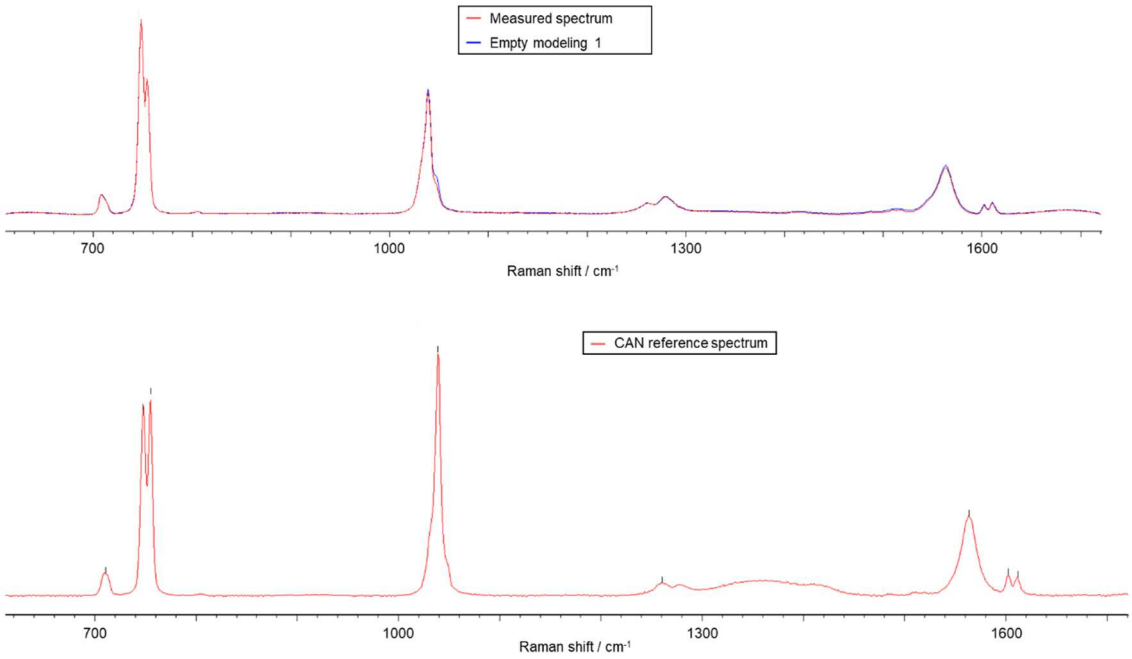

Figure 109: Raman-Mapping with empty modelling (top); random spectrum in the middle of the measured particle (red) and calculated spectrum (blue) (middle) and CAN reference spectrum (bottom)

Due to the rough surface and the resulting differences in height, of the cluster-like particles, described in paragraph 7.3.3, an area mapping is not possible. For this reason, point spectra are taken at three different regions (see Figure 110). Spectra taken on the yellow area are composed mainly of CAN vibrational bands with small amounts of overlap from stearic acid. Spectra taken from the orange areas are pure CAN. Spectra taken from white areas are a mixture of CAN and stearic acid vibrational bands.

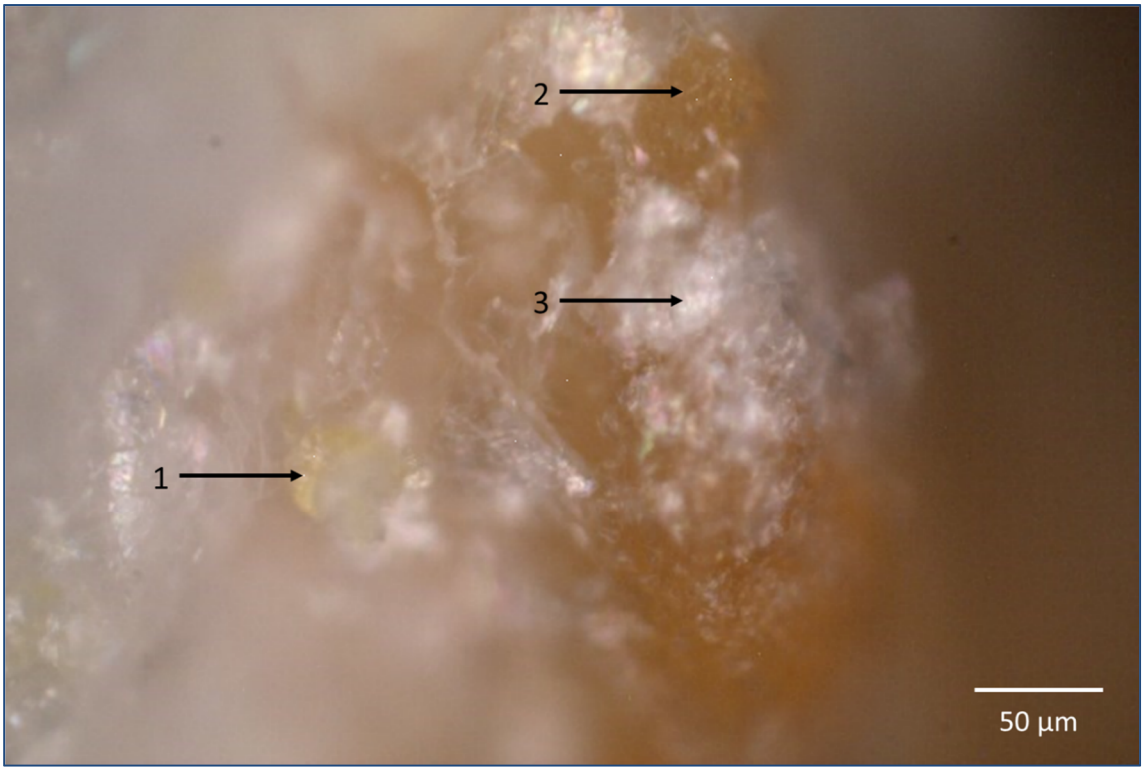
2
3
1
50 µm

(1)

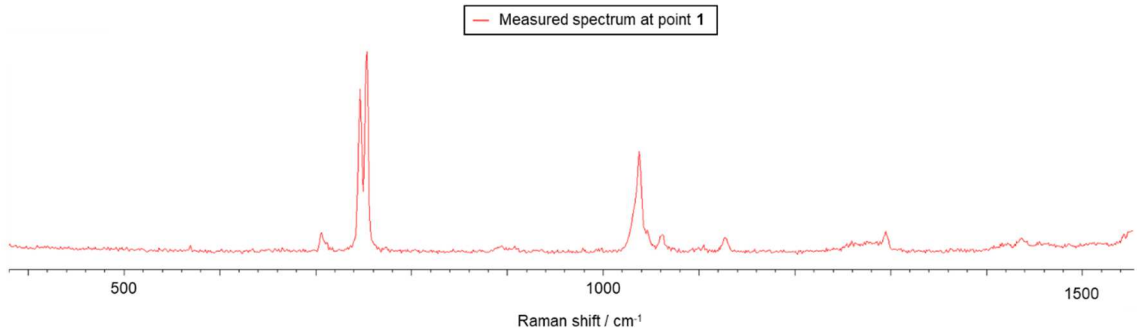
Measured spectrum at point 1
500
1000
1500
Raman shift / cm-1

(2)

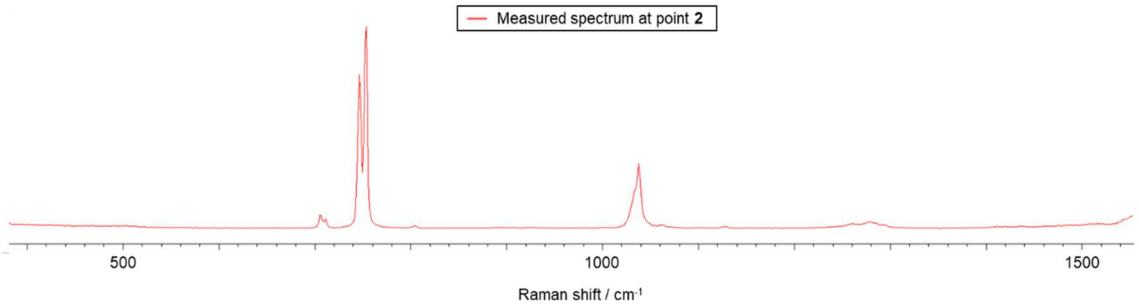
Measured spectrum at point 2
500
1000
1500
Raman shift / cm-1

(3)

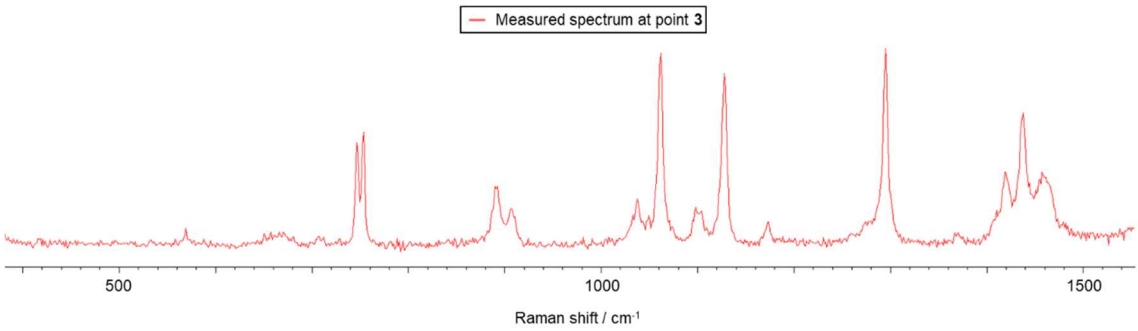

Figure 110: White light image with marked areas (Top), spectrum of the yellow area (1), spectrum of the orange area (2) and a spectrum of the white area (3).

There is no indication that any form of reaction took place during the manufacturing of the mixtures, since only spectra of the pure substances are found.

7.4 Conclusion

Commonly used oxidizers in strobe formulation, usually ammonium perchlorate, as well as their degradation products are toxic. Therefore, there is a need for non-toxic alternative. An oxidizer used in organic synthesis chemistry with promising properties (non-toxic, halogen-free) is ceric ammonium nitrate (CAN). Its only drawback is its hygroscopicity interfering with stable storability. To compensate for this, mixtures with stearic acid (SA) were prepared, substantially increasing stability during storage. These new formulations possess comparable strobe properties compared to standard strobe mixtures. Additionally, sensitivities are improved. Furthermore, CAN/SA mixtures provide positive oxygen balances, which enables the use of a multitude of different colorants. This opens possibilities for completely new, non-toxic green and blue strobe formulations

With the employed imaging techniques, it was found that the manufacturing process does not yield a homogenous coating of CAN with SA. Nevertheless, the powder mixtures do show particle aggregation where SA functions as a binder between smaller CAN particles to form clusters. Micro-CT analysis performed on the CAN raw material and mixtures showed furthermore that CAN particles are reduced in size during mixture manufacturing. In contrast to this, it would be expected that smaller particles possess more surface area, but the average surface area of the particles in the mixtures is reduced by approximately 10%. This might be one reason for the improved resistance against humidity. The mechanical force of the manufacturing process could have a smoothing effect on the CAN particles. Additionally the physical binding of SA on CAN further reduces surface area. With

Raman imaging, no indication of a chemical reaction or chemical change in the raw materials was detected; both substances exist alongside each other (see Figure 111).

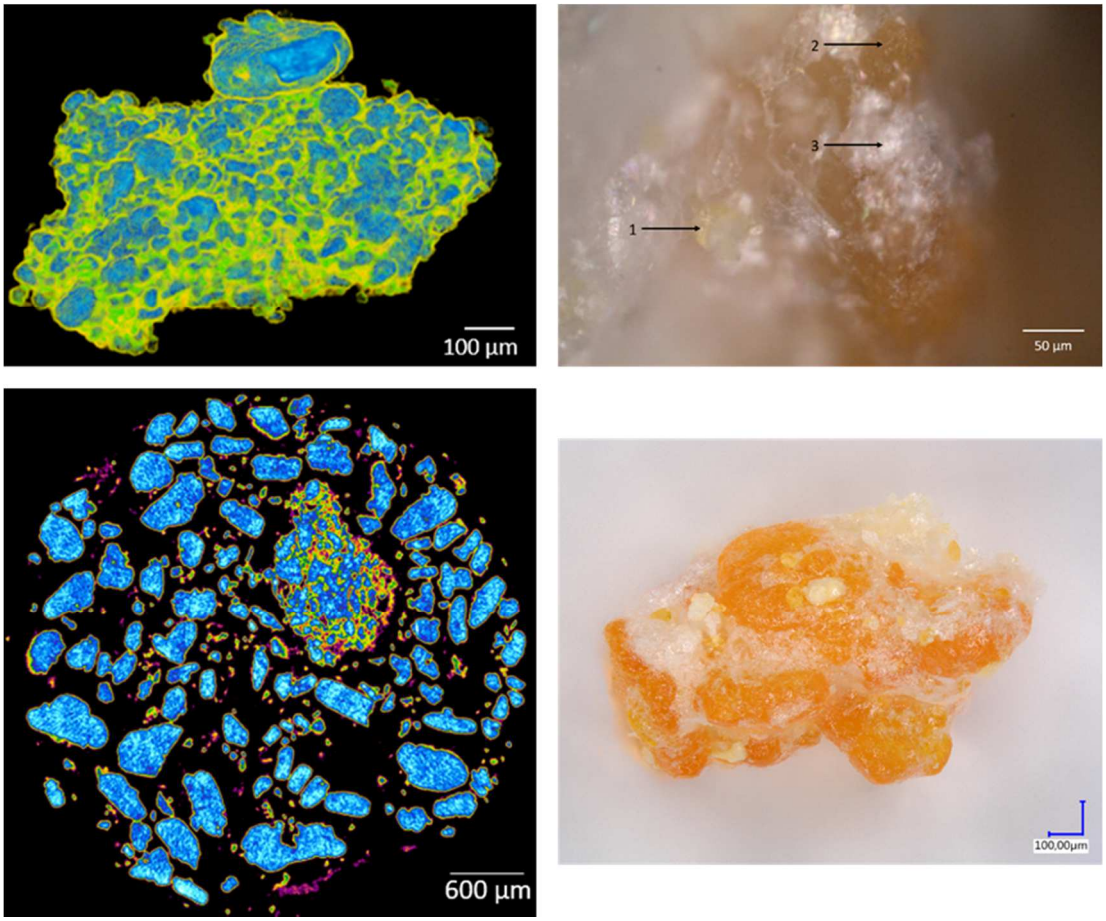

Figure 111: 3D micro-CT image of a singular cluster (top right), white light image with points of Raman microscopy of a cluster (top, right), 2D micro-CT image of a cross section through the mixture (bottom, left) and digitally enhanced microscopy image of a cluster (bottom, left).

References

[1] J.M.L. Corbel, J.N.J. van Lingen, J.F. Zevenbergen, O.L.J. Gijzeman, A. Meijerink, *Angew. Chem. Int. Ed.*, **2013**, 290-303.

[2] C. M. Csernica, *Int. Pyrotech. Sem.*, 42nd, Grand Junction, Colorado, USA, **2016**.

[3] U. Krone, Pyrotechnischer Satz zur Strahlungsemission, patent DE 2164437, **1973**.

[4] U. Krone, *Pyrotech. Grundlagen Technol. Anwend*. **1975**, 225-237.

[5] F. Wasmann in *International Pyrotechnics Seminar*, Vol. 5, IPSUSA Seminars Inc., **1976**, 643-651.

[6] F. Wasmann, *Pyrotech.: Grundlagen Technol. Anwend.*, **1975**, 239-250.

[7] T. Shimizu, *Pyrotechnica*, **1982**, 5-28.

[8] T. Shimizu in *International Pyrotechnics Seminar Vol. 16*, **1991**, 47-53.

[9] M. L. Davies, *J. Pyrotech.*, **2008**, 42-49.

[10] B. F. Gray, M. J. Roberts, *Proc. R. Soc. London Ser. A*, **1988**, 391-402.

[11] L.E. Braverman, X. He, S. Pino, M. Cross, *J. Clin. Endocrinol. Metab.*, **2005**, 700-706.

[12] J.J. Sabatini, E.-C. Koch, J. C. Poret, J. D. Moretti, S.M. Harbol, *Angew. Chem. Int. Ed.*, **2015**, 10968-10970.

[13] W. Christmann, D. Kasiske, K.D. Klöppel, H. Partscht, W. Rotard, *Chemosphere*, **1989**, 387-392.

[14] R. Sen, S. Das, K. Das, *MAS*, **2011**, 416-420.

[15] V. Sridharan, J.C. Menéndez, *Chem. Rev.*, **2010**, 3805-3894.

[16] https://www.merckmillipore.com/CH/de/product/Ammonium-ceriumIV-nitrate,MDA_CHEM-102276#anchor_orderingcomp, (accessed 08.12.2020).

[17] Private Communications with Alicia Dufter-Münster

[18] T. Shimizu in *Fireworks: The Art, Science and Rechnique*, 3rd Ed., Pyrotechnica Publications, Austin, **1996**.

[19] J.P.Goullé, E. Saussereau, J.Grosjean, C.Doche, L. Mahieu, *Forensic Sci. Int.*, **2012**, e8-e12.

[20] A. Stift, J. Friedl, F. Längle, G. Berlakovich, R. Steininger, F. Mühlbacher, *Transplantation*, **2000**, 2454-2455.

[21] J.M.L. Corbel, J.N.J. van Lingen, J.Z. Zevenbergen, O.L.J. Gijzeman, A. Meijerink, *Propellants Explos. Pyrotech.*, **2013**, 634-643.

[22] J.J. Sabatini in *Green Energetic Materials*, 1st Ed. (Ed.: Tore Brinck), Wiley, Chichester, **2014**.

[23] C. Jennings-White, *Pyrotechnica*, **1992**, 33-45.

[24] J. Glück, T. M. Klapötke, T. Küblböck, *ACS Sustainable Chem. Eng.* **2018**, 4400-4404.

[25] J. Glück, T. M. Klapötke, J. J. Sabatini, *Chem. Commun.* **2018**, 821-824.

8 Limitations

As with all measurement techniques, imaging methods are also subject to limitations. These can be inherent to the measuring device itself (physical), can arise from the sample composition (chemical or physical) or from the combination of different influencing factors. A limitation that is found with all imaging techniques is that particles can only be recorded when they are larger than the detection limit and have a sufficient concentration in the specimen. Additionally due to the long acquisition times, samples have to be in solid form and immobilized to ensure sharp images. In the following, limitations unique to the three different imaging techniques, as well as restrictions that may occur when combining methods are described.

8.1 Limitations of Raman microscopy

Depending on the sample size, required step size, suitable laser and type of measurement procedure, Raman microscopy can be very time consuming. Although, auto sampling is starting to emerge as a way of reducing this problem, the technique will always be restricted to selective, qualitative data collection and less applicable for broad screening of large volumes of samples. A related factor is sample preparation, which is usually needed when information should be gathered from inside the sample. In most cases, this also involves damage or destruction of the specimen. Additionally, depending on the sample, extended exposure to the laser can cause damage or alteration of the sample (see Figure 112). The chemical composition of the sample can also influence the analysis results. Substance mixtures with chemically very similar spectral bands (i.e. different types of sugars or polymorphs) can be hard or impossible to differentiate.

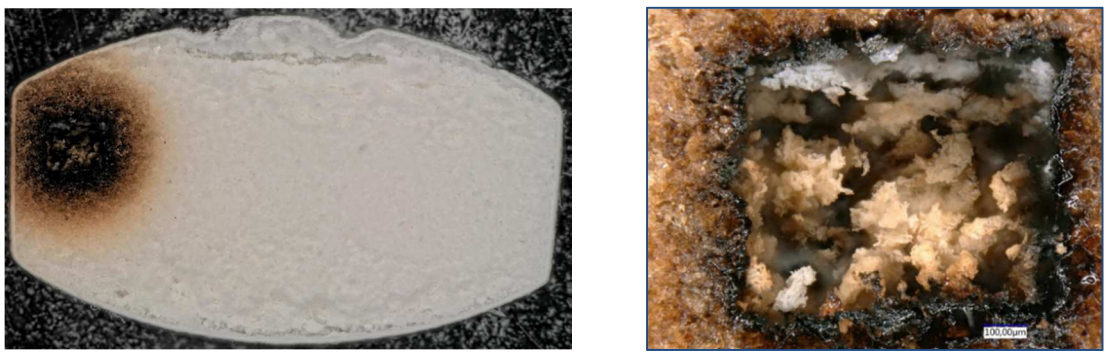

Figure 112: Tablet cross section prepared for Raman microscopy with laser damage (left) and zoomed-in micrograph (right).

8.2 Limitations of Micro-CT

As with Raman microscopy, micro-CT is not suitable for the screening of large amounts of samples, since measurements usually take two hours or more and auto sampling is for the most applications not possible. Further problems can arise from the samples composition. Gathering information on specimens with no or very small differences in relative density, is restricted to analysis concerning the volume and related parameters of the whole sample. However, no information on the structural composition can be gathered. On the other end of the spectrum, samples with very large differences in density (i.e. metallic or mineral particles in organic samples) can suffer from shielding effects.

A problem that arises from the measurement geometry is that samples have to be smaller than a certain size to be measured at full resolution. It can therefore sometimes be necessary to select non-optimal measurement parameters or reduce the size of the sample. Lastly damaging of samples due to effects of the X-ray beam is not impossible.

8.3 Limitations of SEM/EDX

Due to measurements taking place in vacuum, only specimen withstanding these conditions can be used. This factor also limits the throughput of multiple samples, making a broad screening impossible and restricts the size of samples. To characterize the composition of a sample, different atomic species have to be present to enable differentiation between substances. SEM/EDX images of pure organic substances would, yield topographic information but none about the chemical composition or the distribution of individual materials. Analogous to Raman microscopy, SEM/EDX is measuring the surface of the sample, when information from inside specimens is of interest, invasive sample preparation is necessary. Lastly, the sample can be damaged by exposure to the electron beam.

8.4 Problems with the combination of micro-CT and Raman microscopy

In Figure 113, micro-CT and Raman microscopy images of the cross-section of the same bi-layered tablet are shown. Due to the incompatibility of API 1, it has to be separated from the other two APIs to ensure chemical stability. Several problems make an in-depth analysis impossible.

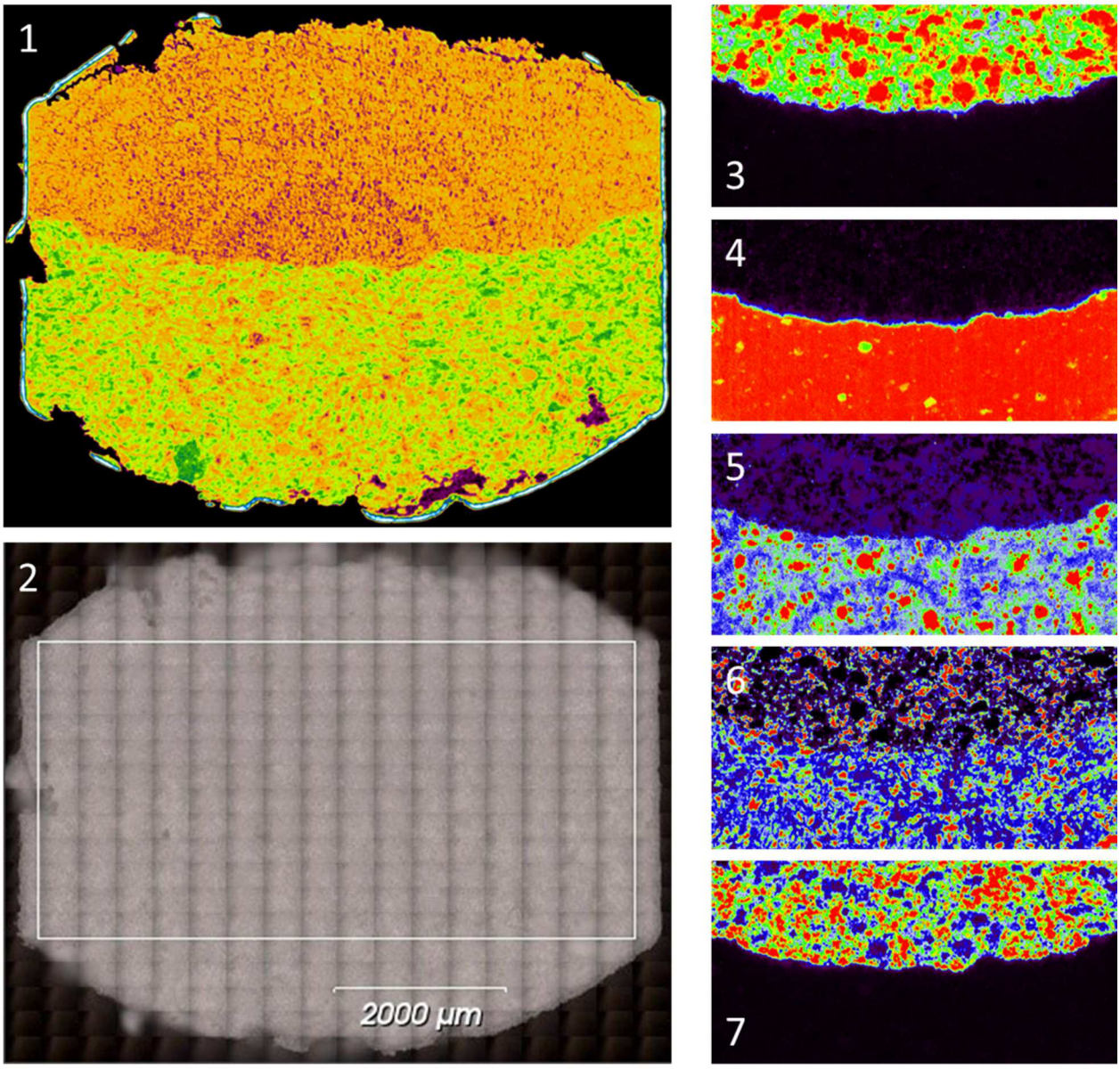

Figure 113: Micro-CT image of the surface of a cross-section of a bi-layer tablet (1), white light microscopy image of the same cross-section (2) and corresponding Raman mapping of the three APIs (3-5) and two excipients (6,7).

When looking at the micro-CT image, the top layer does not show significant differences in relative density so no information about particle sizes can be gathered. The bottom layer shows areas of higher relative density (green) and lower relative density (orange and purple) but cannot be linked to any substance found in Raman microscopy. Here it can be seen, that the top layer is comprised of API and both excipients homogenously distributed. The bottom layer shows discrete particles of API 3 and excipient 2 but API 2 is due to its high Raman efficiency found throughout the layer rendering the location of discrete particles impossible.

9 Summary

9.1 Synergy makes perfect – The dream of looking into samples

In the scope of this work, it was shown that the combination of different analytical imaging methods yielded formerly impossible insights into a variety of pharmaceutical dosage forms. The axiom “a whole is greater than the sum of its parts” (wrongly attributed to Aristotle) proved to be true in this context. Only the linking of information gathered from the individual methods made new information achievable. After proof of concept, different combinations were successfully implemented in different fields of application in on-going projects within the context of pharmaceutical development. In Figure 114, an overview of the used measurement techniques is shown.

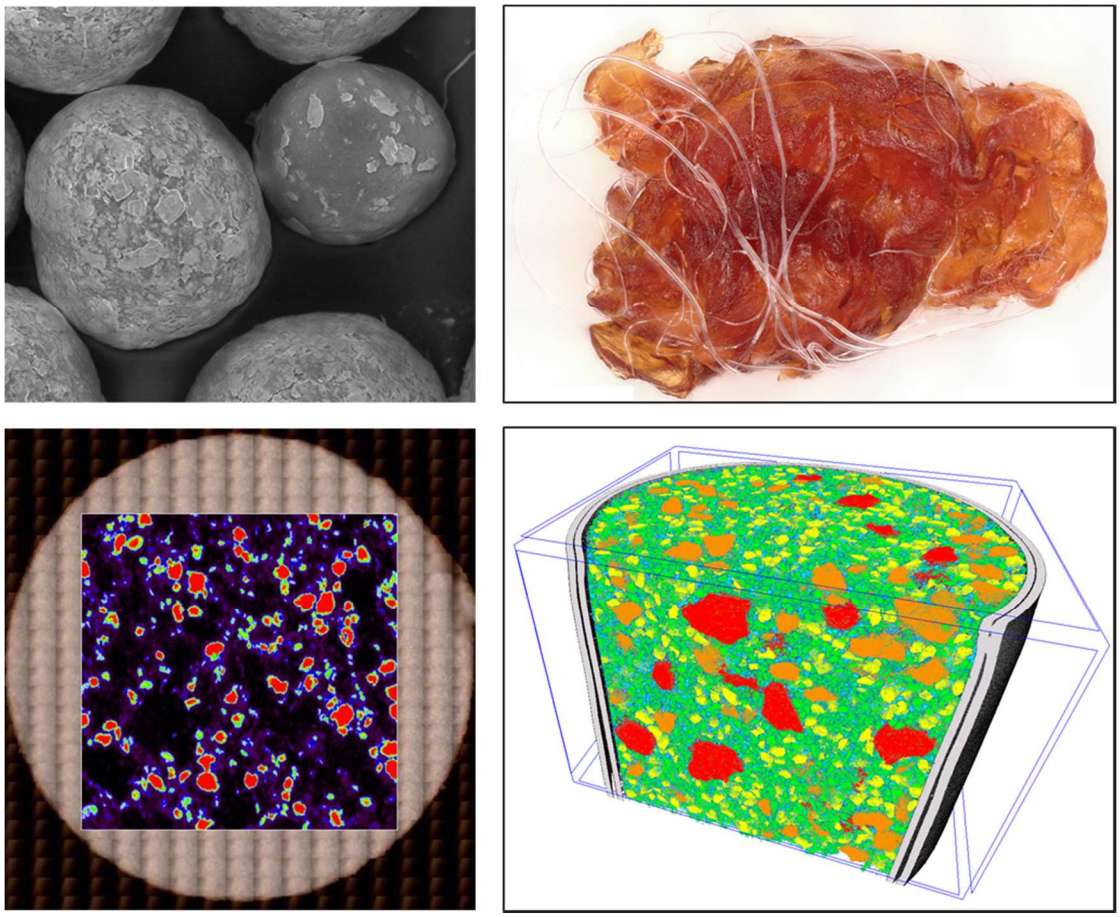

Figure 114: Top left: SEM image of pellet surfaces. Top right: Digitally enhanced microscope image of an unknown particle. Bottom left: Spatial distribution of a tablet component shown with Raman microscopy. Bottom right: Micro-CT model of a powder in a capsule with color according to particle size.

9.2 Patch formulations – A microscopic sandwich

The first application was on a transdermal therapeutic system (TTS), which is a drug-loaded patch dosage form. The API is located in a 50 µm thick adhesive matrix sandwiched between two physical stability-providing layers (see Figure 115). Due to its very small cross section (~ 150 µm overall) and multi-layered composition, TTS present major difficulties for most measurement methods.

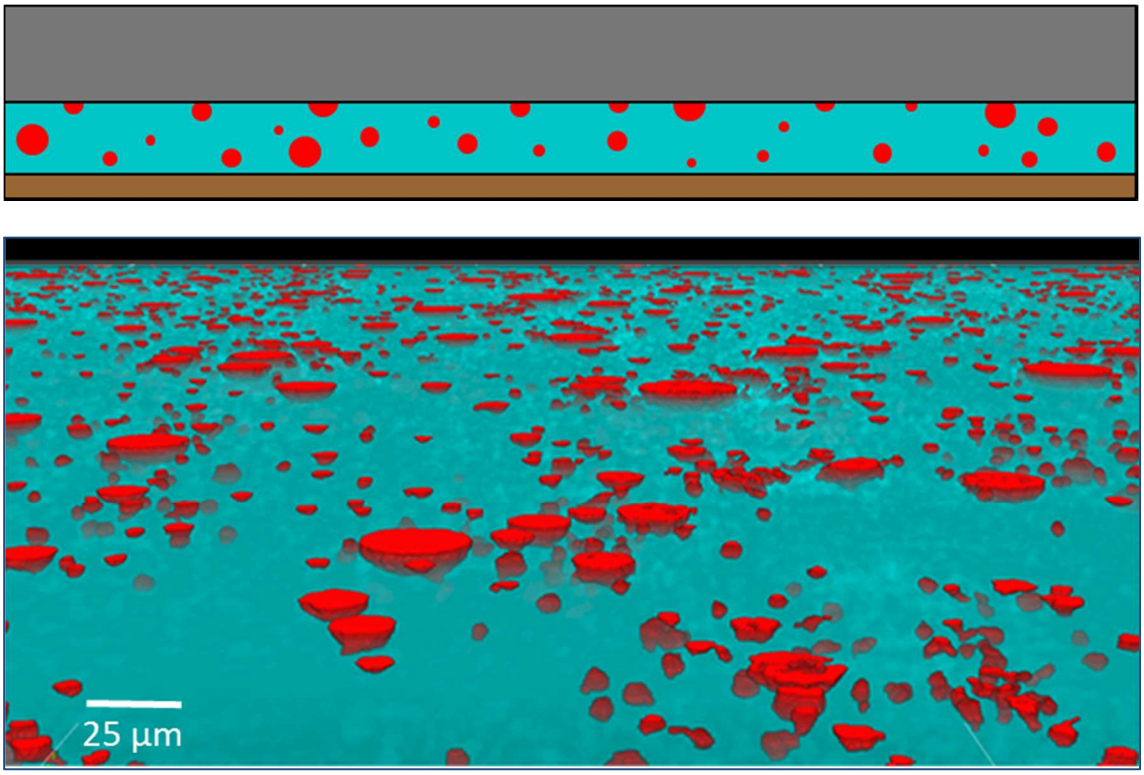

Figure 115: Top: Schematic depiction of the patch dosage form, with release liner (grey) adhesive matrix (cyan), API (red), backing foil (brown). Bottom: Micro-CT image with areas identified as API (red) and adhesive layer (cyan).

Imaging techniques were used to speed up the process of error detection after a manufactured batch showed dissatisfying dissolution results. With standard measurement methods, no conclusive evidence could be found. Normally a time-consuming trial and error procedure would be employed to get information about the possible reasons for error. The combination of Raman microscopy, SEM/EDX and micro-CT enabled a completely new way of gathering information. With micro-CT the presence of spherical shaped areas of high relative density were found. With SEM/EDX and Raman microscopy, the localization of API in the spherical zones could be shown. Due to the semi-transparent nature of the patch, Raman mapping is possible in 3D, which was formerly not known in the literature for the pharmaceutical field.

With the combination of the three imaging techniques, it was possible for the first time to determine the particle distribution of API in drug-loaded patch formulations and its location within the adhesive matrix in 3D. Several key parameters were found to be responsible for the change in dissolution behavior, specifically the amount of large API particles in the region bordering the interface between patch and skin.

9.3 Tablets – Old news / new insights

The next step was to implement the combination of imaging techniques on the most common form of drug application, film-coated tablets (FCT). There is up to this point, no possibility to get detailed information about the distribution of the API inside a tablet, especially not in 3D.

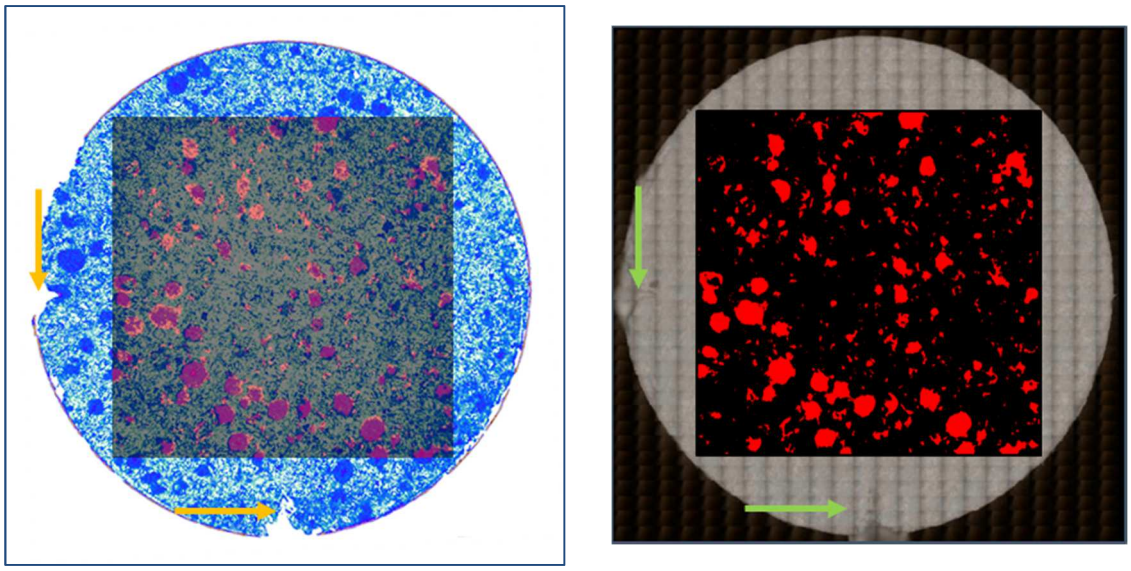

Figure 116: Left: Micro-CT image (blue) with Raman mapping overlay. Right: Raman mapping of the API (red).

As mentioned before, nearly all analytical tools require the destruction of samples, in this case cutting or breaking the tablet open to enable data collection of the interior. Therefore, it can never be excluded that the measured parameters have not been changed by the sample preparation. Raman microcopy was used to measure the spatial distribution of the API in 2D tablet cross-sections and to get a broad idea about its possible particle shapes (see Figure 116 right side). Using micro-CT measurement of the same sample, specific relative density areas could be assigned to the API (left side). This knowledge transferred to micro-CT measurements of intact tablets (with a pixel-size of 8 µm) made detailed analysis of the API particles possible. Through the visualization of the API in 3D, the

determination of key performance parameters such as average particle volume and surface or the particle size distribution was made available. This was of great use when a manufactured batch showed dissatisfactory dissolution results, preventing batch release. With the developed method, it could be clearly shown that the faulty batch had a significantly higher number of large API particles compared to regular batches. With this evidence, the used raw material of the API was revisited and it was found that the prior method to determine the particles size distribution of the powder, laser diffractometric with an upstream sonication step, was not sensitive to agglomerates. The unique information provided by the combination of Raman microscopy and micro-CT gave a comprehensive answer for the detected error and made a quick, selective change to the inspection of raw materials possible.

9.4 Pellet formulations – Layers of information

To show the broad application possibilities of the combination of different imaging techniques another common but complex pharmaceutical dosage form – a capsule formulation filled with gastro-resistant pellets (GRC) – was analyzed. The individual approx. 0.6 mm large pellets are composed of different layers (see Figure 117). Of special interest was the composition of the individual pellets found in capsules of the innovator product, in the so-called deformulation step at the beginning of the development process. Raman microscopy and SEM/EDX were used to analyze the chemical composition of the different layers of the pellets (right side). To get comprehensive information about the pellet layers, a cross-section through the pellets had to be prepared. This information was then linked with the relative density information of micro-CT measurements of entire capsules (see bottom left) to get the 3D location of the different components for each individual pellet.

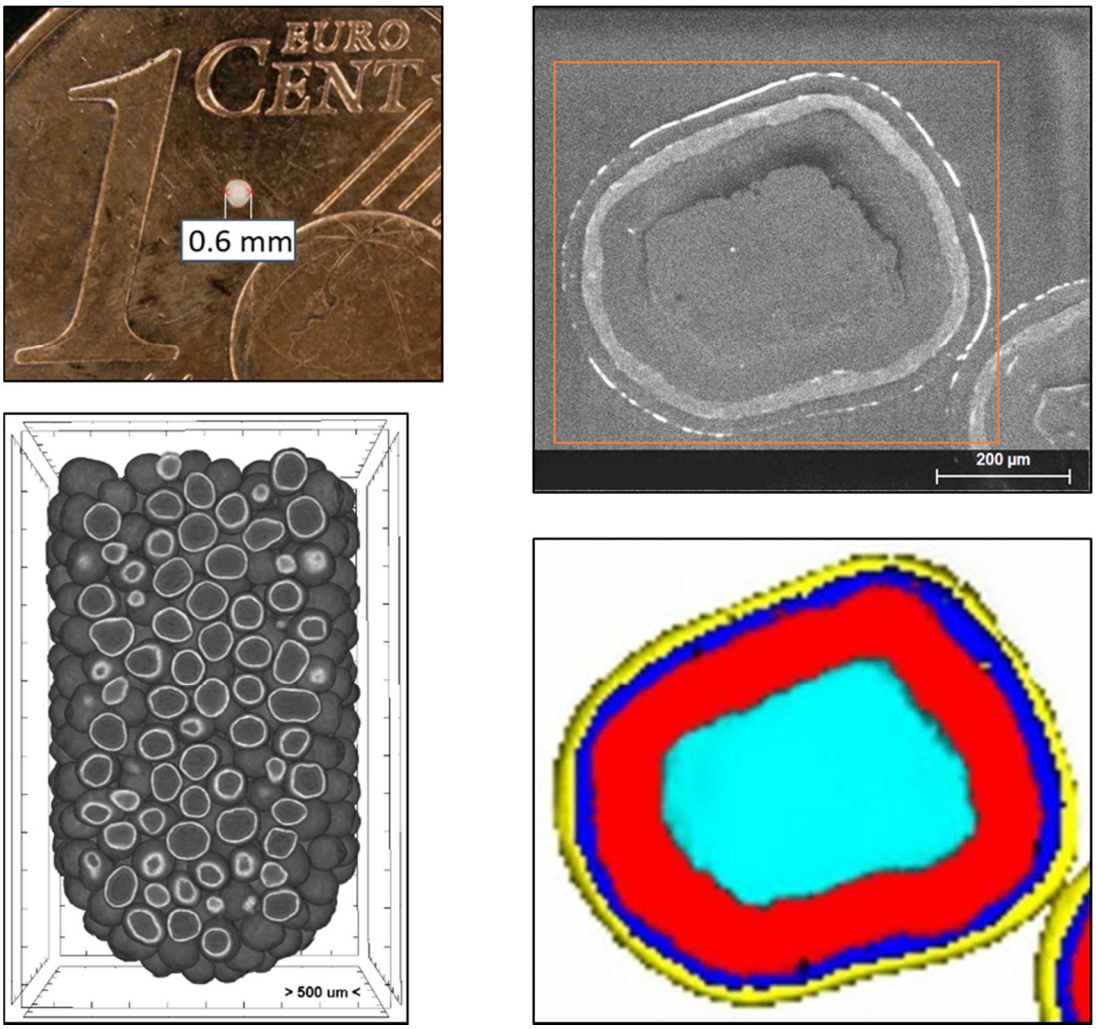

Figure 117: Top, left: Singular pellet on a 1-euro cent coin. Bottom, left: Micro-CT image of a virtual cut through a pellet-fillet capsule. Top, right: SEM image of pellet cross-section. Bottom, right: Raman microscopy image of the same cross-section with mapping of saccharose (cyan), API (red) talcum (blue) and polymethacrylate (yellow).

The exact pellet count per capsule, average pellet size and layer thickness of the different components and defects in different layers could be determined and allowed conclusions to be drawn about the manufacturing process. Later during the development cycle, large-scale comparison using the most significant parameters, between in-house and innovator batches, combined with dissolution testing was used to select batches for bioequivalence studies.

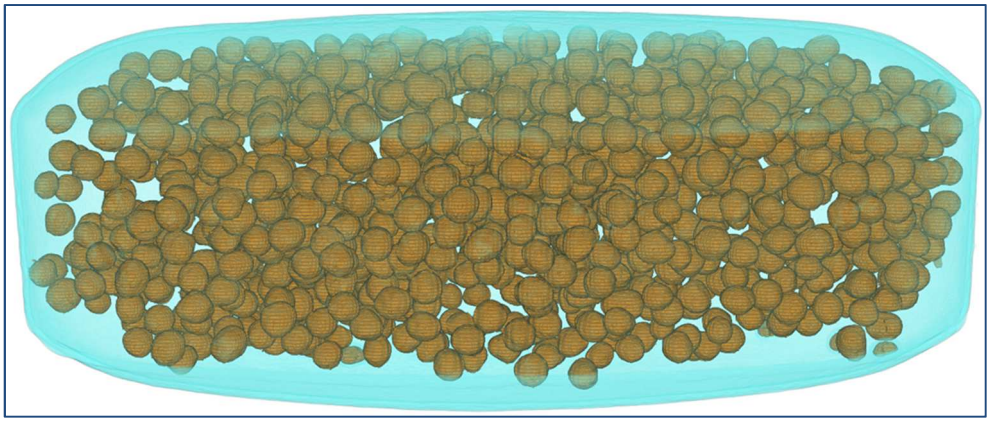

Figure 118: 3D Micro-CT visualization of individual pellets contained in a MUT.

To demonstrate the easy transferability of the developed method to similar projects, multiple unit tablets (MUT) – a dosage form where the pellets are embedded in a film-coated tablet – were analyzed. Following the findings of the GRC-project, investigation of the different pellet components and additionally the location of the individual pellets within the tablet was possible (see Figure 118). An air envelope surrounding the individual pellets could be described for the first time.

9.5 Pyrotechnical strobes – Bringing light into the mystery of oscillating matter

To further challenge the capabilities of the combination of analytical imaging techniques, the developed ideas were implemented on a completely different field of application, pyrotechnical strobes (see Figure 119). To improve the hygroscopicity of the oxidizer ceric ammonium nitrate (CAN) it was mixed with stearic acid (SA).

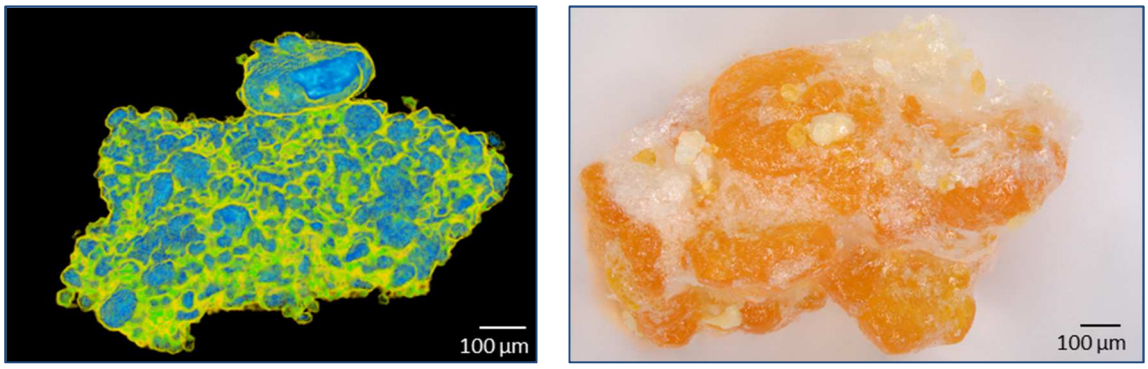

Figure 119: Left: Micro-CT model of CAN / SA cluster. Right: Microcopy image of CAN / SA cluster.

To analyze the morphological and chemical properties of the mixture, micro-CT imaging and Raman microscopy was implemented. Raman microscopy showed that CAN and SA particles exist next to each other, no indication of possible chemical reactions was found. With micro-CT, it could be shown that the manufacturing process does not result in a coating, but the formation of clusters containing CAN and SA. Additionally the particle size distribution and average specific surface area, both parameters of interest for strobe formulations, could be determined for CAN particles in the form of raw material and after the mixing with SA. It could be shown that the developed methods could also provide unique information in this new context.

The combination of analytical imaging techniques provided for previously impossible insights into pharmaceutical dosage forms. The information gathered in this way could be used in different projects for rapid error finding and for deepening the understanding of the 3D composition of samples. In addition, the versatile applicability of the developed methods could be demonstrated with an example outside the pharmaceutical sector.

10 Appendix

10.1 TTS – Rotigotine

10.1.1 Micro-CT measurement and reconstruction parameters

Table 19: Rotigotine: Micro-CT measurement and reconstruction parameters.

Measurement parameter	Value	Reconstruction parameter	Value
Number of Files	1877	Smoothing	4 (smoothing kernel = 2 (Gaussian))
Number of rows and columns	2688x4032	Ring artifact correction	21
Partial width	OFF	Beam hardening correction [%]	30
Source voltage [kV]	40	Minimum for CS to Image Conversion	0.000000
Source current [µA]	200	Maximum for CS to Image Conversion	0.065657
Image pixel size [µm]	0.9		
Exposure (ms)	1000		
Rotation step [deg]	0.100		
360° rotation	NO		
Frame averaging	4		
Random movement	OFF		
Filter	No filter		
Scan duration	3h:26m:18s		

Measurements of TTS sections are performed in 4k resolution. Due to the small region of interest and short task list, analysis can also be performed on 4k data sets.

10.1.2 Micro-CT analysis task lists

For the API isolation, the data set is filtered, converted to black and white using manual thresholding and despeckled. This is followed by one regular data analysis step and a second one that outputs images with color-coding of particles according to size, which lastly have to be adjusted to the 0-255 color-space.

Table 20: Rotigotine: Task list of API isolation and analysis (TL_RGT_01)

1	Reload Image	**8**	Reload Region of Interest
2	Filtering Mode, Anisotropic diffusion (3D space) Type, Privilege high contrast edges (Perona-Malik) Number of iterations, 10 Gradient threshold, 5.000000 Integration constant, 0.068182	**9**	Reload Clipboard

3	Thresholding Mode, Global Lower grey threshold, 63 Upper grey threshold, 255	**10**	Thresholding Mode, Global Lower grey threshold, 63 Upper grey threshold, 255
4	Despeckle Type: Remove white speckles (3D space) Volume : less than 150 voxels Apply to: Image	**11**	Individual object analysis (2D space)
5	3D analysis	**12**	Bitwise operations <Image> = COPY <Clipboard>
6	Save bitmaps “API Particle”	**13**	Arithmetical operations <Image> = <Image> MUL <Value> Value,10.000000
7	Reload Image	**14**	Save bitmaps (only image) “Maj Dm color coded”

10.1.3 Raman microscopy

Table 21: Rotigotine: Raman microscopy 2D measurement parameters

Measurement Parameter for 2D	**Value**
Method type	Streamline HR image acquisition
Laser	532 nm
Grating	1800 l/mm
Center	1000
Confocality	normal
Exposure time	0.3 s
Laser power	100%
Step x / step y [µm]	5 / 5 (47x48)
Magnification	20x
Duration	11 min, 40s

Table 22: Rotigotine: Raman microscopy 3D measurement parameters.

Measurement Parameter for 3D	**Value**
Method type	Volume image acquisition
Laser	532 nm
Grating	1800 l/mm
Center	1000 cm^{-1}
Confocality	high
Exposure time	0.2 s
Laser power	50%
Step x / step y / step z [µm]	5 / 5 / 5
Number of spectra	17x18x12
Magnification	20x
Duration	18min 36min

10.1.4 SEM/EDX

Table 23: Rotigotine: Overview SEM/EDX image

Measurement parameter	**Value**
Observation condition	EDX
Observation mode	Charge-up reduction
Image mode	Mix
Magnification	600x

Table 24: Rotigotine: Zoomed-in SEM/EDX image.

Measurement parameter	Value
Observation condition	EDX
Observation mode	Standard
Image mode	Mix
Magnification	1200x

10.1.5 Dissolution data

Table 25: Rotigotine: Dissolution data of the faulty batch and test batches A and B.

	Faulty Batch		Test Batch A		Test Batch B	
Time [min]	Start	End	Start	End	Start	End
0	0	0	0	0	0	0
5	29	16	29	16	28	27
15	44	30	44	30	43	42
30	59	43	59	43	57	56
45	67	54	68	52	66	66
60	75	62	75	60	74	73
120	93	87	93	84	92	92
180	99	96	97	95	96	97
300	99	98	97	96	97	98
720	101	101	98	97	99	98

10.2 FCT – Ticagrelor

10.2.1 Micro-CT measurement and reconstruction parameters

Table 26: Ticagrelor: Micro-CT measurement and reconstruction parameters.

Measurement parameter	Value	Reconstruction parameter	Value
Number of Files	3600	Smoothing	1 (smoothing kernel = 2 (Gaussian))
Number of rows and columns	2688 x 2903	Ring artifact correction	9
Partial width	72%	Beam hardening correction [%]	55
Source voltage [kV]	40	Minimum for CS to Image Conversion	0.000000
Source current [µA]	166	Maximum for CS to Image Conversion	0.064618
Image pixel size [µm]	4.00		
Exposure (ms)	880		
Rotation step [deg]	0.100		
360° rotation	yes		
Frame averaging	5		
Random movement	off		
Filter	Al 0.25 mm		
Scan duration	6h:54m:0s		

Measurements for the tablets are performed in 4k resolution and downscaled to 2k for analysis. The reason being, 4k files are so large that computational times for analysis are too long to be usable.

10.2.2 Micro-CT analysis task lists

Firstly, manual thresholding, despeckle and dilation is used to achieve a suitable mask, which is subsequently used to isolate the tablet.

Table 27: Ticagrelor: Task list for tablet isolation. (TL_TIC_01)

1	Reload Image	**7**	Despeckle Type: Remove pores (2D space) Detected by: by image borders Apply to: Image
2	Thresholding Mode, Global Lower grey threshold, 76 Upper grey threshold, 255	**8**	Despeckle Type: Sweep (3D space) Remove: all except the largest object Apply to: Image
3	Despeckle Type: Remove pores (2D space) Detected by: by image borders Apply to: Image	**9**	Bitwise operations <Region of Interest> = COPY <Image>
4	Despeckle Type: Remove white speckles (2D space) Area: less than 100 pixels Apply to: Image	**10**	Reload Image
5	Morphological operations Type: Dilation (3D space) Kernel: Round Radius: 1 Apply to: Image	**11**	Bitwise operations <Image> = <Image> AND <Region of Interest>
6	Morphological operations Type: Dilation (3D space) Kernel: Round Radius: 1 Apply to: Image	**12**	Save bitmaps (only image)

To separate the film coating from the tablet, the film coating is isolated using manual thresholding, despeckle and dilation operations, is then saved as a mask and lastly subtracted from the whole image set of the isolated tablet.

Table 28: Ticagrelor: Task list for film coating removal. (TL_TIC_02)

1	Reload Image	**6**	Morphological operations Type: Erosion (3D space) Kernel: Round Radius: 1
2	Thresholding Mode, Global Lower grey threshold, 109 Upper grey threshold, 255	**7**	Bitwise operations <Region of Interest> = COPY <Image>
3	Despeckle Type: Remove white speckles (3D space) Volume : less than 400 voxels	**8**	Reload Image

	Apply to: Image		
4	Morphological operations Type: Dilation (3D space) Kernel: Round Radius: 3 Apply to: Image	**9**	Bitwise operations <Image> = <Image> SUB <Region of Interest>
5	Despeckle Type: Sweep (3D space) Remove: all except the largest object Apply to: Image	**10**	Save bitmaps (only image) “Isolated tablet without film coating”

For the API isolation, the data set is filtered, converted to black and white using manual thresholding and despeckled. This is followed by one regular data analysis step and a second one that outputs images with color-coding of particles according to size, which lastly have to be adjusted to the 0-255 color-space.

Table 29: Ticagrelor: Task list for API isolation and analysis. (TL_TIC_03)

1	Reload Image	**7**	3D analysis
2	Arithmetical operations <Image> = <Image> MUL <Value> Value,1.500000	**8**	Individual object analysis (3D space)
3	Filtering Mode, Gaussian blur (3D space) Kernel, Round Radius, 1.5	**9**	Save bitmaps (only image) “API”
4	Filtering Mode, Anisotropic diffusion (3D space) Type, Privilege wide regions (Perona-Malik) Number of iterations, 10 Gradient threshold, 5.000000 Integration constant, 0.068182	**10**	Bitwise operations <Image> = COPY <Clipboard>
5	Thresholding Mode, Global Lower grey threshold, 120 Upper grey threshold, 255	**11**	Arithmetical operations <Image> = <Image> MUL <Value> Value,15.000000
6	Despeckle Type: Remove white speckles (3D space) Volume : less than 40 voxels Apply to: Image	**12**	Save bitmaps (only image) “Color coded”

10.2.3 Raman microscopy

Table 30: Ticagrelor: Raman microscopy measurement parameters for the reference and faulty batch.

Measurement Parameter	**Values for reference batch**	**Values for faulty batch**
Method type	Streamline HR image acquisition	Streamline image acquisition
Laser	633 nm	785 nm
Grating	1800 l/mm	1200 l/mm
Center	1000 cm^{-1}	1000 cm^{-1}
Confocality	standard	standard
Exposure time	0.4 s	0.4 s
Laser power	50%	100%

Step x / step y [µm]	12.5 / 12.5	12.5 / 12.5
Number of spectra	529x529	529x529
Magnification	1:20	1:20
Duration	1d, 7h, 10min	

10.2.4 Dissolution Data

Table 31: Ticagrelor: Dissolution data of the reference and the faulty batch.

Time [min]	Reference batch	Faulty batch
0	0	0
5	78	65
10	89	77
15	92	81
20	94	85
30	96	90
45	97	95
60	98	98

Table 32: Ticagrelor: Dissolution data of API with high and low amount of agglomerates.

Time [min]	API with low amount of agglomerates	API with high amount of agglomerates
0	0	0
5	72	19
10	82	31
15	85	42
20	87	51
30	89	62
45	91	78
60	93	87

10.3 GRC – Esomeprazole

10.3.1 Micro-CT measurement parameters

Table 33: ESO/GRC: Measurement and reconstruction parameters

Measurement parameter	Value	Reconstruction parameter	Value
Number of Files	2400	Smoothing	0
Number of rows and columns	1344 x 967	Ring artifact correction	4
Partial width	48%	Beam hardening correction [%]	60
Source voltage [kV]	45	Minimum for CS to Image Conversion	-0.013644
Source current [µA]	166	Maximum for CS to Image Conversion	0.096761
Image pixel size [µm]	7.00		

Exposure (ms)	857
Rotation step [deg]	0.150
360° rotation	yes
Frame averaging	4
Random movement	off
Filter	Al 0.25 mm
Scan duration	3h:32m:13s

10.3.2 Micro-CT analysis task lists

TL_ESO/GRC_01 is used to isolate the pellets from the background, remove the capsule and separate pellets that are connected to each other. It starts with a binarization step to roughly obtain the pellets. This is further refined using multiple despeckle and dilation/erosion steps to get a mask. This mask is then applied to a differently binarized data set. Secondly, the data set is prepared for the watershed algorithm for pellet separation using a broader manual threshold, which is then treated with the previously generated mask to obtain a binarized image, only containing areas of the pellets. After separation, this data set is used as a mask on the original data set to receive isolated pellets with full density information.

Table 34: ESO/GRC: Task list for pellet isolation (TL_ESO/GRC_01).

1	Reload Image	**12**	Bitwise operations <Region of Interest> = COPY <Image>
2	Thresholding Mode, Global Lower grey threshold, 103 Upper grey threshold, 255	**13**	Reload Image
3	Despeckle Type: Remove pores (2D space) Detected by: by image borders	**14**	Thresholding Mode, Global Lower grey threshold, 47 Upper grey threshold, 255
4	Despeckle Type: Remove white speckles (3D space) Volume : less than 40000 voxels	**15**	Bitwise operations <Image> = <Image> AND <Region of Interest>
5	Morphological operations Type: Erosion (3D space) Kernel: Round Radius: 1	**16**	Despeckle Type: Remove pores (3D space) Detected by: by image borders
6	Despeckle Type: Remove white speckles (3D space) Volume : less than 10000 voxels	**17**	Morphological operations Type: Watershed separation (3D space) Tolerance: 1
7	Morphological operations Type: Dilation (3D space) Kernel: Round Radius: 1	**18**	Bitwise operations <Region of Interest> = COPY <Image>
8	Morphological operations Type: Dilation (3D space) Kernel: Round Radius: 1	**19**	Reload Image
9	Morphological operations Type: Dilation (3D space) Kernel: Round Radius: 1	**20**	Bitwise operations <Image> = <Image> AND <Region of Interest>
10	Morphological operations	**21**	Save bitmaps (only image)

	Type: Dilation (3D space) Kernel: Round Radius: 1		
11	Morphological operations Type: Dilation (3D space) Kernel: Round Radius: 1		

TL_ESO/GRC_02 is used to obtain the core+ region, the isolation layer and the GR-layer as individual components. The isolation layer is readily available using manual thresholding. For the core+ region, the binarized image of the isolation layer is digitally filled using the pore removal algorithm yielding a data set consisting of the core+ and the isolation layer. To get only the ´core+ region the isolation layer is subtracted. For the GR-layer, the image sum of the isolation layer and the core+ is subtracted from the whole pellets. Several noise reduction and stray particle removal steps are incorporated to get clean images for the core+ and GR-layer.

Table 35: ESO/GRC: Task list for pellet component separation (TL_ESO/GRC_02).

1	Reload Image	**15**	Save bitmaps (only image) “Core+”
2	Reload Region of Interest	**16**	Reload Image
3	Reload Clipboard	**17**	Thresholding Mode, Global Lower grey threshold, 147 Upper grey threshold, 255
4	Thresholding Mode, Global Lower grey threshold, 120 Upper grey threshold, 255	**18**	Save bitmaps (only image) “Isolation Layer”
5	Morphological operations Type: Dilation (3D space) Kernel: Round Radius: 1	**19**	Bitwise operations <Clipboard> = COPY <Image>
6	Despeckle Type: Remove pores (2D space) Detected by: by image borders	**20**	Reload Image
7	Bitwise operations <Region of Interest> = COPY <Image>	**21**	Thresholding Mode, Global Lower grey threshold, 1 Upper grey threshold, 255
8	Reload Image	**22**	Despeckle Type: Remove white speckles (3D space) Volume : less than 50000 voxels
9	Thresholding Mode, Global Lower grey threshold, 1 Upper grey threshold, 147	**23**	Save bitmaps (only image) “Whole Pellets”
10	Bitwise operations <Image> = <Image> AND <Region of Interest>	**24**	Bitwise operations <Image> = <Image> SUB <Region of Interest>
11	Morphological operations Type: Erosion (3D space) Kernel: Round Radius: 1	**25**	Bitwise operations <Image> = <Image> SUB <Clipboard>
12	Morphological operations Type: Dilation (3D space)	**26**	Despeckle Type: Remove white speckles (3D space)

	Kernel: Round Radius: 1		Volume : less than 100 voxels
13	Bitwise operations <Region of Interest> = COPY <Image>	**27**	Reload Region of Interest
14	Despeckle Type: Remove white speckles (3D space) Volume : less than 10000 voxels	**28**	Save bitmaps (only image) “GR-layer”

For analysis, the isolated components generated with TL_ESO/GRC_02 are separately loaded into the software, binarized and individual object analysis is performed in 3D.

Table 36: ESO/GRC: Task list for individual component analysis (TL_ESO/GRC_03).

1	Reload Image	**3**	Individual object analysis (3D space)
2	Thresholding Mode, Global Lower grey threshold, 1 Upper grey threshold, 255		

To obtain the volume and sphericity information needed for the detection of defects in the isolation layer the TL_ESO/GRC_04 is implemented. The isolation layer is binarized using a manually thresholding step (with a slightly broader range compared to TL_ESO/GRC_02. to lessen the effect of measurement artifacts such as beam hardening), the hollow spheres are filled using the “remove pore” algorithm. The resulting data set consist of hollow spheres where the isolation layer is not intact and of spheres where the isolation layer is without defects and is analyzed using individual object analysis. Finally, the data set is colored coded according to the structure thickness, which enables the later presentation of defects using a different color compared to intact pellets.

Table 37: ESO/GRC: Task list for defect detection (TL_ESO/GRC_04).

1	Reload Image	**6**	3D analysis
2	Thresholding Mode, Global Lower grey threshold, 105 Upper grey threshold, 255	**7**	Bitwise operations <Image> = COPY <Clipboard>
3	Despeckle Type: Remove pores (3D space) Detected by: by image borders	**8**	Arithmetical operations <Image> = <Image> MUL <Value> Value,10.000000
4	Despeckle Type: Remove white speckles (3D space) Volume : less than 1000 voxels Apply to: Image	**9**	Save bitmaps (only image) “Color-coded St.Th.”
5	Individual object analysis (3D space)		

10.3.3 Raman microscopy

Table 38: ESO/GRC: Raman microscopy measurement parameters for individual pellets encased in resin.

Measurement Parameter	Values for innovator and in-house batches
Method type	Streamline image acquisition
Laser	785 nm
Grating	1200 l/mm
Center	1000 cm^{-1}
Confocality	standard
Exposure time	0.3 s
Laser power	100%
Step x / step y [µm]	6 / 6
Magnification	1:50

10.3.4 SEM/EDX GRC

Table 39: ESO/GRC: SEM/EDX measurement parameters for the investigation of whole pellets

Measurement parameter	Value
Obeservation condition	EDX
Observation mode	Standard
Image mode	Mix
Magnification	180x

Table 40: ESO/GRC: SEM/EDX measurement parameters for the investigation of pellet layers (zoomed-in image).

Measurement parameter	Value
Obeservation condition	EDX
Observation mode	Standard
Image mode	Mix
Magnification	1000x

10.3.5 Dissolution data

Table 41: ESO/GRC: Dissolution data of the analyzed GRC batches.

Time	Batch 1	Batch 2	Batch 3	Batch Z	Batch A	Batch B	Batch C
0	0	0	0	0	0	0	0
5	0	0	0	0	0	0	1
10	0	0	0	0	0	0	5
15	3	5	4	1	1	0	18
20	32	37	35	8	7	2	53

25	74	77	73	30	27	13	83
30	93	93	91	62	59	40	94
35	96	94	94	87	85	71	95
40	95	93	93	96	94	89	94
50	94	91	91	96	96	95	92
60	93	90	90	96	95	95	91

10.4 MUT – Esomeprazole

10.4.1 Micro-CT measurement parameters

Table 42: ESO/MUT: Micro-CT measurement and reconstruction parameters for the whole tablet.

Measurement parameter	Value	Reconstruction parameter	Value
Number of Files	3600	Smoothing	0
Number of rows and columns	2688 x 2016	Ring artifact correction	2
Partial width	50%	Beam hardening correction [%]	40
Source voltage [kV]	45	Minimum for CS to Image Conversion	0.000000
Source current [µA]	166	Maximum for CS to Image Conversion	0.084494
Image pixel size [µm]	5.50		
Exposure (ms)	1980		
Rotation step [deg]	0.100		
360° rotation	yes		
Frame averaging	5		
Random movement	off		
Filter	Al 0.25 mm		
Scan duration	14h:50m:20s		

Table 43: ESO/MUT: Micro-CT measurement and reconstruction parameters for tablet section.

Measurement parameter	Value	Reconstruction parameter	Value
Number of Files	1252	Smoothing	3 (smoothing kernel = 2 (Gaussian))
Number of rows and columns	2688 x 4032	Ring artifact correction	5
Partial width	OFF	Beam hardening correction [%]	67
Source voltage [kV]	45	Minimum for CS to Image Conversion	-0.067818
Source current [µA]	166	Maximum for CS to Image Conversion	0.130172
Image pixel size [µm]	2.00		
Exposure (ms)	3600		
Rotation step [deg]	0.150		
360° rotation	yes		
Frame averaging	4		
Random movement	off		
Filter	Al 0.25 mm		

Scan duration	6h:49m:23s

Measurements for the tablet sections are performed in 4k resolution and downscaled to 2k for analysis. The reason being, 4k files are so large that computational times for analysis are too long to be usable.

10.4.2 Micro-CT analysis task lists

TL_ESO/MUT_01 is used for the isolation of the whole tablet from the background, the separation of the film coating and the isolation of particles consisting of the core+ and isolation layer.

The first step is the implementation of a filtering algorithm, which conserves high contrast edges, for noise reduction. The film coating is isolated using manual thresholding, despeckle and dilation. For the isolation of the whole tablet, manual thresholding and multiple despeckle and dilation/erosion steps are performed. To receive particles consisting of the core+ and the isolation layer, firstly a manual thresholding step is used. Since the isolation layer of the pellets and the film coating of the tablet share relative density values the film coating is subtracted from the image. The next steps are despeckle operations yielding the desired bi-layer particles. Lastly, these particles are colored coded according to their respective sizes.

Table 44: ESO/MUT: Task list for the analysis of whole tablets (TL_ESO/MUT_01).

1	Reload Image	**15**	3D analysis
2	Filtering Mode, Anisotropic diffusion (3D space) Type, Privilege high contrast edges (Perona-Malik) Number of iterations, 10 Gradient threshold, 5.000000 Integration constant, 0.068182	**16**	Reload Image
3	Thresholding Mode, Global Lower grey threshold, 95 Upper grey threshold, 255	**17**	Thresholding Mode, Global Lower grey threshold, 70 Upper grey threshold, 255
4	Despeckle Type: Sweep (3D space) Remove: all exept the largest object	**18**	Bitwise operations <Image> = <Image> SUB <Clipboard>
5	Morphological operations Type: Dilation (3D space) Kernel: Round Radius: 1	**19**	Despeckle Type: Remove white speckles (3D space) Volume : less than 500 voxels
6	Save bitmaps (only image) “Tablet film coating”	**20**	Despeckle Type: Remove pores (3D space) Detected by: by image borders
7	Morphological operations Type: Dilation (3D space) Kernel: Round	**21**	Despeckle Type: Remove white speckles (3D space) Volume : less than 1500 voxels

	Radius: 1		
8	Bitwise operations <Clipboard> = COPY <Image>	**22**	Reload Clipboard
9	Reload Image	**23**	Save bitmaps (only image) “core+ and isolation layer”
10	Thresholding Mode, Global Lower grey threshold, 73 Upper grey threshold, 255	**24**	Individual object analysis (3D space)
11	Despeckle Type: Remove pores (2D space) Detected by: by image borders	**25**	Bitwise operations <Image> = COPY <Clipboard>
12	Morphological operations Type: Dilation (3D space) Kernel: Round Radius: 1	**26**	Arithmetical operations <Image> = <Image> MUL <Value> Value,10.000000
13	Despeckle Type: Remove pores (2D space) Detected by: by image borders	**27**	Save bitmaps (only image) “core+ and isolation layer color coded”
14	Morphological operations Type: Erosion (3D space) Kernel: Round Radius: 1		

In TL_ESO/MUT_02, the analysis of tablet sections with pellet isolation and pellet component separation is show.

To remove noise and random density fluctuation the data set is treated with two different filtering steps. The first one preserves high contrast edges to enhance the separation of the individual components as well as the differentiation of the pellets from the surrounding tablet material. The second one to reduce density fluctuation in larger areas with similar relative density, especially in the core+ and in regions of tablet filling material. Steps 4 – 16 are used to get the entire pellets starting from a pellet nucleus and building up. This is necessary because pellet components and tablet filler material share many relative density values. After this, the low relative density values are subtracted (step 18 -19) to further separate the pellets from the surrounding medium. After several despeckle and erosion steps a watershed algorithm is implemented to separate pellets that are connected. Finally, in the steps 27-30 the relative density is reintroduced and the isolated pellets saved.

Table 45: ESO/MUT: Task list for the isolation of pellets of tablet sections (TL_ESO/MUT_02).

1	Reload Image	**16**	Bitwise operations <Region of Interest> = COPY <Image>
2	Filtering Mode, Anisotropic diffusion (3D space) Type, Privilege high contrast edges (Perona-Malik) Number of iterations, 10 Gradient threshold, 5.000000	**17**	Reload Image

	Integration constant, 0.068182		
3	Filtering Mode, Anisotropic diffusion (3D space) Type, Privilege wide regions (Perona-Malik) Number of iterations, 10 Gradient threshold, 5.000000 Integration constant, 0.068182	**18**	Thresholding Mode, Global Lower grey threshold, 10 Upper grey threshold, 98
4	Thresholding Mode, Global Lower grey threshold, 131 Upper grey threshold, 255	**19**	Bitwise operations <Image> = <Region of Interest> SUB <Image>
5	Despeckle Type: Sweep (3D space) Remove: all exept the largest object	**20**	Despeckle Type: Remove pores (3D space) Detected by: by image borders
6	Morphological operations Type: Dilation (3D space) Kernel: Round Radius: 3	**21**	Despeckle Type: Remove pores (2D space) Detected by: by image borders
7	Bitwise operations <Clipboard> = COPY <Image>	**22**	Morphological operations Type: Erosion (3D space) Kernel: Round Radius: 1
8	Reload Image	**23**	Despeckle Type: Remove white speckles (3D space) Volume : less than 6000 voxels Apply to: Image
9	Thresholding Mode, Global Lower grey threshold, 126 Upper grey threshold, 255	**24**	Morphological operations Type: Watershed separation (3D space) Tolerance: 1
10	Bitwise operations <Image> = <Image> SUB <Clipboard>	**25**	Despeckle Type: Remove white speckles (3D space) Volume : less than 1000 voxels
11	Despeckle Type: Remove white speckles (3D space) Volume : less than 6000 voxels Apply to: Image	**26**	Individual object analysis (3D space)
12	Morphological operations Type: Dilation (3D space) Kernel: Round Radius: 2	**27**	Bitwise operations <Region of Interest> = COPY <Image>
13	Despeckle Type: Remove pores (3D space) Detected by: by image borders	**28**	Reload Image
14	Morphological operations Type: Dilation (3D space) Kernel: Round Radius: 7	**29**	Bitwise operations <Image> = <Image> AND <Region of Interest>
15	Despeckle Type: Remove pores (3D space)	**30**	Save bitmaps (only image) “Isolated Pellets”

In TL_ESO/MUT_03, the isolation of the individual pellet components is shown for the high-resolution measurements of tablet sections. For the isolation of the GR-layer, the isolation layer is roughly binarized, filled and treated using despeckle and dilation/erosion operations. The results are then subtracted from the whole pellet leaving the GR-layer. The isolation layer is received using manual thresholding and despeckle. For the core+ region, the GR-layer and isolation layer is subtracted from the whole pellets.

Table 46: ESO/MUT: Task list for the analysis of isolation of GR-layer, isolation layer and core+ of tablet sections (TL_ESO/MUT_03).

1	Reload Region of Interest	**14**	Save bitmaps (only image) “GR-layer”
2	Reload Image	**15**	Reload Image
3	Thresholding Mode, Global Lower grey threshold, 125 Upper grey threshold, 255	**16**	Thresholding Mode, Global Lower grey threshold, 136 Upper grey threshold, 255
4	Despeckle Type: Remove pores (2D space) Detected by: by image borders	**17**	Despeckle Type: Remove white speckles (3D space) Volume : less than 1000 voxels
5	Despeckle Type: Remove white speckles (3D space) Volume : less than 500 voxels	**18**	Save bitmaps (only image) “Isolation layer”
6	Morphological operations Type: Dilation (3D space) Kernel: Round Radius: 2	**19**	Bitwise operations <Clipboard> = COPY <Image>
7	Morphological operations Type: Erosion (3D space) Kernel: Round Radius: 2	**20**	Reload Image
8	Bitwise operations <Region of Interest> = COPY <Image>	**21**	Thresholding Mode, Global Lower grey threshold, 5 Upper grey threshold, 255
9	Reload Image	**22**	Bitwise operations <Image> = <Image> SUB <Region of Interest>
10	Thresholding Mode, Global Lower grey threshold, 5 Upper grey threshold, 255	**23**	Bitwise operations <Image> = <Image> SUB <Clipboard>
11	Bitwise operations <Image> = <Image> SUB <Region of Interest>	**24**	Despeckle Type: Remove white speckles (3D space) Volume : less than 15000 voxels
12	Despeckle Type: Remove white speckles (3D space) Volume : less than 500 voxels	**25**	Despeckle Type: Remove pores (3D space) Detected by: by image borders
13	Bitwise operations <Region of Interest> = COPY <Image>	**26**	Save bitmaps (only image) “Core+”

10.4.3 Raman microscopy

Table 47: ESO/MUT: Raman microscopy measurement parameters.

Measurement Parameter	**Values**
Method type	Streamline image acquisition
Laser	785 nm
Grating	1200 l/mm
Center	1000 cm^{-1}
Confocality	standard
Exposure time	1.3 s
Laser power	100%

Step x / step y [µm]	6 / 6
Magnification	1:100

10.4.4 SEM/EDX

Table 48: ESO/MUT: SEM/EDX measurement parameters for the investigation of whole pellets.

Measurement parameter	Value
Obeservation condition	EDX
Observation mode	Standard
Image mode	Mix
Magnification	200x

10.5 LMU – CAN/SA

10.5.1 Micro-CT measurement parameters

Table 49: CAN/SA Micro-CT measurement and reconstruction parameters.

Measurement parameter	Value	Reconstruction parameter	Value
Number of Files	1800	Smoothing	0
Number of rows and columns	1344x 1330	Ring artifact correction	3
Partial width	66%	Beam hardening correction [%]	30
Source voltage [kV]	80	Minimum for CS to Image Conversion	-0.030160
Source current [µA]	125	Maximum for CS to Image Conversion	0.168295
Image pixel size [µm]	5.50		
Exposure (ms)	1314		
Rotation step [deg]	0.200		
360° rotation	YES		
Frame averaging	3		
Random movement	OFF		
Filter	Al 1mm		
Scan duration	3h:8m:39s		

10.5.2 Micro-CT analysis task lists

In a first step, manual thresholding is used to remove the capsule and background fluctuations.

Table 50: CAN/SA: Task list for the isolation of particles (TL_CAN/SA_01).

1	Reload Image	**5**	Reload Image
2	Reload Region of Interest	**6**	Bitwise operations <Image> = <Image> AND <Region of Interest>
3	Thresholding Mode, Global Lower grey threshold, 90	**7**	Save bitmaps (only image)

	Upper grey threshold, 255		
4	Bitwise operations <Image> = COPY <Clipboard>		

In a second step CAN particles are isolated using manual thresholding, despeckle to remove noise, and a watershed algorithm to separate particles that are connected to each other into individual particles.

Table 51: CAN/SA: Task list isolation of CAN particles (TL_CAN/SA_02).

1	Reload Image	**6**	Bitwise operations <Region of Interest> = COPY <Image>
2	Reload Region of Interest	**7**	Reload Image
3	Thresholding Mode, Global Lower grey threshold, 125 Upper grey threshold, 255	**8**	Bitwise operations <Image> = <Image> AND <Region of Interest>
4	Despeckle Type: Remove white speckles (3D space) Volume : less than 100 voxels	**9**	Save bitmaps (only image)
5	Morphological operations Type: Watershed separation (3D space) Tolerance: 2		

In the last step, the processed data set received after TL_CAN/SA_02, is binarized using manual thresholding and individual object analysis is performed in 3D. After this, two actions are implemented to generate images with particles colored according to their respective sizes.

Table 52: CAN/SA: Task list for the analysis of CAN particles (TL_CAN/SA_03).

1	Reload Image	**4**	Bitwise operations <Image> = COPY <Clipboard>
2	Thresholding Mode, Global Lower grey threshold, 155 Upper grey threshold, 255	**5**	Arithmetical operations <Image> = <Image> MUL <Value> Value,10.000000
3	Individual object analysis (3D space)	**6**	Save bitmaps (only image)

10.5.3 Raman microscopy

Table 53: CAN/SA: Raman microscopy measurement parameters.

Measurement Parameter	**Values for point measurements**	**Values for whole particle mapping**
Method type	Single spectrum (5 acquisitions)	Streamline image acquisition
Laser	785 nm	785 nm
Grating	1200 l/mm	1200 l/mm
Center	1200 cm^{-1}	1200 cm^{-1}
Confocality	standard	standard

Exposure time	3s	0.8 s
Laser power	10%	50%
Step x / step y [µm]	n.a.	13 / 13
Magnification	1:20	1:20
Number of spectra		50x48
Duration		149.9 s

Acknowledgement

First of all, I would like to thank Prof. Karaghiosoff for making this work in the context of the pharmaceutical industry possible and always helping with input along the way.

Next, I would like to thank Dr. Müller at the Hexal AG for providing the laboratory and equipment as wells as inspiring conversations about the pharmaceutical world.

A big thank you also goes to the "Analytical Services" group, which gave me a warm welcome and always supported me in my daily work. Namely my incredibly supportive co-workers: Andreas, Brigitte, Carolin, Christine, Fabian, Helmut, Markus, Maria, Michaela, Philipp, Rita. Additionally thank you to all my other co-workers throughout the company helping me understand specifics topics such as IVIVC, manufacturing and generally the inner workings of a pharmaceutical company.

In addition, a sincere thank you goes to Alicia for our successful collaboration, expanding the scope of this work to new horizons.

Furthermore, I want to thank the research group of Prof. Karaghiosoff for being my base camp on the university campus and most notably Marco, who always provided help concerning scientific and administrative questions.

Finally yet importantly, I would like to thank my family and friends who have always supported me in my decade long venture into science.